The Dissertation Committee for Ryan Alan Mesch Certifies that this is the approved version of the following dissertation:

Catalyst and Material Development for Photolithography

Committee:

_____
C. Grant Willson, Supervisor

_____
Adrian Keatinge-Clay

_____
Christopher Ellison

_____
Michael Rose

_____
Keith Stevenson

Catalysis and Materials Development for Photolithography

by

Ryan Alan Mesch, B.A.

Dissertation

Presented to the Faculty of the Graduate School of

The University of Texas at Austin

in Partial Fulfillment

of the Requirements

for the Degree of

Doctor of Philosophy

The University of Texas at Austin

August 2014

Dedication

Dedicated to Keith Mesch

I strive to not only to be a great scientist like you, but also to be an equally great husband and father.

&

In memory of Dr. Nicholas Turro

Acknowledgements

When I earned my Eagle Scout award fifteen years ago, my scoutmaster at the time said, “Congratulations to Mrs. Mesch and also to Ryan for accomplishing the rank of Eagle.” I would never have made it to Eagle without the guiding hand of my mother, and its equally true that I would not be where I am today if it were not for the large number of extremely talented and wonderful mentors and collaborators along the way.

Prof. Grant Willson, thank you. The four and a half years working in your group has made me a better scientist and person. You’ve believed in me when I was not certain I believed in myself. I will forever be grateful for your wisdom and patience. The opportunity you gave me has profoundly changed my life, and I hope I will one day find a way to pass it forward.

I could not have asked for a better mentor my first year in the Willson group than Dr. Xinyu Gu. It’s rare to find someone so humble, so brilliant, and so easy-going. I am thankful to have worked with you and been apart of the pitchdivision project with you. I must also make special mention of Wade Wang, my incredibly talented undergraduate. Your enthusiasm, even if a bit reckless at times, was an inspiration and it was an honor and a pleasure to have worked with you over the years. To all the other students in the Willson group, visiting scientists, and outside collaborators that worked on pitchdivision and the EUV project, especially William Bell, Yuji Hagiwara, Takanori Kawakami, Kensuke Matsuzawa, Andrew Dick, Youngjin Cho, James Blackwell, Steffen Jockusch,

Arun Sundaresan, Nicholas Turro, and Yongjun Li. A special thank you must be made to Greg Wallraff, Hoa Trung, and Dan Sanders of IBM for their work with the final imaging studies of pitchdivision. Their hospitality and effort was well beyond anything I could have ever dreamed of. I am incredibly fortunate to have worked with every person mentioned above on pitchdivision. It was a real honor and a please to meet and work along side of you all.

To everyone in the Willson group that I worked along side of and made my days better: Greg Blachut, Michael Maher, Michael Jacobsson, Benjamin Cassidy, Colin Hayes and Will Durand. Your friendship, ideas, and motivation helped carry me through the past five years.

There were a large number of people outside of the Willson group that I consulted with and went to for advice including Ryan Patman, Prof Dionico Siegel, Caleb Hethcox, and Shawn Blumberg. Thank you for your advice and guidance, you all saved me many months of synthetic headaches!

Finally I want to thank my family and my beautiful wife, Jeeyeon Lee. Your support and encouragement kept me going everyday. A special thank you to my father, Keith Mesch, for taking the time to proofread and edit my hectically written dissertation. The whole dissertation committee thanks you. It could have been so much worse on them!

Catalyst and Material Development for Photolithography

Ryan Alan Mesch, Ph.D.

The University of Texas at Austin, 2014

Supervisor: C. Grant Willson

In recent years the microelectronics industry as found itself at an impasse. The tradition pathway towards smaller transistors at lower costs has hit a roadblock with the failure of 157 nm lithography and the continued delays in 13.5 nm extreme ultra violet light sources. While photolithography has been able to keep pace with Moore's law over the past four decades, alternative patterning technologies are now required to keep up with market demand.

The first section of this dissertation discusses the new resolution enhancement technique develop in the Willson lab termed pitchdivision. Through the incorporation of specifically tailored photobase generators (PBGs) into commercially available resists, the resolution of current 193 tools may be doubled. Special two-stage PBGs were designed and synthesized to increase the image fidelity of pitchdivision patterns.

The next project deals with the design, synthesis, and evaluation of resists that find amplification through unzipping polymers. An aromatizing polyester polymer that acts as dissolution inhibitor in novolac and is inherently sensitive to 13.5 nm exposure is

discussed. Initial results show excellent sensitivity and promise towards a new class of EUV resists.

Table of Contents

List of Tables

List of Figures

Chapter 1. Introduction to Microlithography

1.1 BACKGROUND

The invention of the solid-state transistor in the late 1940's by Bell Labs was a pivotal moment in history, clearing a new path towards smaller and more durable replacements for vacuum tubes (Figure 1.1.A).(*1*) Close to a decade later, Jack Kilby of Texas Instruments and Robert Noyce of Fairchild Semiconductor independently developed various forms of the integrated circuit (IC); a chip with more than one transistor per circuit (Figure 1.1.B). The dawn of integrated circuitry brought about the rapid development of sophisticated electronic devices that consumed less energy, space, and capital. The great achievements in the development of ICs has catalyzed the staggering and unprecedented advancements in nearly every aspect of society over the past forty years.(*2*)

In 1964, Fairchild Semiconductor had produced 64 components on a single chip. A sizeable feat considering the young technology suffered from fairly poor transistor yield only a few years prior. In 1965 Gordon Moore made his famous prediction that transistor count will double every year for the next ten years while the cost per transistor will drop. He arrived at this prediction by extrapolating from only four years of data! (Figure 1.3.A)

A

B

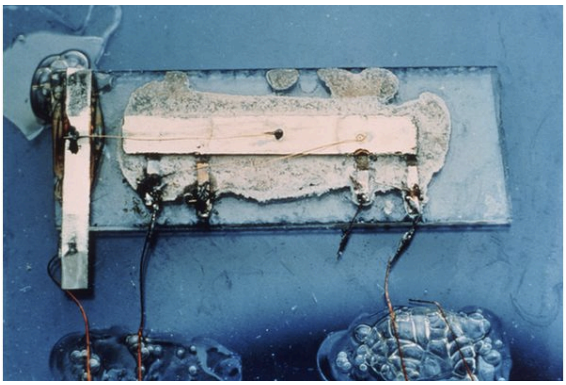

Figure 1.1: Photographs of (a) Schockley's original solid-state transistor (Courtesy of The Porticus Center)(*1*) (b) Kilby's first IC (Courtesy of Texas Instruments)

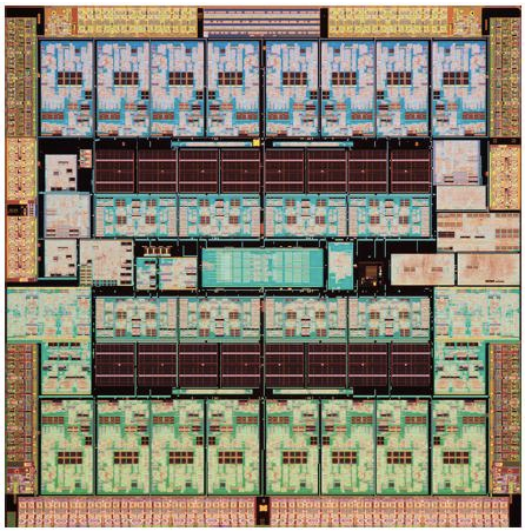

Figure 1.2: Photograph of a modern computer processor, the Oracle SPARC T3.(*2*)

In 1975 he revisited his prediction that was only off by a factor of two, which was remarkably accurate considering his bold initial extrapolation. He surmised that the prediction was and would continue to be upheld by three trends in the industry: 1) continual shrinkage of the transistor size, 2) increased size of the chip, and 3) "device cleverness" or design improvements.(*3*) From 1975 onward, nearly every sector of the microelectronics industry has kept pace with Moore's law doubling density every 18 to 24 months as illustrated in Figure 1.3.B.

This pace of improvement is staggering and is not replicated in any other industry. The price of a transistor today is about 1 millionth the average price of a transistor in 1968, and the processors themselves are thousands of times more powerful and efficient. The auto industry is often used in comparison to add perspective to the staggering rate of innovation and optimization in the semiconductor industry. If auto technology kept the same pace in the areas of improved efficiency and decreasing costs, a new car today would cost about 1 cent and get 26,000 miles on a single gallon of gas.(*4*, *5*) The industry's ability to keep pace with Moore's law has depended on its ability to continually invent "engineering cleverness." This cleverness is particularly well highlighted in the field of photolithography.

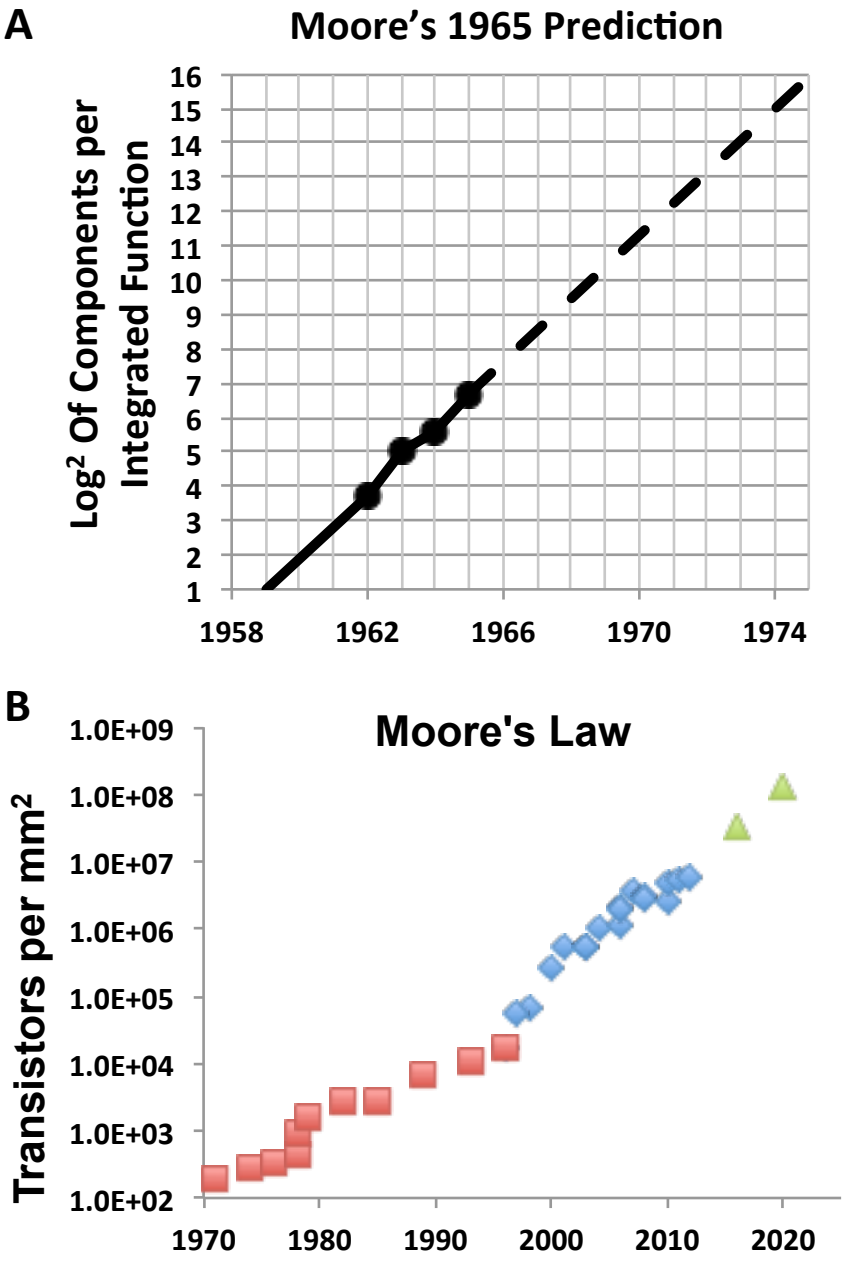

Figure 1.3: (a) Moore's original 1965 prediction. (Copyright © IEEE)(*3*) (b) Realization of Moore's law since 1970 (red squares and blue diamonds). Green triangles show future expectations of transistor density. (Data compiled from manufacturer press releases)

1.2 PHOTOLITHOGRAPHY

The word photolithography comes from the Greek roots *photo-* meaning light and *-lithography,* which means to write in stone. Through photolithography the semiconductor industry uses light to transfer images of circuits into silicon wafers for processing into IC's This technique has been used since the 1960's to continually shrink the size of ICs. Photolithography is in many ways analogous to traditional darkroom photography, where the silicon wafer is the paper upon which a light sensitive emulsion, termed a photoresist, is coated. Instead of enlarging the image from a negative, the exposure system is designed to shrink the image of a photomask, which is traditionally composed of binary opaque and transparent regions. A photoresist is a polymer or resin matrix that is both *photo*sensitive and *resist*ant to etching chemistries. Upon exposure, a photoresist undergoes a solubility change, only in the illuminated region. Subsequent development either removes the non-exposed region, termed a negative-tone resist or more commonly, a positive-tone resist where development removes the exposed region. The development of the photoresist forms a two-dimensional relief pattern. (Figure 1.4)

The patterned resist acts as a mask so the final etch step may transfer the image from the mask into the silicon wafer before stripping away the remaining resist. The etched areas are then subsequently used for the installation of the patterned layers of conductors, insulators and semi-conducting materials that comprise an IC. This iterative layer-by-layer method is done up to 40 times in order to make a single transistor.(*6*)

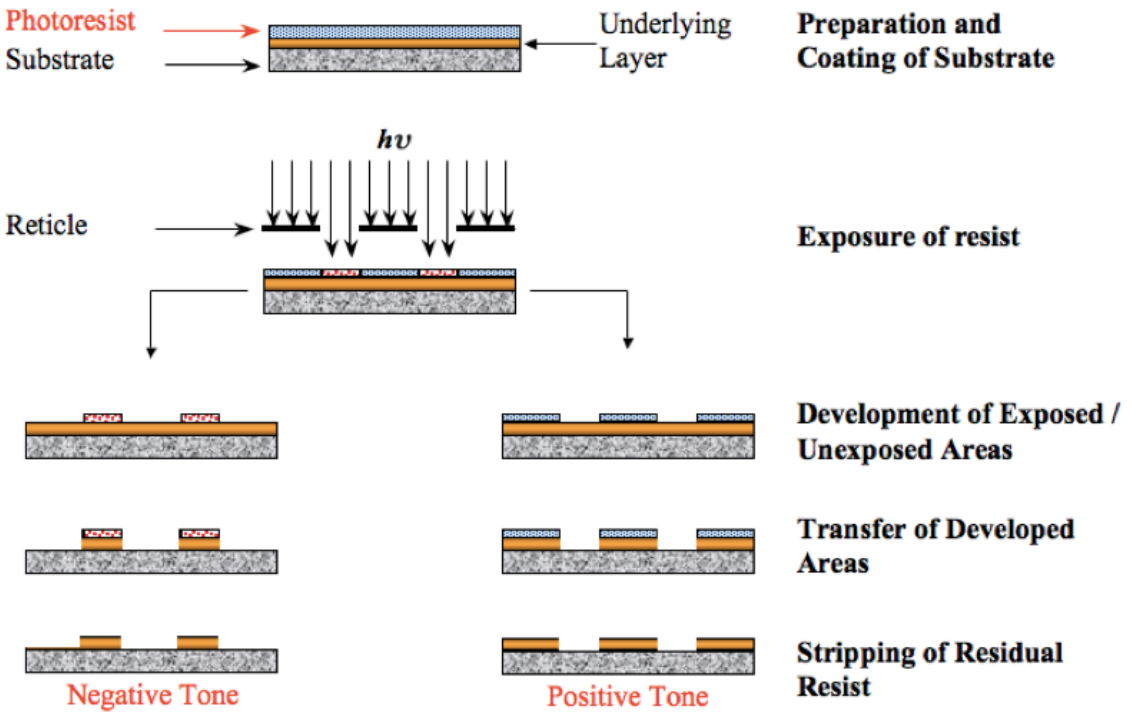

Figure 1.4: Schematic of the simplified pholotlithographic process of negative and positive tone resists.(*7*)

1.3 PHOTORESISTS

One of the earliest and most ubiquitous photoresists in lithography combines Novolac and diazonaphthoquinone (DNQ) based resins (Figure 1.5). Novolac is a phenol-formaldehyde resin resistive to many forms of etching and is soluble in aqueous basic developer. The Lewis basicity of DNQ creates a strong hydrogen bond association with the alcohol of the phenolic resin, resulting in their mixture being insoluble in aqueous base at sufficiently high DNQ loadings. Upon exposure to UV light, DNQ undergoes a Wolff rearrangement which expels nitrogen upon forming a ketene.(*8*) The ketene

undergoes nucleophilic attack from trace water in the resin to form an acidic compound that serves to promote dissolution, thus accelerating the solubility switch. (Figure 1.5)(*9*). DNQ-Novolac blends were the industry workhorse until the 1980s, when manufacturers began switching over to 248 nm light sources.

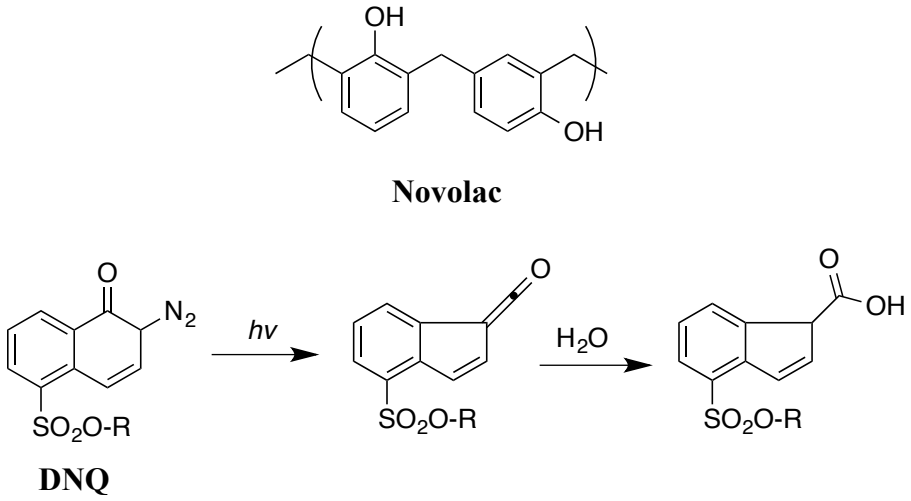

Figure 1.5: Illustration of Novolac and DNQ and an illustration of DNQ's solubility switch upon UV exposure.

The desire for 248 nm sources outpaced the technological development of reliable excimer laser technology. This forced the continued use of mercury arc lamps, even though they generate little energy at 248 nm. (Figure 1.7)(*8*) To avoid long exposure doses and bottlenecks in manufacturing, a new type of ultra-fast photoresist was needed. This pressing problem ushered in a new era for photolithography through the development of chemically amplified resists (CAR). In a DNQ-Novolac blend, every photoreaction creates only one carboxylic acid and frees up one phenol. CARs found

significant amplification through acid sensitive tert-butyloxycarbonyl alcohol protecting groups on poly(4-hydroxystyrene) by incorporating a photoacid generator (PAG) with the polymer. Upon exposure and subsequent post exposure baking, the photo-generated acid rapidly catalyzes deprotection events along the polymer revealing the hydrophilic phenols resulting in the desired solubility switch (Figure 1.6).

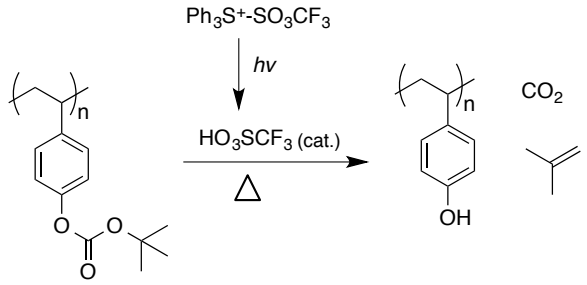

Figure 1.6: Illustration of a positive tone chemically amplified resist.

In this system, each photoreaction can catalyze hundreds of deprotection events. IBM created and commercialized the first fully developed CAR systems in the early 1980's, yet it should be noted that the earliest mention of a photoacid catalyzed system was by George Smith at 3M in 1981.(*10*) Since the implementation of CARs in the 1980's, they have continually evolved with every new node to carry the semiconductor industry along the path of Moore's Law.

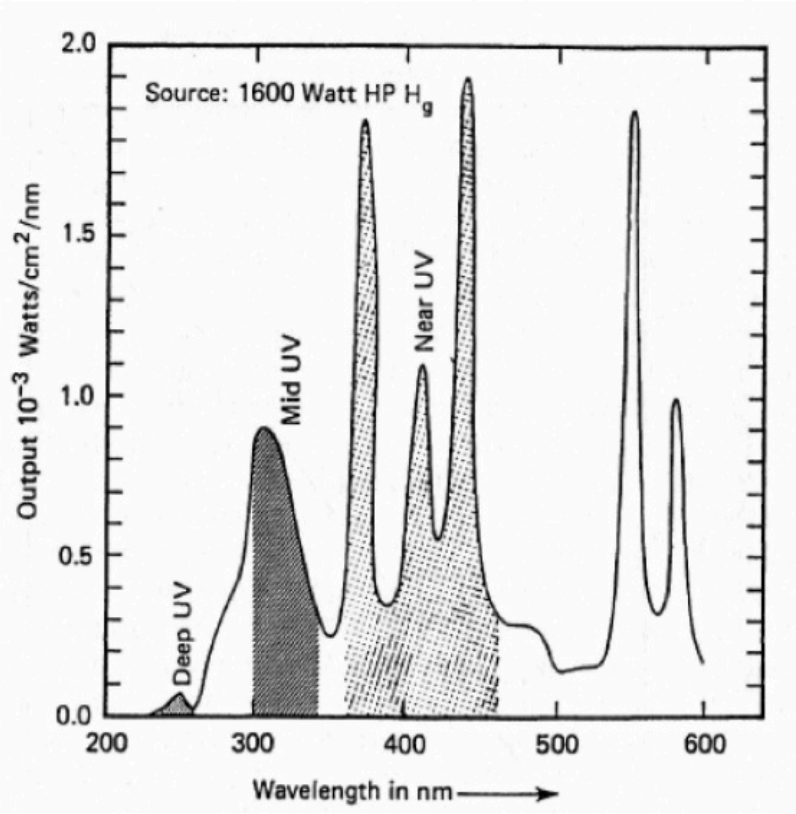

Figure 1.7: Illustration of the power available at the wafer plane from a mercury arc lamp.(*8*)

1.4 RAYLEIGH'S CRITERION

For the past 40 years, projection lithography has been utilized to transfer and miniaturize mask data to the wafer plane. Projection lithography enables the use of reduction lenses, which allow up to a 4:1 minimization of the mask. Figure 1.8 shows a simplified projection scheme in which light passes through a mask and is focused on the wafer through such a reduction lens system. Projection systems are able to avoid small particle contamination on the mask through the use of a thin transparent membrane

known as a pellicle, which covers the mask. The pellicle ensures that small particle contamination is far enough away from the mask pattern to be out of focus. With its ability to shrink mask data and avoid small particle contamination, projection lithography has been the backbone of the semiconductor industry over the past forty years.

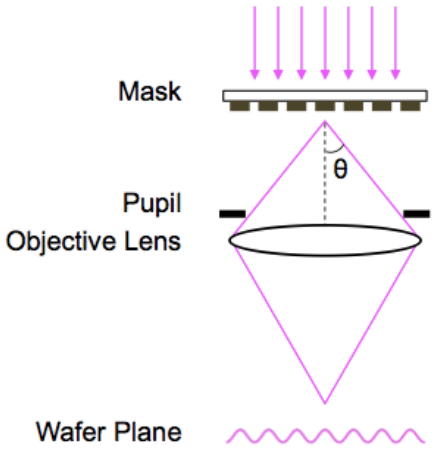

Figure 1.8: Illustration of a simplified projection lithography system.

For every new generation of smaller integrated circuits, the lithographic process must be improved. Since the prevalence of projection lithography, this requires optimizing the tool in relation to the Rayleigh Criterion (1.1).

$$\text{Resolution} = k_1 \cdot \frac{\lambda}{NA} \qquad \text{Eq. 1.1}$$

Named after its discoverer, the avid astronomer Lord Raleigh, the equation defines how close two points of light can be before they are indistinguishable. Originally working with telescopes, Rayleigh discovered that for two stars to be distinguishable, the two airy disks (center of the diffraction pattern) cannot overlap to the point that the distance

between the two centers is equal to or smaller than their radii. Rayleigh's criterion occurs when the center of one disc is at the first minimum of the other disc as illustrated in Figure 1.9.B.

From this definition, Rayleigh formulated the equation shown as Eq. 1.1, which defines the relationship of the light source wavelength (λ), the optical system's ability to capture light defined as its numerical aperture (NA), and a constant k_1 (Rayleigh factor). The Rayleigh factor is equal to 1.220, which describes the minimal distance relationship illustrated in Figure 1.9.

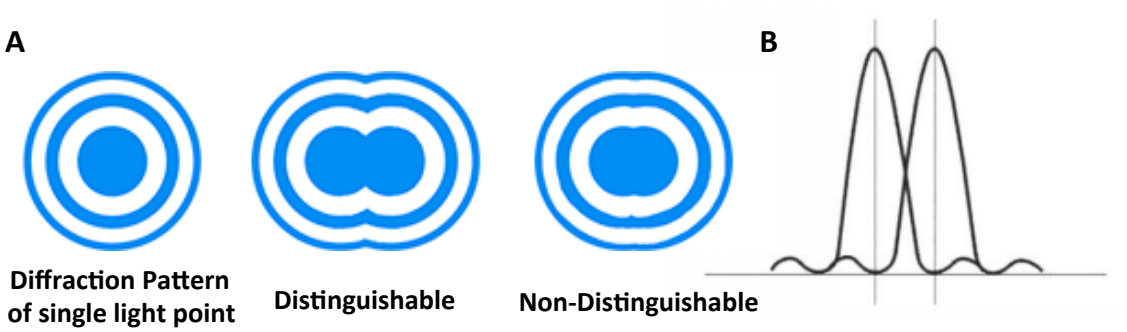

Figure 1.9: Illustration of Rayleigh's Criterion.

The unit-less parameter k_1 was initially derived experimentally, but has adapted a loosely defined physical relationship to projection lithography. For instance, information specific to the exposure setup, mask composition, and resist chemistry are all combined in the k_1 value. In 2001, the International Technology Roadmap for Semiconductors (ITRS),(*11*) set the ''half-pitch'' of densely packed lines and spaces as the benchmark of

lithographic tools, since isolated lines and spaces are easier to print. In the case of light passing though a mask composed of slits, the angular diffraction of the first minimum is defined by Eq. 1.2, which differs from isolated points of light described by Rayleigh in Eq. 1.1.

$$sin\theta' = m\frac{\lambda}{a} \qquad \text{Eq. 1.2}$$

With θ' as the diffraction angle of the light passing through a slit, a is the width of the slit and m is the minimum. In the case of packed lines and spaces, $k_1 = 1$. Fitting the original Rayleigh equation to 1.2 and accounting for the ITRS half-pitch benchmark gives Eq. 1.3:

$$R_{min} = \frac{P}{2} = 0.5\frac{\lambda}{sin\theta} = 0.5\frac{\lambda}{NA}. \qquad \text{Eq. 1.3}$$

To further complicate the Rayleigh factor, many optics-based resolution enhancement techniques exist to improve the image contrast or to increase image resolution. These techniques including phase shift masks, optical proximity compensation (OPC), and many other approaches known as resolution enhancement techniques (RET). Most RETs simply improve the quality of the aerial image, yet some are able to increase the resolution of the projection system, such as off-axis illumination.

When a mask composed of densely packed lines and spaces is illuminated with a conventional photolithographic system, several diffracted light rays are formed by the slits (Figure 1.10.A). Zero-order light proceeds straight through the system, and several rays of higher order generate with diffraction angles of θ (1st order), 2*θ (2nd order), etc, with $\theta \approx \lambda/a$ for small θ. Image transfer from the mask to the wafer plane requires the

transmission of at least two rays, which reconstruct the original grating pattern upon their subsequent recombination. Therefore, at the resolution limit only the zero-order and first-order diffractions are able to pass through the lens pupil.

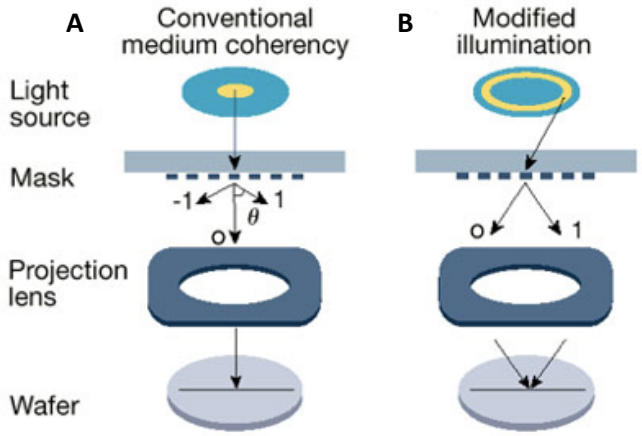

Figure 1.10: Illustration conventional illumination to that of off-axis illumination.(*12*)

Off-axis illumination uses an oblique light source, as shown in Fig. 1.10.B. This results in the zero-order light no longer passing through the center of the pupil, but at an angle to the vertical. The first-order rays still come at an angle of ±θ with respect to the zero-order, but only one of the first order rays is able to pass through the side of the lens pupil opposite to that of the zero-order(*12*). The end results are the doubling of the spatial frequency of the images. (Eq. 1.4)

$$R_{min} = 0.25\frac{\lambda}{NA}. \qquad \text{Eq. 1.4}$$

Optical-based RET techniques allow for projection systems to push closer to the hard physical limit of $k_1 = 0.25$, but none of them allow for this number to be surpassed. Currently, industry operates just above 0.25 to allow for process latitude and well-defined resist responses.

To continually improve the resolution of projection lithography tools, engineers must work within the bounds of the Rayleigh Criterion. As such, the resolution is inversely proportional to the NA of the lens and directly proportional to the exposure wavelength. With k_1 set to a minimum of 0.25, there are only two methods available to increase the strength of the optics, either go to lower λ or increase the nominal aperture, NA.

1.4.1 Optimizing Wavelength

The development of short-wavelength light sources and corresponding compatible photoresist systems have been the center of research since the introduction of photolithography. The earliest light sources used mercury arc lamps with isolation filters to isolate specific bands of light. By the early 1980's arc lamps were reaching the end of their life cycle and were replaced with excimer lasers. The first excimer laser used for lithography operated at 248 nm (KF), which allowed reduction of features down to around 100 nm in size. Currently, the industry standard tool used is an ArF 193 nm excimer source allowing features ~40 nm in size to be generated.(*13*)

When 193 nm tools were first introduced, research was already looking for the next generation light source. For some time, it appeared that F_2 157 nm tools would

replace 193 nm sources, but the supporting technologies such as pellicles and lenses could not be developed in time. Changing from 193 nm to 157 nm provides only a 17% size reduction, which combined with all the delays, caused Intel to drop implementation of 157 nm source from their production plans in 2003.(*14*) There was even some development of 121.6 nm tools, but that too suffered from similar lens issues and low power sources.(*15*, *16*)

Upon abandoning F_2 lithography, the industry then set their sights squarely on the development of 13.5 nm extreme ultraviolet lithography (EUV). In theory, EUV is capable of printing single digit nanometer features; making it the ultimate lithographic tool. Unfortunately, complex compounding of many variables hamper the development of EUV. EUV is absorbed by nearly every material and gas and therefore the optical path must be contained within a vacuum and must be focused through sets of highly complex molybdenum/silicon layered mirrors. These mirrors absorb approximately 30% of the light they receive and since each tool requires at least 6 mirrors, only ~10 % of the initial power ever reaches the wafer. (Figure 1.11)

This complexity requires the source to be extremely powerful, with current estimates predicting the need of a 250W source for high production (~ 120 wafers an hour). As of 2013, the latest generations of tools can boast only 70W sources. The timeline for a stable 250W tool appears to be quite far in the future. With predicted tool costs currently approaching $130 million and with no estimated delivery date of a 250W tool, the future of EUV and its place in manufacturing remains uncertain.

Figure 1.11: Illustration of EUV exposure tool. (Courtesy of ASML).

1.4.2 NUMERICAL APERATURE

The numerical aperture (NA) of the lithographic system describes the amount of light captured by the objective lens and is defined as n*sin (θ), with n being the refractive index of the medium in which the light travels and θ as half the acceptance angle of the lens system (Figure 1.8). The size of the NA has been optimized from 0.16 in the earliest scanners to 0.93, today, which captures a significant amount of mask data while avoiding internal reflections caused by higher orders of refraction. The size of NA is tunable through optimizing the refractive index (n) of the gas or fluid surrounding the projection lens. In an open-air system n = 1 while in water n = 1.44. The use of oil (n = 1.5) and water as immersion fluids for microscopy has been in existence since the 19th century,

with the first example produced by Amici of Modena. The first mention of immersion lithography tools was in a 1985 patent application by Takanashi,(*17*) however, it wasn't until in the early 2000's that ASML and Nikon produced a successful demonstration (Figure 1.12).(*18*) Once material compatibility issues were resolved, immersion 193 nm lithography was fully embraced by the industry and was key to achieve the 45 nm node and beyond.

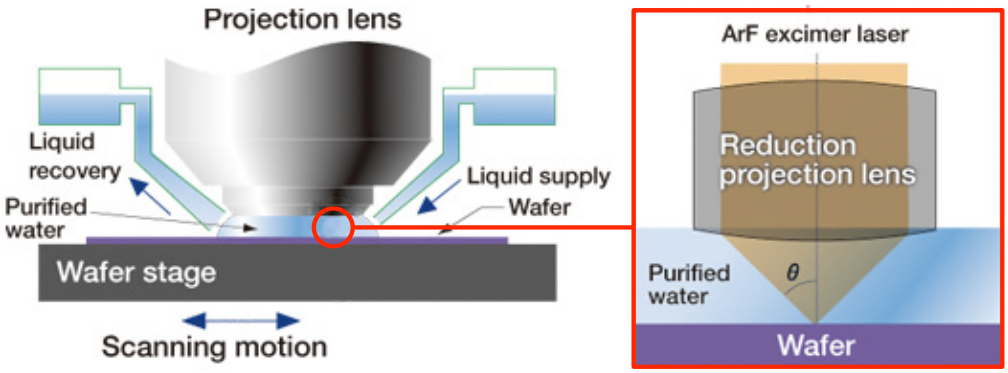

Figure 1.12: Illustration immersion lithography. (Courtesy of Nikon)

Significant research has gone into finding new high refractive index fluids and materials to increase the NA. To date, no new fluids have been discovered that are transparent at 193 while not suffering from degradation. Consequently, the trade-off between high-index and low-absorbance has proven to be too challenging. Transparent single-component organic liquids have been developed, but the refractive index was no higher than ~1.65, affording only a relatively small gain and ultimately not considered worth the investment to optimize further.(*15*)

New lens materials such as lutetium aluminum garnet (LuAG, n = 2.14) and sapphire (n = 1.92) were extensively studied to replace the standard fused silica lenses (n = 1.56), but suffered from contamination issues and manufacturing difficulties.(*19*) Over all, during the past 25 years, all three quantities of the Rayleigh Criterion have so far been optimized to reduce CD_{min}:

- ***NA*** has grown from 0.5 to 1.35
- **λ** has been reduced from 365 to 193 nm
- $\boldsymbol{k_1}$ has been reduced from 0.7 to ~0.27

With the delays in EUV and the abandonment of high-refractive index materials, the industry was forced to use costly and step-intensive double patterning techniques to reach the 32 nm node.

1.5 DOUBLE PATTERNING LITHOGRPAHY

In 2009, traditional immersion 193 nm lithography achieved its physical limit with the production of the 45 nm node. While a 45 nm (HP) only corresponds to a k_1 of ~0.3, processing wafers below a k_1 of 0.3 requires a significant improvement in all aspects of wafer handling including exposure, track laydown and the development processes. Engineering all these aspects to near perfection to allow a k_1 closer to 0.25 is decidedly too costly for the minor improvement that would result. The hard limit of immersion193nm lithography, and the endless delays in a strong stable EUV source have brought the industry to a crossroads with no clear path forward.

With every variable of the Rayleigh equation (1.4) currently optimized, device manufacturers have resorted to multiple step double patterning lithography (DPL). Figure 1.13 illustrates a simple example how printing trenches with larger spaces between them and then using a second mask to print a second set of trenches in these larger spaces, creates more densely packed lines and spaces allowing critical dimensions that are smaller than possible in a single pass. For example, the two sets of trenches may be patterned with a wide process value of 0.5, resulting in lines and spaces with a theoretical value of 0.25. While this technique of DPL seems simple, alignment issues along with the nature of chemically amplified resists are proving a challenge to realize.(*20*)

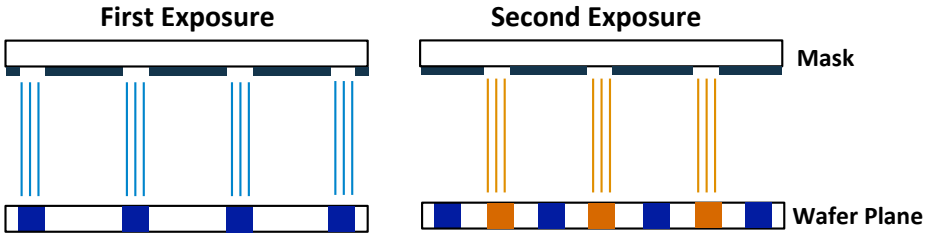

Figure 1.13: Illustration of double exposure lithography.

Figure 1.14 illustrates how the straightforward addition of two sequential exposures upon a standard photoresist sums to create no image. This is caused by some acid generation in the opaque exposed regions due to diffraction and diffusion. Developing new resist chemistry and techniques to allow for double patterning is of great interest.(*21*, *22*)

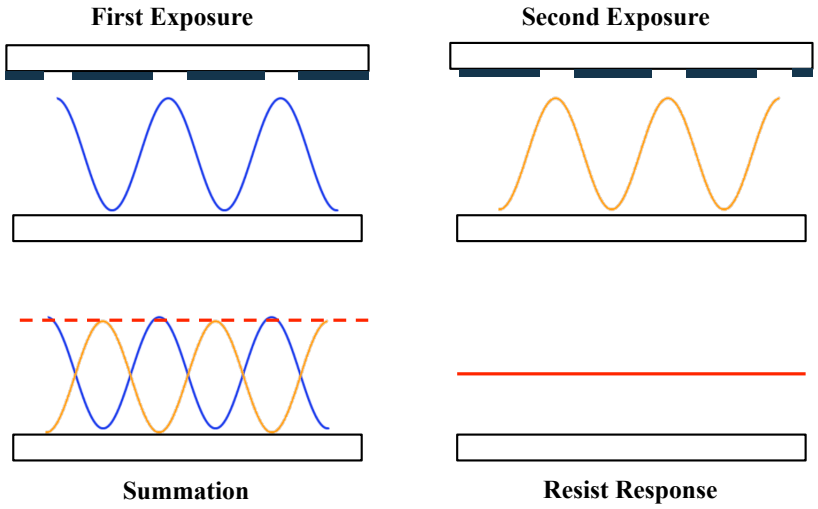

Figure 1.14: Illustration of "zero resist response" from the summation of double exposure doses with a standard CAR.

Some of the new approaches proposed include self-aligned double patterning (SADP), dual tone development (DTD),(*23*) litho-freeze-litho-etch (LFLE),(*24*, *25*) and directed self-assembly lithography (DSA).(*26-28*)

This introduction will briefly describe LFLE, the process that brought about the 32 nm node(*29*) and continues to be used commercially today.

1.5.1 LITHO-FREEZE-LITHO-ETCH (LFLE)

To avoid the net acid generation issue illustrated in Figure 1.14, the LFLE process requires two resist applications, two exposures, and two development steps. Figure 1.15 illustrates the general LFLE process. The process flow begins with standard lithography steps: application of the resist, exposure, bake, and development. The

resulting pattern then undergoes a freeze step before applying a second resist. The freeze changes the solubility of the first pattern preventing it from being dissolved when the second resist solution is applied to the wafer. This freezing is accomplished either through chemical or thermal transformation of the patterned resist. The new resist undergoes another full lithography cycle of exposure, bake, and development. The LFLE process has been demonstrated to produce feature sizes below 30 nm.(*29*) The entire process more than doubles the number of required steps, doubles the number of masks required, and also suffers from strict alignment requirements of the second exposure.

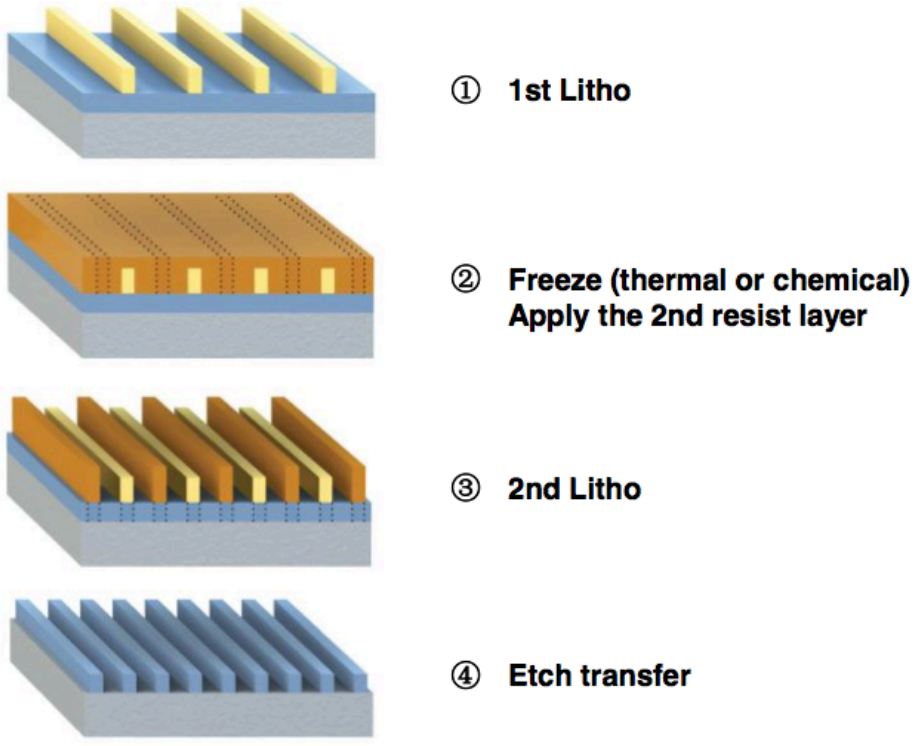

Figure 1.15: Illustration of the LFLE process flow. (*Adapted from Ref* (*28*); Copyright © IEEE)

1.6 MOTIVATIONS & OUTLINE

In a modern fabrication process, it can take a single microprocessor from 30-60 days to go from bare silicon to the final product. The bottleneck of the entire process is the photolithographic steps, which account for up to 30% of the total cost of manufacturing.(*6*) The currently utilized PDL approaches greatly increase the cost of ownership. New resist materials capable of doubling the resolution of current tools currently do not exist. While this situation has created a dilemma for the semiconductor industry, it has created a diverse and exciting arena for chemists and engineers to develop unique, innovative approaches towards the continuation of Moore's Law.

The first part of this dissertation, Chapters 2-4, discusses a resolution enhancement technique termed pitchdivision. Through a simple modification of standard CARs, pitchdivision is able to double the resolution of current 193 nm and 248 nm exposure systems. Pitchdivision has been successfully demonstrated in the Willson group(*30*) and the majority of this dissertation focuses on the improvement of image fidelity through the design and synthesis of novel photobase generators.

The second section of this dissertation, Chapter 5-6, discusses a new route towards EUV resists, which utilize unzipping polymers as a source of amplification rather than catalysis. Current EUV resists suffer from low sensitivity or allow extreme line edge roughness (LER). Increasing PAG loading leads to increases in sensitivity, but increasing the PAG loading also increases LER. Resorting to polymers that unzip from a macromolecule leaving its individual monomers allows for a source of amplification that

does not rely upon the diffusion of a catalyst. Chapters 5 & 6 discuss the design, synthesis and early results of a new form of unzipping EUV resist.

Chapter 2: Introduction to Pitchdivision Lithography

Chapter 1 discusses the current approached to double patterning lithography (DPL), which requires increased tool ownership and exacerbates the existing lithography bottleneck in device manufacturing. This chapter introduces a new method of resolution enhancement that that allows for an effective Rayleigh constant as low as $k_1 = 0.125$. This new approach termed, pitchdivision, was recently described by Dr. Xinyu Gu in the Willson Lab (*31*). In theory, pitchdivision formulations are capable of utilizing currently available resists, track and exposure technologies to bring about the 22 nm node without the need of any extra steps or tools. This chapter discusses the theory and simulation of pitchdivision lithography and a brief review of similar approaches described in literature that are capable of a single-exposure resolution-doubling lithography.

2.1 BACKGROUND

Without a powerful and reliable EUV source, double patterning lithography has proven necessary to achieve the 22 nm node. While the double patterning lithography (DPL) strategies briefly described in Chapter 1 work, many suffer from alignment issues, which quickly sap all 12 percent of the critical dimension error budget. The desire to avoid expensive self-aligned processes has led to research examining single-exposure density-doubling lithography.

The main concept of single-exposure density doubling lithography is based around splitting the aerial image of the lithographic pattern into threes rather than a

normal binary system. Figure 2.1 illustrates this type of pitchdivision where the photoresist responds to two thresholds, one of which is positive (E_0) and one of which is negative (E_n).

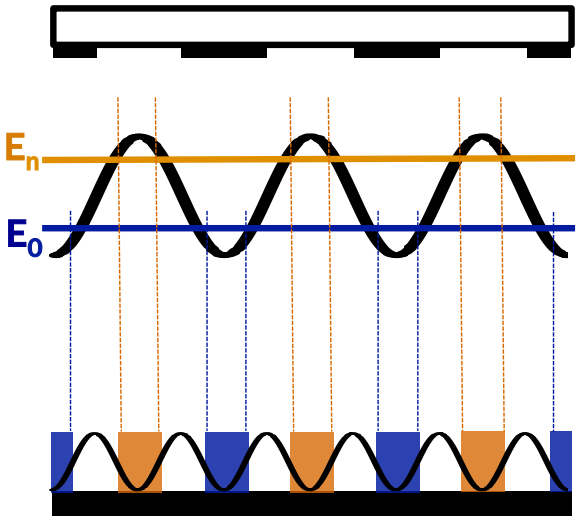

Figure 2.1: Illustration of single-exposure density doubling lithography

As early as 1996, IBM filed a patent for a “frequency doubling hybrid photoresist."(*32*) The approach described by Katnani, *et. al.* is a combination of both a positive and negative tone resist. At low doses the resist behaves as a standard positive tone resist but at higher doses it acts in a negative tone manner and forms an insoluble cross-linked network. IBM achieves this behavior by selecting acid sensitive cross-linkers that require larger doses of acid than the main component positive-tone matrix to reach its solubility-switching threshold.

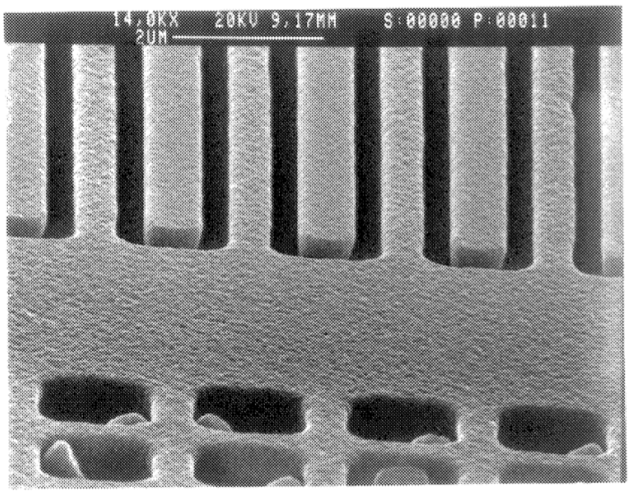

Figure 2.2: Image of single- density doubling lithograpy.(*32*)

Fedynyshyn reported a very similar approach at the MIT Lincoln Labs in a 2008 patent(*15*, *33*). Both of these systems have been demonstrated to work, but suffer from swelling induced line-edge roughness at smaller CDs. While both of these approaches demonstrate how ingenuity and innovative design may accomplish single-exposure pitch division, the inherent nature of these cross-linked designs will likely keep them from practical application at the 22 nm node.

2.2 PITCHDIVSION

The first non-crosslinking form of pitchdivision was demonstrated in the Willson lab(*30*) by altering the net acid profile of a 193 nm resist. Compared to a typical positive-tone photoresist that undergoes pseudo first-order acid generation kinetics upon exposure (Figure 2.3.A), a pitchdivision resist generates a parabolic net acid profile as shown in

Figure 2.3.B. As a pitchdivision resist is exposed, acid generation continues until a mid-dose range where it starts to diminish or get quenched.

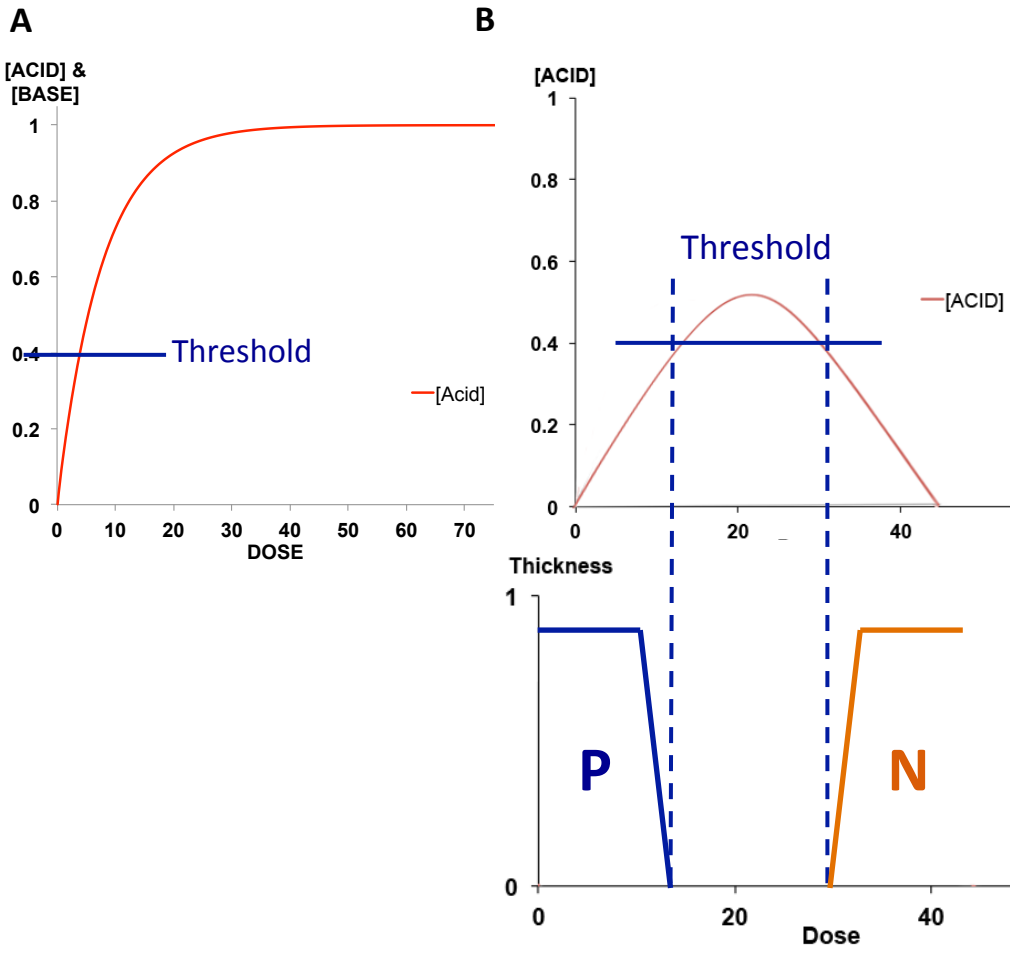

Figure 2.3: Illustration of acid generation in (a) a standard CAR and in (b) a pitchdivision formulation.

This unique net acid profile allows the resist to cross the solubility threshold two times and create a positive tone image at low dose (E_p) and a negative tone image at high dose (E_n). The solubility threshold is the minimum amount of acid needed to make a

polymer soluble in basic developer. Fortunately the solubility as a function of acid concentration is highly non-linear, such that a truly threshold like response is generated. If the net acid concentration of the pseudo-parabolic curve goes above the threshold, the polymer in that region becomes soluble. Crossing the threshold twice in a single exposure doubles the frequency of the aerial image as illustrated in Figure 2.1, where the highest concentration of acid is at the edge of the mask line and at the middle intensity of the aerial image. When the operating parameters are tuned correctly, only the middle dose region of the exposure generates enough acid for the resist to switch solubility, thus doubling the number of lines and spaces for a given mask image.

2.3 PITCHDIVISION FORMULATION

To generate a parabolic-like net acid curve, the resist must incorporate some process to quench acid at an accelerated rate proportional to dose, so that the acid is quenched in the high dose region. In pitchdivision lithography, this behavior is achieved through the incorporation of a photobase generator (PBG). Analogous to a photoacid generator (PAG), PBG's are "neutral molecules" that generate base upon irradiation to UV light. Because PAG's most commonly generate super acids (pKa < -10), even mildly basic amines instantaneously form a non-reversible salt with the active acid. The desired parabolic net acid curve can be realized through the use of both a PBG and PAG in the

$$[\text{Base}] = [\text{PBG}]_0(1-e^{-k_b \times \text{Dose}}) \approx [\text{PBG}]_0 \times k_b \times \text{Dose} \quad (\text{Dose} \rightarrow 0) \qquad \text{eq 2.1}$$

same resist if the kinetics and formulation are both carefully tuned. PAGs and PBGs are pseudo first-order in relation to dose (equation 2.1), therefore to have a full quenching of acid at high dose, the loading of the base generator must be greater than the loading of acid generator ([PBG] > [PAG]). If the loading of PBG is larger than the PAG and both are pseudo first order in relation to dose, the rate of the PBG must be less than that of the PAG ($k_b < k_a$) for there to be a net production of acid. When these requirements are met, a new net acid plot is generated as shown in Figure 2.4.

2.4 PITCHDIVISION SIMULATION

Extensive modeling with a modified version of Prolith was carried out to predict the behavior of an ideal resist formulation(*30*). To find the operating window, two main parameters were screened and optimized, which we term contrast and E-factor.

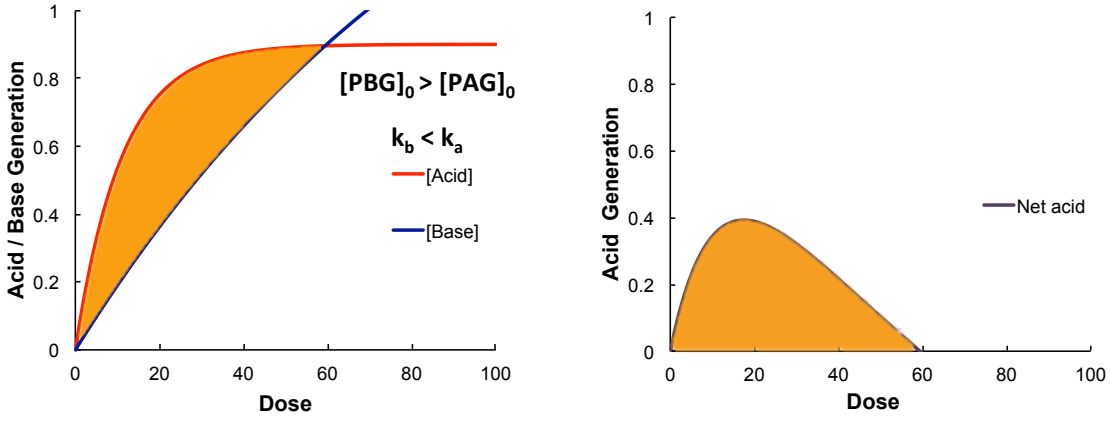

Figure 2.4: Illustration of (a) acid and base generation in a pitchdivision formulation and (b) the resulting parabolic net acid curve.

Contrast, as illustrated in Figure 2.5.A, describes the amplitude of the sinusoidal aerial image and is defined by the "Contrast" equation. The size and shape of the aerial image is determined by pitch size and the characteristics of the exposure system such as illumination source, wavelength, and polarization. For most exposure setups these factors are difficult to adjust. On the other hand, the E-factor is easier to adjust and defines the spatial relationship of E_o and E_n. The E-factor is influenced by PBG loading, dose, and post exposure bake (PEB) temperature. For pitchdivision to be successful, the E-factor must correctly overlay upon the aerial image.

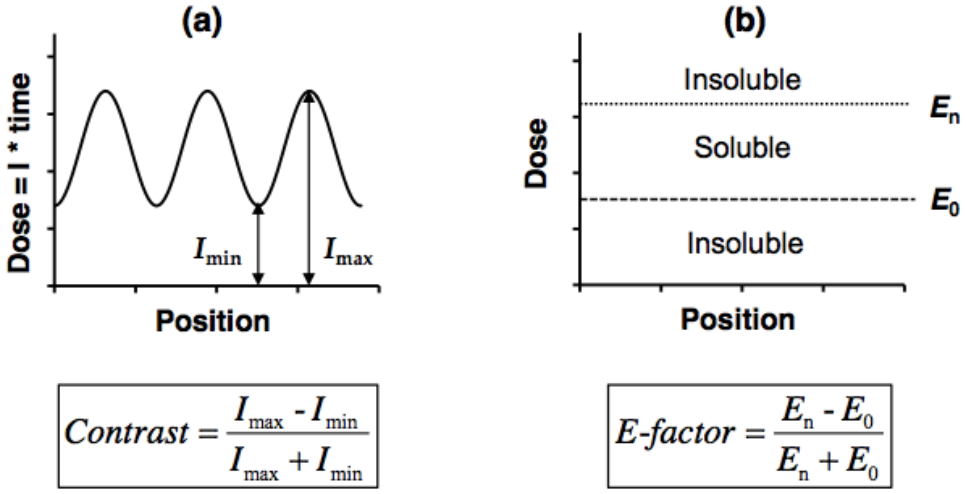

Figure 2.5: Illustration and definition of (a) aerial image contrast and (b) of E-factor. (*Adapted from Ref* (*30*))

Figure 2.6 illustrates the different combinations of the dose-threshold response (E-factor) and the contrast of the aerial image. It is clear that the E-factor must be smaller than the aerial image and that a larger aerial image creates more latitude for pitchdivision

to be successful.(*31*) In general for a medium to high contrast aerial image (0.6-0.9) the appropriate E-factor is between 0.5 and 0.6. For further information on resist formulation simulation and the factors contributing toward aerial image contrast and E-factor, please see the dissertation by Xinyu Gu.(*30*)

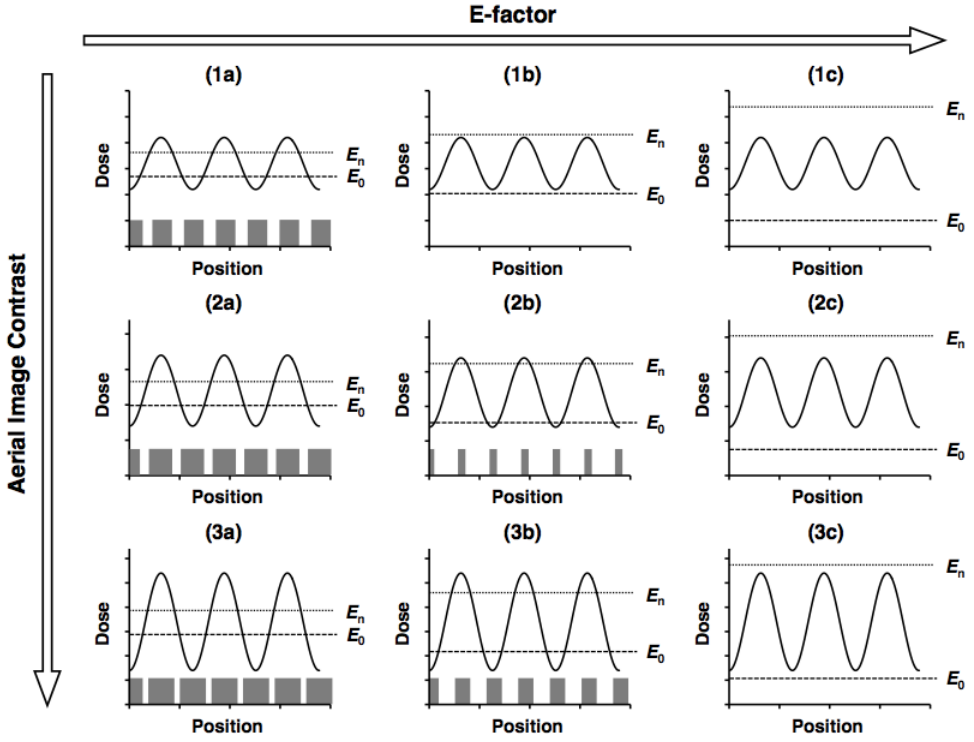

Figure 2.6: Illustration of the relationship between aerial image contrast and the dose threshold response (E-factor). (*Adapted from Ref* (*30*))

2.5 PITCHDIVISION CONSTRAINTS

The success of pitchdivision is found in crossing over the solubility threshold two times to create positive (E_0) and negative tone (E_n) responses. As a reminder, the shape of the parabolic curve for net acid production is mainly dictated by the two parameters:

$[PBG]_0$: $[PAG]_0$ and k_b : k_a. If k_b is approximately equal to k_a all of the generated acid will be quickly quenched resulting in no response from the resist due not enough net acid produced to cross the solubility threshold (Figure 2.7.A).

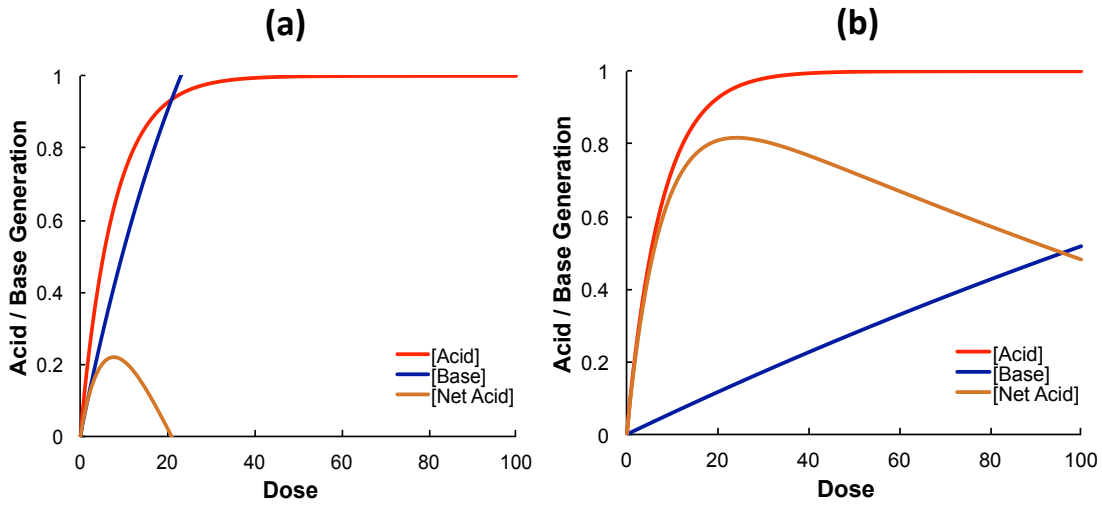

Figure 2.7: Illustration of net acid production when (a) $k_b \approx k_a$ and when (b) $k_b << k_a$.

If k_b is significantly smaller than k_a, then not enough base will be generated to quench the acid to pass through the E_n threshold (Figure 2.7.B). A very small k_b may be compensated for by increasing the loading of the PBG since k_b is proportional to [PBG] in the pseudo first-order regime. There is a limit to the maximum concentration of PBG before the loading begins to negatively impact the dissolution properties, cause a large increase in optical density, and or deteriorate the structural integrity of the of the film.

The final constraint of pitchdivision lithography is a result of its pitch doubling nature. Printing patterns with curves, circles or interconnects is not easily accomplished with resolution enhancing techniques such as pitchdivision or the other DPL approaches.

Figure 2.8 shows the response of pitch doubling techniques on lines, circles, and turns. Due to this unique behavior, traditional mask layouts are not compatible with these approaches. Early adoption in manufacturing has mostly consisted of dense line and space patterns in NAND memory production. During manufacture of NAND devices, patterns printed via SADP must undergo an extra final trim step to remove the connecting loops at the edge of the patters. This loop pattern is seen in Figure 2.2 and 2.8. Any image printed with pitchdivision would require this trimming process in the final step.

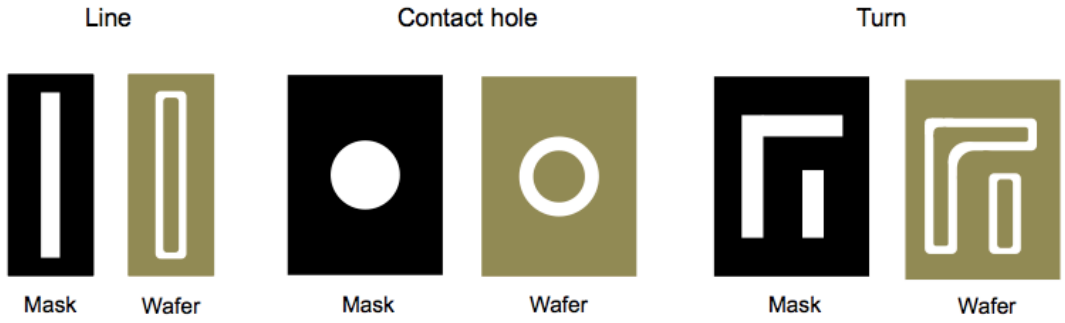

Figure 2.8: Illustration of pitchdivision response to common pattern formations. (*Adapted from Ref* (*30*))

Even with its drawbacks, the double patterning response may be applicable for devices outside of NAND memory. The continuing delay in availability of EUV is slowly forcing the acceptance of DPL methods in the construction of complex patterns. In recent years mask designers have created unique approaches toward incorporating pitch-doubling methodologies into more complex patterns. Figure 2.9 shows an approach towards creating L and U shaped turns through SADP.(*34*) These approaches require

great flexibility and innovative collaboration between electrical engineers and mask developers.(*35*)

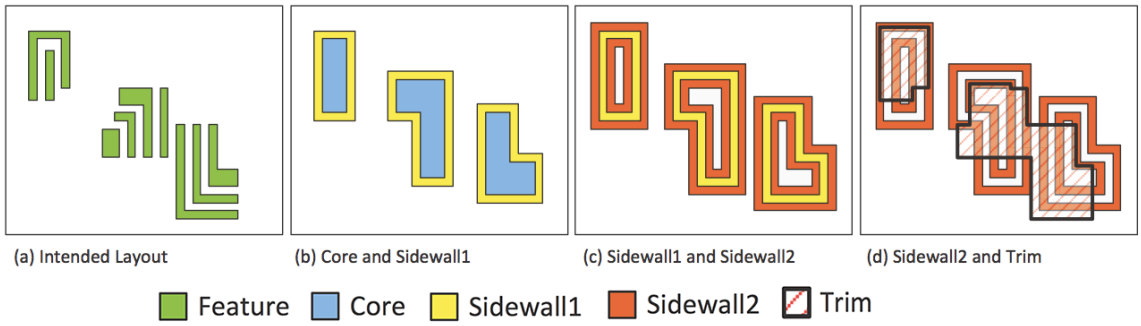

Figure 2.9: Illustration of abstract 2D shape formation through self-aligned resolution enhancing processes. (*Adapted from Ref* (*34*))

While there are some constraints with pitchdivision lithography to keep in mind, it still holds great advantages over the other established DPL methods. It does not require extra steps to double the density nor extra tools to avoid exacerbating the lithography bottleneck. The next chapter discusses the early patterning experiments with pitchdivision formulations.

Chapter 3: Formulation and Patterning of Pitchdivision Resists

3.1 INTRODUCTION

Chemists have long utilized the precision of photo-labile molecules in chemical synthesis as protecting groups.(*36*, *37*) The ability to selectively and precisely induce a chemical reaction with light provides a mild, neutral, and orthogonal pathway towards protection. Nearly every functional group including amines, carboxylic acids, thiols, and carbonyl compounds can have photo-labile protecting groups.(*38*) Biologists also use *in-situ* photo-labile groups in a wide variety of fields including biomolecule release, nucleoside triphosphate studies, and in gene therapy.(*39*)

Photoacid generators (PAGs) have long been in the spot light, while considerably less research has focused on photobase generators (PBGs)(*40*). In the mid 1990's interest in polyamides as directly patternable dielectric materials(*41*) piqued the development of PBGs for use in semiconductor manufacturing. (Figure 3.1) Since that time, PBGs for use in resist materials has continued to develop slowly into a small but diverse field.(*42*)

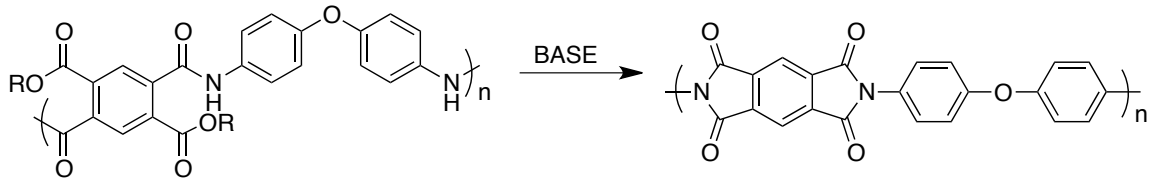

Figure 3.1: Illustration of base catalyzed solubility switch for directly patternable polyimides.

Most PBGs arose from protecting group chemistry. For a photo-labile protecting group (PPG) to make a good PBG it should posses the following characteristics:

(i) The PPG should be strongly absorbing in the UV region. For pitchdivision these should absorb near 193 nm and for directly patternable polyamides, the further red-shifted the better (>350 nm).

(ii) Along with strong absorptivity, they must have decent quantum efficiency, ϕ. In the case of PBGs, quantum efficiency (3.1) is defined as the ratio of the number of photons absorbed by a system to the number of base molecules generated at any given wavelength (λ). (Commonly used PBG and PAGs in lithography have a ϕ as low as 0.08 but more commonly near 0.4(*43*))

$$\phi = \frac{n_{base}}{n_{photon}}$$

(iii) The overall photoreaction should possess only one main pathway, and the photo byproducts should be inert. To measure the quantum efficiency a clean photoreaction is favorable, as recombination obfuscates most analytical techniques.

(iv) For a PPG to be useful as a base generator in lithographic systems it must be stable at temperatures up to 150 ºC.

(v) Ideally the absorption of the PBG bleaches at the exposed wavelength upon conversion to amine. Photo bleaching avoids competitive absorption and increases

the overall efficiency of base conversion. Bleaching allows for larger PBG loadings and thicker resist films.

Figure 3.2 illustrates the core skeleton of typical amine producing PBGs. In general, many of these share some common features. Aromatic groups are present throughout so as to increase absorption in the UV region, a critical feature for PBGs. Many also possess a carbonyl group that is regularly conjugated with the aromatic moiety. Carbonyls also add to the absorption in the UV region and are the central structure of Norrish-Type I and II elimination reactions. Half of the examples in Figure 3.2 have a carbamate or oxime ester moiety. Excited carbamates and oxime esters can easily decarboxylate to irreversibly eliminate CO_2, pushing the reaction forward towards the product. There are many other types of PBGs (not listed here) that are specifically tailored to red shift the absorption spectrum and generate stronger bases, such as DBU, commonly used in biological applications or patternable dielectrics. In general, almost all of the common PBG's follow a similar structure-function pattern as illustrated here.

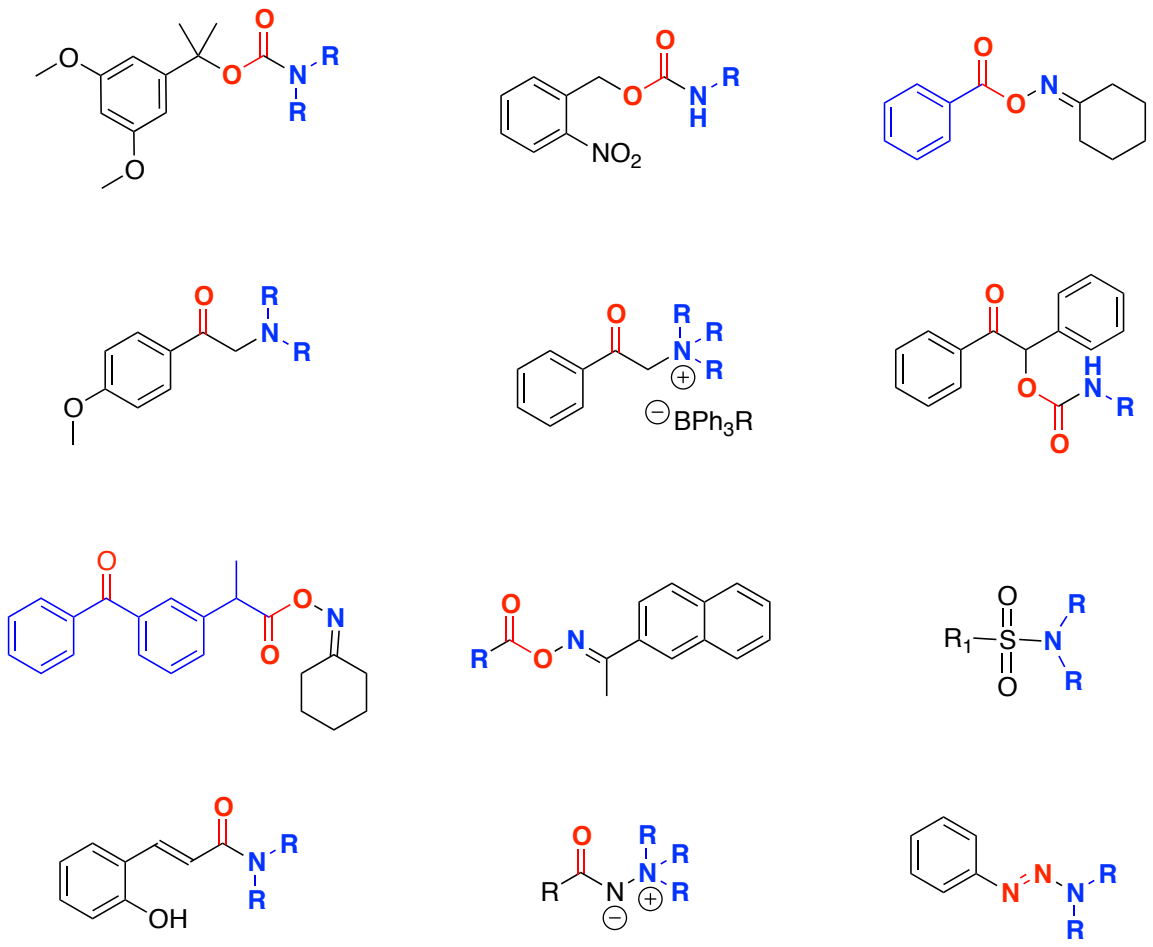

Figure 3.2: Illustrations of some of the common PBGs.

3.2 PBGs FOR PITCHDIVISION

The first group of PBGs examined for pitchdivision is illustrated in Figure 3.3, and were chosen due to their prevalence in the literature and their previous use in the Willson labs.

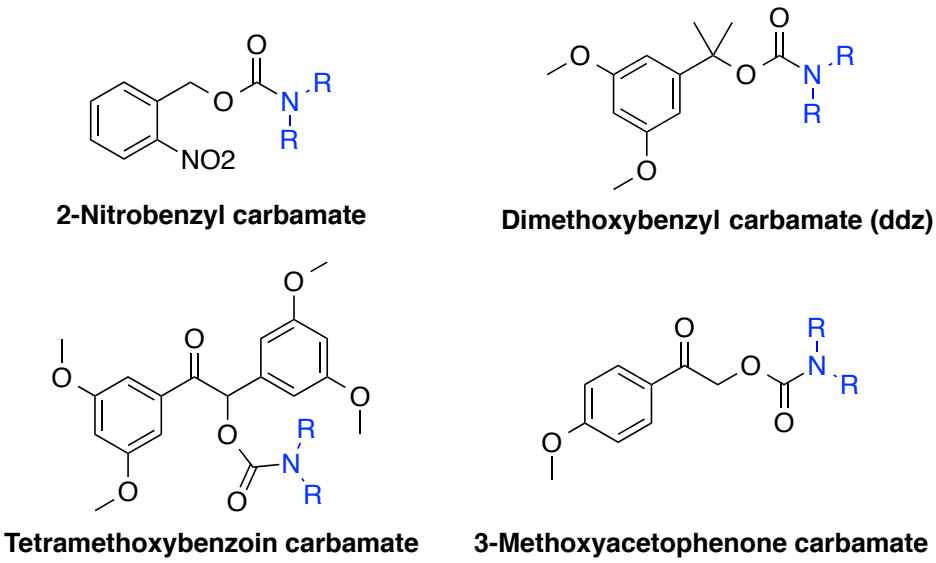

Figure 3.3: Illustration of PBGs used in pitchdivision formulations.

The most common PPG chromophore is the ortho-nitrobenzyl moiety. It possesses strong UV absorption, high thermal stability (>200 º), a clean photoreaction, and modest efficiency.(*44*, *45*) For these reasons, it was one of the first structures studied as a PBG for use in resist materials(*46*, *47*) and for pitchdivision formulations. The proposed photodecomposition pathway is illustrated in Figure 3.4.(*48*) The primary photochemical process of the reduction-oxidation decomposition pathway is the intramolecular hydrogen abstracted by the excited nitro group. This abstraction creates a separated radical pair that is stabilized through conjugation with the diene and nitro group. Upon recombination, an aza-orthoxylene intermediate is created. This intermediate is electrophilic and allows for an attach by the oxygen from the nitro group on the ortho-benzylic carbon position before undergoing disproportionation to give an amine, carbon dioxide, and ortho-

nitrosobenzalydehyde. The photo byproducts are able to recombine to form imines and secondary bicyclic structures such as indazoles.(*49*, *50*) More detail on the side reactions is discussed in Chapter 4. For the sake of pitchdivision, the recombination of the photoproducts is of little concern since PAG's commonly generate super acids (pKa < -10), and imines and indazoles are basic enough to irreversibly quench these strong acids.

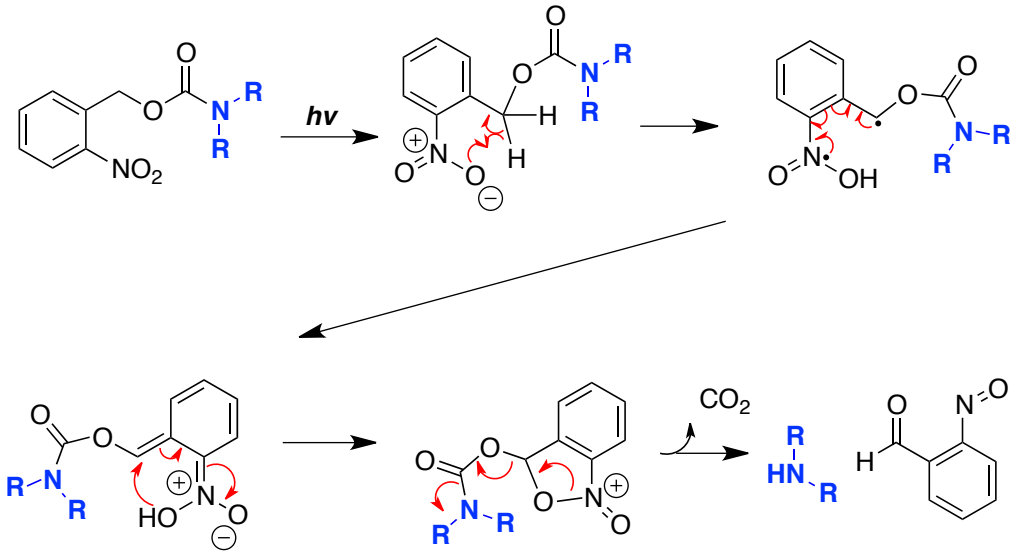

Figure 3.4: Proposed photodecomposition pathway of *o*-nitrobenzylcarbamates.(*49*, *50*)

The 3,5-dimethoxybenzylcarbamate (Ddz) was originally used as an orthogonal amine protecting group in solid-phase peptide synthesis(*51*). It was first studied and characterized by Cameron and Fréchet for use in photolithography (*52*). They proposed the decomposition pathway illustrated in Figure 3.5, based on HPLC analysis of the photoproducts. The methoxy groups help promote benzyloxy bond cleavage, which

results in immediate decarboxylation to generate the free amine and dimethoxy-α-methylstyrene.

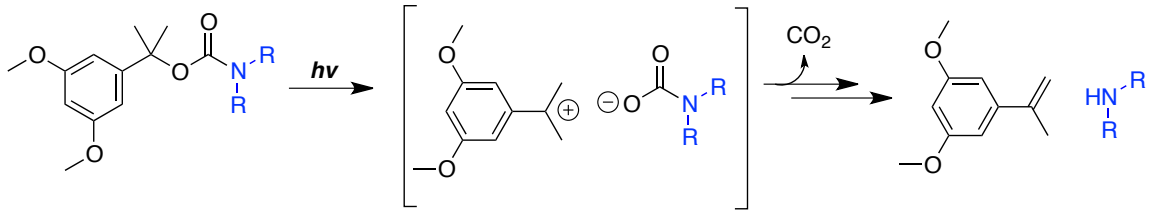

Figure 3.5: Proposed photodecomposition pathway of Ddz-lcarbamates.(*52*)

Cameron and Fréchet also pioneered the adaptation of the benzoin class of chromophores into PBGs. Benzoin groups were previously shown to be effective carboxyl PPGs.(*53*, *54*) The reactivity of benzoin PBGs may be tuned through the modification of the functional groups on the aromatic rings. With methoxy groups in the meta position, the photoreaction cleanly forms a benzofuran with reportedly good quantum efficiency (ϕ =0.61).(*36*) The efficiency and the inertness of the benzofuran byproduct make benzoin PBGs attractive compounds. A significant amount of research has gone into the mechanism of base and benzofuran generation.(*55-57*) Non-substituted benzoin PPGs do not form the benzofuran in the presence of common triplet quenchers, whereas the meta methoxy derivatives do. This has led researchers to conclude that the bare benzoin PBG likely goes through a triplet state transition where the methoxy modified benzoins may undergo ion pairing.(*58*) Figure 3.6 illustrates the proposed mechanism of benzofuran from benzoin carbamates.

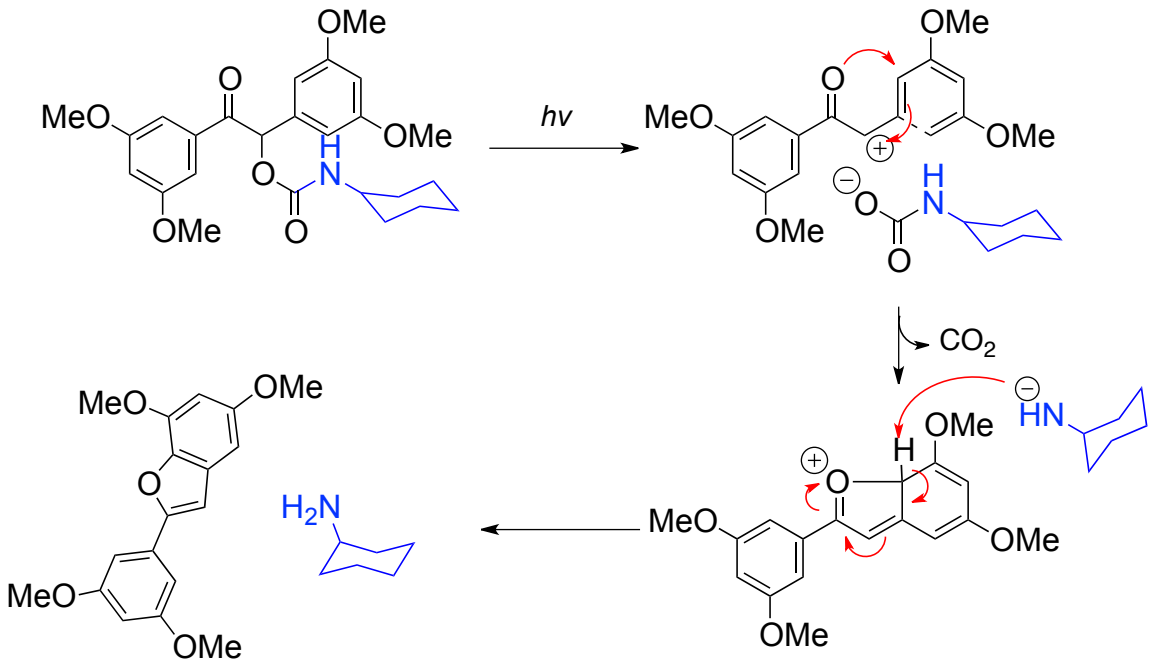

Figure 3.6: Proposed photodecomposition pathway of benzoin carbamates.(*58*)

The final PBG screened for pitchdivision and discussed in this dissertation are para-methoxyacetophenone carbamates. Para-methoxy and para-hydroxy acetophenone chromophores have good quantum efficiencies, moderately simple decomposition pathways, and are easily synthesized.(*59*) Epstein originally studied the efficiency and decomposition pathway for use as a phosphate ester PPG in the1980s.(*60*) Figure 3.7 shows the proposed triplet-state pathway in dioxane, via hydrogen abstraction. The mechanism was determined by following the generation of p-methoxyacetophenone and quenching studies with naphthalene. They propose that the irradiated chromophore enters an excited triplet state and abstracts a solvent proton creating a stabilized benzylic

radical. The benzylic radical intermediate then decomposes to release carbon dioxide, the free amine, and the acetophenone tautomer.

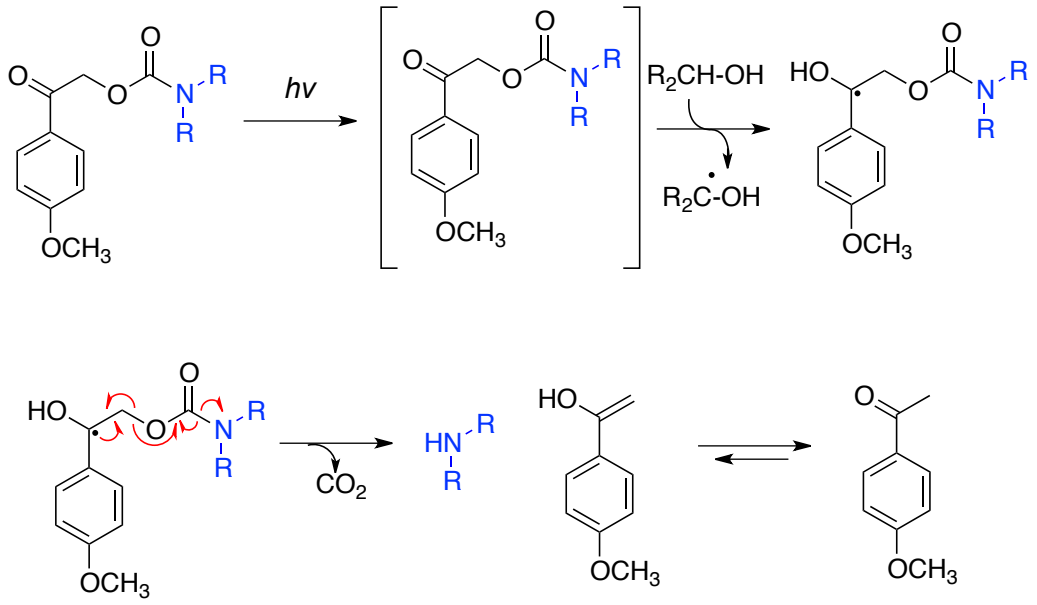

Figure 3.7: Proposed photodecomposition pathway of *p*-methoxylacetophenone carbamates.(*60*)

In the early 1990's, Givens found conflicting evidence of the decomposition pathway than previously reported in the literature (*60*, *61*). Givens found when the reaction is run in tert-butanol that the major byproduct was not the expected acetophenone but a tert-butyl phenylacetate. During the investigation of the conflicting results, Givens discovered the reaction pathway depended largely upon the polarity and hydrogen donating ability of the solvent (*57*, *62*). His results confirmed the original pathway proposed by Epstein in non-nucelophilic solvents such as dioxane, however, he also found evidence of a competing pathway when the reaction was run alcohols.

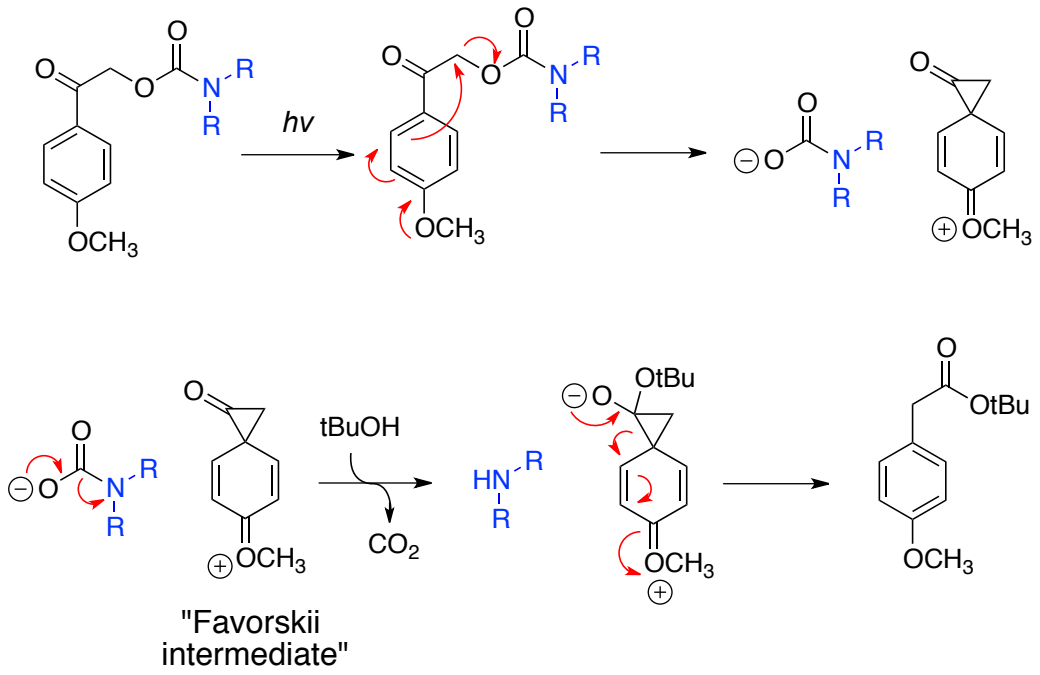

Figure 3.8: Proposed photodecomposition pathway of *p*-methoxylacetophenone carbamates by Givens *et al*.(*62*)

Figure 3.8 illustrates the proposed pathway by Givens when the photolysis is run in tert-butanol, a solvent known for being a poor hydrogen donor. When hydrogen abstraction becomes unfavorable, the expulsion of the carbamate is realized through a Favorskii-type reaction. The unstable bicyclic intermediate is readily attacked by tert-butanol to give *t-butyl*(4-methoxypenyl)acetate in nearly quantitative yield. When the reaction is run in methanol, a moderate hydrogen donator, a mixture of the acetophenone (62 %) and acetate (38 %) is found. A similar photo-Favorskii mechanism is reported for *4*-hydroxyacetophenone chromophore, which undergoes a diradical intermediate in the presence of water.(*63*)

3.3 SYNTHESIS OF PBGS

The four PBGs examined in this chapter are all carbamates, allowing each to be prepared from the alcohol of the main chromophore. Figure 3.9 outlines the synthesis of tetramethoxybenzoin(*58*) and *2*-hydroxy-1-(4-methoxy-phenyl)-ethanone.(*64*) Tetramethoxybenzoin is made through a benzoin condensation of 3,5-dimethoxyaldehyde. The addition of catalytic cyanide to benzaldehyde forms an umpolung cyanohydrin, which is able to react with the standard benzaldehyde to form the benzoin, and release the cyanide.

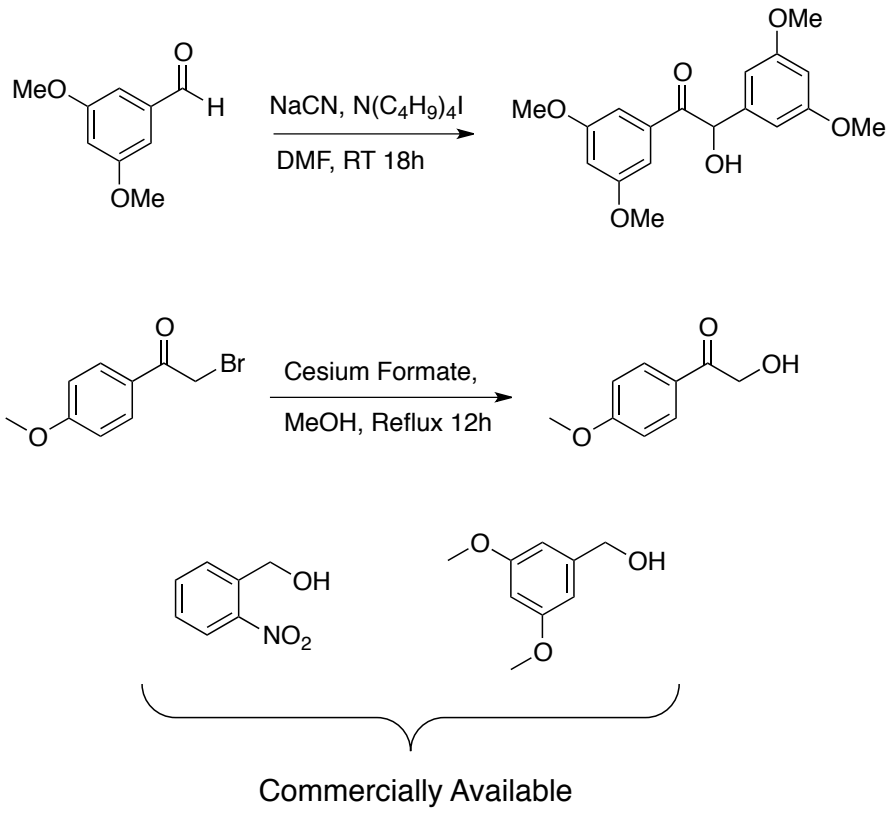

Figure 3.9: Illustration of the chromophore alcohols used in the synthesis of the carbamate PBGs.

The formation of 2-hydroxy-1-(4-methoxy-phenyl)-ethanone is prepared by mixing an α-haloketone with either an alkali hydroxide or formate. The best yields were received by following the procedure of Wong and Lin,(*64*) utilizing cesium formate as the source of neucleophilic oxygen. After halide displacement by formate, the α-hydroxyketone is generated when methanol generates methyl formate as a side product. The alcohols of the other two chromophores, *o*-Nitrobenzyl alcohol and 3,5-dimethoxybenzyl alcohol, are commercially available.

The corresponding carbamates were synthesized using three different approaches, as outlined in Figure 3.10, depending on the desired amine. Pathway **I** is the most direct and simple way to make mono-substituted carbamates. The alcohol of the desired chromophore is simply mixed with the isocyanate of choice and refluxed over night to yield the desired PBG in high yield.(*65*)

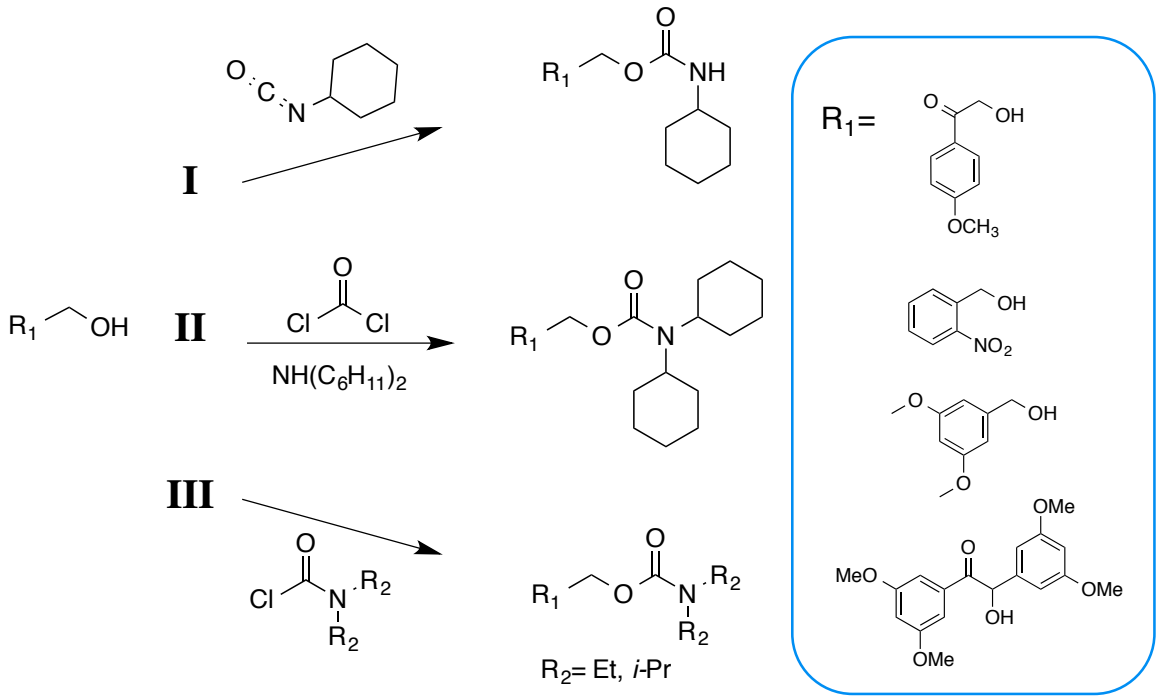

Figure 3.10: Schematic of carbamate PBG synthesis.

Mono-substituted carbamates are easily made, yet they do not always produce the ideal base for use in lithography. In some cases, the carbamate proton is thermally labile causing the PBG to decompose below 150º.(*65*, *66*) There is also a strong correlation between steric hindrance and small molecule diffusion in resist materials leading to the blurring of the printed image;(*67*) therefore a disubstituted amine is preferred to limit diffusion. Both routes **II** and **III** are approaches toward disubstituted carbamates. The phosgene route (**II**) is the most versatile as the intermediate is a chlorocarbonate, which is able to couple with almost any mono or disubtituted amine available.

We utilize route **II** to make dicyclohexane carbamates, which have high boiling points, low UV absorption and large steric hindrance. While the dicyclohexane carbamate has its advantages, the synthesis does involve the highly toxic and corrosive phosgene. Phosgene was used as a chemical weapon in WWI, and avoiding its usage on a large scale is preferable. There are slightly safer forms of phosgene available that are liquids or solids, such as diphosgene and triphosegene respectively, yet these compounds tend to be less reactive and if put under harsh conditions to improve their reactivity have a propensity to explode. To reduce hazard risks in the lab, route **III** was utilized with commercially available diethyl and diisoproply chlorocarbamates. Figure 3.11 displays the synthesized PBGs that were tested in pitchdivision formulations and discussed in this dissertation

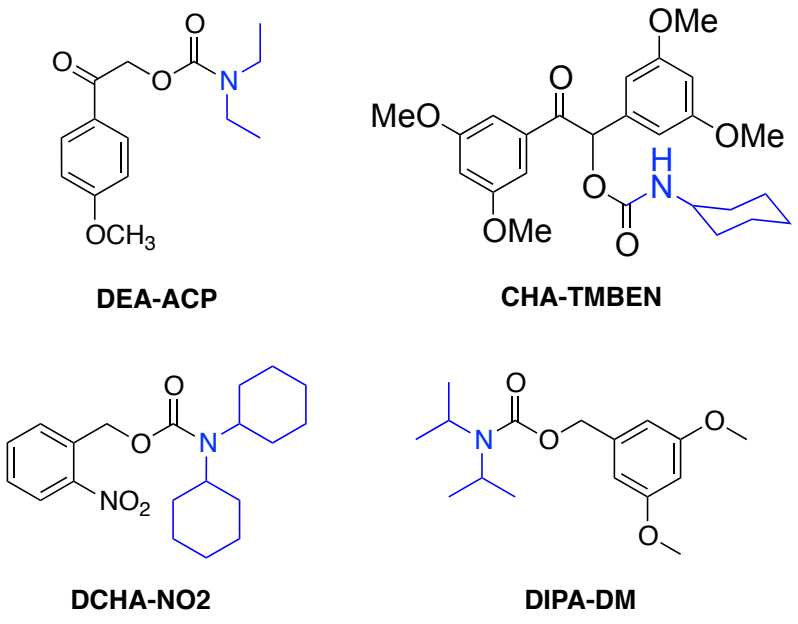

Figure 3.11: Illustration of carbamate PBGs

3.4 CHARACTERIZATION OF PBGS FOR PITCHDIVISION

For optimizing pitchdivision formulations, the rate of base generation (k_b) in relation to the rate of acid generation (k_a) is an important parameter to know. This is especially true if computational modeling is desired. Finding the rate of generation and the quantum efficiency (ϕ) is not a trivial task. In an ideal situation the photoreaction goes directly from starting material to the desired products. In this situation, the rate is found by simply monitoring the disappearance of starting material in relation to dose. This may be accomplished by following the change in the UV-Vis spectrum, if the photoreaction undergoes bleaching upon decomposition. The main complication in this method is adjusting the experiment to account for the bleaching with regards to the changing opacity of the solution during exposure. The IR spectrum is also particularly useful, if applicable, as clean measurements are possible even in fully opaque films or solutions resulting in a more straightforward experiment. Unfortunately these measurements only monitor the consumption of starting material and not the generation of base.(*68*)

Directly measuring the rate constant and quantum efficiency of PBGs is a long-standing challenge. The great hurdle is in the radical nature of photolysis, which often leads to dimerization and recombination of photo byproducts. Several former students in the Willson group have attempted to resolve this issue with varying degrees of success. (*65*, *66*) Xinyu Gu(*31*) examined the decomposition of starting material for DCHA-NO2,

DIPA-DM, and an oxime ester in thin films and in solution by UV-Vis and IR following procedures set forth by Cameron and Fréchet.(*48*, *58*) His results for the DCHA-NO2 study mostly agreed with each other and appear to give a good approximation of k_b. The pitfalls of these studies are seen in the stark differences of the results Gu found for DIPA-DM and the oxime ester. Some of the results have fluctuations in k_b with differences up 3 times for the same chromophore. For further discussion and details on studying quantum efficiency and rates by monitoring the disappearance of starting material, Cameron & Fréchet(*58*) and Givens(*69*) each give good explanations, as well as in the dissertation of Xinyu Gu.(*30*) Further discussion and methodology to study the direct generation of amines to determine kinetics and efficiency of PBGs is in Chapter 4, which examines two-stage PBGs.

3.4.1 CONTRAST CURVE STUDIES

While measuring the rate of base generation is not a trivial task, testing a PBG as to whether or not it is compatible in pitchdivision is fairly straightforward via a contrast curve experiment. A contrast curve gives information about the solubility threshold of a resist material within set processing conditions, which include initial film thickness, post exposure bake, development, and light source. A more common and formal version of a contrast curve is a Meyerhoff plot, which details the dissolution rates of a resist material measured via a quartz crystal microbalance, interferometry or ellipsometry. While Meyerhoff plots give more pertinent information in regards to resist performance, they are also more time consuming to produce. A contrast curve simply measures the response of a resist to dose, which shows quickly if a particular PBG allows for pitchdivision.

3.4.2 EXPERIMENTAL

For screening PBGs and process parameters via contrast curve plots, two types of 193 nm resists were used. The first is a generic 193 nm resist, which is illustrated in Figure 3.12.A. The generic resist was formulated with triphenylsulfonium trifluoromethanesulfonate (TPS-Tf) as the PAG at a 5 wt% loading with respect to the polymer. Simulated pitchdivision optimization(*31*) showed that approximately three equivalents of PBG resulted in the best net acid production and was used as the initial loading of PBG. Propylene glycol monomethyl ether acetate (PGMEA) was used as a casting solvent at 5 wt% polymer concentration. The second resist used is a commercial 193 nm resist generously donated by TOK (Pi6-001ME). The exact makeup of the resist such as PAG and base quencher loading remains proprietary. For these formulations the initial loading of PBG was set to 5 mM and adjusted as necessary to find an E-factor between 0.3 and 0.6.

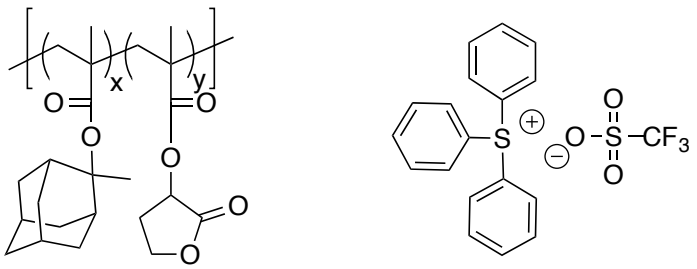

Figure 3.12: Illustration a generic 193nm polymer and TPS-Triflate, generously donated from Dupont.

Silicon wafers were prepared with a 72 nm AR29 antireflective coating, which was generously donated by Brewer Scientific. Pitchdivision resist formulations were filtered through a 0.20 μm filter just prior to use. The coated resist was soft-baked at 110 ºC for 60 minutes to give approximately 115 nm thickness.

A bench-top Lambda Physique 193 nm ArF excimer light source was used for in-lab exposures. A light guide directs the laser from the horizontal source perpendicular to the bench top. A diverging lens used underneath the light guide helps to create a more uniform beam. The exposure contact mask used to create open frame dosage steps was made from a small piece of aluminum foil with a 1 cm by 0.5 cm rectangular hole. This mask was manually shuffled around the wafer as the dose was incrementally increased between each exposure. A post-exposure bake (PEB) followed immediately after the final exposure dose for 1 minute at the desired temperature (usually between 110 ºC - 130 ºC). The wafer is then cooled to room temperature and developed with an aqueous solution of 2.38 % tetramethylammonium hydroxide (TMAH). The development is unagitated for 1 minute before washing with deionized water and blown dry. The film thickness in the exposed open frame patches is measured on a J.A. Woollam ellipsometer.

3.4.3 RESULTS AND DISCUSSION

All four of the initial PBGs give dual-tone pitchdivision behavior. The best exposure window was produced by DCHA-NO2 shown in Figure 3.13.A, followed by that of CHA-TMBEN in Figure 3.13.B. Both formulations show good tolerance to the initial concentration of PBG and produced fairly sharp dual-tone contrasts.

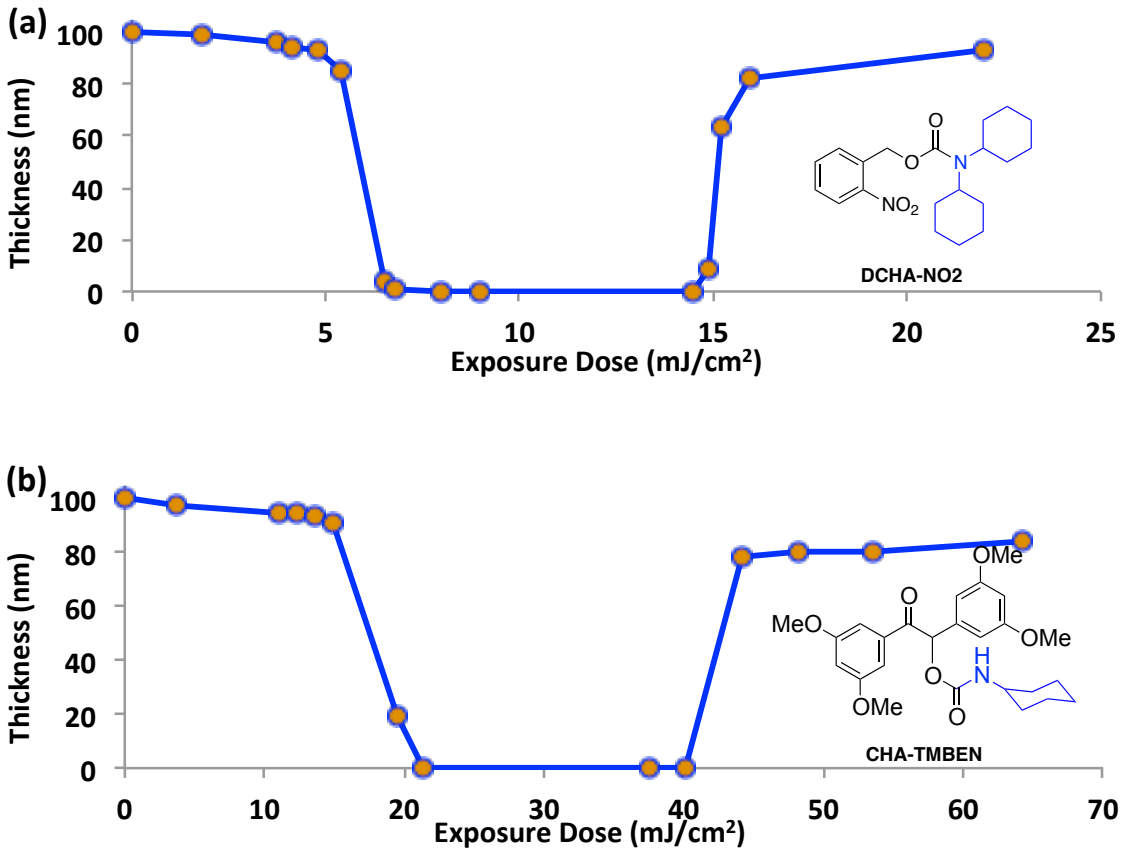

Figure 3.13: Contrast curves of resist formulations containing different PBG: (a) DCHA-NO2; (b) CHA-TMBEN.

While both the DEA-APC and DIPA-DM were able to produce pitchdivision contrast curves, neither was able to make sharp windows or produce high enough E-factors (near E = 0.5). One reason for the low contrast may be due to the low boiling point of diethyl and diisopropyl amines, which boil at 55 ºC and 85 ºC respectively, well below the required PEB temperatures of 110-130 ºC. The fast E_0 seen in these two formulations along with the large E_n show that both PBGs are considerably slower than

the tetramethylbenzoin and *o*-nitrobenyl PBGs. A smaller E-factor can be produced by increasing the [PBG] : [PAG] ratio or by increasing the PEB. Unfortunately increasing the PBG : PAG ratio led to contrast curves that didn't fully clear to the resist (Figure 3.14.B). One possible reason for this could be that the high loadings were too absorbent.

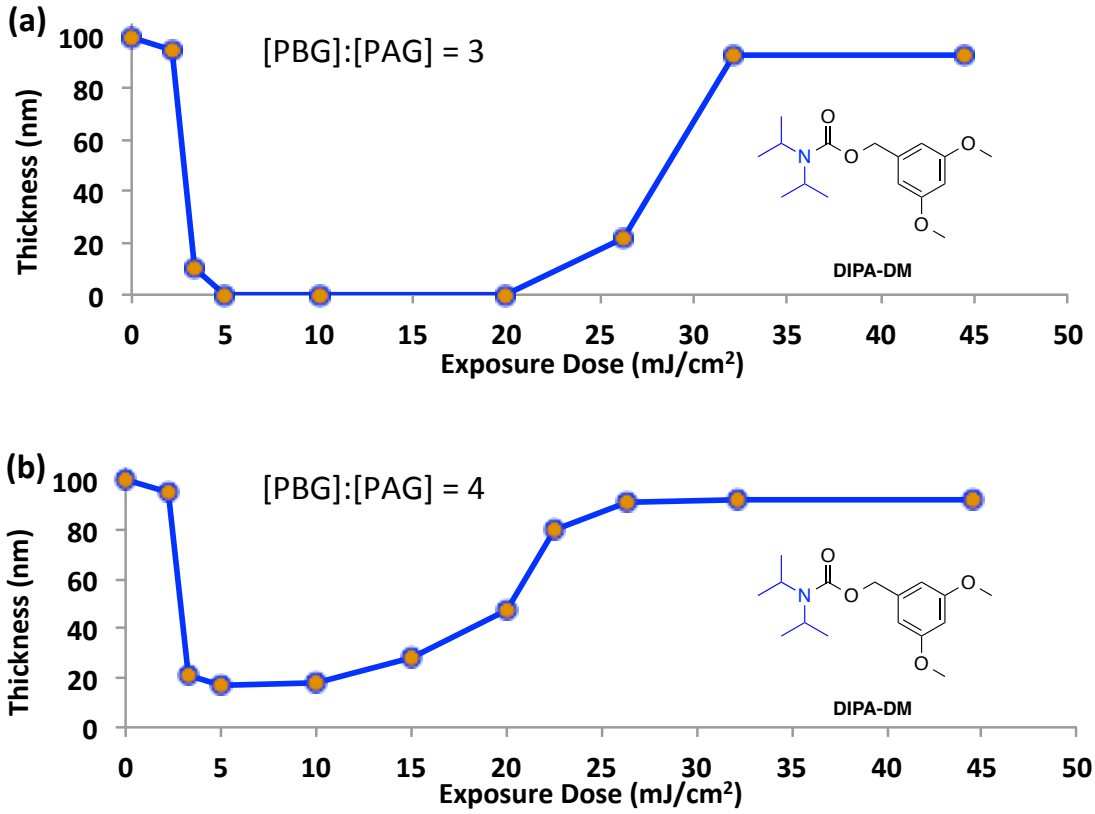

Figure 3.14: Contrast curves of resist formulations containing different PBG loadings: (a) three equivalents; (b) four equivalents.

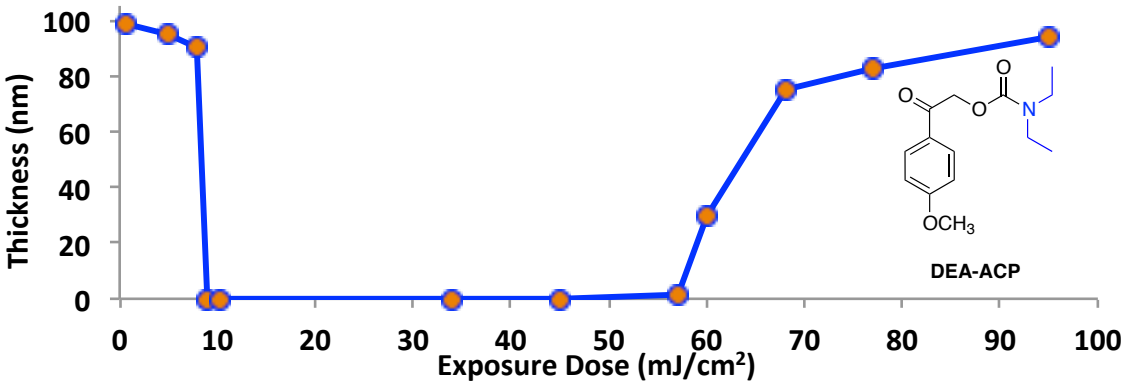

Figure 3.15: Contrast curve of resist formulations containing DEA-APC in a commercially available resist.

3.5 IMAGING AND ANALYSIS

The contrast curve studies showed the DCHA-NO2 was the best PBG for pitchdivision formulations and was thus used in the preliminary imaging studies. Robert Bristol, at Intel , ran the first patterning experiments in Portland, OR. The exposure source used in patterning was an interferometric lithography tool. This type of tool is common in photolithography research because they function well at the k_1 limit of 0.25 and produce a pure sinusoidal aerial image with all available NA values. A sinusoidal aerial image is beneficial to pitchdivision lithography since the middle dose region is where the solubility switch occurs. The generic 193 nm resist formulation, similar to the one described in section 3.5.2 was used in the Portland experiments with the exception that a base quencher was added to modify the acid baseline in order to tune the E-factor.

Figure 3.16 shows the first successful SEM images of pitchdivision.(*70*) With a

220 nm half-pitch (HP) mask, 0.22 NA and operating at $k_1 = 0.25$, the pitchdivision resist produced 110 nm HP features. By doubling the resolution pitchdivision lithography allows for an effective Rayleigh factor of 0.125 without any additional processing steps.

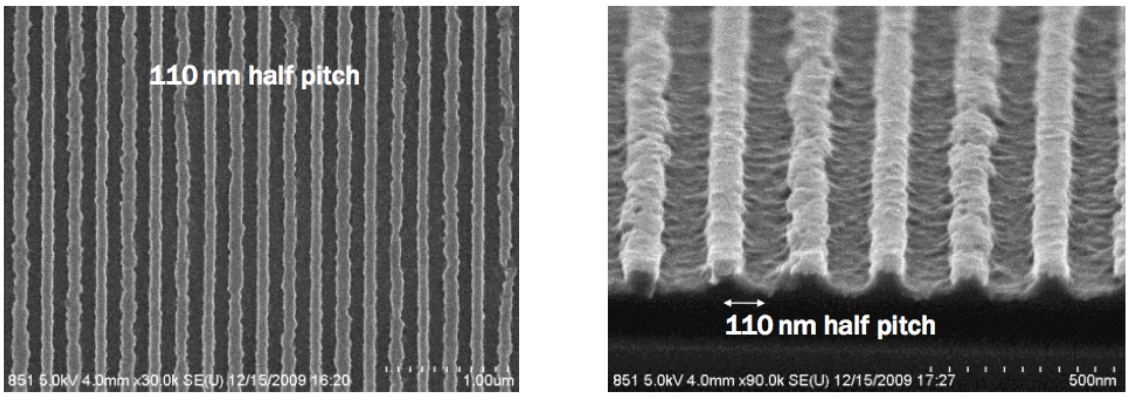

Figure 3.16: SEM images of pitchdivision patterning. 110 nm half pitch features from a 220 nm half pitch feature mask. (*From Ref*. (*30*))

The same formulation used in Figure 3.16 was also pattered with a mask of 90 nm HP. Again pitchdivision was successful! The resulting pattern showed 45 nm HP features (Figure 3.17). Unfortunately the line edge roughness (LER) is exceedingly high in the 45 nm HP image. One cannot help but notice though that the LER is significantly worse on every other line. The initial hypothesis correlated this alternating LER pattern to the chemical contrast of pitchdivision resists. Chemical contrast defines the acid gradient across the solubility threshold. The simulations of the net acid profile (Figure 2.4) show that the positive threshold has a steeper net acid profile than the negative threshold. For this reason we believed that the negative tone lines were the ones suffering from poorly

defined LER.

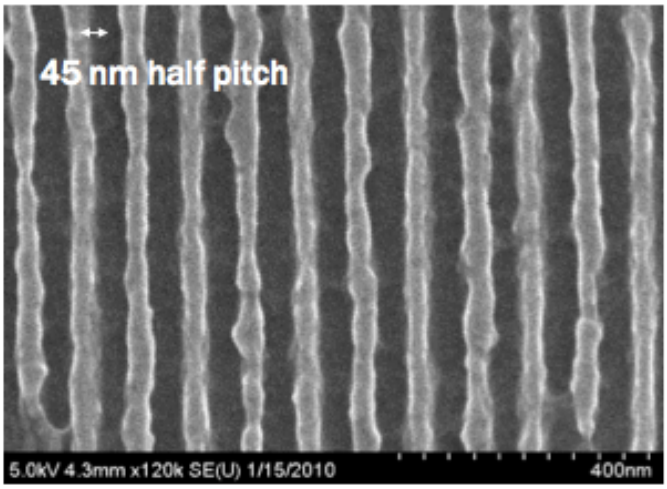

Figure 3.17: SEM images of pitchdivision patterning. 45 nm half-pitch features from a 90 nm half-pitch feature mask. (*From Ref*. (*30*))

3.5.1 SOURCE OF LER

Xinyu Gu worked in collaboration with IMEC and JSR Micro to find the source of the LER pattern. The exposure tool used for patterning was an ASML TWINSCANTM XT:1250, which is a dry ArF tool with a maximum NA of 0.85. The illumination was a non-polarized dipole source with an NA of 0.85. The resist formulation was a commercial ArF resist with an additional of 5.5 mM of DCHA-NO2 PBG.(*30*)

Using a mask with an array of 9 trenches, the confident identification of the positive and negative tone lines was realized. Figure 3.18 shows the comparison of the

PROLITH simulated aerial image in comparison to the printed image. From this experiment it is clear that the lines alternate positive-tone and negative-tone. The dosage intensity drop towards the outermost sides of the mask allows for a conclusive identification of the furthest and thinnest line as negative tone.

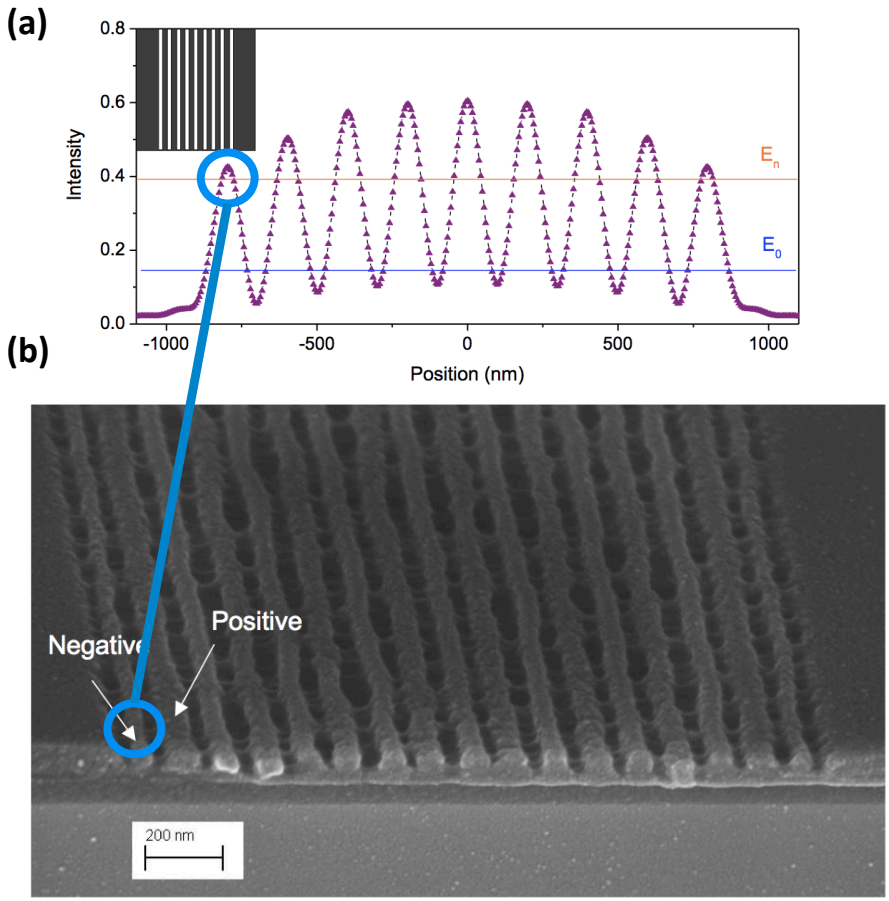

Figure 3.18: (a) Simulated aerial image of a 9-trench mask. (b) SEM images of pitchdivision patterning with a 9-trench mask. (*From Ref.* (*30*))

This experiment demonstrates that our original assignment of positive and negative tone features by LER was correct. Further modeling and experimentation by Gu found that this assignment is only true for 1:1 line and space images. The size of the critical dimensions (CD) of each line and the dose directly affect the chemical contrast of each line. Figure 3.19 shows an SEM of the same 9-trench mask patterned at an excessively large dose, which was successfully predicted to give sharper negative-tone lines than positive-tone lines. For further background on the simulation and experimentation on how CD and dose affect LER please refer to the studies of Xinyu Gu.(*30*) Unless otherwise stated, all images in this thesis focus on low dose 1:1 CD images, where the LER assessment is an accurate predictor of line tone.

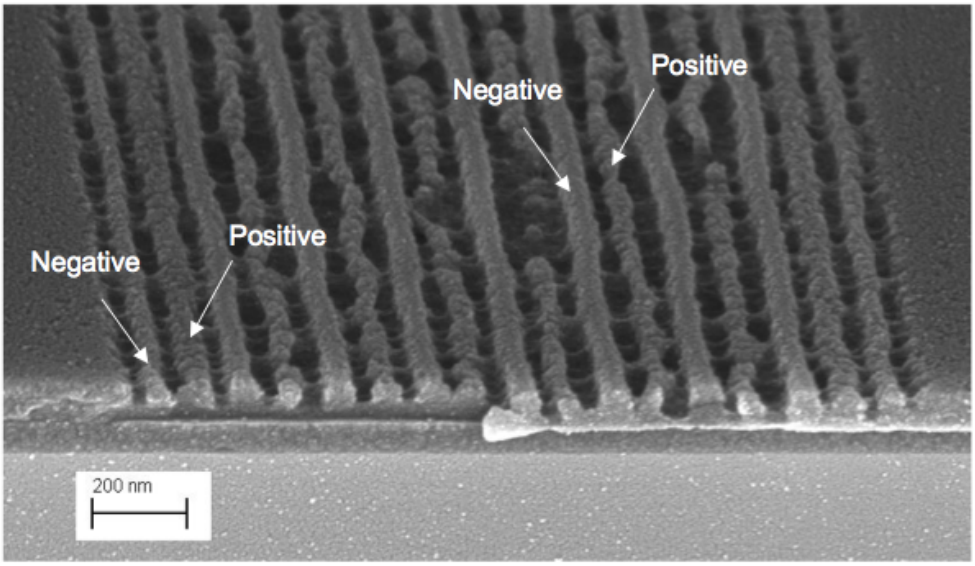

Figure 3.19: An SEM image of 49 nm HP pitch division pattern printed with a mask of 85 nm trenches with 195 nm pitch under an incident exposure dose of 80 mJ/cm^2. (*From Ref.* (*30*))

3.6 IMPROVING PITCHDIVISION LER

For pitchdivision to be successful, the LER needs to be greatly improved. While the images with 110 nm CD have acceptable LER, the issue is greatly worsened at smaller CDs. According the international technology roadmap for semiconductors (ITRS), the LER must be < 8% (3σ) of the CD.(*71*, *72*) There are two main factors that contribute to the LER:

(i) The first factor evolves from the fact that the positive and negative tone images are simultaneously printed with the same aerial image. Therefore the images are printed from both the high and low dose areas of the aerial image. In contrast, standard lithography uses the mid-dose region of the aerial image. Since the inception of photolithography, the light sources, masks, and resolution enhancement techniques all have focused on producing an aerial image with greater contrast in the mid-dose region, often resulting in more convoluted high and low dose regions. Coupled with the fact that defocusing of illumination in the resist affects both the high and low tones simultaneously, and even more so than in conventional resists, poses a difficult challenge for pitchdivision. Further review of these issues and how they can be circumvented, please refer to the simulations and models found in the dissertation of Xinyu Gu.(*30*)

(ii) The second factor is due to poor chemical contrast in pitchdivision resists in comparison to standard resists. As mentioned earlier, the slope of the net acid curve at the solubility thresholds of both the positive and negative tone is shallower than a conventional resist. This leads to reduced chemical contrast and

increased LER of the final image.

This discussion focuses on methods to mitigate LER through a chemistry-based approach. Two distinct tactics are presented: (i) tethering the PAG and PBG molecules to the polymer backbone to limit diffusion and increase distribution uniformity and (ii) to create a new class of PBGs with unique kinetics to increase the chemical contrast of the resist system.

3.6.1 POLYMER-BOUND PAG & PBG

LER resulting from the diffusion of photo-generated acid is a long-standing issue of chemically amplified resists.(*67*, *73*, *74*) As the critical dimention of semiconductor features continue to shrink, LER is becoming an increasing challenge, even with conventional resist materials.(*75*) A common approach to alleviate diffusion is to bind the PAG to a polymer backbone.(*76*, *77*) Some of the earliest efforts to reduce LER in pitchdivision centered on securing PAG and PBGs to the resist polymer backbone.ben

Through tethering PBGs and PAGs to the resist polymer backbone a direct comparison to non-bound formulations can be made. Thus allowing the determination of the effects of diffusion on LER. The two polymers synthesized for this study are illustrated in Figure 3.20. Details on the design, synthesis, and characterization of this project maybe found in the published work of Yongjin Cho.(*78*)

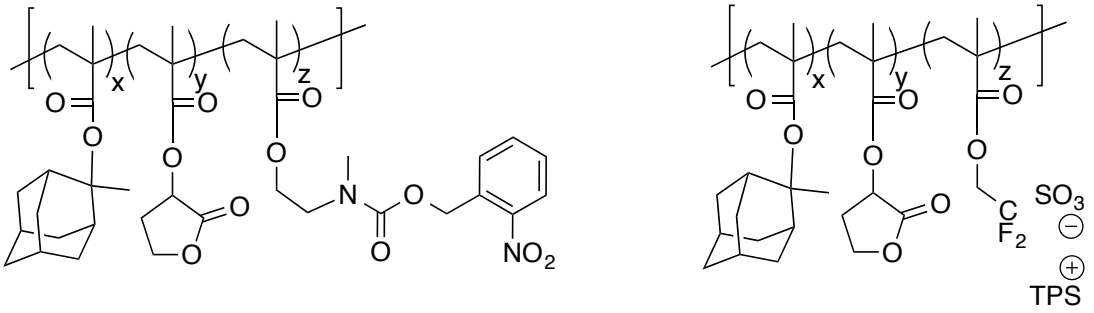

Figure 3.20: Illustration of polymer bound PBG synthesized by Yongjin Cho. The PAG bound polymer was generously donated from Central Glass.(*78*)

Figure 3.21.A shows the results of the polymer bound PAG. It's likely that the lack of clearing in the middle dose region results from the lack of mobility with a bound PAG. Since each generated acid molecule can no longer migrate, fewer deprotection events may be realized. While increasing the amount of bound PAG in the polymer backbone could rectify this issue, further work in this feature was not pursued. Rather studies focused on comparing polymer bound PBG's, since quenching the acid is the chemistry directly related to pitchdivision and therefore most likely to contribute towards the increased LER compared to a conventional resist.

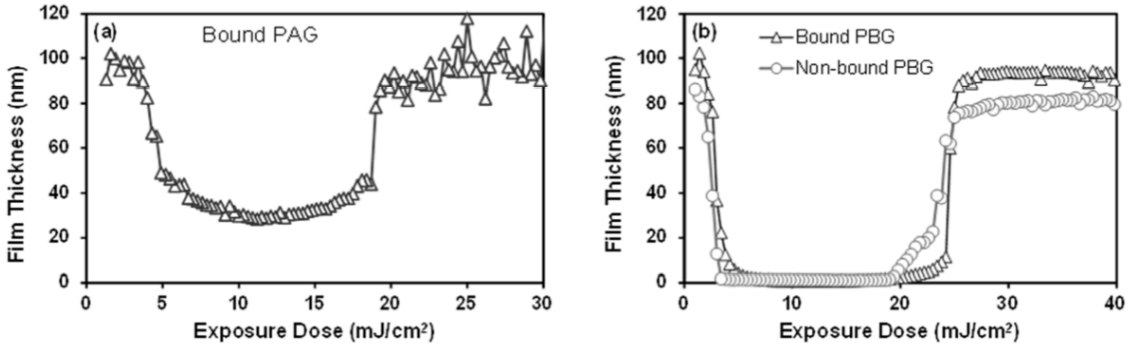

Figure 3.21: Contrast curves of pitchdivision resists with (a) polymer bound PAB and (b) polymer bound PBG. (*From Ref*. (*78*))

To make a direct comparison between bound and non-bound formulations, the E-factor was held constant. By constraining the diffusion of the base, the E_0 is expected be to lower whereas the E_n is expected to be larger, leading to an overall larger E-factor. This creates a situation in which the exact loading of PBG and PEB cannot be the same. Figure 3.21.B shows the comparison of bound versus non-bound PBG with nearly identical E-factors. In this comparison a distinct improvement is evident in the negative-tone threshold. To evaluate the potential LER improvement, the formulations were each imaged with a 150 nm HP feature mask with a NA of 0.85. (*79*) Unfortunately when the two formulations were compared, the results proved inconclusive. Figure 3.22 shows some improvement by simple observation, neither formulation produced clear line and space patterns to allow for an actual LER measurement. While its interesting to note that the unbound PBG hardly produced an image and the bound PBG shows a greater extent and larger process latitude of pitchdivision, its clear that PBG diffusion is not the greatest contributor to LER.

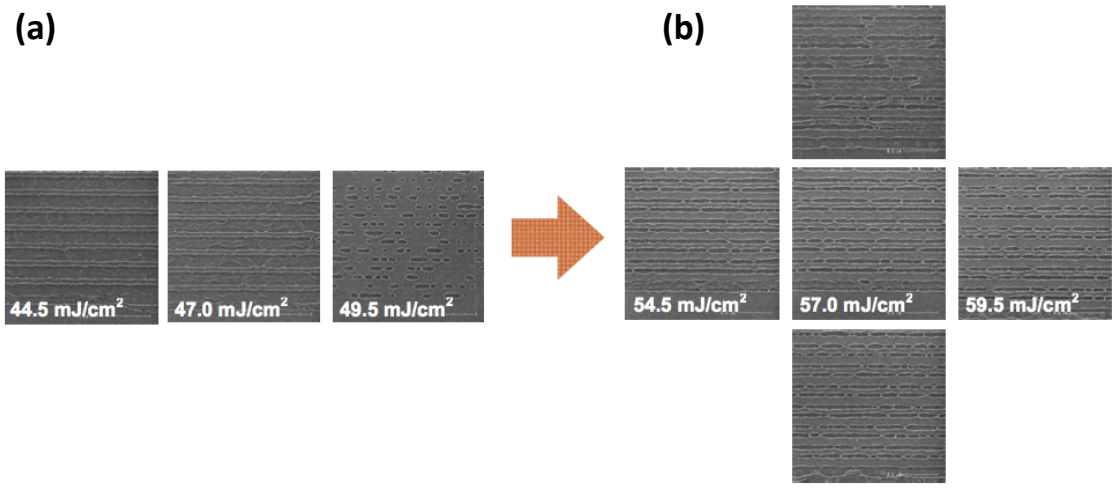

Figure 3.22: SEM images of 75 nm HP pitchdivision pattern printed with a mask of 150 nm HP features. (a) non-bound standard pitchdivision formulation vs (b) polymer bound PBG formulation. (*From Ref* (*78*))

3.6.2 SHARPENING THE NET ACID PROFILE

After excluding diffusion as a major contributor to LER, effort shifted towards improving the chemical contrast. As discussed earlier, a likely source of the alternating LER pattern shown in images printed via pitchdivision is due to the shallow slope of the net acid production in the high dose region compared to the higher slope of the low dose region.

Improving the slope of the negative tone region is achieved through tuning the [PBG] / [PAG] ratio: the higher the loading ratio, the sharper the slope at high dose. This trend is illustrated in Figure 3.23, with the highest loadings showing the sharpest high dose slope. This optimization provides a quick and easy route towards improving LER.

Unfortunately the extent of its utility is limited. As the PBG concentration is increased in the resist, the optical density, dissolution and structural properties begin to negatively impact overall performance. Figure 3.23.B illustrates how the net acid production is decreased proportionally to PBG loading. The kinetic constants and loadings used for the simulation in Figure 3.X are as follows: k_a = 0.0722 cm^2/mJ, k_b = 0.013 cm^2/mJ, [PAG]$_0$ = 1. If the net acid production becomes too small, the process parameters shrink and ultimately lead to no process window at all. Therefore it is necessary to find pathway towards sharpening the net acid production.

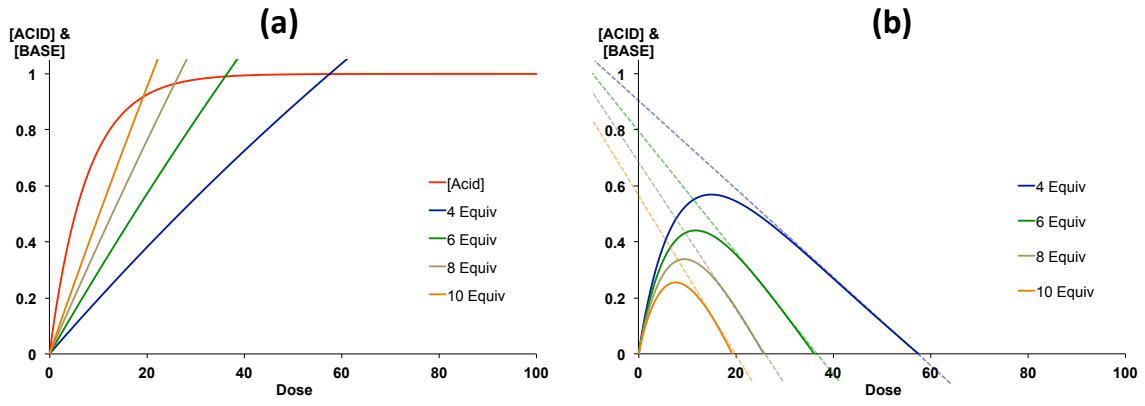

Figure 3.23: Illustration of (a) increasing the [PBG]:[PAG] ratio on the (b) total net acid generation.

It should be noted that while there is an alternating pattern to the LER, even the positive tone lines are not free of LER. Gu calculated nearly a three fold decline in the acid gradient at the solubility threshold of a pitchdivision resist when compared to a conventional resist (*30*). Using similar values to Gu's calculations, the plot in Figure 3.24

clearly illustrates the difference in slope at the same threshold. (Replotted from Figure 3.23, 4 equivalents of PBG)

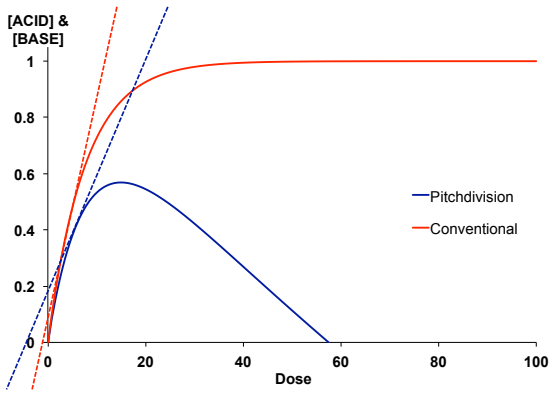

Figure 3.24: Illustration of the slope difference between standard CAR (red trace) and that of a pitchdivision formulation with 4 equivalents of base (blue trace).

This difference in slope is directly caused by base generation. As soon as acid is produced, it is simultaneously quenched by base proportional to the value of k_b. To avoid this low dose quenching, a PBG must have a built in delay, which later accelerates at high dose. Such a delay would allow for an acid gradient comparable to a conventional resist and acceleration at high dose would provide the high dose quenching necessary for the dual tone response. To achieve such a delay and to help remedy the LER via chemistry, we envisioned a two-stage PBG that undergoes two discrete photoreactions to produce one molecule of base. A PBG with built in latency would undergo a reaction pathway similar to that below:

$$Latent\ PBG \xrightarrow{k_{b1}} PBG \xrightarrow{k_{b2}} BASE.$$

For a delay to be realized, k_{b1} needs to be nearly identical to k_{b2} to avoid a pseudo first-order regime where one rate constant is so slow it defines the rate of the overall reaction. Figure 3.25.A illustrates the delay in base generation from a two-stage PBG and its impact on the overall net acid generation. (Parameters for Figure 3.25: k_a = 0.0722 cm^2/mJ, k_{b1} = 0.02 cm^2/mJ, k_{b2} = variable, [PAG]$_0$ = 1, [L-PBG]$_0$ = 2.5). If k_{b1} is close to k_{b2}, the delay at low dose is maximized and accelerates until about 25% conversion prior to achieving a steady state. This delay produces a net acid curve with a similar slope to that of a conventional resist.

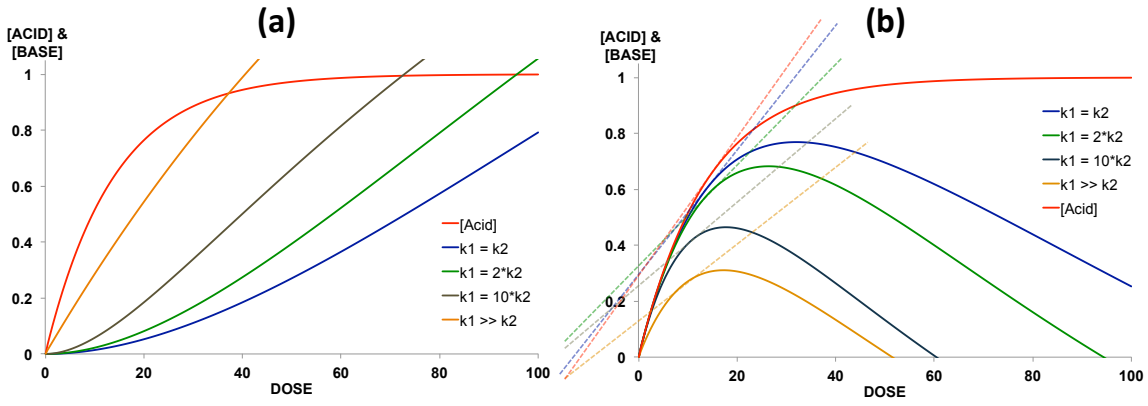

Figure 3.25: Illustration of (a) two-stage base generation at various differences in k_{b1} and k_{b2} and (b) its affect on the low dose slope of the net acid production.

With a two-stage PBG and optimal [PBG] : [PAG] loading, a net acid production with significantly improved slope at both the high and low dose regions can be realized (Figure 3.26).

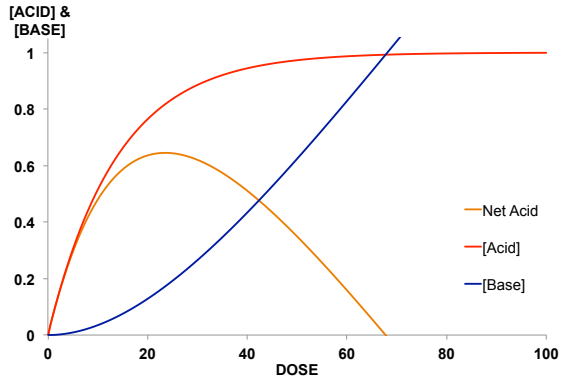

Figure 3.26: Illustration of the net acid production curve through use of a two-stage PBG (k_{b1}= k_{b2}) and optimized loading [PBG]:[PAG] = 5.

3.7 CONCLUSIONS

Photobase generator enabled pitchdivision lithography is capable of doubling the resolution of lithographic systems and achieving an effective k_1 of 0.125. Although line-edge roughness becomes a limiting factor for pitchdivision when printing images at or below 45 nm HP features. Two main areas were identified as the source of the LER. The first area involves standing wave phenomenon and the fidelity of the aerial image at the high and low intensity intervals. Possible solutions to this issue were previously discussed in detail by Xinyu Gu.(*30*) The second major contribution to LER identified is related to the chemistry of chemically amplified resists comprised of two parts: diffusion related blurring and low chemical contrast. Previous studies by former colleagues within the Willson group on polymer-bound PAG and PBG showed some improvements in contrast, but failed to elucidate major improvements.(*78*) Lastly, a two-stage PBG is proposed to improve the slope of the net acid profile at the high and low dose thresholds.

Following, in Chapter 4, is a detailed discussion on the strategy for the design, synthesis and characterization of 2-stage PBGs.

Chapter 4: Two-Stage Photobase Generators

A thorough review of the literature on linked two-stage photoreactions found little precedence(*80*) despite significant interest in photoreactions where rate constants, k_1 and k_2 are approximately equal.(*20*, *21*, *81-84*) The combination of high interest and lack of antecedence meant that a multifaceted strategy was needed to achieve success. This chapter discusses the Willson group collaboration with Columbia University, the University of Ottawa, Portland State University, and Sigma Aldrich Chemical Company. We chose three fundamental approaches to attain a kinetically matched two-stage PBG: (i) symmetrical biscarbamates, (ii) "protected" latent chromophores, and (iii) photoinduced aromatization.

4.1 INTRODUCTION

The most direct approach towards the design of a two-staged PBG with matched kinetics is to build the desired amine around two identical chromophores. With this strategy in mind, the most obvious targets are symmetrical carbamates as illustrated in Figure 4.1. A symmetrical carbamate requires two nearly identical photoreactions before generating a free amine. Except for the absorptivity differences between the two-stage and one-stage variants, this approach should lead to similar k_1 and k_2 values. This strategy also allows for the adaptation of the most successful PBG for pitchdivision, *o*-nitrobenzyl carbamates, as a two-stage generator.

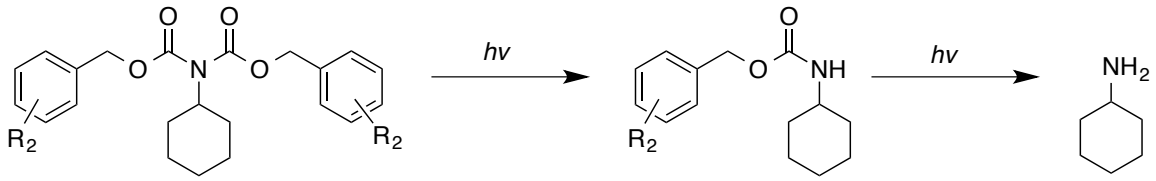

Figure 4.1: Symmetrical biscarbamate requires two photoreactions to release the primary amine.

The second approach is more general and is termed the "Protected PBG" strategy. This approach looks to exploit functional groups that act as the "Achilles' Heel" of the active chromophore. As discussed in Chapter 3 and illustrated in Figure 3.2, many of the known PBGs share common functional groups necessary for base generation. In particular, the ketone moiety stands out as a reoccurring and necessary group for chromophore conjugation in many PBGs, and also lends itself to potential chemical manipulation. Our central strategy focuses on the use of photo-labile phenacylether ketone-protecting groups as illustrated in Figure 4.2.A. The phenyl group lends itself to kinetic tuning through the addition of electron donating or withdrawing groups,(*85*) allowing for the opportunity to tune in adjustments in the photochemical rates of the final two-stage PBG. An alternate protected PBG strategy pursued is shown in Figure 4.2.B. Here a *o*-nitrobenzylcarbonate is used to mask the alcohol in cinnamic acid, to prevent lactone formation upon photoinduced isomerization of the cinnamic alkene.

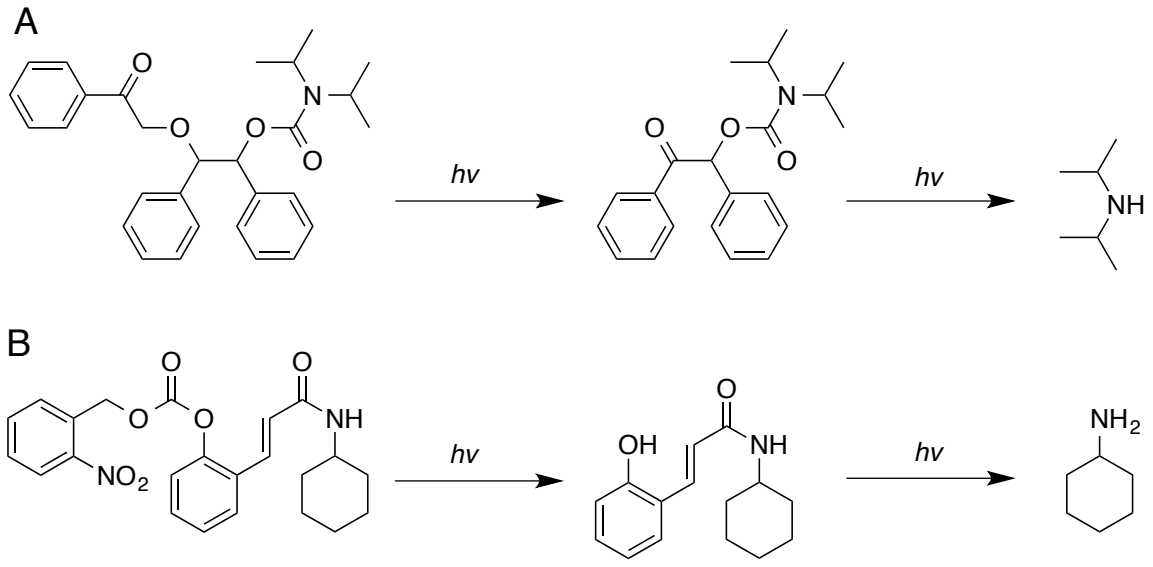

Figure 4.2: Examples of two "Protected PBG" strategies. A) Photolabile phenacylether ketone protecting group. B) *O*-nitrobenzyl carbonate used to mask the alcohol of cinnamic acid.

The third and final approach could loosely be termed a "protected PBG," however it focuses on the specific fact that nearly all lithographically useful PAGs and PBGs contain an aromatic chromophore. The strategy illustrated in Figure 4.3 looks to manipulate the well studied oxime ester photochemistry(*86*) and induce latency in the PBG by introducing a photoaromatization step to form the active chromophore. The majority of the synthesis and characterization of the work on photoaromatization was accomplished by Yuji Hagiwara. This dissertation summarizes the main synthetic challenges and the kinetic evaluation of these PBGs. For more detailed information on the synthesis and photokinetics of this PBG please see the cited papers.(*87*, *88*)

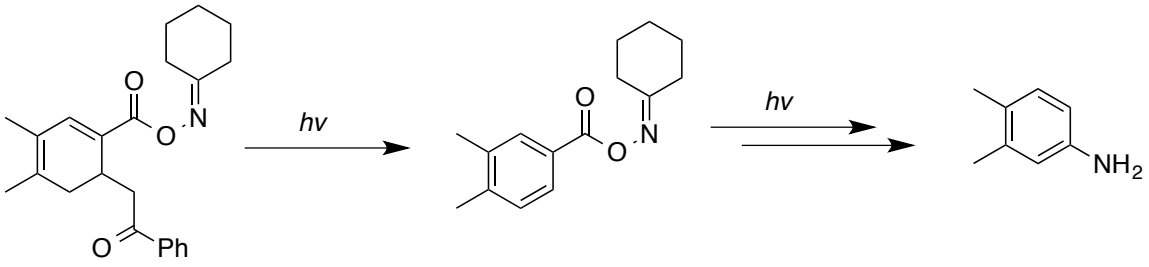

Figure 4.3: Photoinduced aromatization strategy.

This chapter explores the challenges and accomplishments in the design, synthesis, and characterization of each class of two-stage PBG. While each approach was pursued simultaneously, successes in each strategy were achieved at different points throughout this project. The results in this chapter are delivered chronologically to give a better sense of the experiments and decision-making process throughout this project.

4.2 PROTECTED PBGS

The first successful synthesis path to two-stage PBGs was the protected PBG class. Three of the four PBGs in this group, illustrated in Figure 4.4, share the same phenacyl ether photo-labile ketone protecting group originally described by Roger Binkley in the little-known Journal of Carbohydrates, Nucleosides, Nucleotides.(*89*) By masking the ketone, our aim was to temporarily inactivate the chromophore by disrupting the necessary absorption and/or conjugation the ketone provides. The other protected strategy investigated is the coumarin-based PBG,(*38*, *90*) CHA-COUM2. By blocking the phenol with a *o*-nitrobenzyl protecting group, we sought to create a two-stage process by

requiring the deprotection and the isomerization to both take place independently before the intramolecular amine generating lactonization may take place.

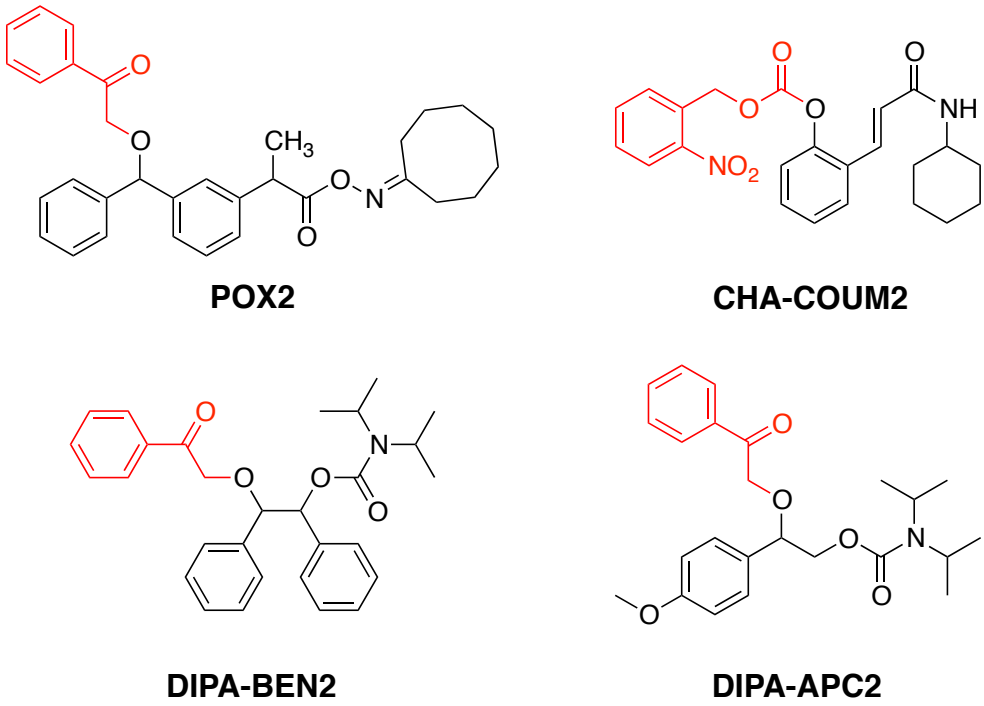

Figure 4.4: Illustration of the four "Protected PBGs" synthesized and characterized for pitchdivision lithography. Protecting groups shown in RED.

4.2.1 PHENACYLETHER CHARACTERIZATION

A post-doctoral researcher, Arun Sundaresan, originally led the phenacylether synthesis and characterization from the former Turro Group at Columbia University; therefore it affectionately became termed the Arun protecting group. The Arun protecting group is proposed to undergo the well-characterized and reliable Norrish Type II intramolecular hydrogen abstraction, as illustrated in Figure 4.5. The accepted

mechanism for Norrish Type II reactions is illustrated as occurring from the β-cleavage of the 2–3 bond of the 1,4-biradical intermediate to produce benzophenone and the acetophenone enol.

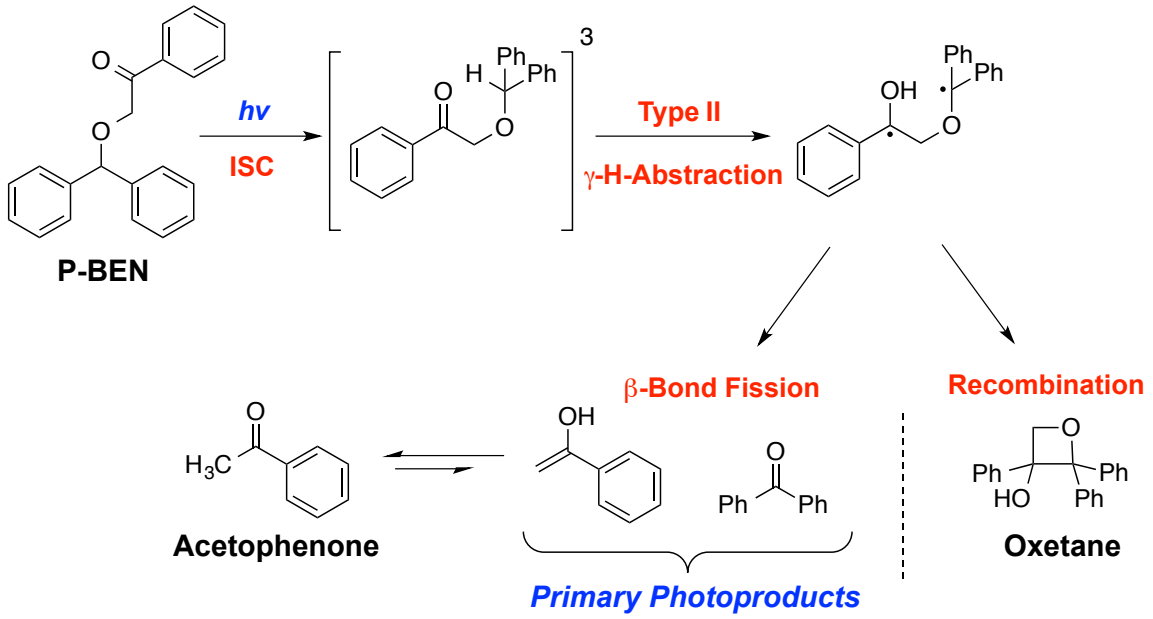

Figure 4.5: Predicted photoreactive pathway of phenacylether protected ketones.

Because the photoreaction goes through a biradical mechanism, other, non-favorable pathways are possible. The primary Norrish Type II, 1,4-biradical pathway allows for recombination to form an oxetane rather than the desired ketones. Further, radical recombination is not the only competing pathway. Figure 4.6 shows the products that may result from the potential Norrish Type I α-cleavage route.

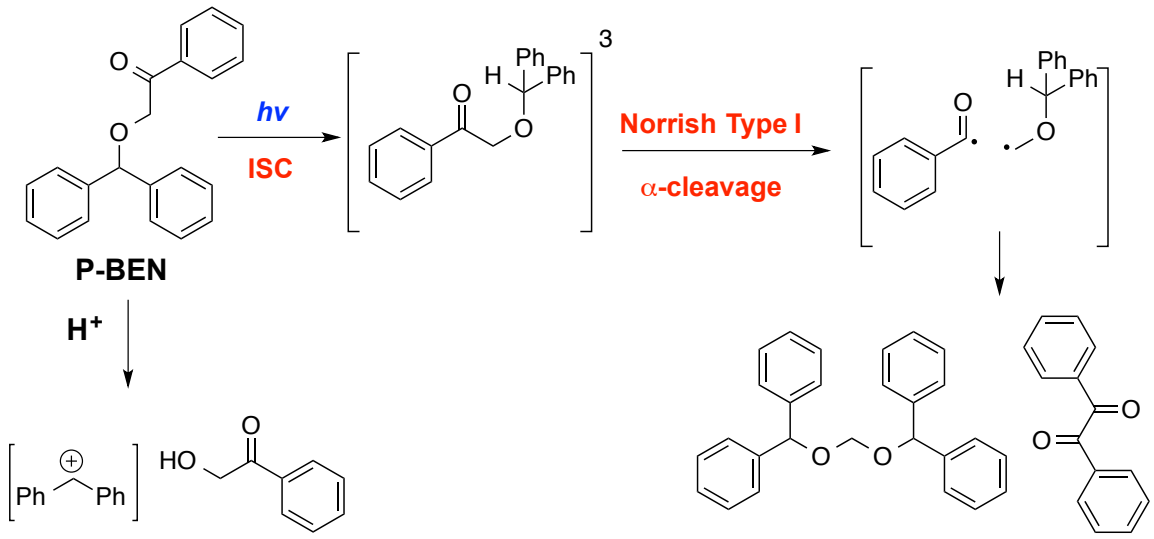

Figure 4.6: Photochemical pathways of the competing Norrish Type I reaction.

To assess the utility of the Arun protecting group as a possible first stage photoreaction, the phenacylether-protected benzophenone (P-BEN) was synthesized as a model compound. P-BEN was prepared in oxygen free deuterated acetonitrile (2 mM) and exposed to 254 nm light. The reaction was monitored by proton NMR, HPLC, and GC analysis. The ^{1}H-NMR showed the reaction was predominantly clean and produced only a few unknown by-products and a minor amount of identified oxetane (Figures 4.7 & 4.8).

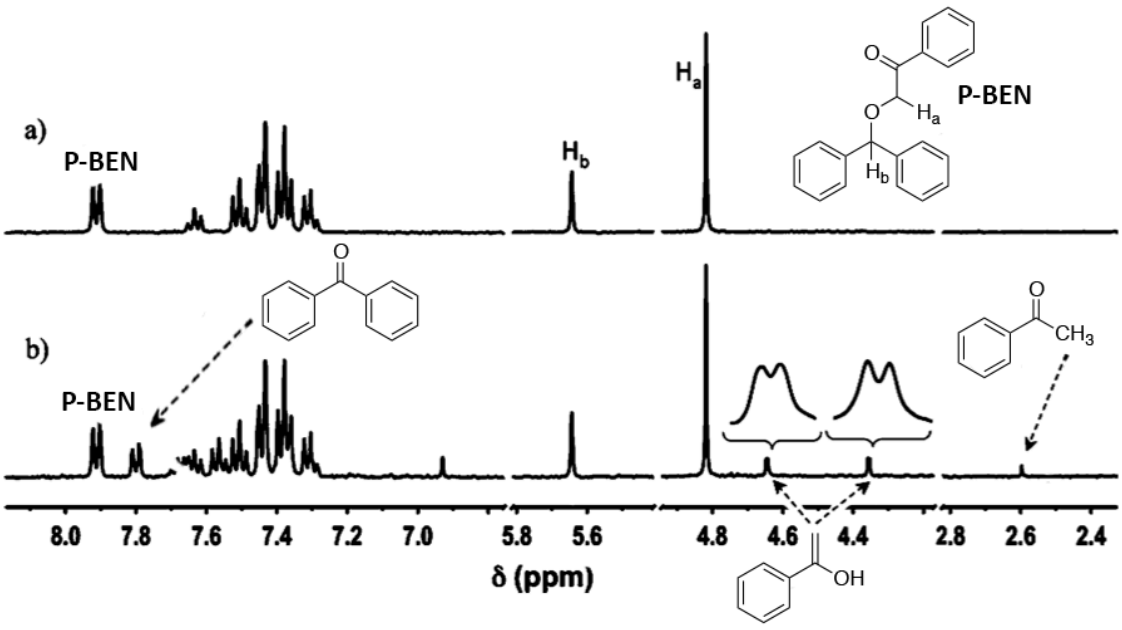

Figure 4.7: Proton NMR spectrum of exposed P-BEN.

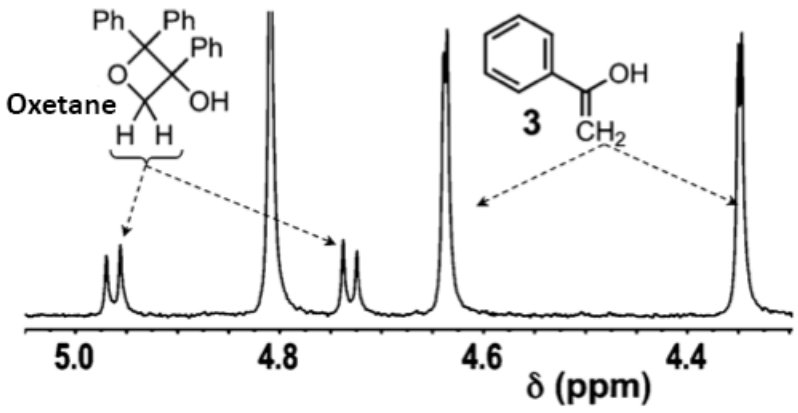

Figure 4.8: Proton NMR identification of the recombination product oxetane.

The quantum efficiency of the reaction was monitored using valerophenone (Figure 4.9.A) as an internal actinometer.(*91*) Valerophenone shows similar absorption properties to the Arun protecting group and undergoes efficient Norrish type-II reaction upon photolysis with a quantum yield of Φ = 1.0 (loss of valerophenone) in acetonitrile.(*92*) Using valerophenone as actinometer a quantum yield of 0.80 for benzophenone 0.65 for acetophenone was determined at 254 nm, as shown in Figure 4.9.B. The discrepancy in quantum yield is seen in HPLC analysis, as the ratio of benzophenone to acetophenone was not 1 : 1 but 1 : 0.8. The exact reason for this discrepancy is unknown, and it is assumed that acetophenone must be reacting with either itself or with the starting material in some fashion.

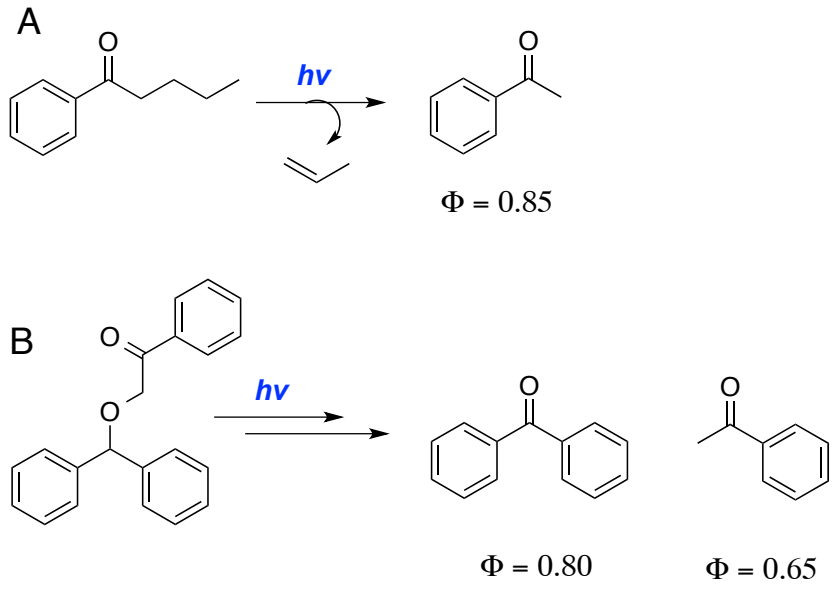

Figure 4.9: (A) Photoproduct and quantum efficiency of valerophenone. (B) Major products and their respective quantum efficiencies of phenacylether photolysis at 254 nm.

4.2.2 OX2 SYNTHESIS & CHARACTERIZATION

In the protected PBG scheme, we first studied the benzophenone-based oxime esters OX2 and its Arun-protected variant POX2 (Figure 4.2). O-Acyloximes are known to generate primary amines upon exposure to UV. The mechanism drawn in Figure 4.10 is proposed by Lalevee and coworkers(*86*) based upon the identification of the stable intermediate benzyl and inminyl radicals.

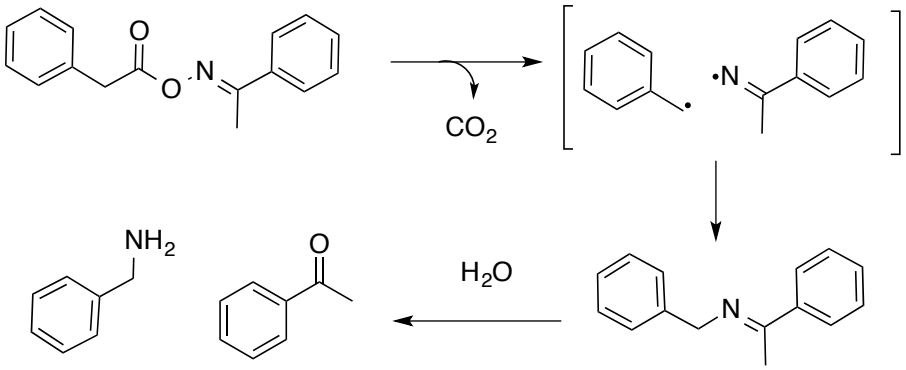

Figure 4.10: Proposed photodecomposition pathway of O-acyloximes. The imine, already a weak base, can undergo hydrolysis during the resist development to generate the stronger base 3-aminophenol.(*86*)

Unfortunately, most acyloxime PBGs are very slow (low ϕ), and earlier studies showed that the presence of a triplet sensitizer is necessary for various O-acyloximes to generate the desired base.(*86*, *93*) To increase the reaction rates of the acyloxime PBGs, the phenyl acetyl chromophore was altered from a simple phenyl group to the well-known triplet sensitizer, benzophenone.(*94*) This adaptation attempts to create a simple and self-contained base generator by physically tethering the sensitizer to the oxime ester.

As it happens, the ideal test compound to determine if securing the sensitizer to the PBG works is the commercially available drug known as ketoprofen. To test whether ketoprofen expels CO_2 and ultimately generates a free amine, a simple experiment was preformed by exposing a solution of ketoprofen in deuterated acetonitrile and water (80 : 20) to 254 nm light and subsequently monitoring the photoproducts by electrospray ionization mass spectrometry (ESI-MS). The results shown in Figure 4.11 support the working hypothesis, as the main product is the recombined dimer of the stabilized benzyl radical, as predicted, after the loss of CO_2.

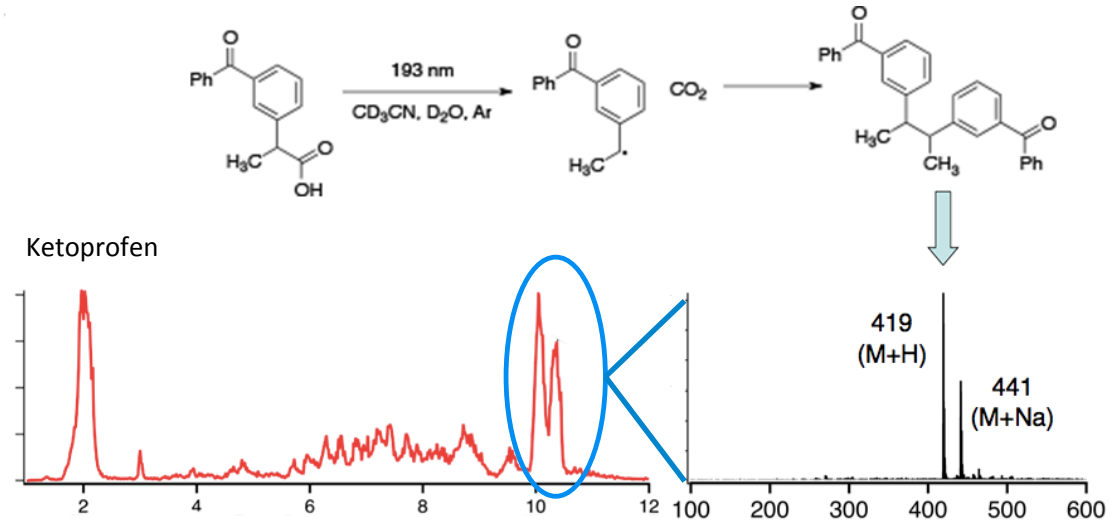

Figure 4.11: ESI-MS Data of the photolysis of ketoprofen. Two major peaks are identified as ketoprofen (left) and the recombination product (circled right).

Producing PBG OX-2 from ketoprofen simply requires the formation of an oxime ester via carbodiimide (EDCI) facilitated coupling of the carboxylic acid and the desired oxime as outlined in Figure 4.12.

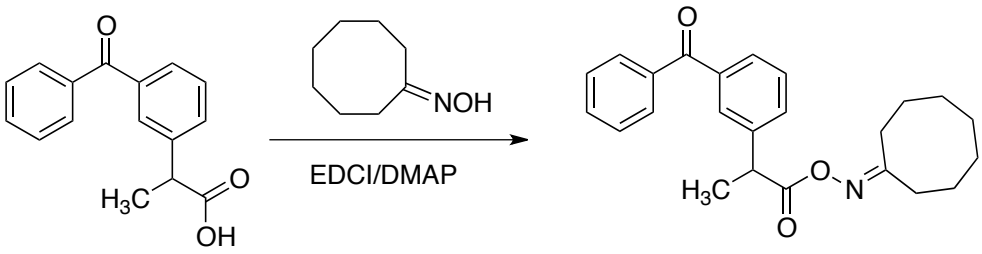

Figure 4.12: Reaction scheme for synthesis of PBG OX2.

Former group member Brandon Rawlings preformed initial studies with OX-2 during an internship with the Intel Corporation. Using the generic 193 nm resist described in Chapter 3.4.2 with 7 wt% TPS-NfO PAG loading, a [PBG] : [PAG] = 2 and a PEB of 115 ºC, Brandon created the contrast curve in Figure 4.13.

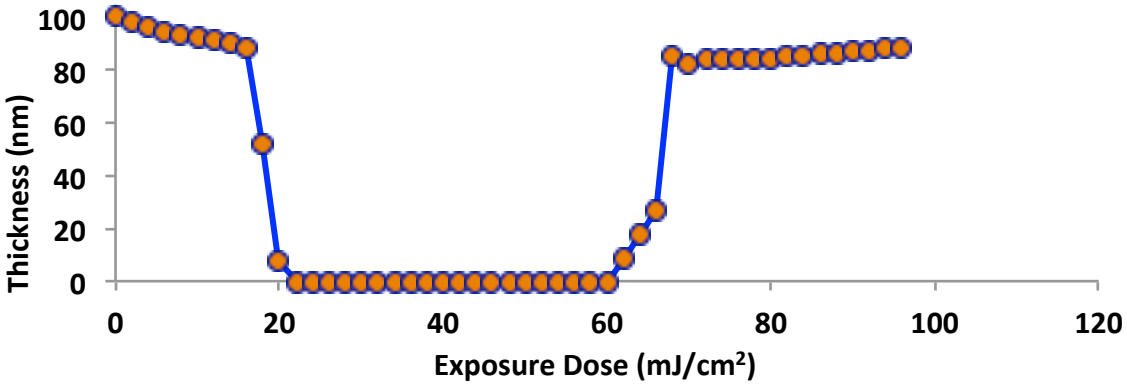

Figure 4.13: Exposure window of OX-2 and a generic 193 nm resist formulation. PEB = 115 ºC, [PBG] : [PAG] = 2.

Using the same resist and PEB conditions as the exposure window, the image in Figure 4.14 was printed with a NA = 0.22 , k_1 = 0.25, and a 200 nm HP feature mask. The image

in 4.14 suffers from large LER, but it is also free of bridging and collapsed lines, which makes it a good candidate to test the two-stage PBG hypothesis.

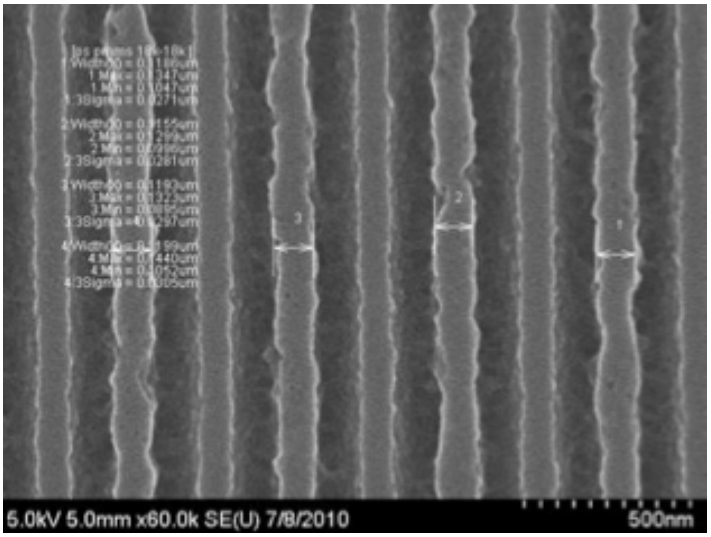

Figure 4.14: SEM image of pitch divided line and space patterns at NA = 0.22. The half-pitch (HP) size defined by the mask is 200 nm, and the resulting resist pattern reveals a feature size of 100 nm HP.

4.2.3 POX2 SYNTHESIS AND CHARACTERIZATION

Having a working benzophenone-based oxime ester PBG (OX-2) and a strategy to disrupt the active chromophore via the Arun protecting group, the groundwork was set to synthesize the first two-stage PBG (POX-2). The final synthetic pathway is outlined in Figure 4.15. The methyl ester is formed by treating ketoprofen with methanol and sulfuric acid (not shown). The ketoprofen methyl ester is then reduced with sodium borohydride to the phenyl-benzyl alcohol to allow for the placement of the phenacylether.

The purity of the phenacyl triflate ether proved to be a key factor in the overall yield of the protecting group installation. Great care was taken to form the triflate ether in anhydrous and oxygen-free conditions with subsequent sublimation to remove impurities.

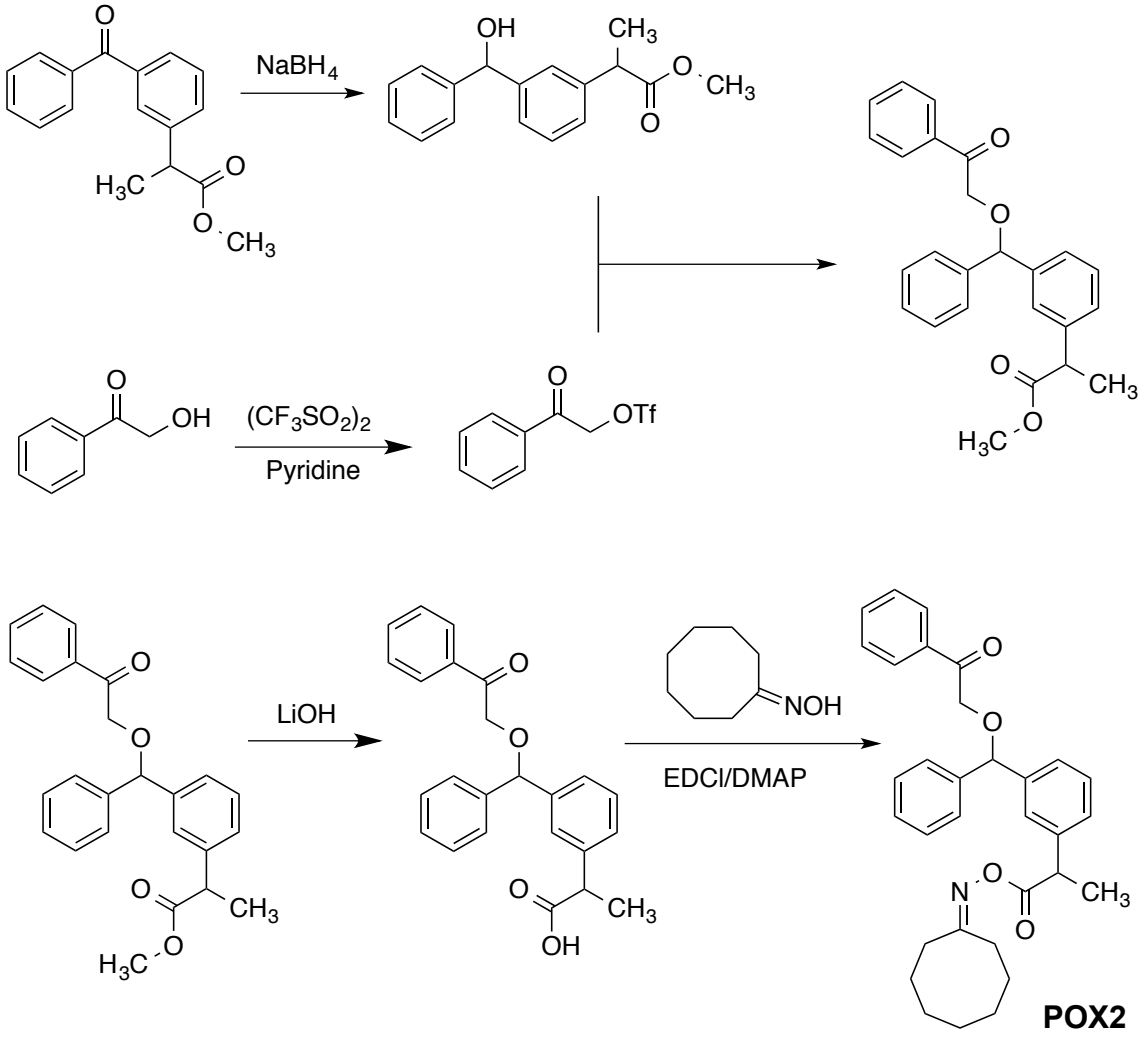

Figure 4.15: Illustrated reaction scheme for the synthesis of POX-2.

With the Arun protecting group in place, the final steps of the synthesis appeared straightforward. Yet the methyl ester proved challenging to remove because the

phenacylether is sensitive to both mildly acidic and basic conditions. After screening many acids and bases in an attempt to hydrolyze the ester, lithium hydroxide proved to be the Goldilocks reagent; just strong enough to cleave the ester and just weak enough to not harm the phenacylether. The installation of the oxime ester was installed as described earlier for OX-2, through an EDCI mediated coupling reaction.

Excitement swirled when POX-2 was finally synthesized. The characterization began immediately. As mentioned in Chapter 3, finding the quantum efficiency of a simple PBG is not trivial. A significant analytical challenge arises when addressing a linked two-stage photoreaction. The ideal photodecomposition pathway is illustrated in Figure 4.16. Already known from previous experiments, (Figures 4.8 & 4.11) neither the first stage nor the second stage is perfectly clean and these results are both without a generated primary amine in the mix!

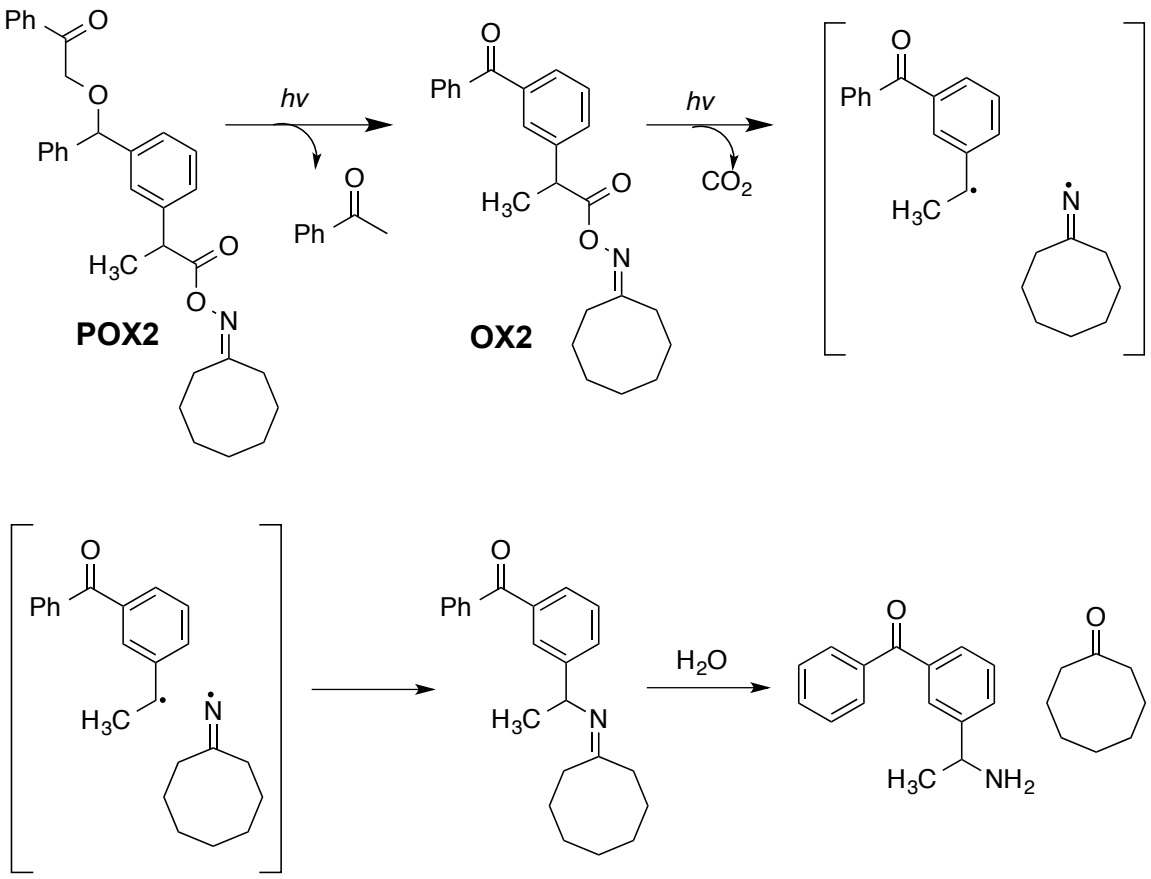

Figure 4.16: Illustrated reaction scheme for the photodecomposition of POX-2.

A number of excellent experiments were run by Arun to find the approximate rate of base generation. Using HPLC, gas chromatography (GC) and ^{1}H-NMR, both OX2 and POX2 photoreactions were exhaustively monitored. The generation of acetophenone, cyclooctanone, and various benzophenone derivatives could be identified, although the direct characterization of the free amine proved to be elusive. In conclusion, low conversion experiments, monitored by ^{1}H-NMR, were used to monitor the generation of acetophenone and OX-2 from POX-2. The difference between OX-2 and acetophenone

was then used to give an approximation for base generation. In general, the results were inconclusive as to whether or not kinetically matched 2-stage behavior was observed (Figure 4.17).

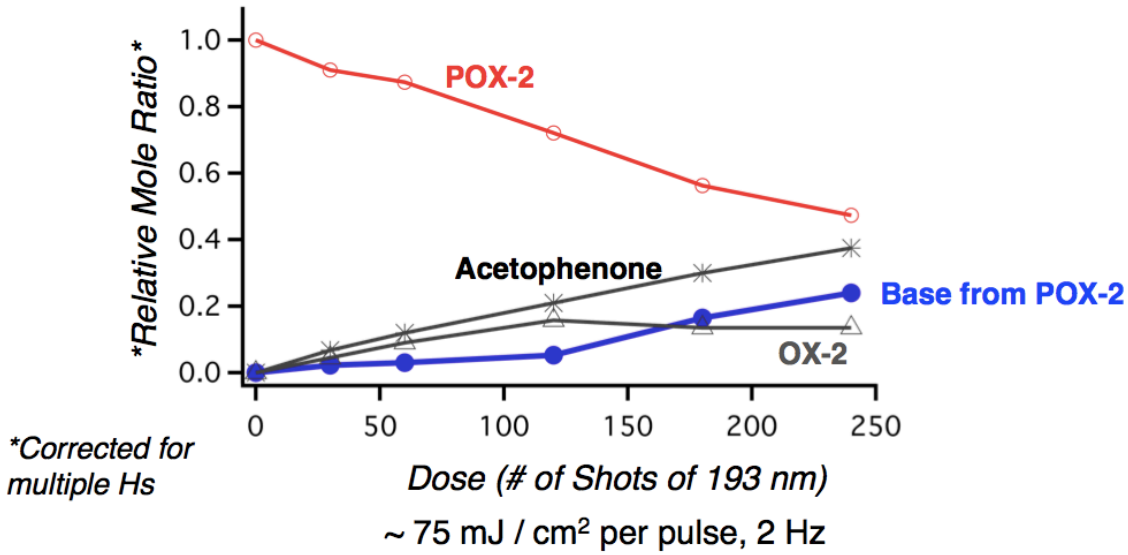

Figure 4.17: Plot of POX-2 photolysis monitored by HPLC detection of OX-2 and acetophenone. Base is approximated from the difference of OX-2 and acetophenone.

In an attempt to better clarify whether or not two-stage behavior was taking place, POX-2 was directly compared to the known first-order photoreaction and base generation of DCHA-NO2 (Figure 3.4). Figure 4.18.A plots the base generation from equal concentrations (5 mM) of POX2 and DCHA-NO2. Figure 4.18.B plots the comparative base generation of POX2 (1 mM) and DCHA-NO2 (5 mM), formulated to have the matched optical density at 193 nm.

Unfortunately, no direct evidence of kinetically matched two-stage behavior was observed. The failure to directly detect amine generation along with the formation of many side products obfuscated much of the analytical data. In the end, the decision was made to move past POX-2 and to continue focussed efforts towards the development of other candidates.

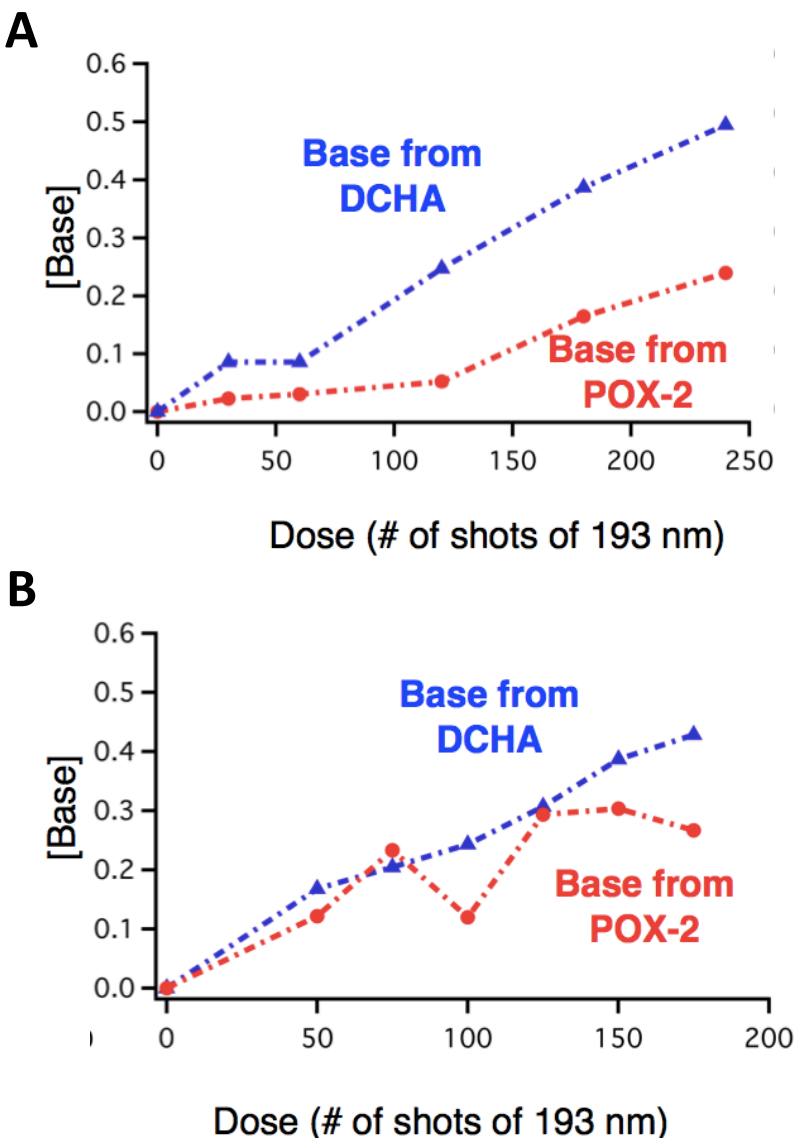

Figure 4.18: (a) Comparison of approximated base formation between DCHA-NO2 and POX-2 at equal concentrations (5 mM). (b) Concentration corrected comparison of base formation. (DCHA-NO2 = 5 mM; POX-2 = 1 mM.)

4.2.4 CINNAMIC-COUMARIN PBGS

The utilization of the well-established photo-isomerization of cinnamic acids to yield coumarin(*95*) as a protecting group and PBG is well documented.(*38*, *42*, *96*) The photo-induced cis-trans isomerization places the carbonyl in an ideal position to form the intramolecular α-β unsaturated δ-lactone of coumarin with the ortho-positioned alcohol as illustrated in Figure 4.19.(*97*)

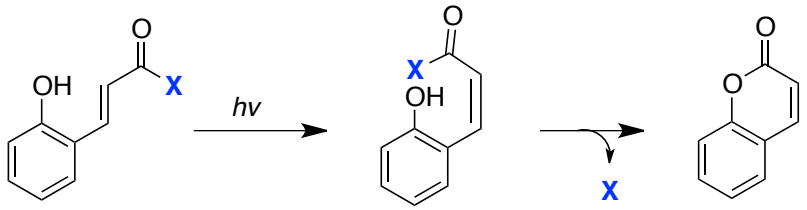

Figure 4.19: Illustrated reaction scheme of the photoinduced isomerization of cinnamic acid and the subsequent coumarin forming lactonization.

The two-stage coumarin PBG, CHA-COUM2, (Figure 4.4) was a promising target since its synthesis is a sequence of two straightforward steps. The carbamate is readily formed via carbodiimide mediated coupling, and the installation of the *o*-nitrobenzyl carbonate is quantitatively accomplished from the *o*-nitrobenzyl chlorocarbonate. Unfortunately, the coumarin PBG is not compatible with the pitchdivision formulations we attempted. The literature reports that some investigators conduct the photo-deprotection in the presence of acid to catalyze the intramolecular lactone formation. Without the presence of acid, the generation of base is far too slow for lithographic purposes.

4.2.5 PROTECTED BENZOIN PBGS

In addition to the *o*-nitrobenzyl carbonates, the best PBGs tested for pitchdivision were from the benzoin class of chromophores (Chapter 3.4). Originally characterized as base generators by Cameron and Fréchet(*58*), they showed that the large conjugated chromophore increases the efficiency of amine generation in comparison to the smaller benzyl variants. This difference in efficiency is evident in our initial PBG screening in the comparison of contrast curves between CHA-TMBEN (Figure 3.13.B) and DIPA-DM (Figure 3.14). The benzoin chromophore conjugation is dependent on a ketone alpha to a benzyl group, which is analogous to the benzophenone PBGs such as OX-2. We predict that this ketone acts as the Achilles' heel of the chromophore, which allows for full conjugation and increased photo-efficiency.

To create the greatest latency in the PBG, we chose to focus on the straight benzoin PBG. Previous work in the Willson group showed that benzyl carbamates do not generate base on a timescale suitable for lithography; whereas the 3,5-dimethoxybenzyl carbamates (DIPA-DM) are known produce base, but not at a rate ideal for pitch division (Figure 4.20).

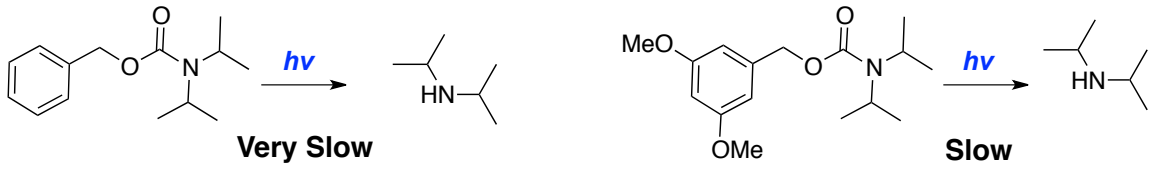

Figure 4.20: Illustration of benzyl carbamates.

The earliest synthetic attempts focused on the N-cyclohexyl benzoincarbamate (CHA-BEN). This amine is aligned with the benzoin carbamates characterized by Cameron and Fréchet and also provides easy installation, requiring only the mixing of benzoin and cyclohexylisocyanate (Figure 4.21). The selective reduction of the benzoin ketone was accomplished with sodium borohydride in a methanol : tetrahydrofuran (1 : 6) solvent mixture. Without tetrahydrofuran, the benzoin carbamate was not sufficiently soluble to allow the reaction to go to completion. The final step and installation of the phenacylether did not proceed under the same conditions previously used for POX-2. The main products of this reaction were N-cyclohexyl phenacylcarbamate and 2-(cyclohexylamino)- phenylethanone, with no sign of the desired product.

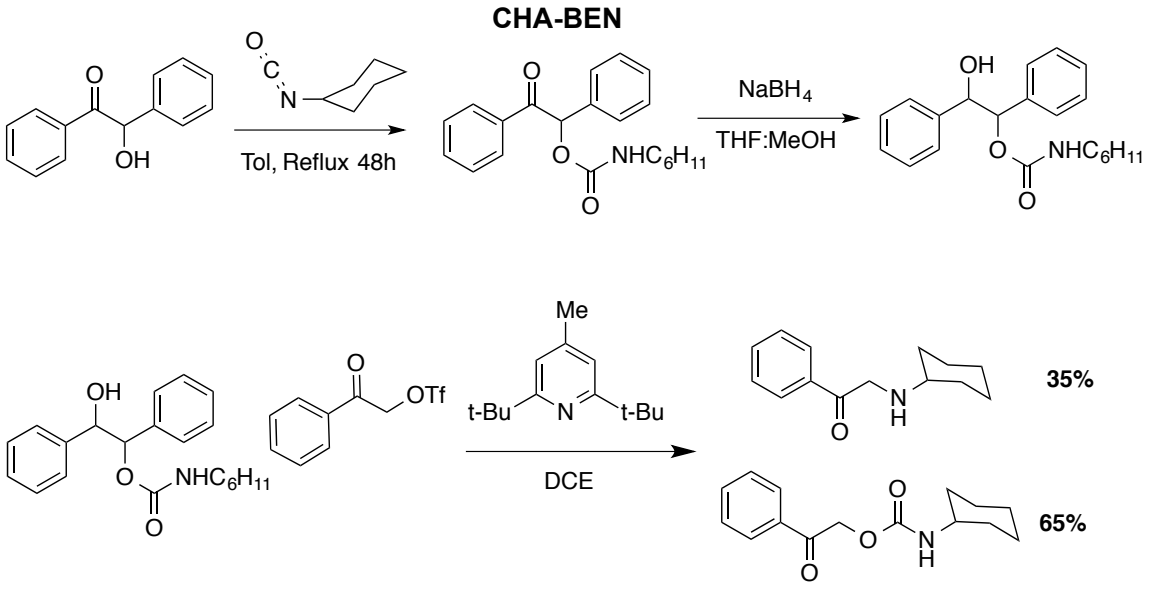

Figure 4.21: Schematic of the attempted CHA-BEN2 synthesis.

We propose the outcome of this reaction is due to the large electron density around the carbamate that is capable of quickly reacting with the strong triflate electrophile as shown in Figure 4.22. The favorable disassociation of the carbamate-benzoin bond leads to the formation of N-cyclohexylphenacylcarbamate, and a stabilized benyl cation, which can decompose to multiple products such as toluene, benzaldehyde, and stilbene oxide.

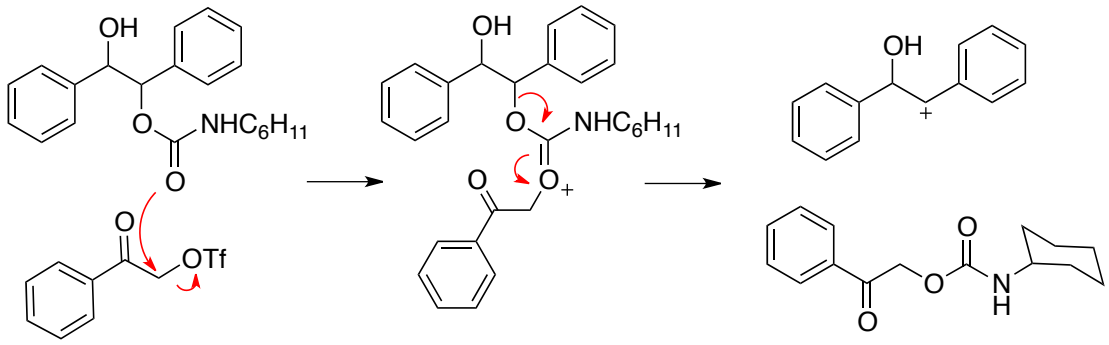

Figure 4.22: Illustration of the proposed mechanism leading to the formation of N-cyclohexylphenacylcarbamate during the attempted synthesis of CHA-BEN2.

After several attempts, a new strategy was devised to install the phenacyl ether first, followed by the carbamate. The first path chosen examined stilbene oxide as an electrophile. In theory, if the nucleophilic 2-hydroxyphenylethanone opens the epoxy, the ether is formed and the benzylic alcohol would be ready to react with the chosen isocyanate (Figure 4.23.A). The second approach examined hyrdobenzoin as a nucleophile for installation of the Arun protecting group (Figure 4.23.B)

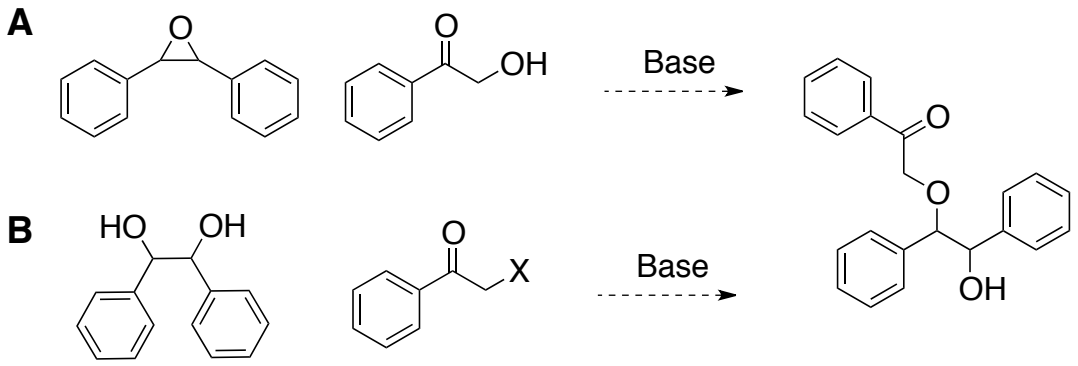

Figure 4.23: Schematics of two proposed alternate routes towards CHA-BEN2.

The stilbene oxide approach, although tested extensively, was ultimately unsuccessful by this author. Amine bases, alkali bases and Lewis acids were all screened. A sampling of the reactions tested is illustrated in Figure 4.24. Often times no reaction would take place, or in the case of the Lewis acids, the stilbene oxide often rearranged to 2,2-diphenylacetaldehyde. Control reactions using the potassium salts of benzyl alcohol and phenylethanol showed that a stronger nucleophile is required to open the epoxide, therefore the decision was made to move beyond this strategy to explore the reactions with hydrobenzoin. Figure 4.25 shows a sample of the reactions that were run with hydrobenzoin.

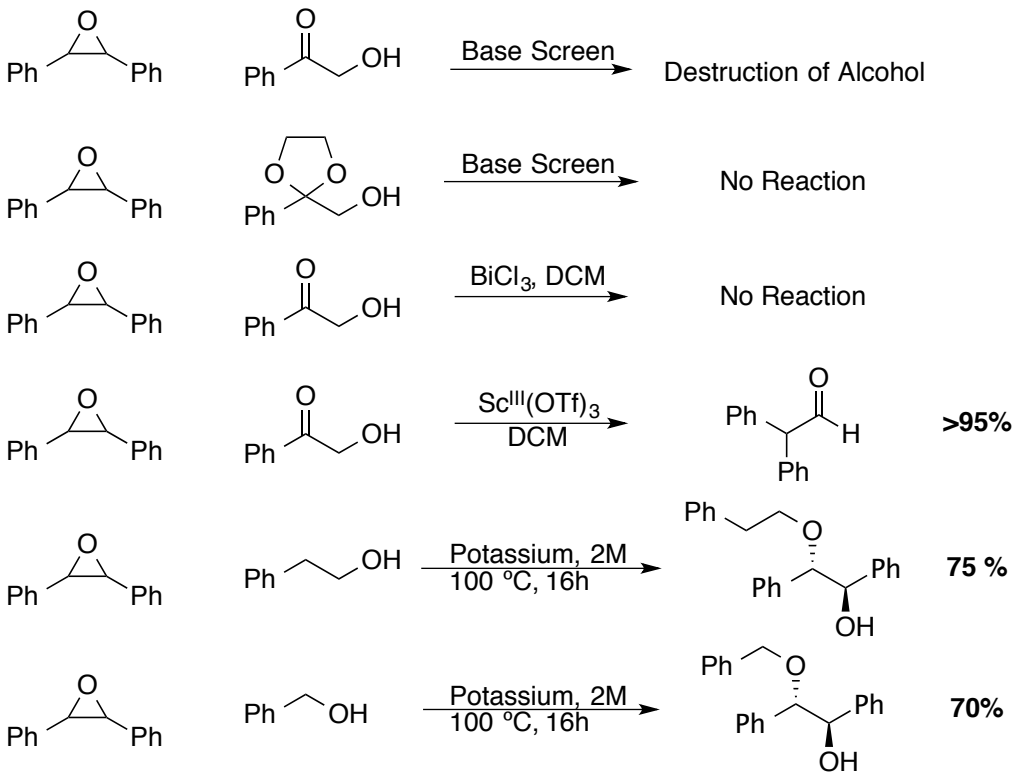

Figure 4.24: Illustrated list of stilbene oxide reactions run in attempt to install the Arun protecting group.

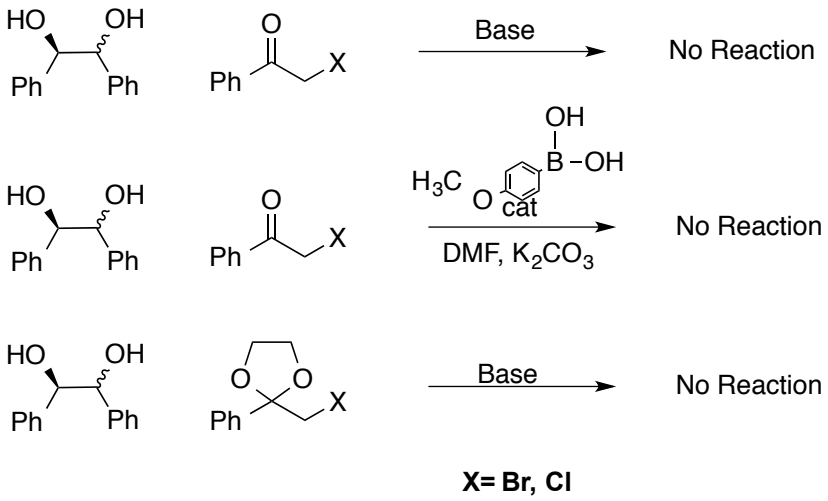

Figure 4.25: Illustrated list of hydrobenzoin reactions run in attempt to install the Arun protecting group.

While screening the hydrobenzoin pathway, tertiary carbamates were also explored. Surprisingly, the tertiary carbamates allow for the installation of the Arun protecting group via the original triflate ether synthetic pathway (Table 4.1). While the CHA-BEN is known to be stable up to 110 ºC,(*55*) it is possible that at the required high reaction temperatures, the presence of the strong triflate electrophile promotes the formation of the unfavored N-cyclohexylphenacylcarbamate. The disubstituted carbamate avoids the presence of a thermally labile carbamate proton, leading to increased thermal stability. Disubtitution also significantly increases the steric hindering around the carbamate, which likely plays a role in promoting the desired reaction pathway.

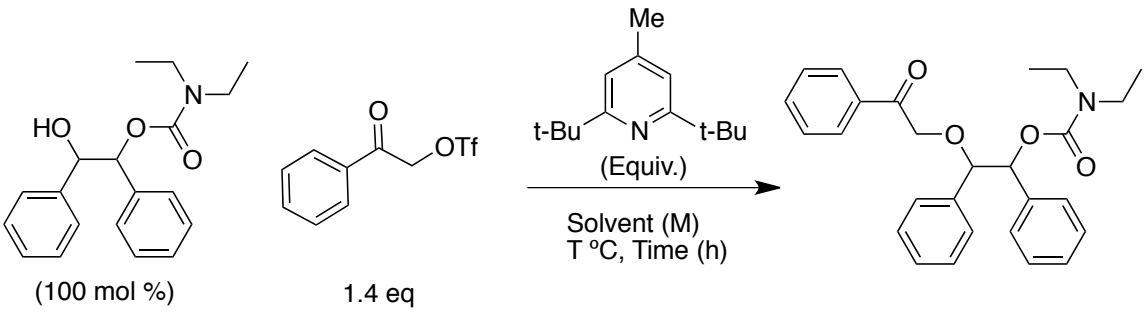

Entry	Pyr (Equiv)	Solvent (M)	T °C	Time	Yield
1	2	DCM (1 M)	40	24	NR
2	2	DCM (1 M)	40	48	~ 15 %
3	0.9	DCM (1 M)	40	48	< 5 %
4	2	THF (1 M)	66	48	0 %
5	2	DCE (1 M)	84	48	40 %

Table 4.1: Optimization table for installation of phenacylether to form DEA-BEN2.

The discovery of the stable tertiary carbamate led not only to our target two-stage PBG, it also allowed for a comprehensive control experiment to test the "reduced benzoin" hypothesis. Diisopropylbenzoin carbamate (DIPA-BEN) was synthesized along with the methoxyether variant illustrated in Figure 4.26.B. The two benzoin compounds were then exposed to broadband UV light in deuterated THF (20 mM) while the generation of free amine was monitored by ^{1}H-NMR. Figure 4.26 shows the disrupted methoxyether benzoin shows no change in spectrum after 120 minutes of exposure, whereas the DIPA-BEN sample showed generation of free amine after only 30 minutes. The identification of diisoproyl amine (DIPA) (the orange highlighted peaks in Figure 4.26.A) was confirmed through a standard addition, which increased the amplitude and integration of the signal.

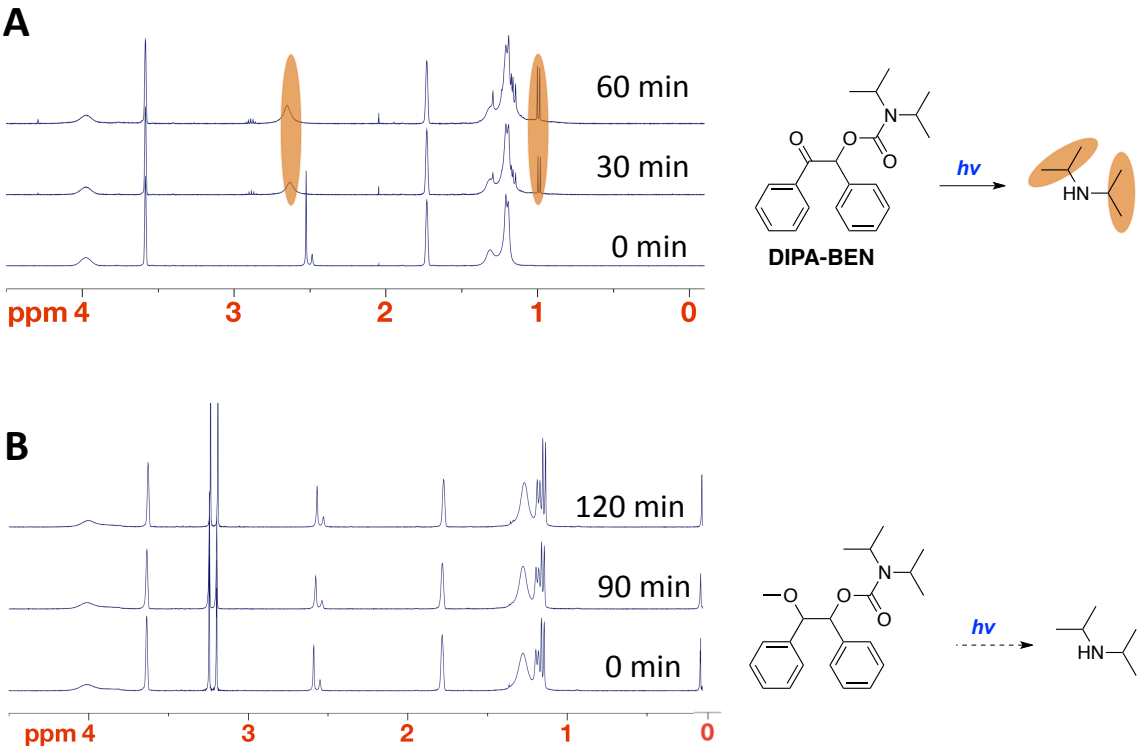

Figure 4.26: ^{1}H-NMR spectrum of exposed DIPA-BEN (A) and the reduced ketone variant of DIPA-BEN (B). Free amine generation is highlighted in orange.

Contrast curves were produced as described in Chapter 3.4.1 on both the one and two-stage benzoin carbamates (Figure 4.27). Each benzoin exposure window was made using a commercially available 193nm resist. The DE-BEN formulation had 5 mM PBG loading and a PEB of 126 ºC. The DIPA-BEN2 formulation had 6 mM loading and a PEB of 125 ºC. Comparing these benzoin contrast windows, it is noteworthy to see that even at higher PBG loading with lower PEB temperatures that the E_0 stays about the same. In general, decreasing the PEB increases the E_0 acid threshold as does increasing

the amount of PBG loading, therefor it appears that the DIPA-BEN2 has some latency causing little to no increase in E_0.

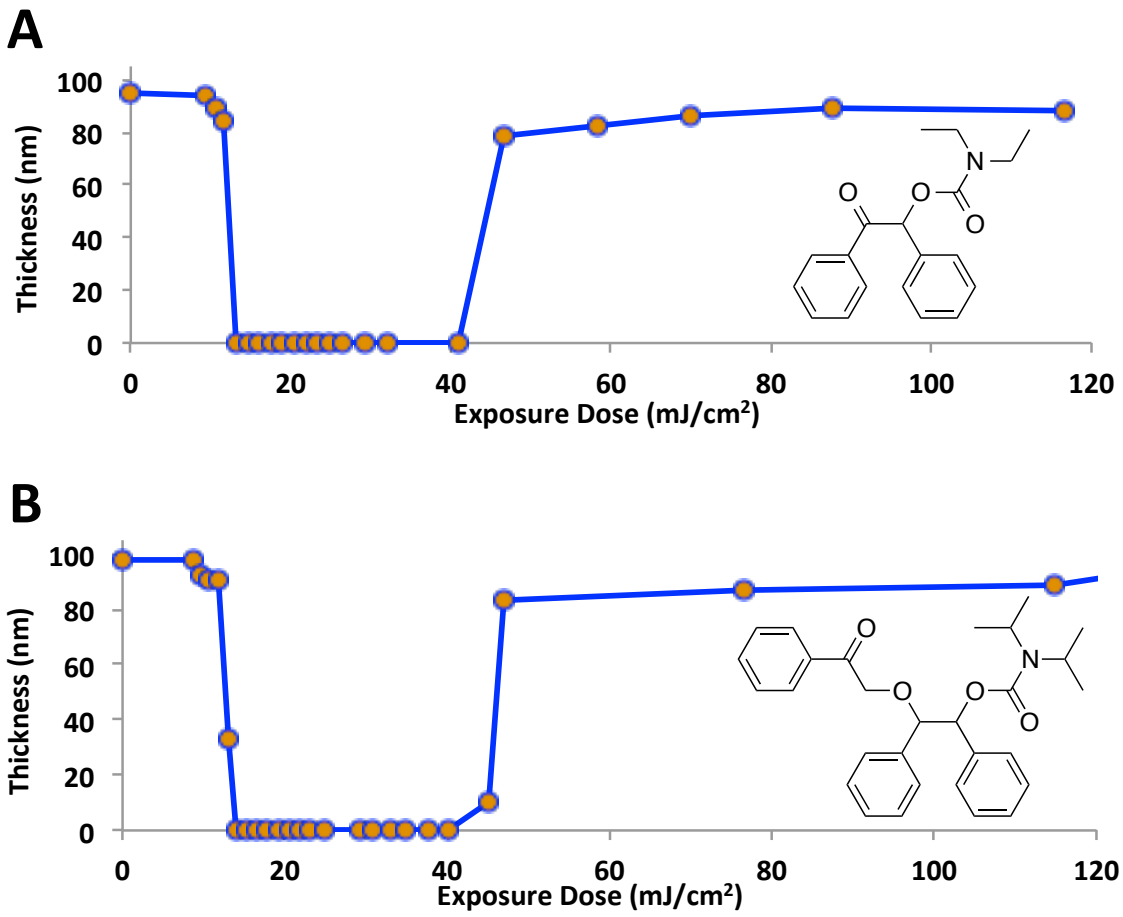

Figure 4.27: Contrast curves of resist formulations containing different PBG: (a) DE-BEN; (b) DIPA-BEN2.

The earlier control experiment represented in Figure 4.26 shows that ^{1}H-NMR may be used to monitor benzoin amine generation. The photoproducts of the two benzoin PBGs are complex, which limit this type of experiment to qualitative analysis. At low

dose conversion, the high field, ~1 ppm, NMR spectrum is fairly clean allowing for integration of free DIPA. Both compounds were concentration corrected to matched absorbance at 360 nm in deuterated THF with exposure to broadband UV. The results of the NMR experiment are shown in Figure 4.28.

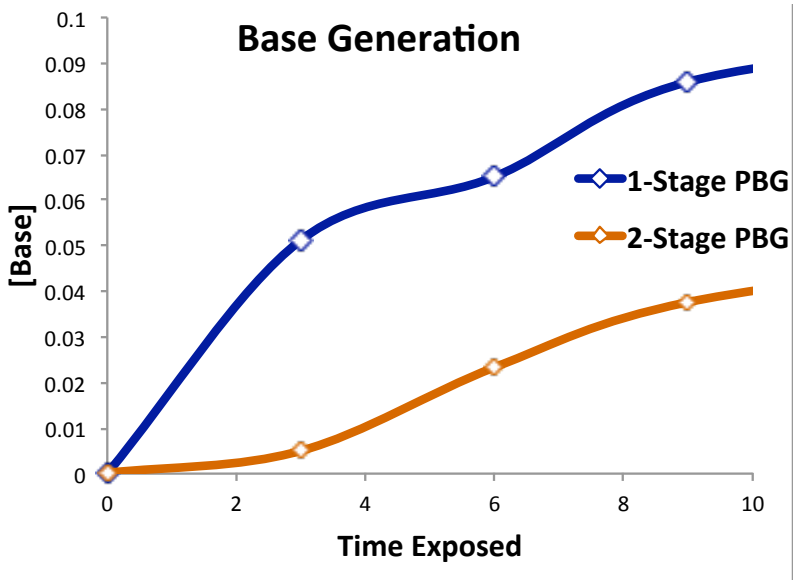

Figure 4.28: Plot of low dose conversion of **DIPA-BEN** and **DIPA-BEN2** to free amine.

Motivated by the delay in base generation of DIPA-BEN2 seen in Figure 4.28, we sought a more qualitative method of amine generation. Monitoring by GC and HPLC proved infeasible due to the "noise" of complex side reactions. In an attempt to circumvent the numerous organic side reactions, ion chromatography (IC) was tested as a method to determine quantum efficiency. IC is capable of accurately detecting amines in

concentrations below 1 ppm, therefore represents a promising tool for use in quantum efficiency studies.

For the case of the benzoin PBGs, IC did not resolve the complexity problems. The photoreactions are cleanest in ethereal solvents such as diethylether and THF and do not appear to work in acetonitrile. THF is incompatible with the IC eluent, methanesulfonic acid, since it promotes the polymerization of THF and damages the instrumentation. Diethylether proved too volatile to provide accurate reproducibility since the IC instrument only allowed for auto-injection and the syringe system used could not be optimized for a high vapor pressure solvent. Due to the highly complex photoreaction owing to the particular solvent conditions necessary to study the benzoin PBGs, further analytical studies were halted. Focus was redirected into imaging studies.

Takanori Kawakami performed the following image studies at the former SVTC Technologies lab in Austin, TX. All images were printed with a dry 193 nm ASML tool operating at NA = 0.75 with an effective k_1 = 0.46 and a 120 nm half-pitch phase-shifted feature mask. To make a LER comparison between the two PBGs, each was formulated and processed to print equal lines and spaces with an E-factor of 0.55. Figure 4.29 shows the final results of the optimized imaging for each PBG. While an improvement in LER is seen with DIPA-BEN2, the overall LER of the two images is too extreme to take an actual measurement.

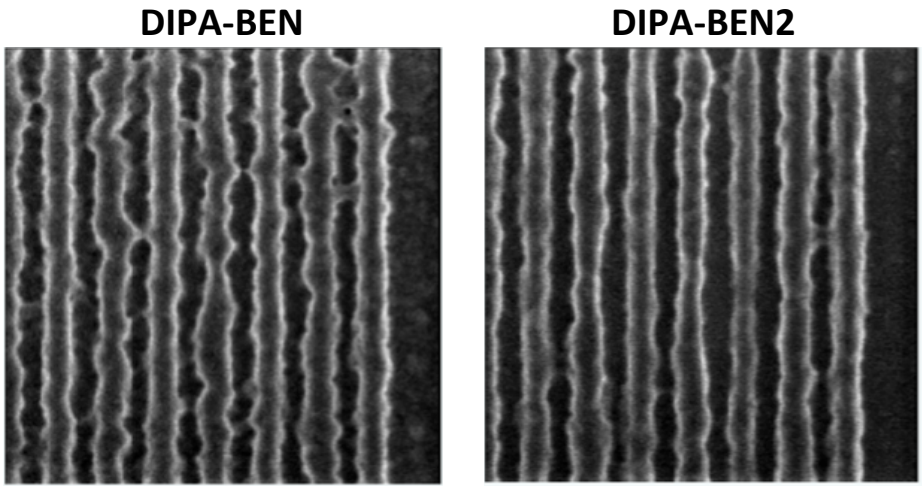

Figure 4.29: An SEM images comparing 60 nm HP line and space pattern with pitch division resists using DIPA-BEN and DIPA-BEN2 PBGs. The half-pitch size of the optical image as defined by the mask is 120 nm HP

The process windows for DIPA-BEN (Figure 4.30) and DIPA-BEN2 (Figure 4.31) are very narrow and the LER becomes overwhelming with minor adjustments in the dose or focus. To put the LER of these two formulations in context, Figure 4.32 shows comparative line/space patterns printed of the plain commercial resist and the pitchdivision formulation of DCHA-NO2 with the two benzoin PBGs. To make a baseline comparison between each PBG is printed with an E-factor of 0.55 ± 0.05.

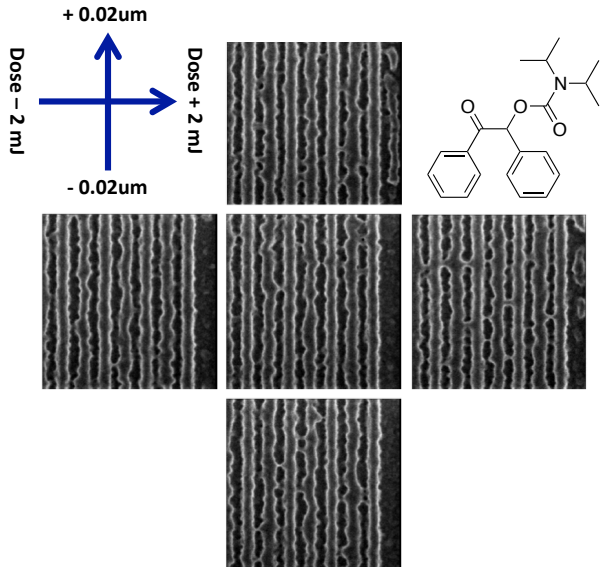

Figure 4.30: Effective process window for DIPA-BEN. Center is optimum exposure, E_{op}= 94 mJ and focus and a PEB of 105 ºC.

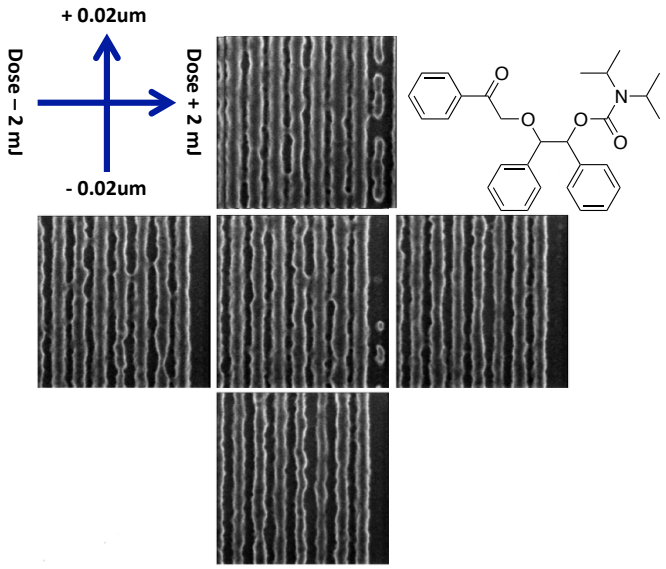

Figure 4.31: Effective process window for DIPA-BEN2. Center is optimum exposure, E_{op}= 88 mJ and focus with a PEB of 126 ºC.

The imaging experiments conducted at SVTC show a distinct improvement in LER between DIPA-BEN and DIPA-BEN2; yet both images suffer from such severe LER that a measurement is not feasible. These experiments also show that DCHA-NO2 continues to be an optimum PBG for pitchdivision formulations, as its LER appears to be equal to or better than DIPA-BEN2.

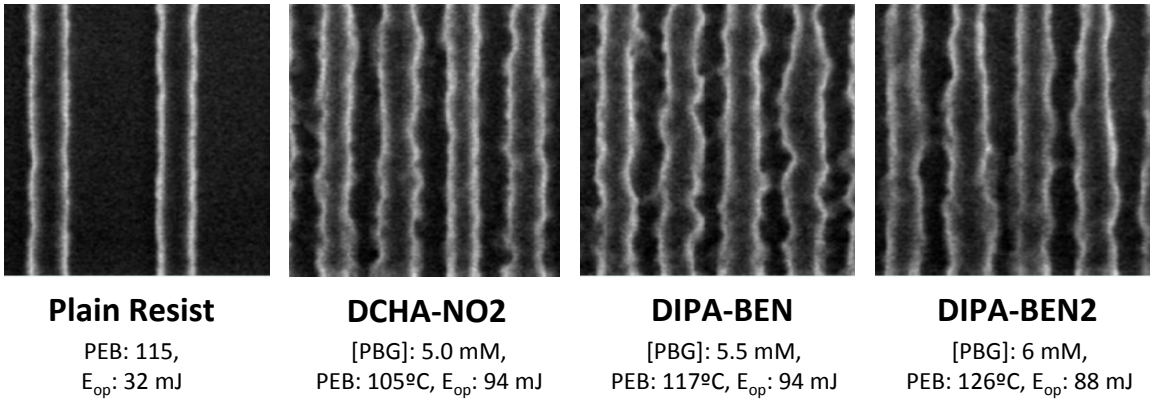

Figure 4.32: Comparison of LER of among various pitchdivision formulations.

The third Arun-protected PBG for this study was DIPA-ACP2, previously introduced in Figure 4.4. The DIPA-ACP2 strategy is quite similar to that of the benzoin PBGs, owing to its straightforward synthesis following the previous optimization work with the benzoin chromophores (Table 4.1). Figure 4.33 illustrates the three-step path to the Arun protected *p*-methoxy acetophenone two-stage PBGs. The ketone was reduced by sodium borohydride with installation of the Arun protecting group and subsequent treatment protocols used for the DIPA-BEN2.

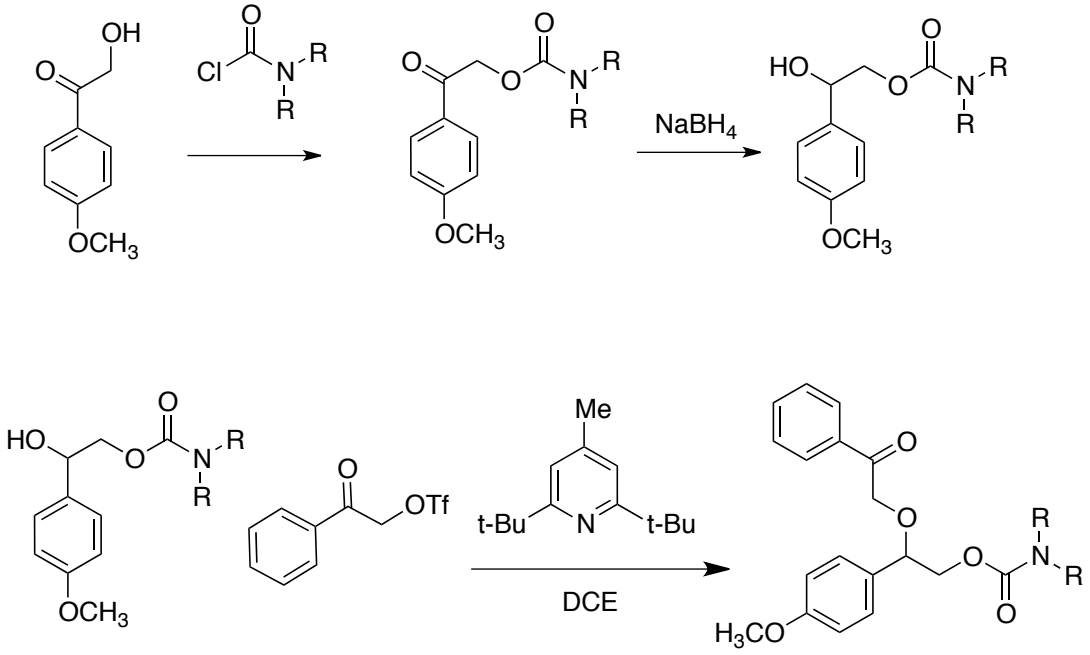

Figure 4.33: Comparison of LER of among various pitchdivision formulations.

Exposure windows were produced to compare the single and two-stage variants and are shown in Figure 4.34. The contrast curves have very high loadings, nearly three times that of comparable pitchdivision formulations. Even at extremely large 13 mM loadings and 120 ºC PEB, DE-APC and DE-APC2 have E-factors of 0.78 and 0.68 respectively. Increasing the loading above 13 mM in an attempt to pattern pitchdivision lines and spaces at an E-factor ≈ 0.55 caused the resist to stop functioning properly by either not fully clearing to the wafer or by totally quenching all the acid and preventing any response from the resist during the imaging study at SVTC. These results clearly suggest that the *p*-methoxyacetophenone PBGs are too slow to work in pitchdivision, and thus further work and characterization was halted.

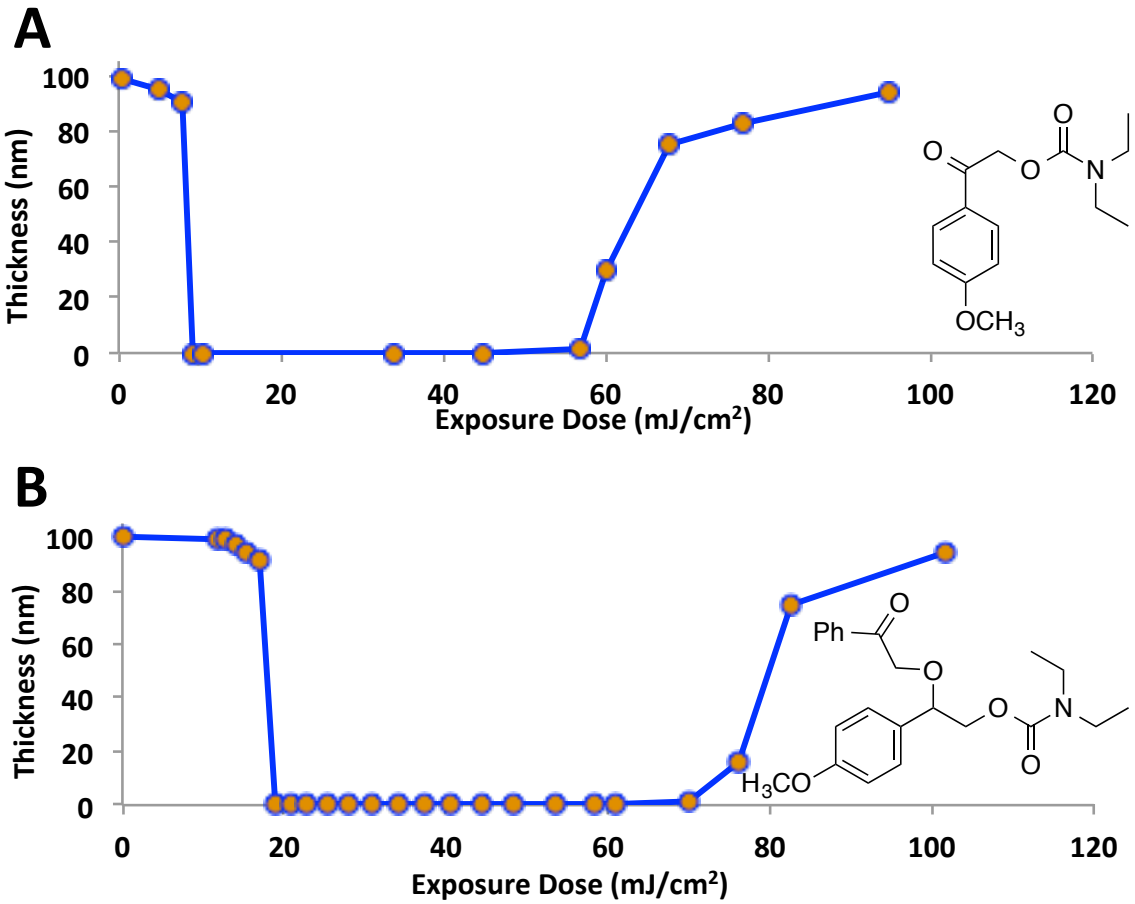

Figure 4.34: Contrast curves of resist formulations containing different PBG: (a) DE-ACP and (b) DE-ACP2.

4.3 AROMATIZING OXIME ESTER PBGS

The section reviews the work on photoaromatization-based two-stage PBGs. As mentioned in the introduction, complete synthetic and analytic details on this class of PBG are found in the following references.(*87*, *88*)

4.3.1 INTRODUCTION TO PHOTOAROMATIZING PBGS

As discussed earlier, oxime esters of aromatic acids are a well-studied class of PBGs;(*86*) since their aliphatic counterparts do not produce base at a significant rate upon exposure at 193nm, we chose this chromophore as our candidate for photo-induced aromatization. We envisioned an oxime ester of an aliphatic acid that undergoes a photoaromatization reaction to create an active aromatic PBG, which can serve as a latent PBG as illustrated in Figure 4.35.

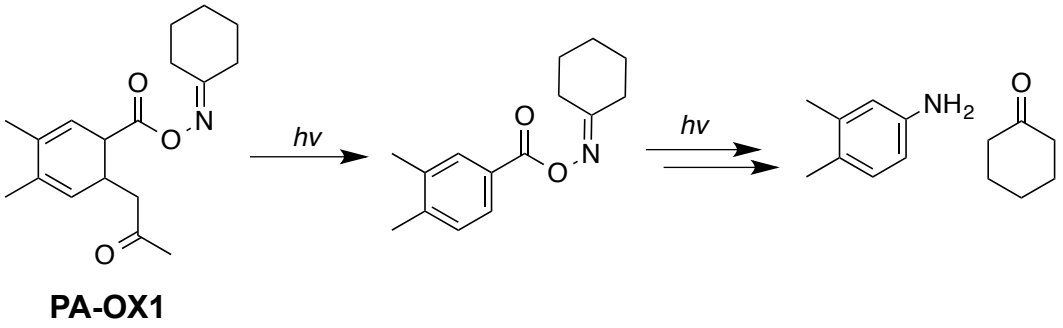

PA-OX1

Figure 4.35: Illustration of proposed photo-aromatizing oxime ester PBG.

4.3.2 FIRST APPROACH

Several examples of photoaromatization reactions are known, but most are based on 1,4-dihydropyridines(*98*) or more complicated systems that are not suited for our purpose. (*99*, *100*) Our basic design of a photoaromatization type two-stage PBG (Figure 4.35) is based on a mechanism achieved by the Norrish Type-II photoelimination.(*91*) A major obstacle in this design is the fact that dienes are efficient triplet quenchers.

Luckily, they are not efficient singlet quenchers. According to Wagner the strength of the γ-CH bond of the ketone dictates whether the Type-II reaction proceeds via the singlet or triplet state.(*101*) Figure 4.36 shows the results of Wagner's studies, which state that ketones with stronger γ-CH bonds such as those in 2-pentanone (*D* = 98 kcal/mol) proceed via a triplet state, whereas those with weaker γ-CH bonds such as 5-methyl-2-hexanone (*D* = 91 kcal/mol) proceed via the singlet.(*91*) Since we need a singlet-state intermediate, our initial design of PA-OX1 consisted of an oxime ester with an allylic tertiary γ-H, as shown in Figure 4.35. After an arduous synthetic journey to make the desired two-stage aromatizing PBG (PA-OX1), it was disheartening to find that the photoaromatization does not proceed. Despite our design efforts, the diene appeared to rapidly quenched any Norrish Type-II photoelimination.(*88*)

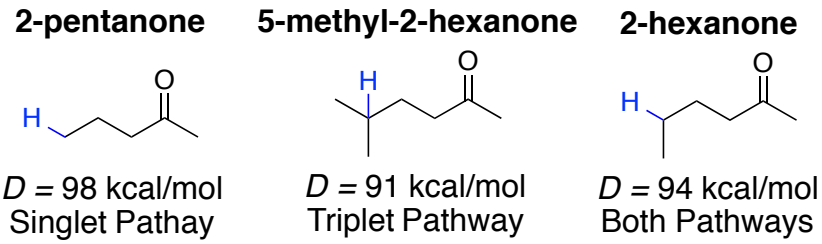

Figure 4.36: Illustration of γ-H strength of three alkyl ketones and its relation to excitation pathway for Norrish Type II photoreactions.(*91*)

4.3.3 SECOND APPROACH

The rationale of the second design (PA-OX2) avoided a diene altogether favoring an enone to achieve aromatization following elimination via a favorable tautomerization.

(Figure 4.37) While enones are also known to quench triplet states, we hoped this new structural variation would change the rates in our favor.

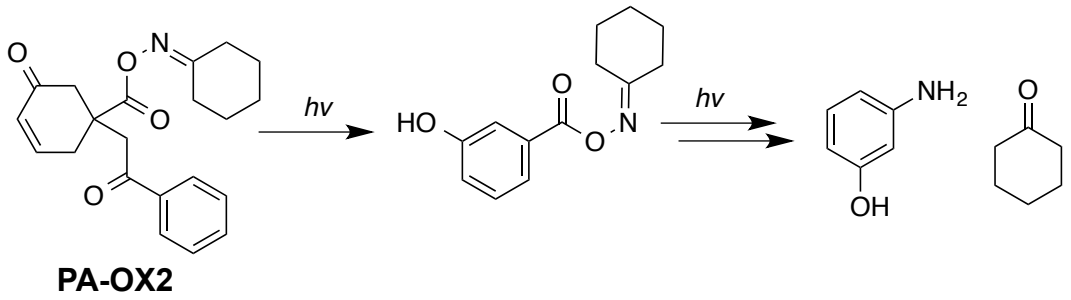

Figure 4.37: Second approach to photoaromatization. Elimination followed by tautomerization to form an active oxime ester chromophore.

An additional goal of the second design was to increase the UV absorption efficiency of the chromophore in the first reaction step. By substituting acetophenone for an acetone chromophore we get three orders of magnitude increase in molar absorption. The successful exposure window of the phenolic acid based oxime ester shown in Figure 4.38 validated the PA-OX2 design.

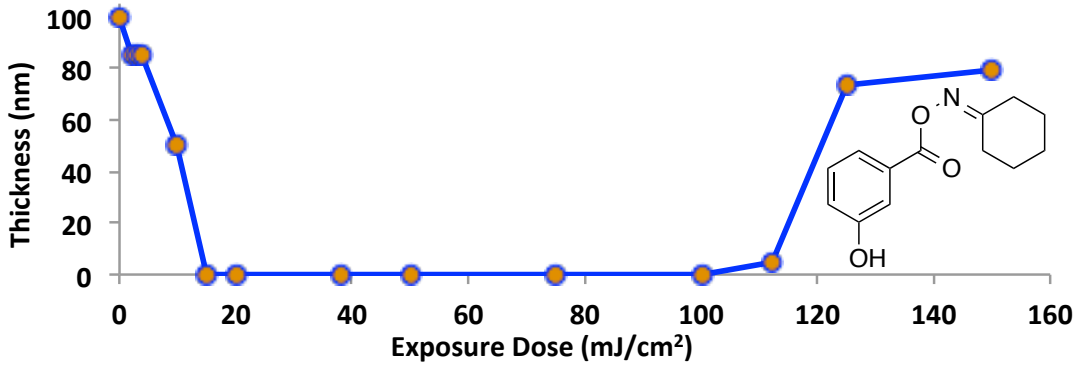

Figure 4.38: Contrast curve of pitchdivision resist formulation using phenolic acid based oxime ester and a generic 193 nm resist. (5.5 wt% TPS-Nf, 16.5 wt % PBG, 115 ºC PEB)

The synthesis PA-OX2 was achieved via a Birch reduction of methyl 3-methoxybenzoate (a) followed by installation of the photo-labile groups via-enolate chemistry (b) (Figure 4.38). Reduction and installation of acetophenone proceeded in acceptable yields, but attempts to cleave the methyl ether and hydrolyze the ester simultaneously were unsuccessful so these deprotection steps were carried out in sequence (c – d) followed by installation of the oxime via carbodiimide mediated esterification (e). Even in the absence of extensive reaction optimization, this pathway gave a greater than 15 % yield over six steps and is sufficiently flexible to allow synthesis of acetophenone derivatives.

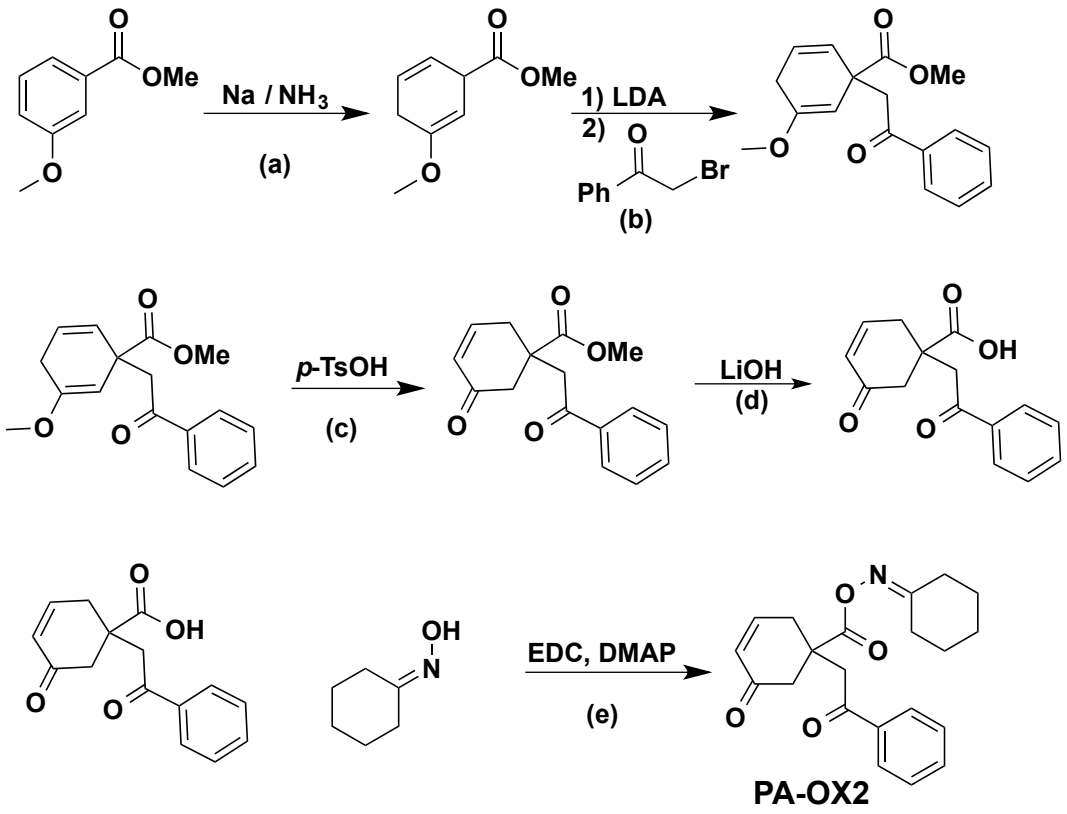

Figure 4.39: Illustrated schematic of the synthesis of PA-OX2.

4.3.4 CHARACTERIZATION OF PA-OX2

The two-stage PA-OX2 functions effectively in pitchdivision formulations. The exposure window in Figure 4.40 was produced using a commercial resist with 4 mM PA-OX2 and a 120 ºC PEB. The two control compounds in Figure 4.41 were synthesized to isolate and test the reactivity of PA-OX2. Compound **A** was tested in pitchdivision formulations and proved that the aliphatic cyclohexenone moiety shuts down base generation and does not produce a two-tone contrast window.

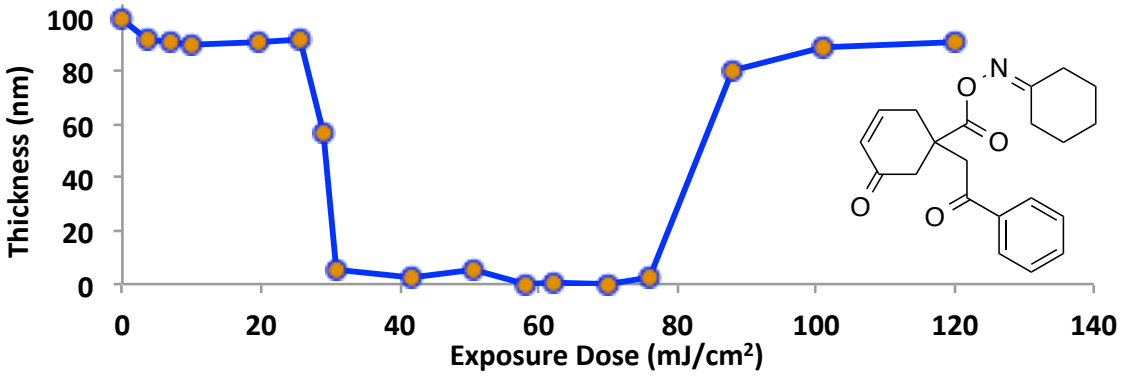

Figure 4.40: Contrast curve of PA-OX2.

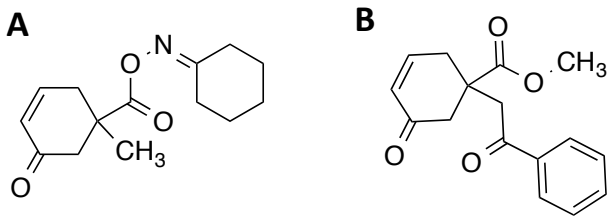

Figure 4.41: Illustration of two control compounds to isolate and test the reactivity of PA-OX2.

The methylester variant of PA-OX2, compound **B**, was used to study the photodecomposition of the first photoaromatization stage (Figure 4.42). The quantum yield of the photoconversion of compound **B** to acetophenone and 3-methoxylphenylmethylester was determined using valerophenone as an actinometer.(*91*) Using the reference valerophenone, a quantum yield of $\Phi = 0.04 \pm 0.01$ for the production of acetophenone from **B** was determined at 254 nm. A smaller quantum yield,

Φ = 0.02 ± 0.01, was observed for photolysis at 300 nm because of competing light absorption by the cyclohexenone chromophore.

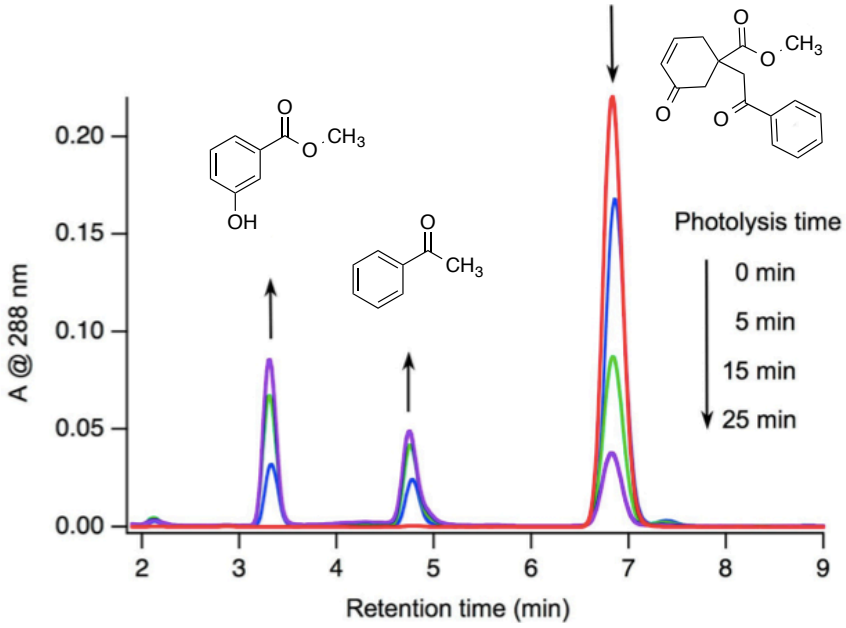

Figure 4.42: HPLC analysis of irradiation at 300 nm of methylester control compound B in deoxygenated acetonitrile solutions. Analyte detection by UV spectroscopy at 288 nm.

To study the efficiency of the second photolysis step, the generation of the immine base precursor from the one-stage PBG, deoxygenated acetonitrile solutions of the one-stage PBG were irradiated at 254 nm and analyzed by HPLC. Figure 4.43 shows HPLC traces after different photolysis times. The major product peak at 1.9 min was identified as the expected imine intermediate by HPLC-MS. A quantum yield for loss of the phenolic oxime ester of Φ = 0.56 ± 0.02 was determined using valerophenone as actinometer, which demonstrates the impressive efficiency of this photoreaction.

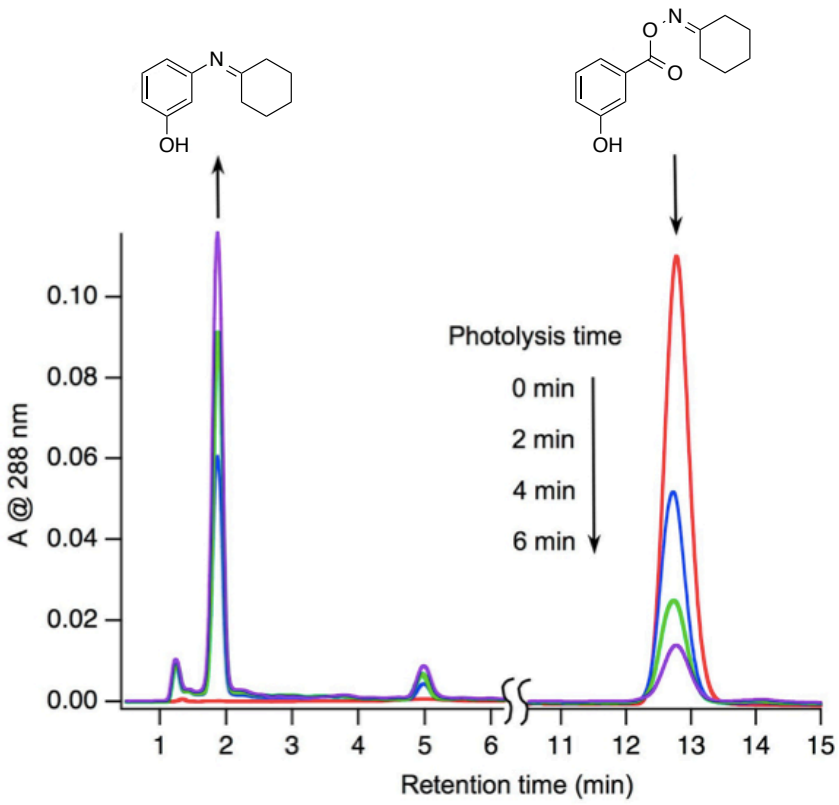

Figure 4.43: HPLC analysis of photolysis at 254 nm of the phenolic oxime ester in deoxygenated acetonitrile solutions. Analyte detection by UV spectroscopy at 288 nm.

In the photoaromatizing step, the acetophenone triplet is relatively low ($\Phi \sim 0.04$ at λ_{ex} = 254 nm) due to competition with the more efficient triplet energy transfer from the acetophenone to the cyclohexenone moiety. This energy transfer negatively impacts the quantum yield of the first-stage reaction ($\Phi = 0.04$), which ultimately leads to a the first stage being significantly less efficient than the second stage ($\Phi = 0.54$). The large disparity between the two stages creates pseudo-first order kinetics in base generation, which does not suffieciently sharpen the slope of the net acid production. The end results

are not completely surprising, as the contrast windows in Figures 4.38 & 4.40 highlight the disparity between the one and two-stage PBG. The E-factor in Figure 4.38 is 0.84 and any attempt to increase the PBG loading led to quenching of the formulation. The PA-O2 on the other hand forms an exposure window with a very large E_o even at low PBG loading (4 mM). While PA-OX2 is not an ideal photobase generator it represents an impressive design and synthetic acomplishment adding a new simplistic strategy to the field of photoaromatization.

4.4 SYMMETRICAL PBGS

The ideal two-stage PBG for pitchdivision is the symmetrical di-*o*-nitrobenzylcarbamate (BisNO2). To generate a free amine, BisNO2 must undergo two identical photoreactions that are known to work well with pitchdivision. Before the Arun protecting group was coined and benzoin PBG strategies were drawn on the white board, a significant effort was made to synthesize a BisNO2 PBG. Chemists from Columbia, UT, Portland State University, the University of Ottawa and Intel all attempted and failed to make the molecule. Intel even went as far as to contract the synthesis from Sigma Aldrich, whose chemists concluded after three months of work, that the molecule could be temporarily made but was fundamentally unstable due to the two nitro groups. It was only after the initial failed attempts by each collaborator that the primary efforts were diverted into the alternate strategies. Fortunately, perseverance led to a successful path to the target Bis NO2 PBG. This section discusses the synthesis, optimization, quantification and patterning evaluation of symmetrical carbamates.

4.4.1 EARLY WORK

Intel and Portland State University put significant efforts into the initial synthetic attempts of a symmetrical carbamate. After several unsuccessful months attempting to synthesize the BisNO2 , they changed their target molecule to a symmetrical version of the DIPA-DM PBG described in Chapter 3. The two-stage variant (AD-DM2) is illustrated in Figure 4.44.

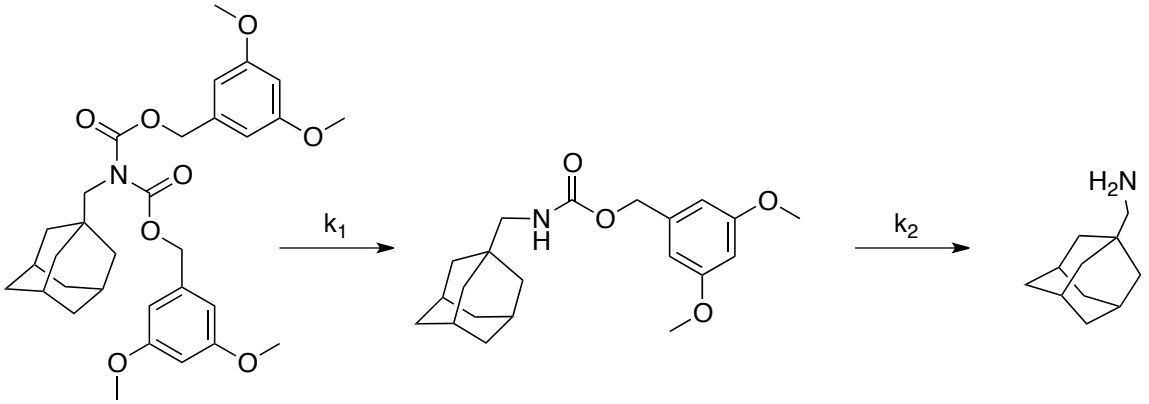

Figure 4.44: Illustration of AD-DM2 an early symmetrical biscarbamate.

This target was chosen out of the frustration over the many failures to synthesize BisNO2. The control compounds shown in Figure 4.45 were synthesized after the BisNO2 failed to form under expected conditions.

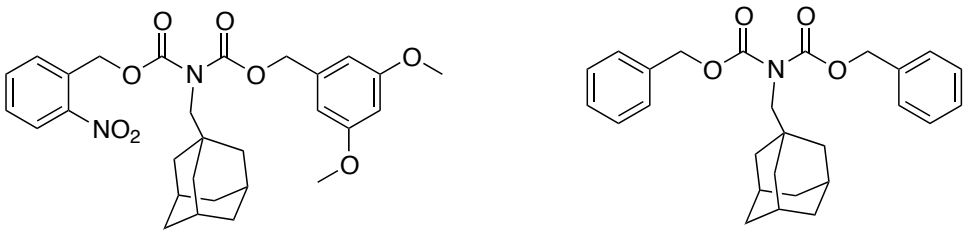

Figure 4.45: Symmetrical carbamates synthesized in high yield.

When both of the controls were synthesized in yields >30 % and with no sign of the BisNO2, the Sigma Aldrich team came to the conclusion that the di-*o*-nitrobenzyl-biscarbamate was inherently unstable. Alternately, AD-DM2 was successfully synthesized via classic acid chloride chemistry as shown in Figure 4.46.(*102*)

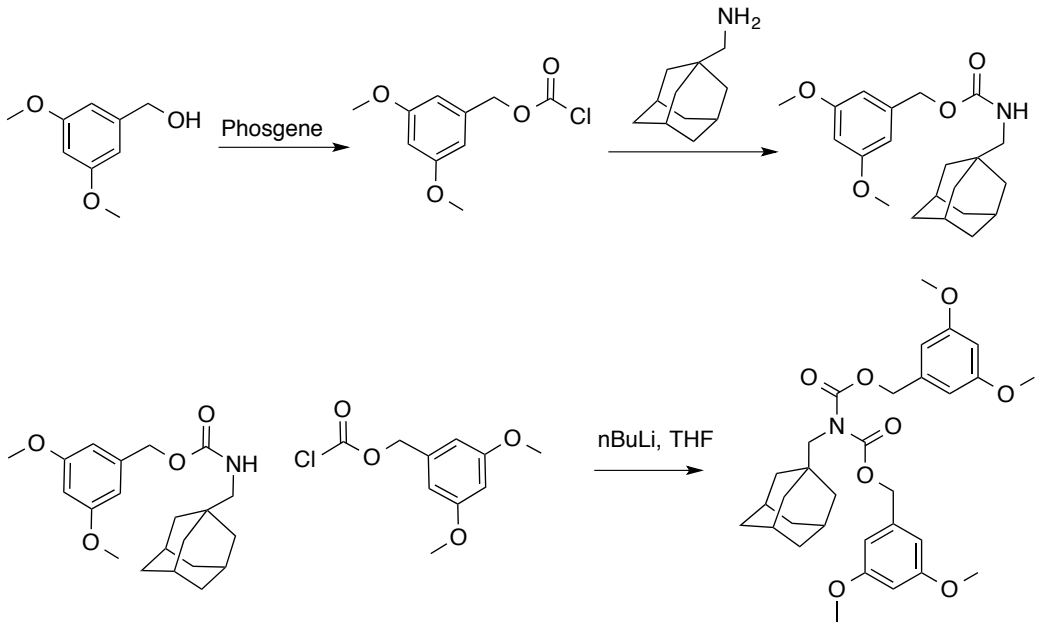

Figure 4.46: Synthetic scheme of DIPA-DM2

The Portland State group monitored the decomposition of DIPA-DM2 by ^{1}H-NMR and GC-MS to identify the three major photogenerated compounds circled in Figure 4.47. The weak imine base (blue circle) illustrated in Figure 4.47 forms quickly in solution and is accounted for as part of the total base generation. The generation of free amine and imine was monitored by NMR during exposure to 248 nm light (Figure 4.48) and compared to a kinetic model (Figure 4.48 insert).(*102*) Upon complete decomposition of DIPA-DM2, only 70 % of the expected total base was detected, because the photodecomposition suffers from secondary non-favorable reactivity. The results in Figure 4.48 do not match the expected model shown in the insert. Both imine and amine formation appear to be generated without any delay. The best evidence of two-stage behavior is in the initial rise in DIPA-DM concentration at low dose and the eventual depletion later on. Overall, the results of the DIP-DM2 experiments are inconclusive due to interference from several secondary reactions during the photoreaction.

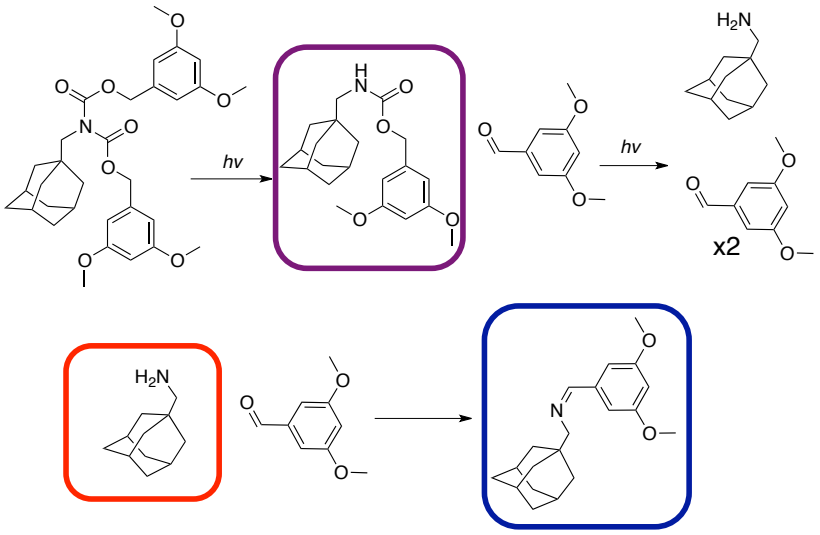

Figure 4.47: Schematic of the photodecomposition of DIPA-DM2. The circled compounds were identified by NMR and GC-MS. (Copyright © IEEE.*From Ref* (*102*))

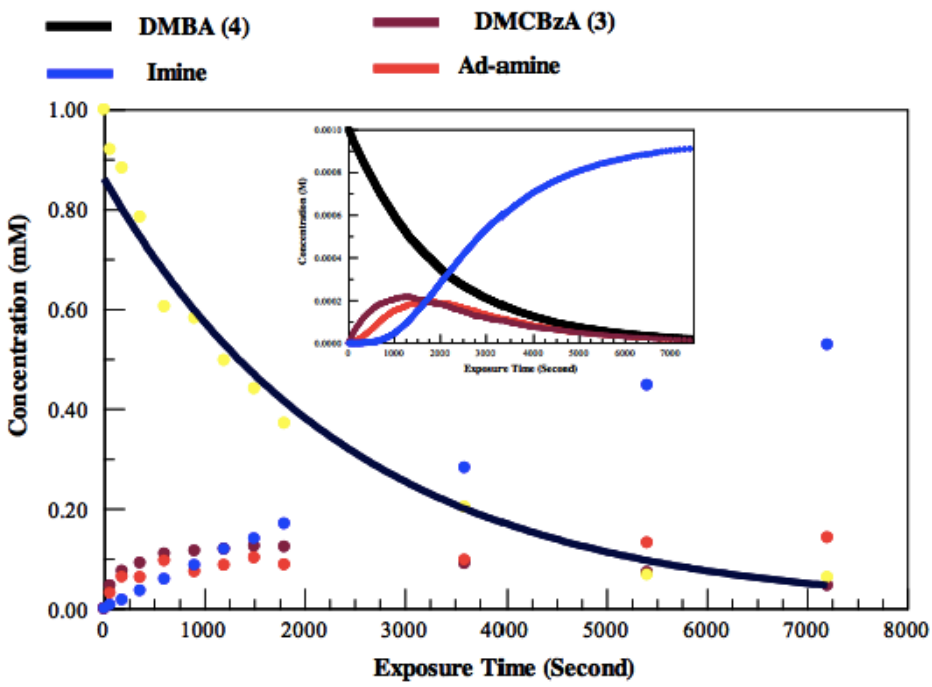

Figure 4.48: [1]H-NMR analysis of photolysis of DIPA-DM2 in deoxygenated acetonitrile solution. (Copyright © IEEE. *From Ref* (*102*))

The work by our collaborators at Portland State shows the challenges of quantifying base generation in complex photochemical systems and helped lay the groundwork in the synthesis of symmetrical carbamates. Since previous studies with DIPA-DM (Figure 3.14) showed that it is a poor fit for pitchdivision,(*30*) further optimization and characterization of DIPA-DM2 was not pursued.

If future work on DIPA-DM2 is pursued, this author recommends altering the structure of the PBG to avoid the formation of 2,5-dimethoxybenzaldehyde. Although the formation of dimethoxytoluene or benzylalchol is expected for this chromophore(*103*), modifications are available to ensure the aldehyde can be avoided upon photolysis. The dimethylbenzyl-substituted version of this benzyl carbamate (Figure 4.49) is a known and was characterized.(*52*) Due to the substitution at the benzylic position, benzaldehyde is a very unlikely photoproduct. The disubtitution may also likely speed up the reaction through hyperconjugation. Overall this modification would likely help clarify the NMR data and show more conclusively whether or not higher order kinetics of amine generation are taking place.

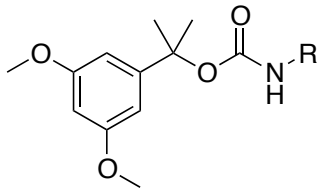

Figure 4.49: Dimethyl substituted variant of DIPA-DM developed by Cameron and Fréchet.(*52*)

4.4.2 BIS-CARB SYNTHESIS

The majority of the Willson group efforts to create two-stage PBGs were focused on the protected route and photoaromatization route, yet we also dedicated some time towards the infamous BisNO2 synthesis. About the time that we finished the benzoin PBG synthesis and the cinnamic-coumarin PBG, we started to seek alternate routes towards biscarb (Figure 4.50).

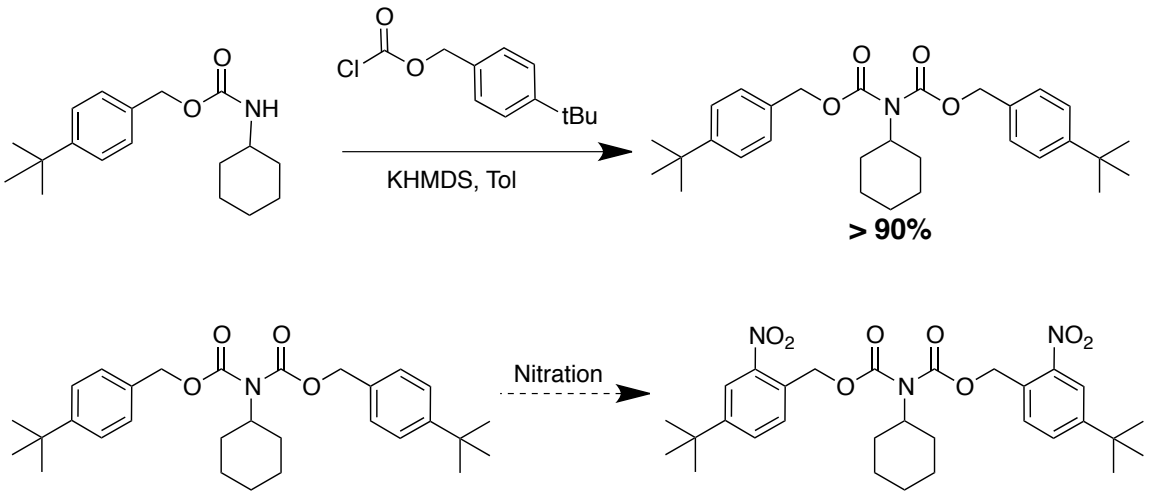

Figure 4.50: Illustration of late-stage nitration to form BisNO2.

Relying on the hope that BisNO2 is a stable compound, but that the formation is hindered due to an unfavorable combination of steric constraints and electronics, we devised a route towards biscarb which installs the two nitro groups during the final stage of the synthesis. To avoid the preferred para-position nitration, we installed tertbutyl groups in the para-position to direct the nitration to the desired ortho position. To form the symmetrical tBuBisCarb, the one-stage carbamate was treated with a bulky base,

potassium hexamethyldisilizane (KHMDS), before reacting with the requisite chlorocarbonate. The formation of the t-BuBisCarb was complete in less than 30 minutes in quantitative yield. Our first attempts to nitrate tBuBisCarb always led to the oxidation product *p*-tertbutylbenzaldehyde (Figure 4.51).

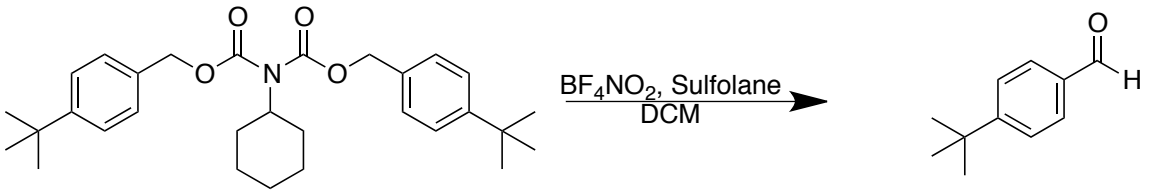

Figure 4.51: Illustration of *p*-tertbutylbenzaldehyde formation upon the failed nitration reaction of tBuBisCarb.

During the nitration experiments, the author gave a presentation at the annual SPIE lithography conference on our current progress with the recently patterned benzoin PBGs. While at the conference, Dr. Willson declared a monetary bounty for the successful synthesis of BisNO2. Within 24 hours, an undergraduate chemist in the Willson lab, Wade Wang, synthesized BisNO2 using the exact same conditions described above for tBuBisCarb. Upon depleting the tBuBisCarb from running the many failed nitration experiments, Wade decided to run the BisNO2 synthesis with KHMDS in toluene (Figure 4.52), a reaction that had been discussed a month earlier as "definitely worth trying," but "unlikely to work" in our weekly group teleconference. Wade found and isolated the CHA-BisNO2 in 5 % yield, thus claiming the freshly announced cash prize!

The exact, R_f of CHA-BISNO2 shows that it is significantly more polar than expected and co-runs with the starting carbamate in most TLC solvent systems. From this, we concluded that it is possible other chemists had in fact synthesized biscarb but didn't readily identify it since it fails to separate under standard TLC solvent conditions. To see if improved yields were possible we screened various bases and solvents, some of which were previously attempted at UT or by our collaborators. A small table of the results from this screening is presented in Table 4.2. Surprisingly, the only base and solvent mixture that worked in our labs was that of KHMDS and toluene! As can be seen in Table 4.2, the red-circled conditions show an increase in yield to 20 % was realized after some optimizing and experience running the reaction.

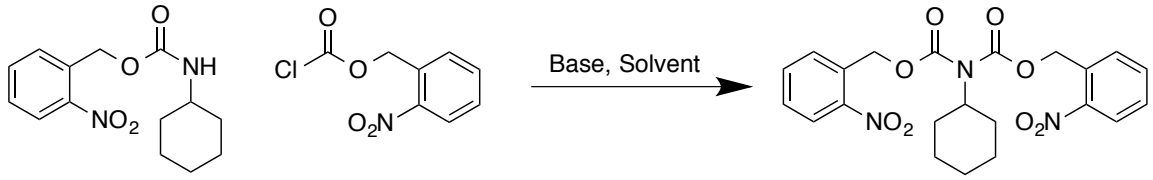

CHA-BisNO2

Entry	Base	Solvent (M)	E^+ (equiv)	T °C	% Yield
1	sec-BuLi	THF	2.0	-78 -> RT	0
2	n-BuLi	tol	1.5	-78 -> RT	0
3	TEA	tol	2.0	110	0
4	DBU	tol	1.5	110	0
5	KHMDS	THF	1.5	0 - RT	0
6	KHMDS	tol-HMPA	2.0	0 - RT	0
7	KHMDS	tol	2.0	0 - RT	20

Table 4.2: Optimization table describing a sample of the reactions run to improve synthesis of CHA-BisNO2.

During the search for optimal conditions, experiments were run to determine whether it was the nucleophile, the electrophile, or both that lead to the lower yields in this reaction versus the other symmetrical carbamates. We hypothesized that the reaction was unfavorable due to the electronics and mismatched pKa's of the system. Figure 4.52 illustrates the known pKa's of similar carbamates and benzyl protons. Clearly, there is some competition between the acidity of these two positions in this system. Secondly, ortho-nitro groups are known to cause significant steric interferences due to their large, flat conjugated shape. It is conceivable that the conjugated nitro group pushes the carbamate or acid carbonate into a less reactive configuration.

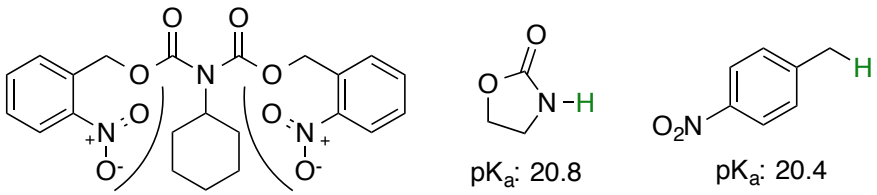

Figure 4.52: Illustration of pKa and steric issues in the formation of CHA-BisNO2.

The results of the control study are shown in Figure 4.53, and it is clear that the nucleophile holds the key for the majority of the low yield, which we postulate is due to the similarity in the carbamate and benzylic pKa's. After optimization of our reaction conditions and achieving yields up to 20% and finding that no product in any reaction not based on KHMDS and toluene, we opted to scale up the synthesis for characterization and imaging studies.

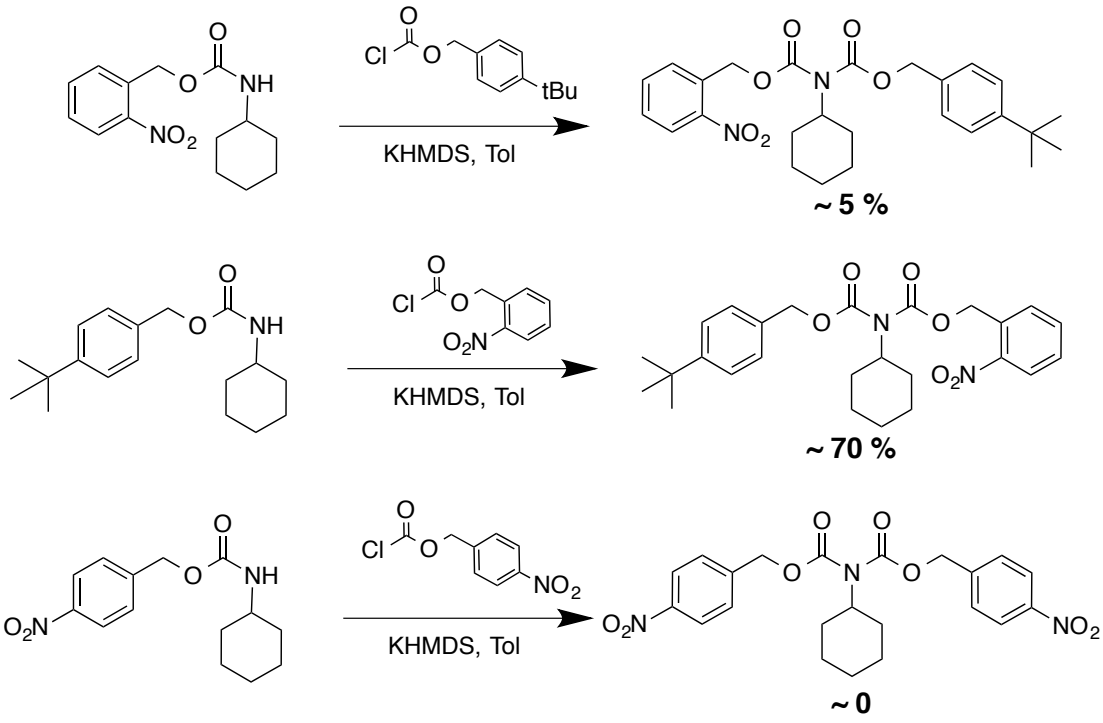

Figure 4.53: Schematics of the control reactions run for BisNO2.

Ion chromatography (IC) was introduced in the benzoin PBG characterization section as a novel method to quantify base generation. While the instrument we used was not amendable to the photoreaction conditions required for benzoin PBGs, it proved to be useful for the optimization of BisNO2 PBGs. Figure 4.54.B shows the base generation detected by IC for DIPA-NO2 in relation to the change in UV-Vis spectrum.* (*Previously used by Xinyu Gu to approximate the rate of base generation for DIPA-NO2) For this experiment, a 0.075 mM solution of DIPA-NO2 in dry degassed acetonitrile was exposed to 193 nm light, and the difference in UV-Vis was recorded until little noticeable change occurred (~740 mJ).

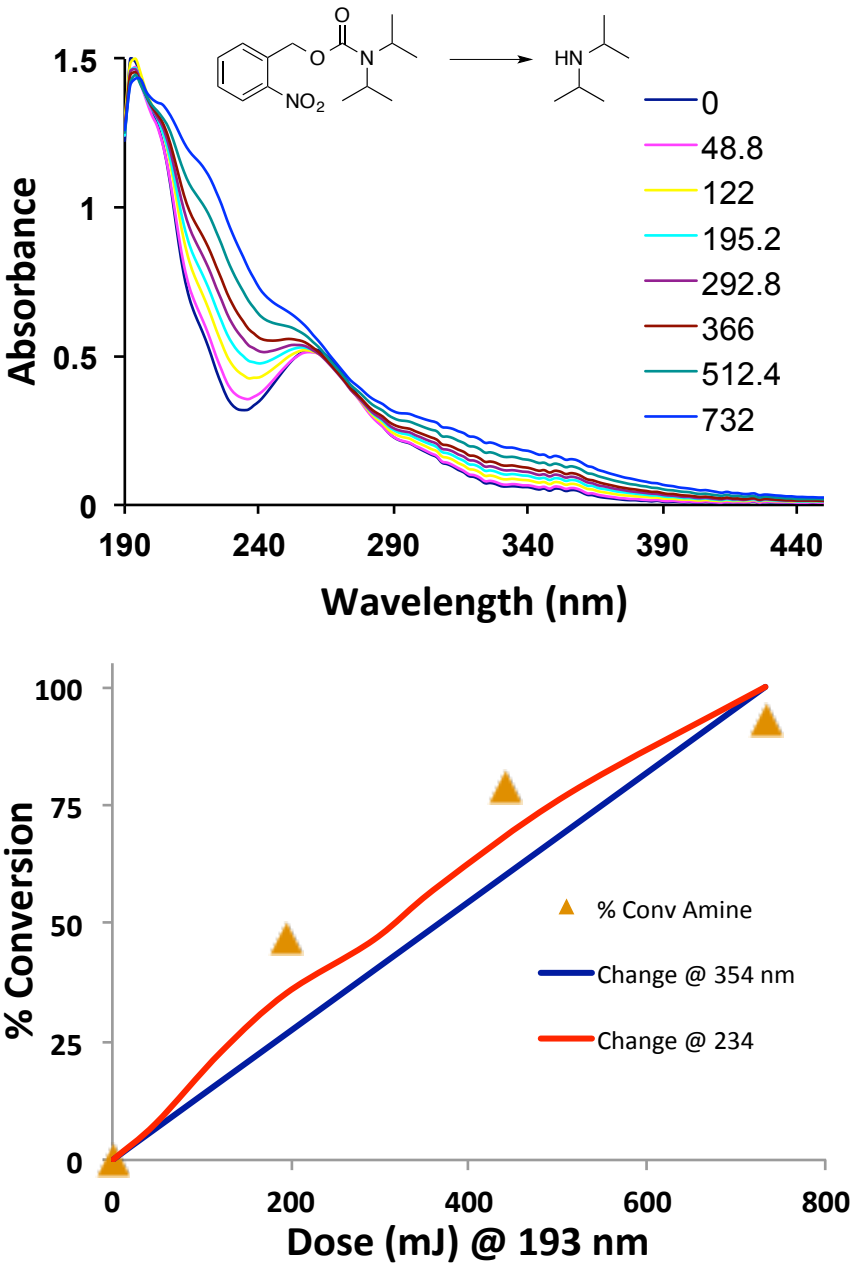

Figure 4.54: (a) Change in UV-Vis spectrum of DIPA-NO2 upon exposure to 193 nm light in deoxygenated acetonitrile solutions. (b) Comparison of percent conversion of UV change at 354 and 234 nm and percent conversion of amine detected by IR.

From the UV-Vis results shown in Figure 4.54.A, a presumed "100 % conversion" was set at 732 mJ and the change in spectrum at 354 nm and 234 nm was plotted comparing percent conversion and dose.

From these results, three samples were prepared and exposed to give approximate conversions of 25 %, 66 %, and 100 % for characterization of amine generation by IC. The resulting detection of amine was calibrated by an analytical standard and then plotted percent conversion versus dose to compare the results to that of the UV-Vis spectral changes (Figure 4.54.B). These results suggest that UV-Vis spectrum changes of DIPA-NO2, weakly correlate with the generation of free amine and provide a fair qualitative approximation. The plot also shows that the photoreaction of DIPA-NO2 to the free amine is free of by-products and reacts to about 90 % conversion at high dose. It should be noted that the shape of the IC amine plot suggests that 740 mJ is not 100 % conversion, as it appears to only cease first-order kinetics around 600 mJ. Further studies with IC were conducted with a 248 nm light source capable of higher doses.

The same experiment with CHA-BisNO2 (106 μM, Abs @ 248 = 0.87) only 10 % of the expected amine concentration was detected at the highest dose! Figure 4.55.B shows the percent conversion in relation to the change in UV-Vis spectrum at 235 nm (blue line) and the amount of amine detected by IC (orange diamond). To ensure consistency between runs, a UV-Vis spectrum was taken after each exposure and before analysis by IC, these points are plotted as the red circles in 4.55.B.

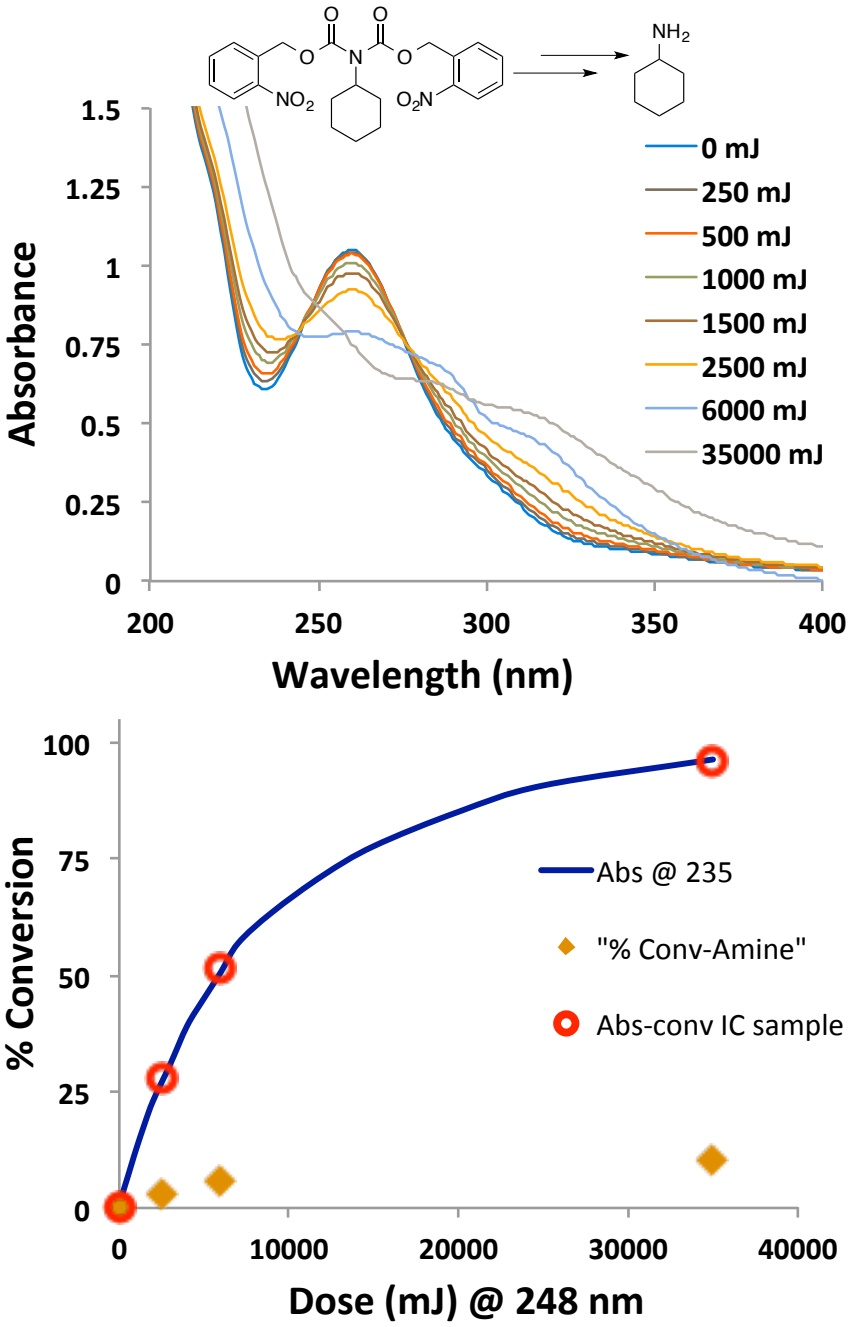

Figure 4.55: (a) Change in UV-Vis spectrum of CHA-BisNO2 upon exposure to 248 nm light in deoxygenated acetonitrile solutions. (b) Comparison of percent conversion of UV change at 235 nm (blue line) and percent conversion of amine detected by IC (orange diamond). Red circle shows UV-Vis of the respective IC.

After the unexpected IC results with CHA-BisNO2, we stepped back to run the single-stage CHA-NO and observed similar results with very low amine detection. Assuming the decomposition pathways of DIPA-NO2 and CHA-NO2 are the same, these results point to a recombination of the photoproducts. According to the accepted photoreaction pathway(*104*) for *o*-nitrobenzyl protecting groups, (Figure 3.4) the chromophore transforms into an *o*-nitrosobenzaldehyde upon exposure. In the case of CHA-NO2, a primary cyclohexylamine and nitrosobenzaldehyde are generated, which quickly combine to form an imine. To further complicate this scheme, the imine continues to slowly transform into bicyclic products such as indazalone(*50*) (Figure 4.56).

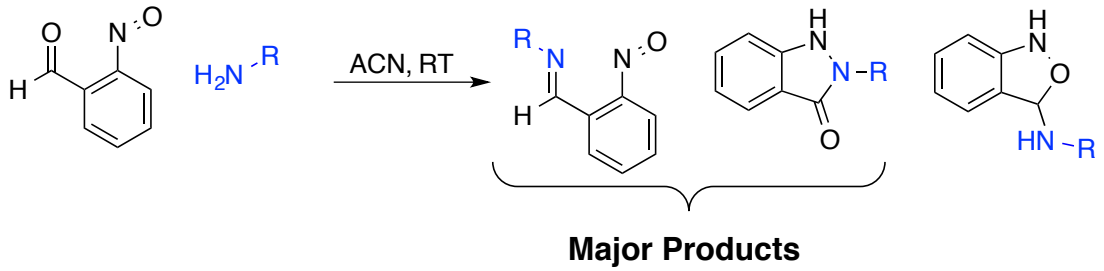

Figure 4.56: Illustration of 2-nitrosobenzyaldehyde and primary amine recombination chemistry. R = cyclohexyl

To test this hypothesis we synthesized the pure 2-nitrosobenzaldehyde according to literature procedure(*50*) and reacted it with cyclohexylamine and diisopropyl amine in ACN for 30 minutes and then ran the samples through the IC to determine the remaining amine concentration. The results of this test are shown in Table 4.3. It is clear that 2-

nitrosobenzaldehyde reacts quickly with primary amines preventing IC detection. The secondary diisopropylamine undergoes statistically minor recombination. From these results it is clear that a modification of our Bis-NO2 is needed to prevent recombination.

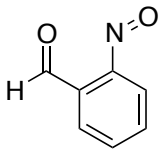

150 PPM

Amine (PPM) —ACN, RT→ Free Amine (PPM)

Entry	Amine	Amount	Detected	Difference
1	CHA	150	74.5	75.5
2	CHA	300	197.3	102.7
3	DIPA	150	141.9*	8.1
4	DIPA	300	286.5*	13.5

*PPM Based on single point calibration, not the standard 5-point

Table 4.3: Table of recombination control experiments.

Two approaches were pursued in tandem to suppress imine formation: (i) to make the electrophilic benzaldehyde less reactive and (ii) to make the nucleophilic amine less reactive. Figure 4.57 illustrates the basic strategies towards these goals, which were based upon published imine formation rates.(*105*) Benzaldehyde is considered an activated aldehyde and forms imines 6-20 times faster than other non-hindered non-aromatic aldehydes. To prevent benzaldehyde as a photoproduct we proposed a benzylic methylation of the BisNO2 (orange highlights of Figure 4.57). Methylation provides a final acetophenone photoproduct, whose imine formation is 60x slower with benzyl amine than benzaldehyde.(*105*)

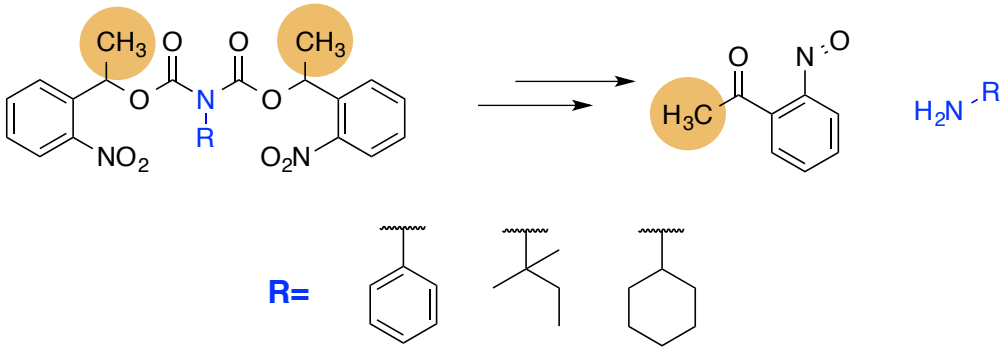

Figure 4.57: Illustration of proposed BisNO2 modifications. Orange circles highlight benzylic methylation to form the less reaction acetophenone. R-groups give the amine increased sterics and or decreased electron density.

To weaken the nucleophile, we explored both sterically hindered and electronically deficient amines. In particular, we explored aniline and tert-amyl amine, which takes 3-4 hours to form an imine with benzaldehyde versus the 45 minutes it takes for cyclohexylamine in similar conditions. By combining the benzylic methylation and a weaker nucleophilic amine, we proposed to retard imine formation long enough to quantify amine generation by either IC or HPLC.

4.4.3 METHYLATED *O*-NITRO CARBAMATE

To test our hypothesis, we made three different PBGs illustrated in Figure 4.58.

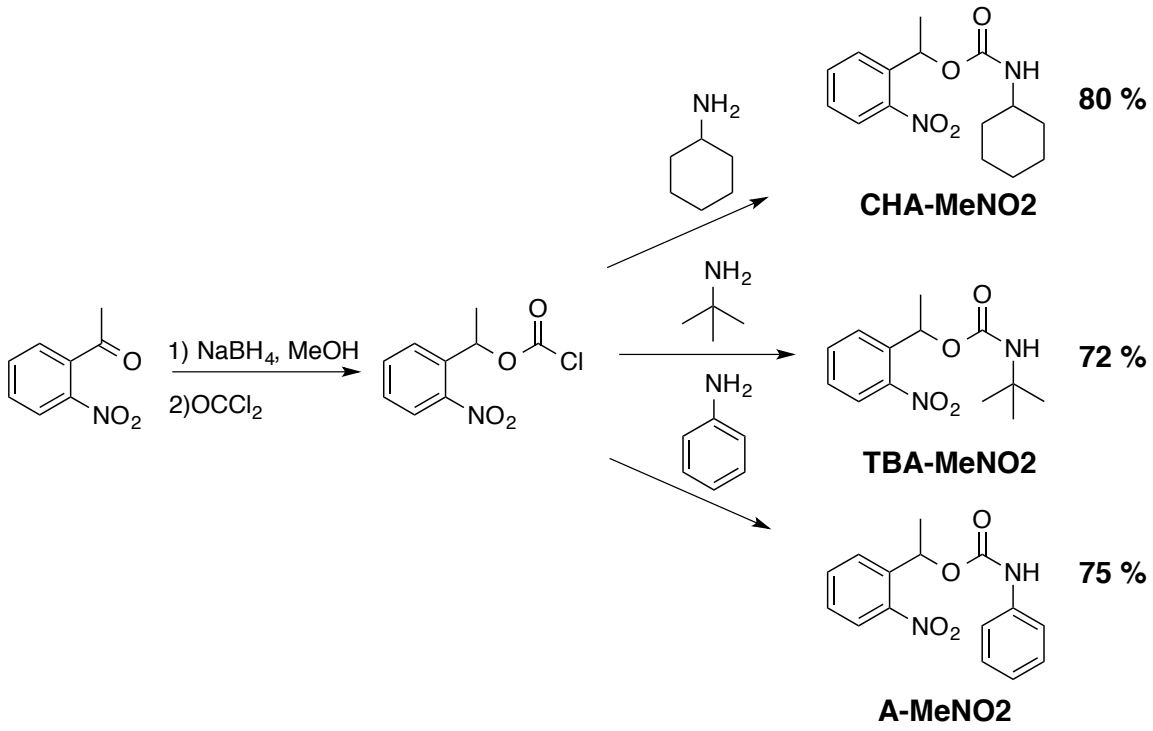

Figure 4.58: Illustrated synthetic schematic of MeNO2 PBGs to prevent photoproduct recombination.

The first PBG examined was CHA-MeNO2, which was formulated at 144μM (Abs @ 248 nm = 0.63) in acetonitrile and exposed to 248 nm light. Figure 4.59.A displays the change in UV-Vis upon exposure to 248 nm light, and 4.59.B compares the change of the UV-Vis spectrum at 311 nm to the detection of amine by IC at approximately 10 %, 33 %, 66 %, and 100% conversion. At low dose, detection of amine and the change in absorbance at 311 nm closely correlate, but at higher dose amine detection plateaus while the UV-Vis spectrum continues to change. At the highest doses IC detected ~8.3 ppm

free amine of the expected 14.5 ppm, only 53% conversion. By comparison, the non-methylated CHA-NO2, gave only ~ 10% conversion. These results show a significant increase in free amine detection. Since each IC run requires approximately 1.5 hours, there was concern that the high-dose samples were recombining while sitting in the sample queue. To test how time affected the detection of amine, the same IC samples were rerun after 72 hrs. These results, plotted as red-triangles in 4.59.B, indicate a minor drop in amine detection after this incubation period. The result suggests imine formation reaches equilibrium quickly or does not form at an appreciable rate. Yet in comparison to the control results of DIPA-NO2 (4.53.B), which show around 90 % yield in free amine, we assumed that there was still some form of photoproduct recombination.

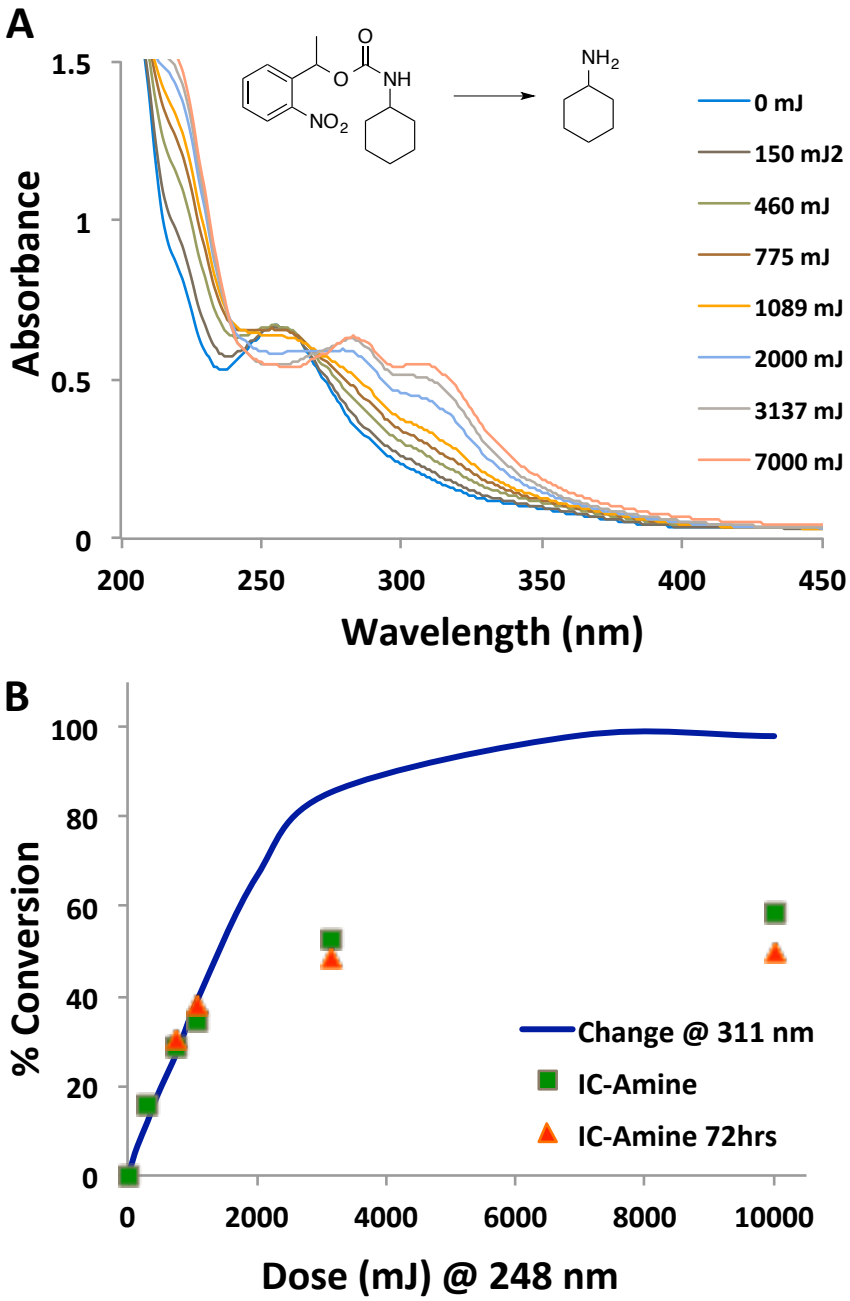

Figure 4.59: (a) Change in UV-Vis spectrum of CHA-MeNO2 upon exposure to 248 nm light in deoxygenated acetonitrile solutions. (b) Comparison of percent conversion of UV change at 311 nm (blue line) and percent conversion of amine detected by IC (orange diamond). Green squares show amine concentration after 72 hrs.

TBA-MeNO2 was the next in the series of PBG's tested. TBA-MeNO2 forms the more sterically hindered tert-butylamine upon exposure. Tert-butylamine (bp: 45 ºC) was used in place of tert-amylamine (bp: 77 ºC) or another higher boiling point tertiary amine for early proof of concept testing.) The results in Figure 4.60.B shows that the change in UV spectrum at 219 closely matches that of amine formation detected by IC, and our hypothesis on increased steric hindering leading to less recombination is correct. At high doses *t*-butylamine was detected at 9.5 ppm compared to the 11.5 ppm expected (114 μM solution, Abs @ 148nm = 0.74), showing the highest yield of free primary amine yet at 83 %.

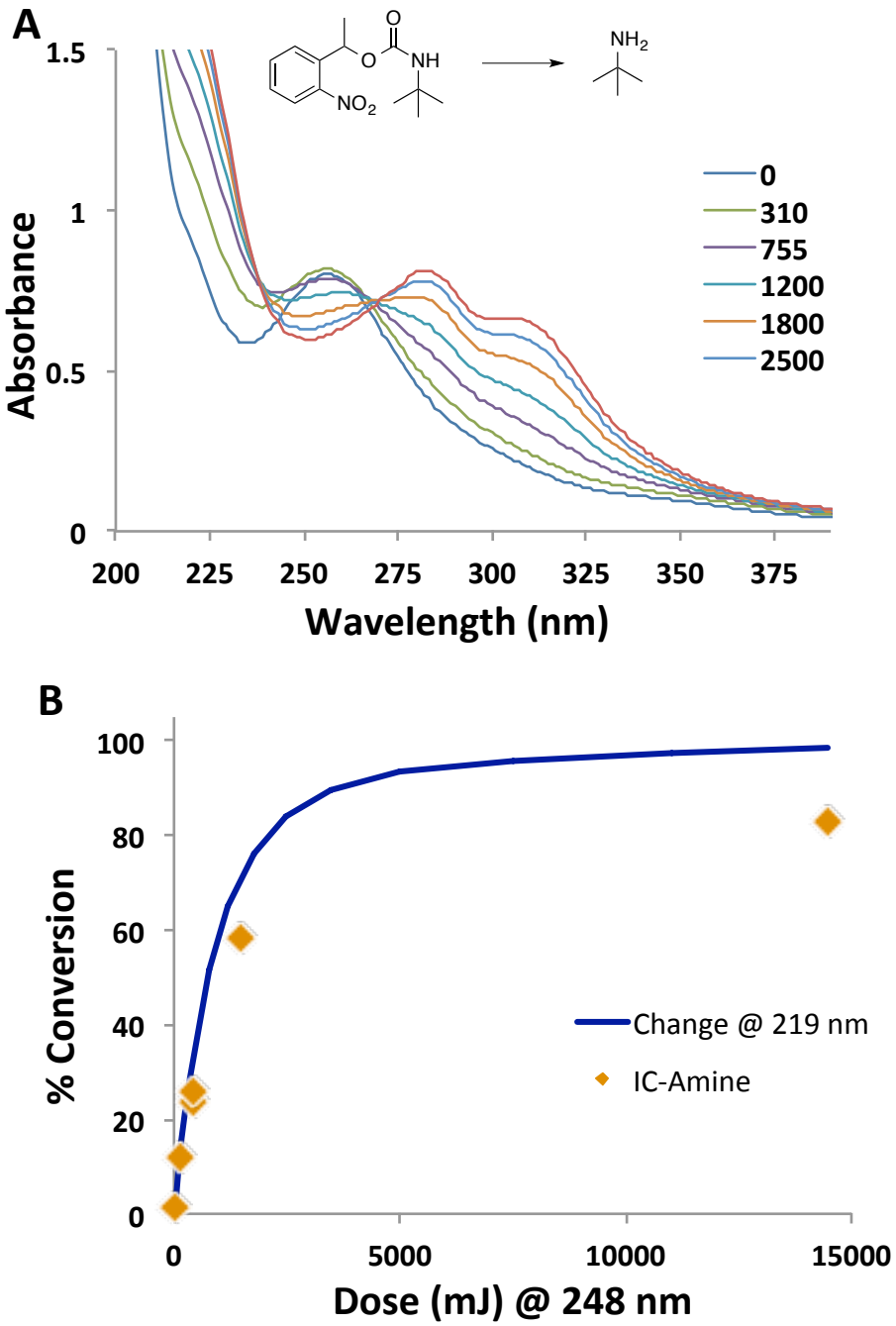

Figure 4.60: (A) Change in UV-Vis spectrum of TBA-MeNO2 upon exposure to 248 nm light in deoxygenated acetonitrile solutions. (B) Comparison of percent conversion of UV change at 219 nm (blue line) and percent conversion of amine detected by IC (orange diamond).

The last variant tested was A-MeNO2, which generates the electron deficient aniline. The drawback to using aniline as the generated base is its increased absorbance at 248 and 193 nm, which results in significant increases in the optical density of resist formulations at high PBG loadings necessary to improve LER. An advantage of aniline besides its weak nucleophilicity is that it is easily and quickly monitored by HPLC equipped with a UV detector. Aniline is not detected via standard IC and requires highly special, expensive columns that may not work in all reaction conditions. Therefore, a direct experimental comparison to the other MeNO2 PBGs is not presented here. Andrew Dick, of the Willson Group, led the HPLC analytical work. Figure 4.61 shows Dick's results from a simple A-MeNO2/ACN experiment exposed to broadband UV light and monitored by HPLC. The results are spectacularly clean. There is little to no deviation in the total integration of the PBG and aniline traces (orange circles) after an hour of exposure and ~85 % conversion.

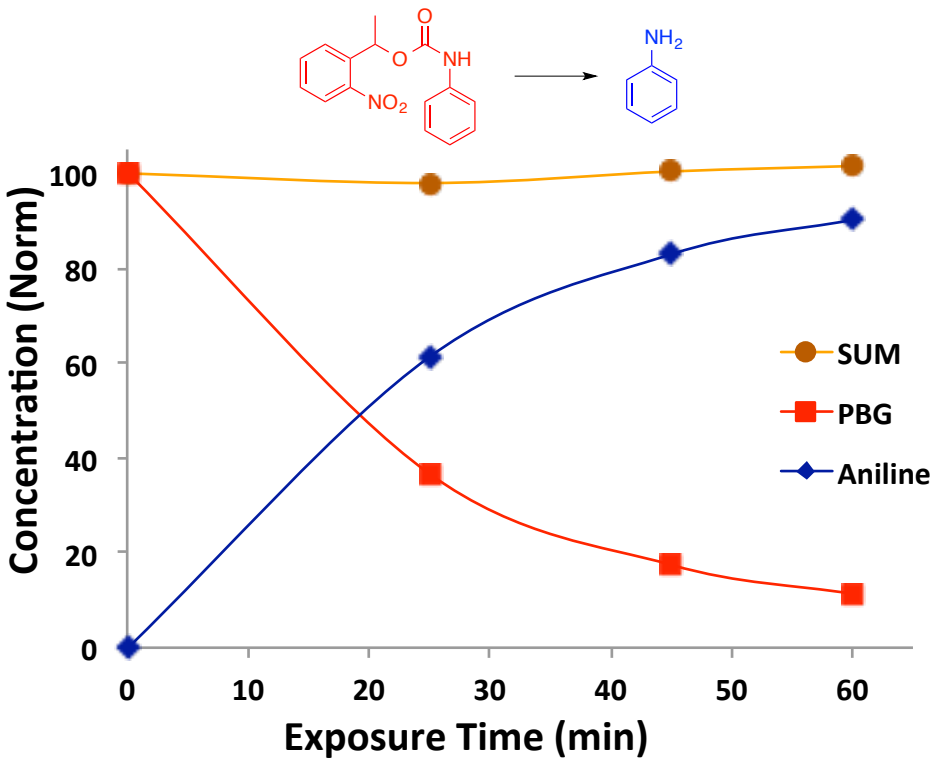

Figure 4.61: HPLC analysis of photolysis broadband UV of A-MeNO2 in deoxygenated acetonitrile solutions. Analyte detection by UV spectroscopy at 260 nm.

4.4.4 METHYLATED BIS-CARB SYNTHESIS

Because God likes to punish chemists, the synthesis of the methylated bis-carb could not be accomplished using the reaction conditions previously developed for the standard CHA-BisNO2. Therefore we undertook another extensive screening process to find amendable reaction conditions for the methylated derivative. A representative sample of the series of experiemnts is shown in Table 4.4, which highlights our fruitless initial efforts.

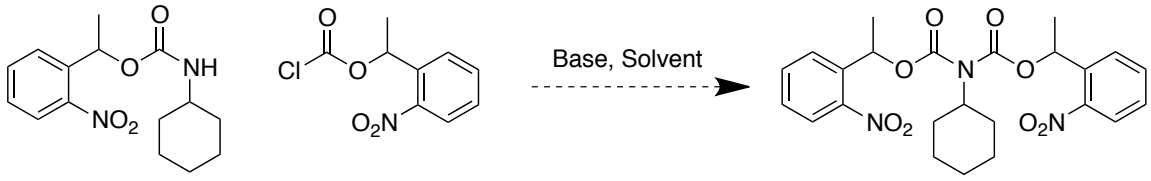

Entry	Base	Solvent (M)	E^+ (equiv)	T °C	% Yield
1	KHMDS	tol	2.0	0 - RT	0
2	KHMDS	THF	1.5	0 - RT	0
3	KHMDS	tol	4.0	RT	0
4	sec-BuLi	THF	1.5	-78 - RT	0
5	n-BuLi	tol	1.5	-78 - RT	0
6	TEA	tol	1.1	110	0
7	DBU	tol	2.0	110	0

Table 4.4: Table outlining the scope of reactions run in the attempt to synthesize CHA-BisMeNO2.

Because the traditional acid chloride route did not work in our labs, the test reaction shown in Figure 4.62 was run, yielding only enough product to afford identification.

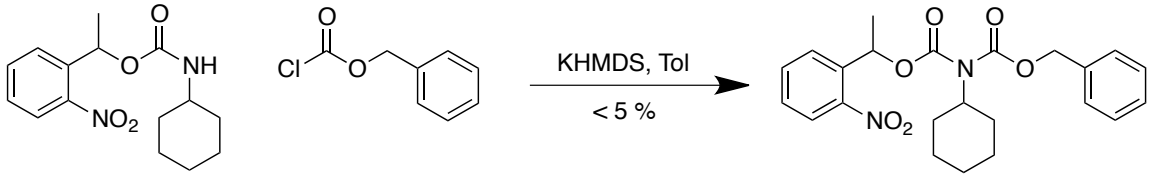

Figure 4.62: Illustration of the control bis-methyl-NO2 reaction run to explore reactivity.

Compared to previous control reactions on the BisNO2 system, which yielded between 5-20 %, it appears that the benzylic methylation significantly disrupts the nucleophile. With these results in mind, a number of new leaving groups were screened, such as imidazole,

methylimidazole, *p*-nitrophenol, and pentafluorophenol. All to no avail. Before exploring orthogonal routes towards the synthesis, we also explored switching the nucleophile and electrophile in the acid chloride-coupling step as shown in Table 4.5. But again to no avail.

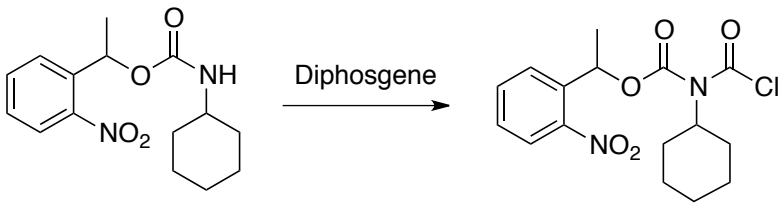

Entry	Base	Solvent (M)	Phos (eq)	T °C	% Yield
1	KHMDS	tol	3.0	0 - RT	0
2	n-BuLi	tol	6.0	0 - RT	0
3	Hünigs	tol	3.0	100°	0
4	NONE	THF	11	130°	0

Table 4.5: Table of reactions run to switch nucleophilicity.

Fortunately, little time passed before we succeeded in finding an alterative route towards CHA-BisMeNO2. Figure 4.63 illustrates how the target compound was prepared via Lewis acid catalyzed di-transcarbamylation.

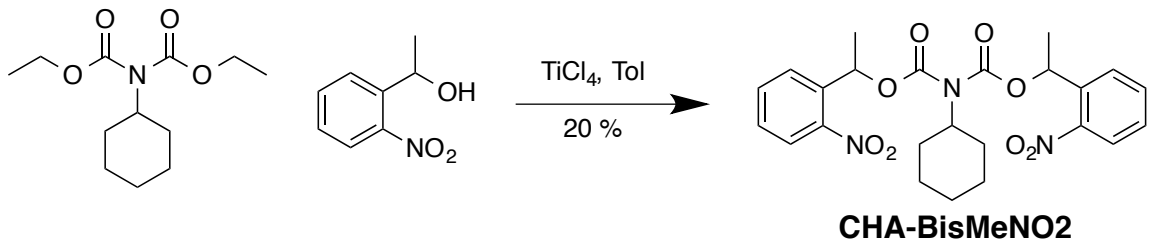

Figure 4.63: Reaction scheme of the successful transbiscarbamylation mediated by $TiCl_4$.

At this point, the astute reader of this section can readily predict the outcome of our attempted adaptation of this new methodology for the synthesis of A-BisMeNO2. The slight modification of aniline substitution in the di-transcarbamylation yielded no product. As Figure 4.64 shows, even simplifying the transcarbamylation by pre-installing one of *o*-nitrobenzyl groups first yielded no success.

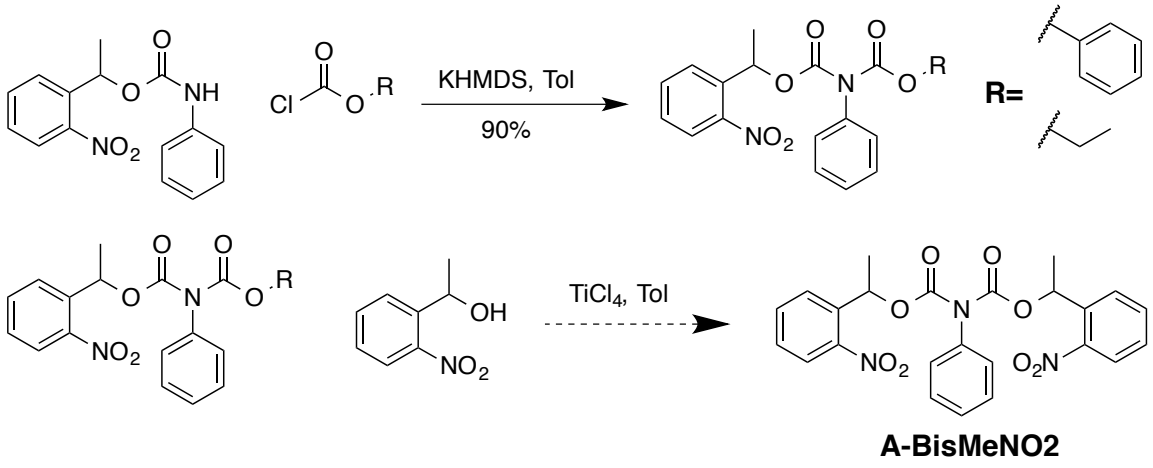

Figure 4.64: Schematic of failed transcarbylation route towards A-BisMeNO2.

Determined to not give up and to synthesize the ideal model biscarbamate for testing two-stage photokinetics, we undertook one more set of screening experiments. As Table 4.6 shows, A-BisMeNO2 was synthesized in acceptable yield through the use of a different counter ion on the silylamide base. The fact that the counter ion made such a stark difference in yield was surprising. Potassium was originally chosen as the counter ion for these reactions as it is known to favor O-alkylation over the smaller Na and Li alkali metals.(*106*, *107*) The larger size of K causes it to be more polarizable, allowing the nucleophilic oxygen to be less encumbered and more reactive. The earliest BisNO2 reaction screens looked at closely matching the counter ion with the proper solvent. Therefore, crown ethers, THF and HMPA were examined exhaustively.(*108*) At the time, it was surprising that the only solvent combination that worked in our hands was toluene, which is counter-intuitive to what is often taught in organic textbooks.(*109*) We speculate that the switch from K to Li led to favorable coordination of Li to the carbonyl oxygens, or it may have assisted with the acid chloride reactivity through beneficial coordination(*110*).

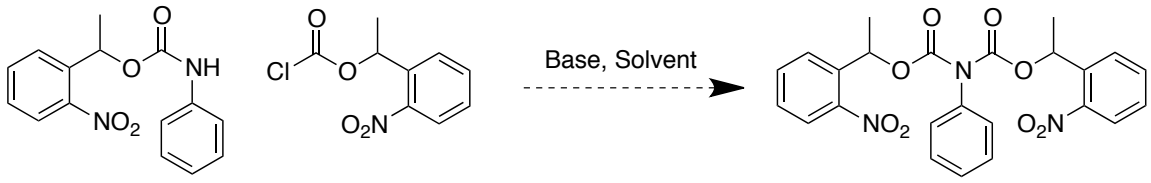

Entry	Base	Solvent (M)	E^+ (equiv)	T °C	% Yield
1	KHMDS	tol	2.0	0 - RT	0
2	KHMDS	tol	4.0	0 - RT	0
3	sec-BuLi	THF	1.5	-78 - RT	0
4	DBU	tol	1.1	-10 - RT	0
5	LiHMDS	tol	2.0	0 - RT	37

Table 4.6: Table outlining the final reaction screen towards the synthesis of A-BisMeNO2.

4.4.5 METHYLATED BIS-CARB ANALYSIS

A-BisMeNO2 was examined for base generation via broadband illumination and monitoring by HPLC. From our knowledge, the results in Figure 4.65 show the first kinetically matched two-stage photoreaction! Figure 4.65.B focuses on the low dose region, where the red trace shows the first-order generation of the 1-stage PBG and the blue trace shows a delay and acceleration of aniline upon exposure to UV light.

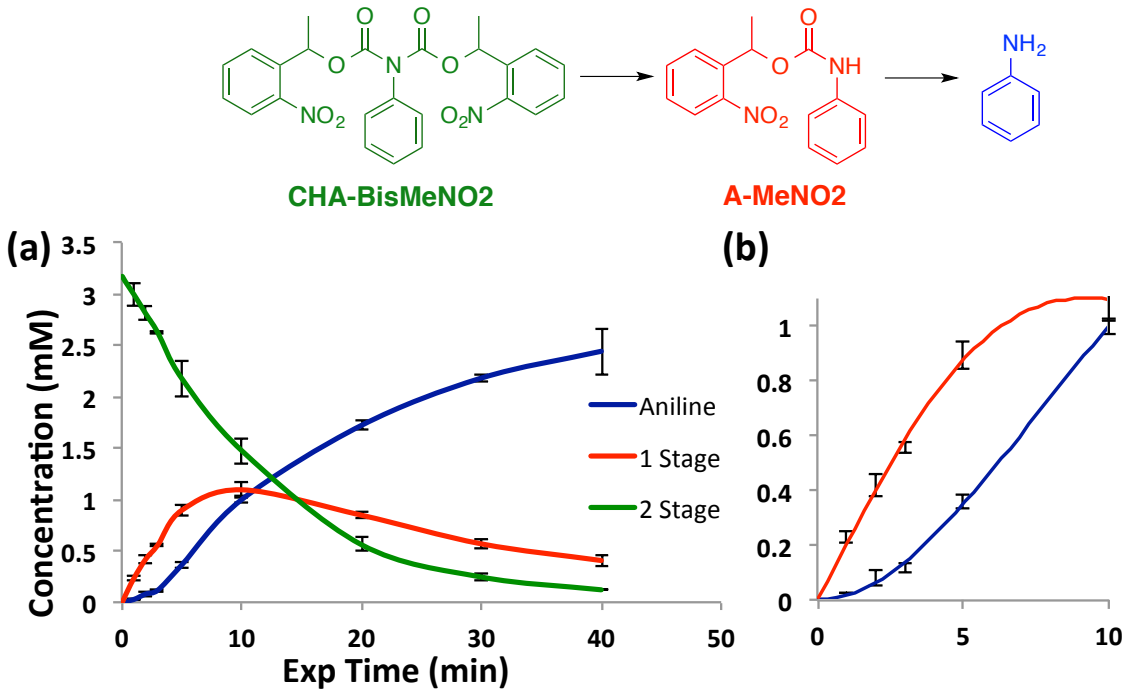

Figure 4.65: HPLC analysis of photolysis broadband UV of A-BisMeNO2 in deoxygenated acetonitrile solutions. (b) Magnification of lose dose region. Analyte detection by UV spectroscopy at 260 nm.

After these exciting preliminary results by HPLC, we immediately shipped samples of the aniline carbamates to our collaborators at Columbia University, Steffen Jockusch and Yongjun Li, for chemical analysis. Figure 4.66 shows the HPLC traces of the exposure a 5 mM sample of A-MeNO2 in acetonitrile to 254 nm light. After two minutes of exposure the reaction cleanly produces two new peaks. The peak at ~ 4 minutes matches that of the aniline standard. The unidentified peak at 5 minutes was

isolated and identified by mass spectrometry to be the *o*-nitrosoacetophenone ($C_8H_7NO_2$: 149.05. Found: M+1: 150.02 & M+Na: 172.03).

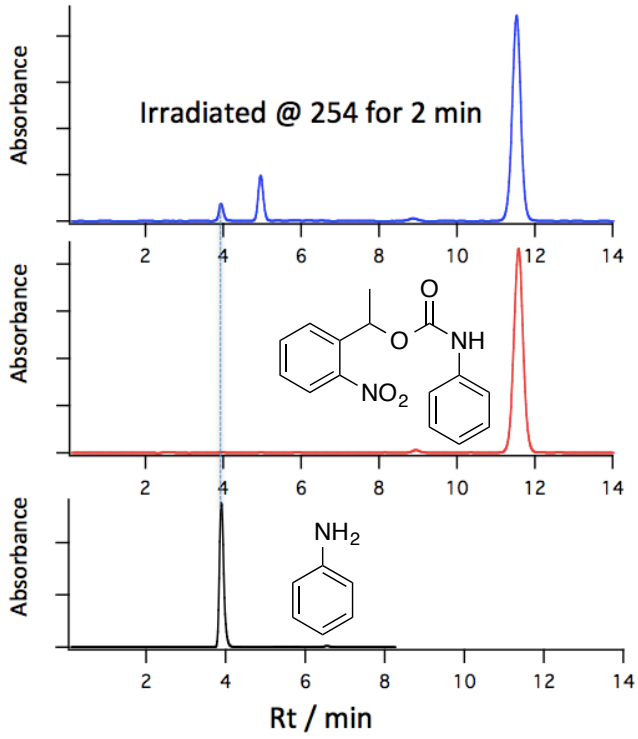

Figure 4.66: HPLC analysis of photolysis at 254 nm of A-MeNO2 in deoxygenated acetonitrile solutions. Analyte detection by UV spectroscopy at 260 nm.

Using the same exposure conditions as above, BisA-MeNO2 was monitored by HPLC. Figure 4.67 shows the HPLC traces at 2 and 5 minutes of exposure, where again, the photoreaction proves to be remarkably free of by-products, generating only the 1-stage PBG, aniline, and nitrosoacetophenone.

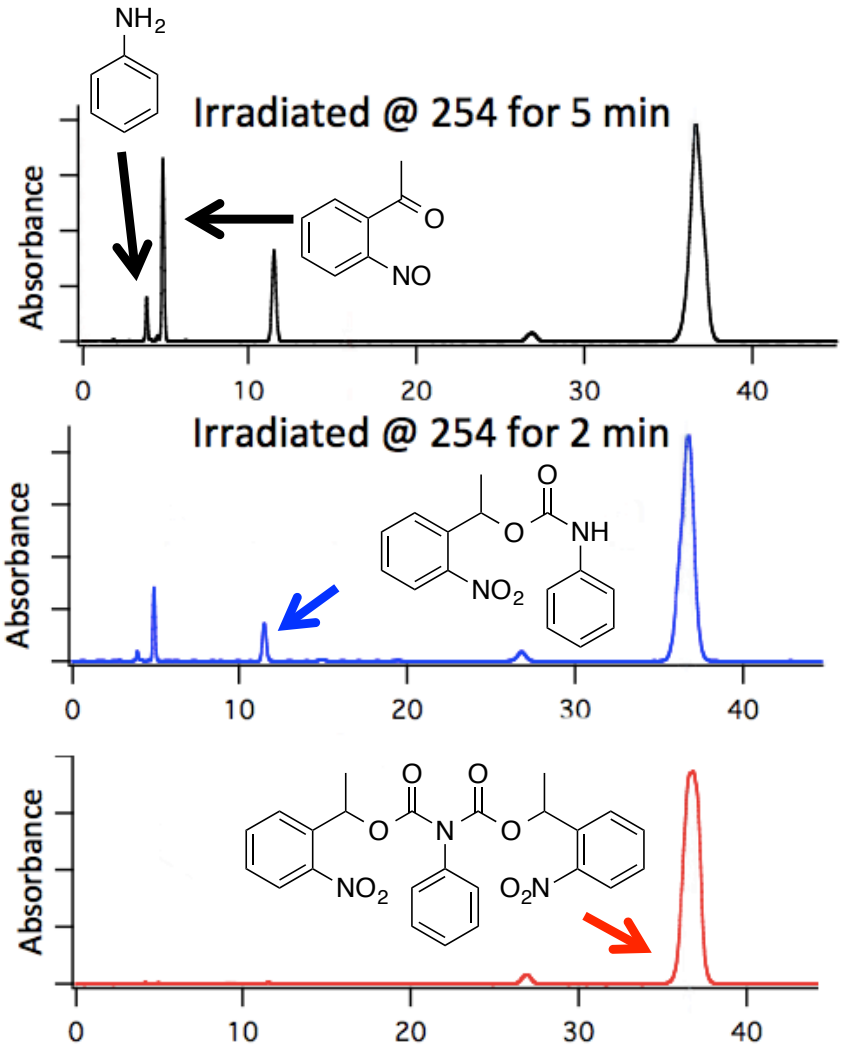

Figure 4.67: HPLC analysis of photolysis at 254 nm of A-BisMeNO2 in deoxygenated acetonitrile solutions. Analyte detection by UV spectroscopy at 260 nm.

With valerophenone as the internal actinometer, as described in the earlier sections with the Arun protecting group and photoaromatizing PBGs in Section 4.2.1, Jockusch and Li found the quantum efficiencies for A-MeNO2 and BisA-MeNO2:

$$\phi_{1-PBG} = 0.21$$

$$\phi_{2-PBG} = 0.12$$

The quantum efficiencies of the two stages are extremely close to one another. At a ratio of 0.75 : 1, the quantum efficiencies are in the ideal range to improve the slope of the net acid profile according to predictions made by earlier kinetic modeling. With quantitative data showing that our two-stage PBG performs as predicted, new experiments were planned to compare and contrast the LER of 1-stage and 2-stage pitchdivision formulations.

4.4.6 IMAGING COMPARISON

The imaging comparison between CHA-NO2 and CHA-BisNO2 PBGs was conducted with each PBG formulated and processed to have equal E-factors to result in one-to-one lines and spaces. The substantial difference in kinetics between the PBGs results in process parameters such as PEB, loading, and dose varying between the two formulations. Comparing these at ~1:1 ratio allows for evaluation at the most lithographically relevant patterning, along with ensuring each formulation is printed at the same part of the aerial image. Imaging evaluation was completed at the IBM Almaden research center by the author aided by IBM researchers Hoa Truong, Greg Wallraff, and Dan Sanders.

For each formulation, contrast curves were studied at various PBG concentrations and across a temperature gradient from 90 ºC to 125 ºC to establish the optimum formulation and process for an E-factor in the range of 0.5 – 0.65. In the case of the CHA-BisNO2 a small amount of acid quencher (DBU = 50 mg/mL stock resist) was necessary to decrease the E-factor to within the desired range. Once the loading and approximate PEB were confirmed, a custom interferometric 194 nm tool was used with line and space mask size of 200 nm. As discussed in Chapter 3.6, interferometric tools produce a pure sinusoidal image, which is ideal for patterning pitchdivision and allows for excellent comparison between the one-stage and two-stage formulations. The LWR/LER measurements were made with Summit software. The results of the imaging study are shown in Figures 4.68-4.70.

(a) Plain TOK Resist

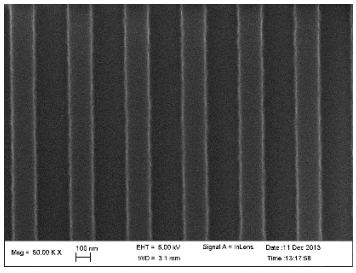

Eop=1.3mJ PEB=116C

	CD	LWR	LER
P	174	9	5

(b) CHA-NO2

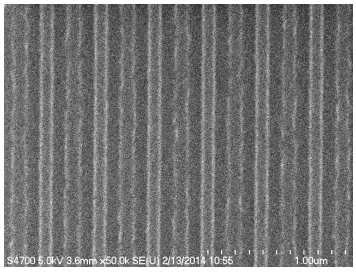

Eop=16mJ PEB=109C

	CD	LWR	LER
P	103	12	9
N	113	44	23

(c) CHA-BisN02

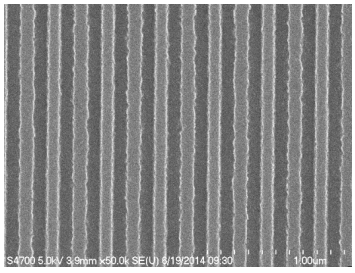

Eop=10.9mJ PEB=100C

	CD	LWR	LER
P	100	9	6
N	110	17	12

Figure 4.68: LER and LWR data and SEM images of (a) plain TOK 193 resist (b) 1-stage PBG and (c) 2-stage PBG pitchdivision formulations. Each image printed with identical illumination conditions with a 200 nm HP feature mask.

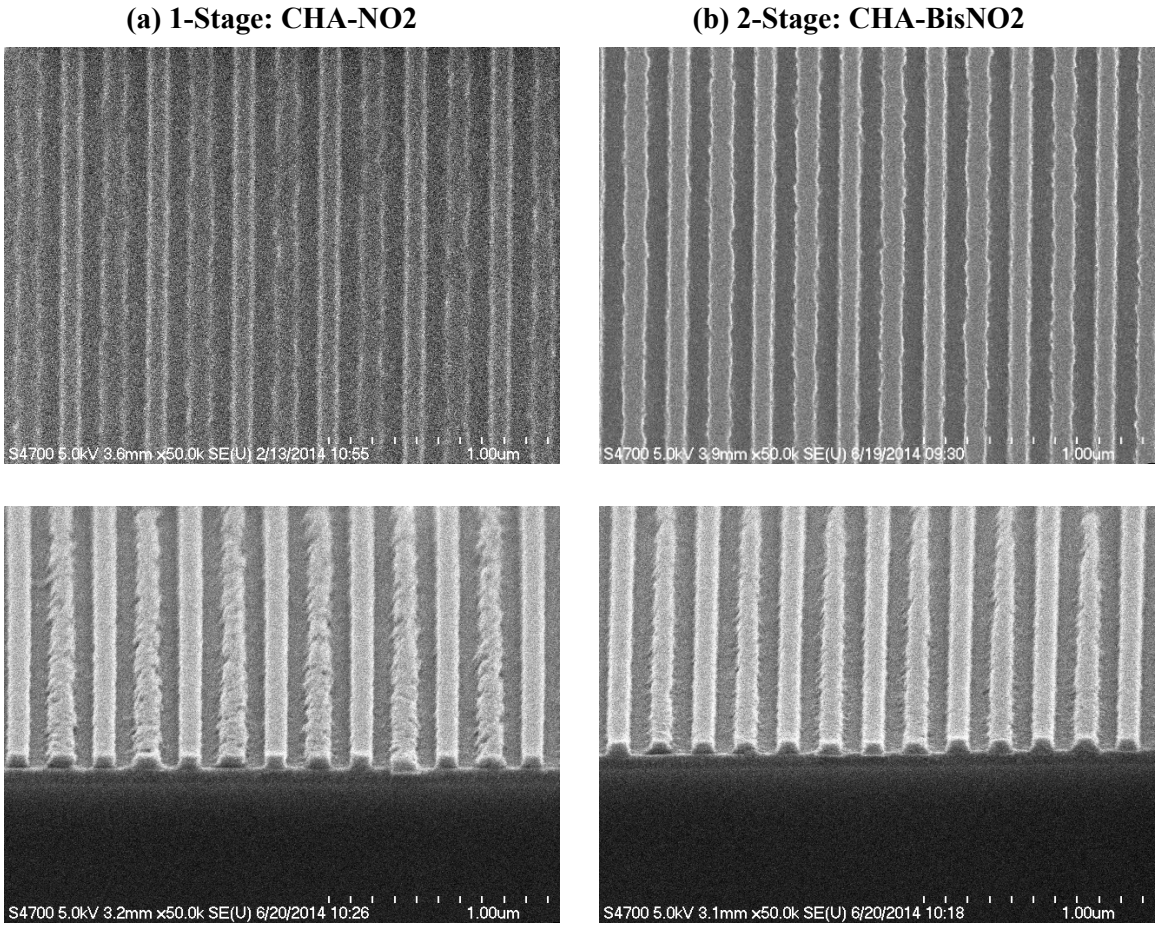

Figure 4.69:Top down and cross-sectional (45º) SEM images of pitchdivision patterns. The HP defined by the mask is 200 nm and the resulting resist patterns each have ~100 nm HP. (a) Left image printed with 1-stage PBG, CHA-NO2 and (b) right images printed with 2-stage PBG, CHA-BisNO2.

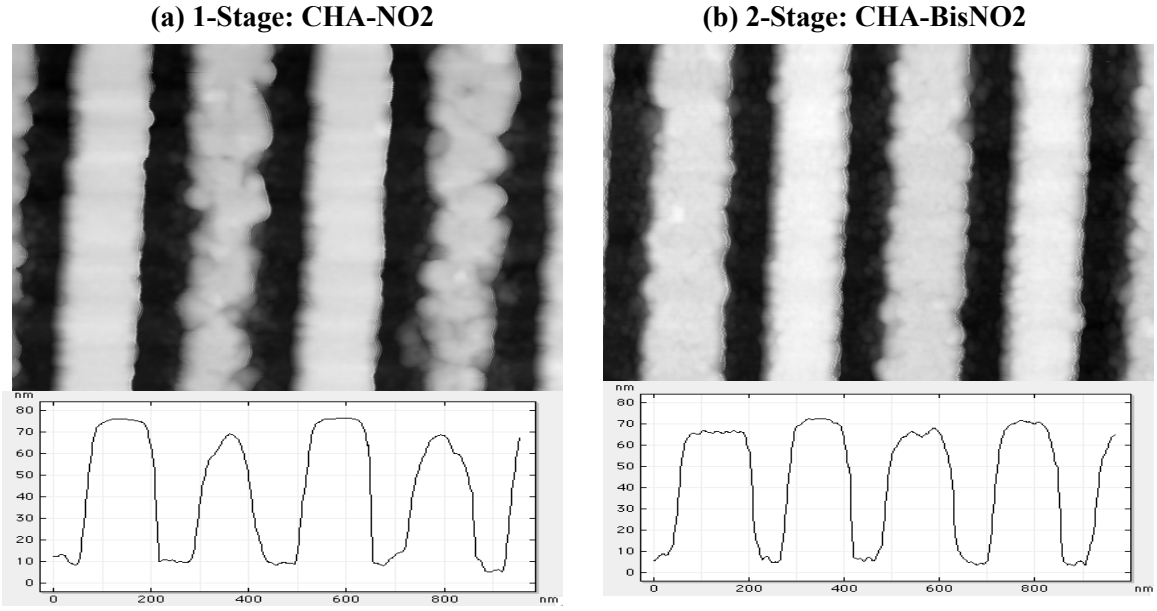

Figure 4.70: AFM images of pitch divided line and space patterns. The HP defined by the mask is 200 nm and the resulting resist patterns each have ~100 nm HP. (a) CHA-NO2 and (b) CHA-BisNO2 pitchdivision formulations

The LER and LWR data presented in Figure 4.73 show a distinct improvement with the two-stage formulation over the single stage. As predicted by the kinetic modeling, the LER of the two-stage positive-tone line is nearly identical to that of the native resist. The LWR and LER of the negative-tone lines is approximately 60 % and 48 % improved, respectively, with the use of a two-stage PBG. The AFM imaged in Figure 4.75 also show that the negative tone lines on CHA-NO2 suffer not only increased X-axis roughness but also Z-axis roughness that is less prominent in the two-stage formulation. Clearly the two-stage PBG improves image fidelity in comparison to the standard one-stage PBG.

4.5 CONCLUSION

The successful development of a number of two-stage PBGs was accomplished. In many cases, the unpredictable nature of photoreactions and side product formation proved to be a difficult challenge in the quantification of amine generation. Other times, such as the photoaromatization PBG, the kinetics of the first stage and second stage are too different to result in any real improvements in chemical contrast. Ultimately the best two-stage PBG in this study, was the first one imagined but, by far, the most elusive to synthesize. Through collaborative effort, CHA-BisNO2 was synthesized, and its model compound A-BisNO2 is the first reported kinetically matched two-stage photoreaction developed. This CHA-BisNO2 showed a marked improvement in imaging fidelity compared to the one-stage variant, CHA-NO2. In alignment with the original hypothesis, this improvement results from improved chemical contrast obtained through higher order kinetics. The initial delay of the two-stage PBG reaction allows for the resist to maintain more of its native chemical contrast in the low dose region. This also allows for increased PBG loadings that lead to sharper contrast in the high dose region. The optimized formulations used to print the images shown in Figures 4.73-4.75 have a difference in PBG loading of 233 %, resulting in a 60 % improvement in negative-tone LWR. Further refinement of pitchdivision chemistry has even greater potential to improve the LER. Extensive modeling and screening of various PAGs to L-PBGs and the use of a higher boiling point amines would allow for a more uniform net acid production with decreased diffusion and evaporation of the base; although the effort for the reward may not be worth it in the end. In the fast paced world of semiconductor development, windows of

opportunity are easily missed. Currently, industry trends are already focusing its sight on the sub 22 nm node and beyond, even significant improvements in pitchdivision lithography are not likely to allow it to print images at these resolutions.(*111*) In the end, a significant improvement in LWR and LER was realized through novel two-stage PBGs, which are the first kinetically matched cascade photoreactions.

Chapter 5: Non-Catalytic Amplification of Photoresists

Chemically amplified resists (CARs) have served as the backbone of the photolithography industry for the past 35 years. The amplification realized through catalysis allows efficient pattern transfer with low doses of deep UV (DUV) light. The industry has evolved from 248 nm to 193 nm and onto immersion 193 nm light sources to continually improved the resolution of projection tools. For each transition, the basic concept of CARs has not changed since they were first introduced,(*112*) even though the components and chemistry have adapted and evolved for the needs of each new wavelength. Valiant efforts were made to continue this progression to 157 nm, but for a variety of reasons, mostly concerning lens material and pellicle development, the worldwide effort has been abandoned.

CARs were developed during the early move to 248 nm, (DUV). IBM and Perkin developed the first DUV tools based on light from high-pressure mercury lamps. The output of these lamps in the DUV is a small fraction of that at the characteristic mercury emission wavelengths of 436 nm and 365 nm (Figure 1.7) resulting in abysmal throughput. Either a much brighter light source or a much faster resist was necessary to use DUV for manufacturing. Ultimately, both the light source (Excimer lasers)(*13*) and the faster resists (Chemically Amplified Resists (CARs))(*113-115*) were developed. The fast resists were implemented in manufacturing with mercury lamp tools long before the KrF laser tools became available.

5.1 EUV Resist Material Requirements.

The industry is now engaged in efforts to implement Extreme Ultraviolet (EUV) Lithography, which projects 13.5 nm radiation. The EUV wavelength was selected because it is possible to build mirrors for that narrow bandwidth. Because there are no bright sources at 13.5 nm, this technology is seriously photon limited. This situation is analogous to the mercury-lamp based DUV tools, but at a much shorter wavelength. While minor improvements in source power and energy efficiency continue to progress, it is likely that EUV will be photon limited for the foreseeable future as predicted production timelines are pushed further into the future nearly every year (*116-120*). Hence, EUV lithography demands very high resist sensitivity, much higher sensitivity than that of CAR formulations that are in use for 193 nm today. This higher sensitivity is required because a 193 nm resist that typically requires an imaging dose of ca. 20 mJ/cm^2 would require nearly 400 mJ/cm^2 of EUV radiation in order to capture the same number of incident photons per unit area, since EUV is so inherently photon limited. The issues are more complex than presented; yet the principle is clear: A very fast resist is required to support EUV lithography.

5.2 The limitations of Chemically Amplified Resists.

CAR resists provide a sensitivity improvement of approximately two orders of magnitude over the diazoquinone / novolac systems that were used for 365 nm resist systems. This speed increase is achieved by introducing gain (via catalysis) in the information transfer system.(*115*) The photons generate a catalyst and the catalyst

mediates hundreds of chemical reactions. These reactions modify the solubility of the surrounding medium and enable the exposed areas of the resist (or the unexposed areas of the resist, depending on the developer) to be dissolved selectively.

This speed increase is achieved at a price, however. The price is loss of image fidelity that manifests itself in bias and line-edge roughness. The catalyst must diffuse within the film to access many reactive species, or the gain is not achieved. That movement is not limited to those areas addressed by the exposure. The catalyst diffuses into the un-exposed areas and produces images that are larger than the exposed area—this difference between the size of the exposed area and the developed image is called bias. The movement of the catalyst is not governed simply by Fickian diffusion. Instead, the catalyst ultimately stops moving on the lithography time scale even though the concentration gradient that drives it remains.(*67*, *121*, *122*)

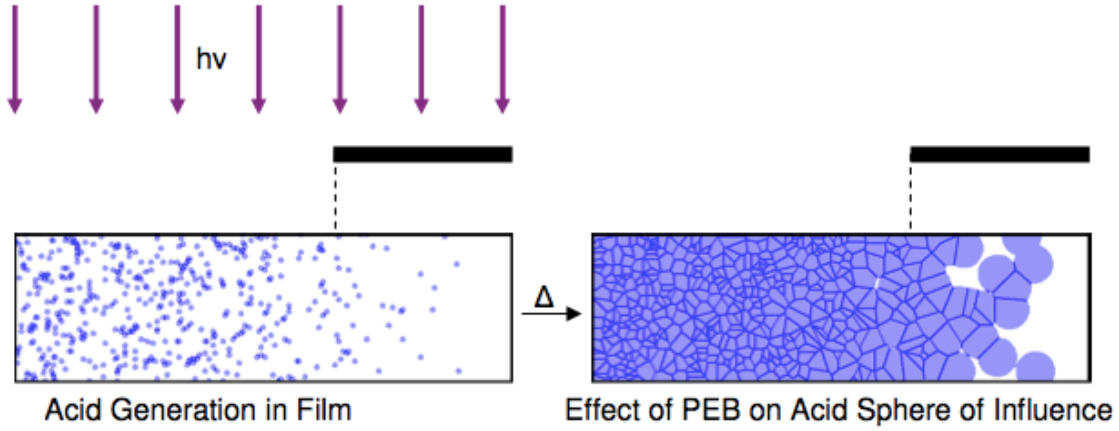

Figure 5.1: Illustration of bias as a result of catalyst diffusion in a dark film. (*From Ref*. (*123*))

This catalyst movement, causing bias, has been studied (Figure 5.1) and is understood, at least partly.(*122-124*) For example, the mass transport process that is responsible for bias is stochastic. The average distance that the catalyst molecules move in the film defines the bias. Unfortunately, each individual catalyst molecule moves at a different rate and thus a different distance. The variance in that distance creates a blur at the line edge. That blur coupled with the blur of the optical image and further convolved with the statistics of the dissolution process generates line-edge roughness (Figure 5.2).

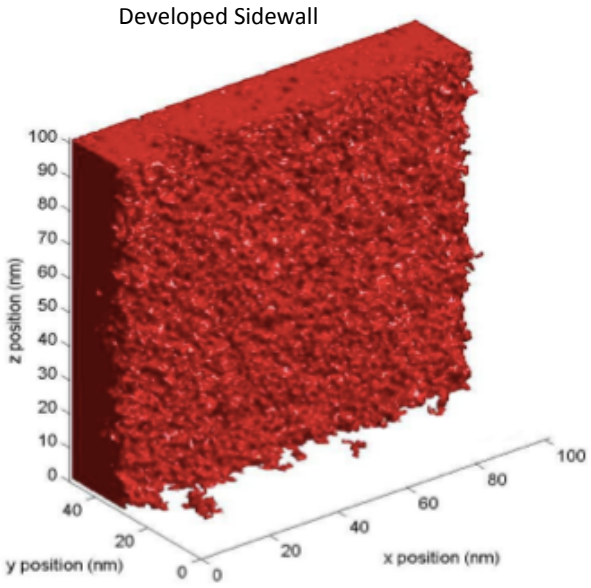

Figure 5.2: Computer model of sidewall profile upon resist development. If the catalyst did not diffuse, the image would, in theory, be approximately smooth. (*From Ref.* (*123*))

As the critical dimension (CD) continues to shrink, CARs have been pushed to the physical limit of their chemistry. The tolerance for imperfections in pattern transfer

greatly diminishes along with the shrinking of the CD. For large feature sizes, deviations in line edge roughness (LER) are easily tolerated, yet beyond the 45 nm node even minor imperfections lead to significant performance degradation. For example, a LWR (3σ) < 10% of the gate CD leads to ~2% performance degradation.(*72*) Therefore the ITRS requires a LWR below 8% of the CD(*71*). Keeping LER and LWR (3σ) < 8% is only increasing in difficulty as the 22 nm and 11 nm nodes quickly approach. Using CARs for generating small features with weak EUV sources is challenging. The more you increase the sensitivity of the resist (> $[PAG_0]$), the more significant the bias.(*122*, *123*) The larger the bias, the larger the line-edge roughness. Adding quenchers to the resist formulation,(*125*) or tethering the catalyst to polymer chains(*126*) limits the blur and the bias, at the cost of speed.

This three way trade-off has been called many things, but the most memorable description is "The Triangle of Death".(*127*) In this description, the area of the triangle that links resolution (bias), line-edge roughness, and speed is constant for a given CAR system. One can change the length of any of the legs of the triangle, but then the other two will change because these variables are not independent, thus area will always remain constant.

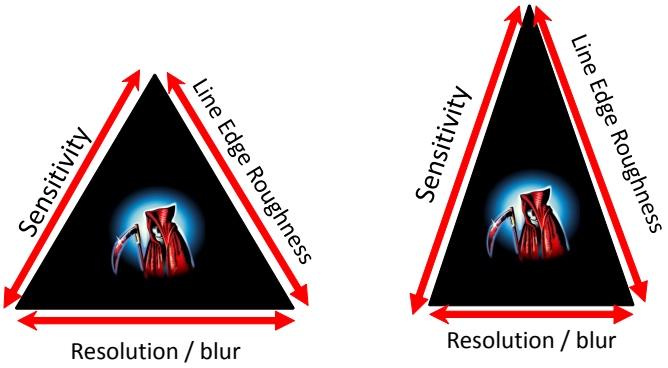

Figure 5.3: The "Triangle of Death". In the cartoon, the resolution is improved (shortened), but to hold the area of the triangle constant, both of the other variables have been degraded (lengthened). (*Adapted from Ref* (*128*))

A great deal of effort has been expended in attempts to reduce the total area of the triangle of death and some of that work has been fairly successful. Modifying the characteristics of the resins,(*129*) increasing the latent catalyst (PAG) loading,(*130*) adding absorbers, optimizing the bake conditions, as well as other techniques, all have led to incremental improvements. The linkage between the legs of the triangle, however, will always remain in variants of the original CAR design.

To escape the bounds of the triangle of death for EUV lithography, a fundamental change in the design of the resist must be made. Since EUV is photon limited, high resist sensitivity of CARs is required along with the resolution and line-edge roughness performance of non-chemically amplified systems such as PMMA. Long ago, it was shown that very high quality EUV images could be printed in non-chemically amplified

resists (Figure 5.4), albeit at high exposure doses.(*131*) The challenge is to develop a new EUV resist with large sensitivity (gain) without blur or bias.

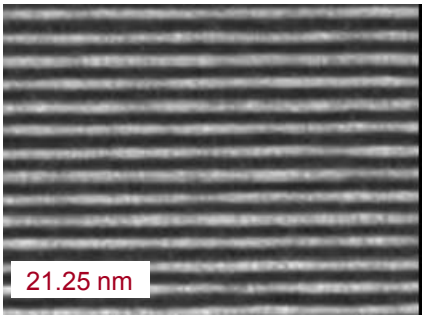

Figure 5.4. SEM micrograph of 21.25 nm lines and spaces printed in PMMA by 80 mJ/cm^2 EUV exposure at The Paul Sheering Institute. (*From Ref*. (*131*))

5.3 GAIN WITHOUT BLUR

The approach taken by the Willson group and the Phillips group (Penn State) to achieve gain without blur and bias is to avoid catalysis as the mechanism to increase sensitivity. Therefore a single photochemical event must break or form a large number of chemical bonds that affect the solubility of the resist without a catalyst, since a catalyst *must* diffuse to achieve the gain. Our approach is to exploit the thermodynamic driving force for de-polymerization (unzipping) of certain polymers when they are heated to a temperature above their *ceiling temperature,* T_c.

Polymers are formed by reversible reactions. That is, the monomer and the polymer are in equilibrium and the position of that equilibrium, defined by the equilibrium constant, is temperature dependent. While most polymers do not have an

accessible T_c since the heat of formation is significantly larger than that of depolymerization, some polymers due to their electronic and steric constraints are only accessible at low temperatures (>200 ºC). When a reaction is at equilibrium, the Gibbs free energy (ΔG), of the system is zero. The Gibb's Function states that the free energy of a system is equal to the change in enthalpy (ΔH) minus the temperature multiplied by the change in entropy (ΔS). That is, $\Delta G = \Delta H - T\Delta S$. If ΔG is zero, then $T_c = \Delta H/\Delta S$. Odian defines T_c as the temperature "at which the propagation and depropagation rates are equal";(*132*) Stevens states that the T_c is the point at which "the forward and back reactions are equal" and "G of polymerization is zero";(*133*) while Allcock contends that "no polymer can exist" above its T_c.(*134*)

However this concept is stated, it offers access to the required gain. This idea is best understood by exploring an example: commercially available *o*-phthalaldehyde (PHA) undergoes anionic polymerization to give polyphthalaldehyde (PPHA) in an equilibrium reaction. The T_c of PPHA is –40 °C. If one mixes an initiator (B^-) and PHA at room temperature, nothing happens. If the mixture is cooled to a temperature below T_c, the polymer forms and the solution becomes viscous. If the solution is warmed again above T_c, the polymer "unzips" back to monomer and the mixture becomes fluid again. In a closed system, this cycle can be infinitely reversed. If the system is cooled below T_c and then the reaction ion of the polymer chain is treated with an alkylating or acylating agent (such as CH_3I or Ac_2O) at low temperature, the polymer chain end is "capped" and the equilibrium is blocked. End-capped PPHA may be isolated and handled at room temperature—it behaves like a "normal" polymer. However, this polymer will be

switched back to a thermodynamically unstable form if the end-cap is removed or the chain is broken in some way to re-establish an ionic chain end. If the ionic chain end is revealed at a temperature above T_c, then the entire chain will unzip back to monomer spontaneously and quickly.(*7*) This chemistry is depicted in Figure 5.5, where the capped PPHA chain is converted to an ionic form by exposure to acid.

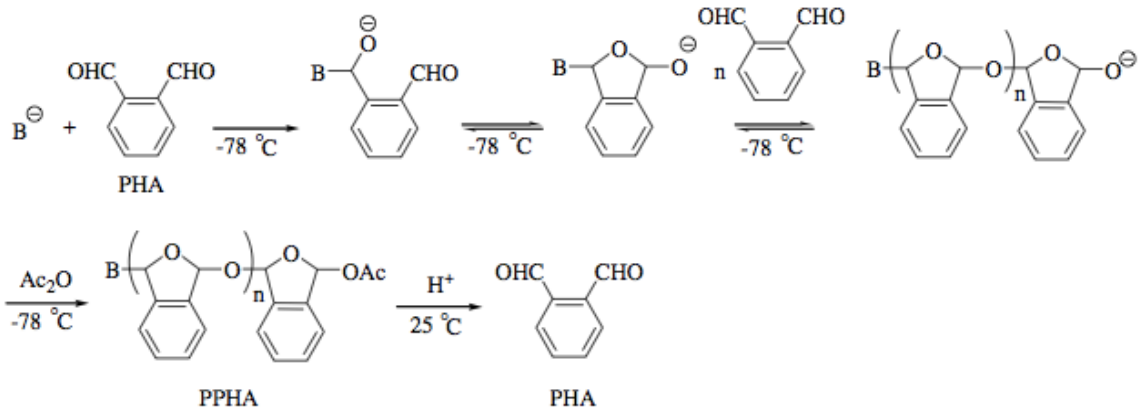

Figure 5.5: Anionic polymerization, end-capping, and acidic 'unzipping' of PPHA.

5.4 Early Demonstrations

This unzipping chemistry was exploited in the very first chemical amplification experiments that were reported by IBM in the early 1980's,(*113*) In that demonstration, the PPHA polymer was formulated with the PAG triphenylsulfonium arsenate. Exposure to 248 nm light (and electron beams) generated strong acid, which cleaved the PPHA chain and caused rapid depolymerization. The high degree of exotherm of this reaction was sufficient to vaporize the PHA monomer to spontaneously create a relief image. This polymer/PAG combination remains one of the most sensitive imaging systems yet

discovered. It can be imaged at 1–2 mJ/cm^2 at 248 nm, and 1-10 mC/cm^2 by electron beam exposure. The gain is enormous: not only is the reaction catalytic, it has a second stage of amplification in the form of the unzipping reaction. Of course, the PPHA material is not a resist. It does not resist anything very well and the combination of PPHA and a PAG has very high bias due to the diffusing acid. The principle, however, is clear: we can get substantial gain just from the unzipping reaction since many bonds are broken as a result of a single chemical event.

Several years later IBM,(*135*) Bell Labs,(*136*, *137*) and Hitachi(*138*) all explored electron beam resists that were comprised of a base soluble resin such as novolac blended with a low T_c polymer, a polyolefinsulfone. The polyolefinsulfone served as a dissolution inhibitor that limited the solubility rate of the novolac in aqueous base. Exposure caused main chain cleavage and unzipping of the polyolefinsulfone, and the chemical fragments resulting from depolymerization did not inhibit dissolution of novolac. In this way, the sensitivity of the resist derived from the radiation sensitivity of the polyolefinsulfone, and the etch resistance derived from the novolac. Hitachi commercialized such a resist.(*139*) The IBM group also explored use of PPHA as a blended dissolution inhibitor, and formulated a chemically amplified three-component resist comprised of novolac, PPHA, and a PAG. The performance of the resist was excellent, but it was never commercialized. Of course, this system works on the basis of acid catalysis, so it is subject to the dictates of the Triangle of Death. The demonstration proves, however, that the dissolution inhibition of PPHA is lost upon depolymerization to PHA.

The Willson lab revisited this PPHA/novolac material and successfully duplicated the IBM result. PPHA is a powerful dissolution inhibitor, as shown in Figure 5.6, and films that are similar to those reported by IBM were imaged by contact printing at 248nm using commercially available novolac and the industry standard TMAH developer. (Figure 5.7.A) The resist was not pursued further, however, because of its opacity at 193 nm. The opacity problem is avoided by going to EUV. The absorbance of the resist in the EUV is not the result of p-p* electronic excitations; it is simply the convolution of the elemental absorbance of its constituent atoms.

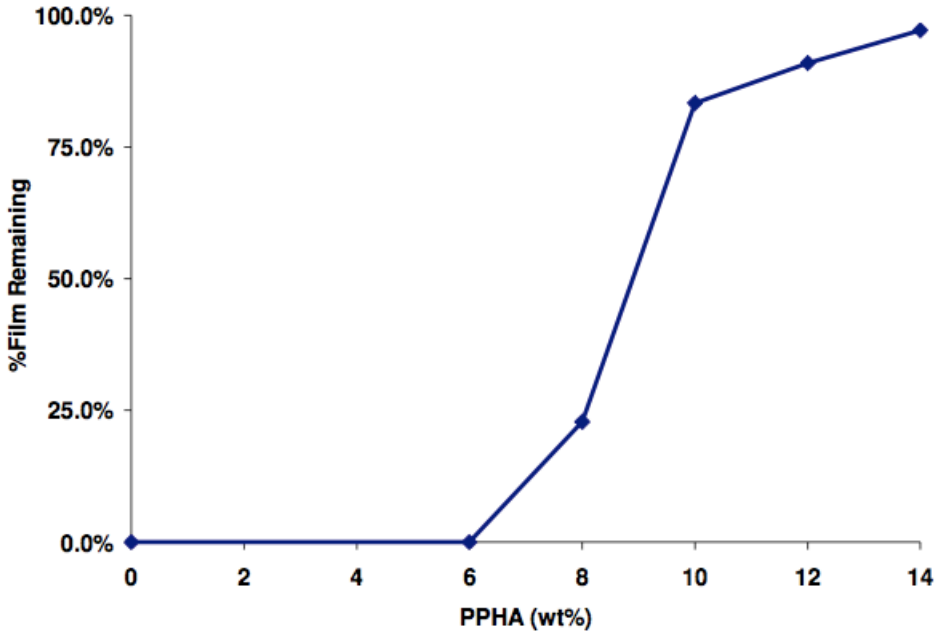

Figure 5.6: Percent film remaining vs PPHA wt% for novolac. (*From Ref*. (*7*))

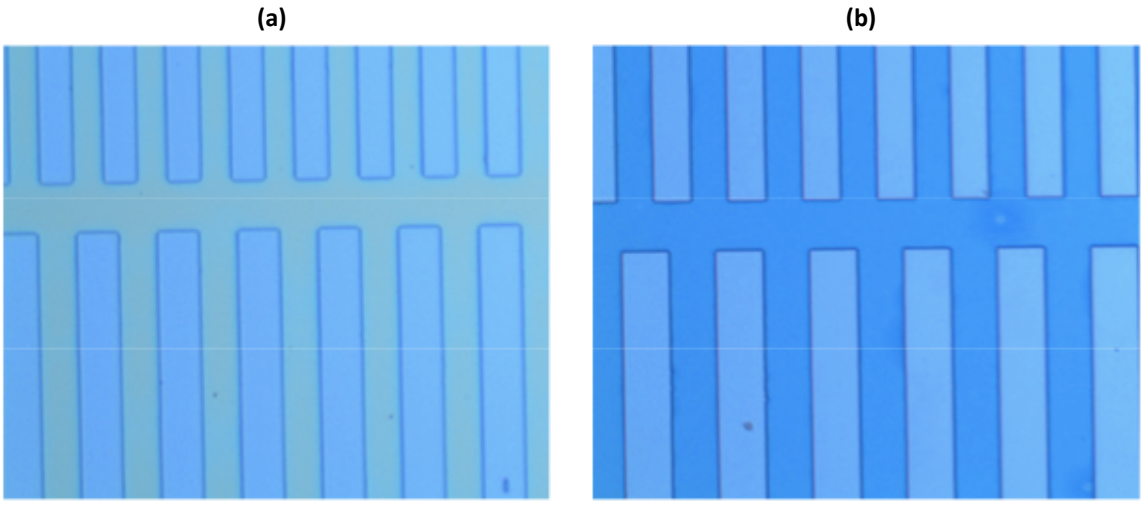

Figure 5.7: 248 nm exposure features of (a) novolac/PPHA/PAG formulation and (b) novolac and o-nitrobenzyl capped PPHA formulation. (*From Ref*. (*7*))

5.5 PHASE COMPATIBILITY

PPHA-Novolac is a good proof-of-concept low T_c polymer dissolution inhibitor (PDI) resist matrix. An important aspect of PDIs is their phase compatibly with a resist matrix. Phase compatibility is a serious challenge since approximately 99% of binary polymer blends are not phase compatible due to unfavorable enthalpic and entropic interactions.(*140*, *141*) To achieve phase compatibility, some interaction between the low T_c polymer and the matrix is required. With PPHA, it is the Lewis basic nature of the oxygen atoms on the PPHA and the acidic character of the phenolic hydroxyl on the phenol that we believe to be responsible. Even with favorable conditions, it is still necessary to limit the molecular weight of the PPHA to achieve phase compatibility. Decreasing the molecular weight of one of the components in the blend is often done to

increase compatibility, as described by Flory-Huggins theory.(*140*, *141*) PPHA >20 kDa results in optically phase separated films with novolac, whereas molecular weights <5 kDa achieve good phase compatibility.(*7*)

5.6 EUV Reactivity

PPHA is not inherently sensitive to EUV, and PMMA is not sensitive enough to allow high throughput manufacturing. Two methods explored by the Willson group and Phillips group are quenching low T_c polymers with a photolabile end-group or incorporating a monomer with a photolabile trigger to install EUV sensitivity to otherwise non-reactive polymers. Early results using a PPHA capped with an ortho-nitrobenzyl group illustrated that end-cap methodology works, even if it requires significant dose at 248 nm (Figure 5.7.B). Polybenzylethers from the Phillips group have successfully demonstrated unzipping via UV exposure and a nitrobenzyl end-cap as well.(*142*)

A potential drawback of using an end-cap strategy for EUV resists is the lack of reactive sites. Because EUV is photon and dose limited, having only the end of the polymer be photo-sensitive decreases the likelihood of a photoevent to occur. An ideal polymer would be inherently sensitive or contain photo-triggers on every monomer. The Phillips group is currently working towards a polybenzylether that contains photolabile protecting groups on every monomer.

5.7 PROPERTIES OF A PDI FOR EUV RESISTS

For a low T_c binary polymer resist system to be successful for EUV applications, the following attributes must be met:

(i) The low T_c polymer must first and foremost act as a dissolution inhibitor, whereas the fragmented polymer or monomer does not. For the case of standard resist polymers, this entails the PDI to contain Lewis basic sites to block alcohol and carboxylic acid sites through hydrogen bonding. First generation PDIs specifically focus on Novolac-based systems.

(ii) The two polymers must be phase compatible. Low molecular weights and complimentary acid-base paring is likely to facilitate.

(iii) The PDI must be reactive to EUV. If the polymer is not inherently sensitive to EUV, it needs to be fitted with an appropriate photolabile end-cap.

(iv) Lastly, the T_c must be near the range of standard processing conditions. (30 ºC-200 ºC). Out-gassing of the resist is a justifiable concern about this design. PPHA, for example vaporizes upon de-polymerization. This is not acceptable for EUV applications, and the problem must be corrected. One method to avoid this problem is by disconnecting the depolymerization step from the exposure step. By employing polymers with the T_c tuned to just above room temperature, the gain would not be manifested until a post exposure bake is carried out.

The successful design and synthesis of a polymer that fits the mandatory properties for this type of system is challenging. Early proof of concept work has been demonstrated in

the lab with an end-capped PPHA/novolac system,(*7*) but suffers from out-gassing upon depolymerization. Chapter 6 reviews work on dissolution inhibiting poly-polyester, which is inherently sensitive to EUV and undergoes a non-reversible aromatizing unzipping.

Chapter 6: Aromatizing Polyester Unzipping Polymer

There are five general classes of polymers that depolymerize from head-to-tail when a reactive ion is formed at the chain end, including those that (i) depolymerize via formation of quinone or azaquinone methide,(*143-146*) (ii) depolymerize via cyclization reactions,(*147*) (iii) combination of alternating cyclization and quinone or azaquinone methide elimination reactions,(*148-150*) (iv) unzip below their ceiling temperature (T_c) via acetal chemistry such as the previously described PPHA(*7*, *113*, *151*, *152*) and (v) stericly hindered alpha-methylstyrenes that depolymerize to create the monomeric styrene below their accessible T_c.(*4*, *153-155*) The area of unzipping or "self-immolative" polymers was recently reviewed by Andrew Boydston and co-workers.(*156*)

6.1 BACKGROUND

A major drawback to the quinone, azaquinone methide (i), and cyclization depolymerization (ii) mechanisms is the long length of time it takes to unzip the polymer. As illustrated in Figure 6.1, the benzene-based depolymerizable polymers that proceed through azaquinone methide elimination pathways exhibit slow rates of depolymerization requiring many hours in polar liquid-phase environments and exceedingly slow rates (i.e. days) in thin films.(*146*) The slow rates are due to the large thermodynamic threshold that the benzene-based polymers must surpass to form the azaquinone methide; breaking aromaticity is no small feat.

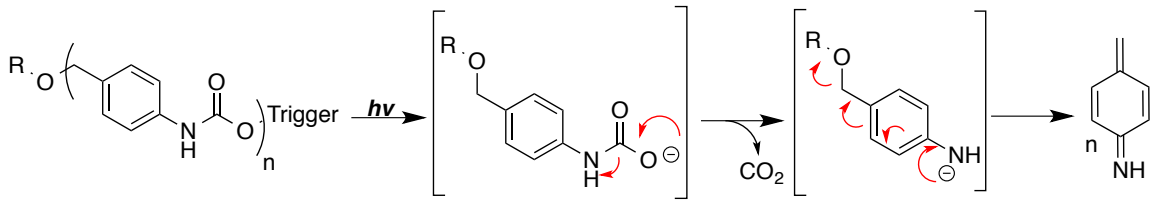

Figure 6.1: Illustration of benzyl-based polycarbate and its "unzipped" products.

Figure 6.2 shows the estimated difference in the heat of formation between the aromatic aniline repeat unit versus the resulting azaquinone methide.(*104*) Clearly an aliphatic polymer that unzips to form aromatic compounds would be more favorable!

	C_b - (N)	-0.50
4	C_b - (H)	13.20
	C_b - (C)	5.51
	C - (O)(C_b)(H)2	-8.10
	O - (C)(H)	-37.90
	N - (C_b)(H)2	4.80
		-22.99 kcal/mol

	N_I - (H)	16.30
2	C_d - (C_d)2	9.2
4	C_d - (C_d)(H)	27.12
	C_d - (H)2	6.26
		58.88 kcal/mol

Figure 6.2: Heat of formation for the aromatic repeat unit vs. the non-aromatic azaquinone methide.

The original concept for an aromatizing polymer is illustrated in Figure 6.3. Similar to the benzyl-based polycarbamates, a trigger could be installed at the end, which promotes the expulsion of CO_2 allowing for spontaneous formation of benzene, which in

turn, will drive off another molecule of CO_2 to continue down the depolymerization path. The hypothesis is founded on the fact that benzyl carbamates efficiently expel CO_2, which prevents the forward re-polymerization reaction to take place and allows for the rate limiting dearomatization step to occur.(*145*) The proposed mechanism of the aromatizing polyester shown in Figure 6.3 also begins with CO_2 expulsion but is followed by a fast and favorable aromatization to form benzene.

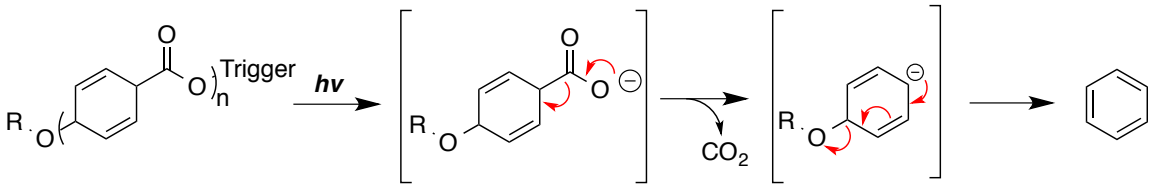

Figure 6.3: Illustration of the proposed depolymerization mechanism of the aromatizing polymer unzip.

6.2 SYNTHESIS OF AROMATIZING MONOMER

The final form of the monomer was modified following multiple failed attempts to synthesize the repeat unit illustrated in Figure 6.3. As illustrated in Figure 6.4, a methyl group was installed alpha to the carboxyl group. This methyl group creates a quaternary carbon in the six-membered ring, which locks the two olefins in place and prevents tautomerization to form the conjugated acid. The methyl group is installed in the first step of the synthesis **(a)**, which begins with the Birch reduction of benzoic acid and is quenched with iodomethane.

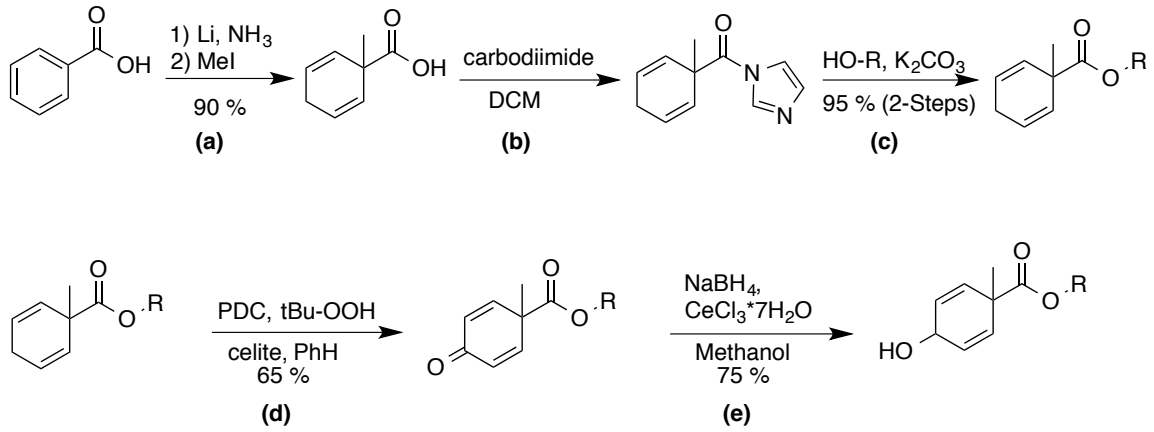

Figure 6.4: Synthesis schematic of aromatizing monomer.

Steps **(b)** and **(c)** use a carbodimide intermediate to yield the desired ester from the carboxylic acid and alcohol in high yield. The locked, non-conjugated diene proved essential for the oxidation step **(d)**, since only epoxides and aromatic fragmentation products could be isolated when the methyl group was absent. Both acidic (AcOH-Ac_2O)(*157*) and basic (3,5-dimethylpyrazol)(*158-160*) chromium (CrO_3) oxidation conditions were attempted with the non-methylated substrate. It was at this stage that the synthetic scheme shown in Figure 6.4 was developed to allow for the successful allylic oxidation. The pyridinium dichromate (PDC) conditions shown in step **(d)** gave lower yields than the corresponding CrO_3 conditions, 65 % vs 85 % respectively, but were chosen for scale up as the chromium oxide reaction led to a small explosive event in the lab. Celite is used in combination with the PDC to avoid the oxidant from clumping and slowing the reaction. The final reduction was completed using Luche conditions(*161*) to promote the reduction of the cross conjugated ketone over 3,4 reduction.

6.3 TESTING AROMATIZATION

An early concern with the aromatizing unzip polymer was whether the repeat unit would expel CO_2. In the case of the benzyl-based polycarbamates, the expulsion of CO_2 requires the breaking of the N-C=O bond, which is relatively facile in the presence of reactive ions. For the case of the aromatizing compound the expulsion of CO_2 requires the breaking of an alkyl carboxylate bond. It is known that alkyl carboxylic acids do not undergo decarboxylation readily without the presence of heat and strong acid or base.(*109*) Examining trends in bond dissociation energy (BDE) does suggest that there is good reason to believe our system may readily undergo the desired decarboxylation. The 1,4-cyclohexadiene backbone is known to stabilize ions and thus weaken the C-H and C-C bond strengths.(*162*, *163*) The BDE of the 1,4-cyclohexadiene C-H is 69 kcal/mol in comparison to an average alkyl C-H of 98.2 kcal/mol.(*164*, *165*) While the BDE of a molecule such as our monomer is unknown, there are clear trends in BDE of similar compounds. Table 6.1 compares the BDE of various alkyl, allyl, and α-carbonyl moieties.(*164*, *166*)

	BDE	SE	(ref.)		BDE	SE	(ref.)
	89	n/a	166		83.5	5.5	166
	85.6	3.4	166		79.4	9.6	166
	76.5	12.5	166		67.1	21.9	164
	73.2	15.8	166		?	?	

All values reported in kcal/mol. SE=Stabilization energy in relation to C2H5-CH3

Table 6.1: Table illustrating trends in alkyl bond dissociation energies.

The trend indicates that the weakest bond in the monomer backbone is likely the alkyl-carboxylate bond in question; the fission of which would lead to the formation of CO_2 and a resonance stabilized pentadienyl radical. The quaternary carbon alpha to the carboxylic acid further weakens this bond due to steric preference and hyperconjugation. The carboxylic acid should also weaken the bond in comparison to acetate and be more susceptible to bond cleavage, especially in terms of heterolytic cleavage. Even if the alkyl-carboxylic acid bond is not the weakest, it would only be slightly weaker than the ester bond, which upon cleavage provides an ion in an ideal position to promote decarboxylation. Again, the exact strength of the bonds in question are unknown, but they are very likely to be lower than 1,3-hexadiene, which has the largest stabilization energy (SE) of 21.5 kcal/mol.(*163*, *164*) Overall, the diallylic quaternary aromatizing monomer is expected to decarboxylate quickly in the presence of a reactive ion, which can originate from a terminal photosensitive end-cap as illustrated in Figure 6.3.

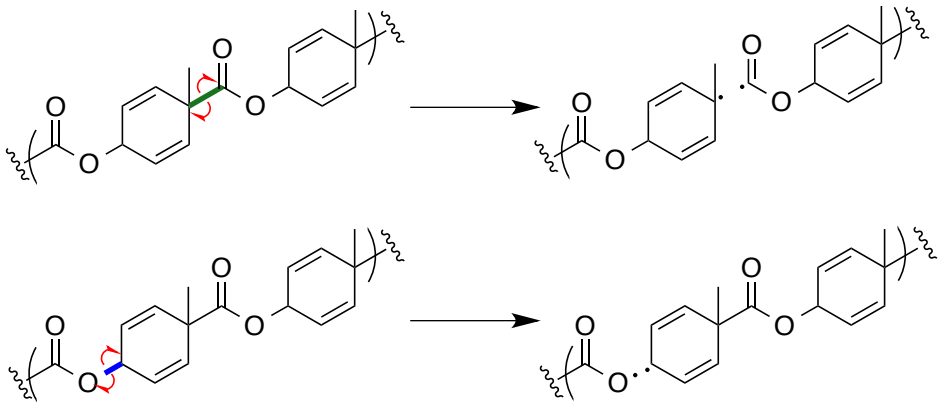

Figure 6.5: Illustration of heterolytic cleavage of the diallylic C-C bonds and the resulting radical ion formation.

To test the stability of the monomer, the model compounds in Figure 6.6 were synthesized. The intention was to selectively hydrolyze the ester to yield the carboxylic acid and then subject the free acid to basic conditions to monitor the rate of toluene formation. Initial attempts to hydrolyze the ester in basic conditions (LiOH, MeOH) resulted in rapid destruction of the starting material; therefore the use of the acid labile *t*-butyl group was explored for these control experiments.

The first candidate tested was with the acetate capped compound (a) illustrated in Figure 6.6. A 32 mg solution of the acetate test compound was formulated in deuterated chloroform (1 mL) and subjected to ~ 4 µL of trifluoroacetic acid (TFA) and monitored by ^{1}H-NMR. The acetate capped compound rapidly degraded into toluene. According to the hypothesis, TFA hydrolyzed the *t*-butyl group to give the free acid, which then immediately decarboxylated in the acidic environment to give toluene. Although, the rapid rate of hydrolysis at room temperature suggests that another mechanism may take

precedence. TFA may have protonated the acetate and promoted the cleavage of the acetate bond resulting in decarboxylation from the reverse direction.

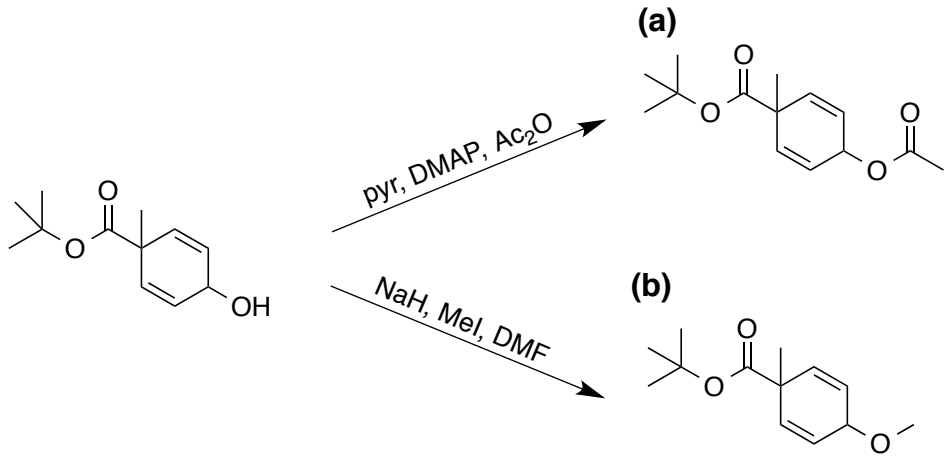

Figure 6.6: Schematic of the synthesis of the control compounds. (a) is acetate capped and (b) is methyl ether capped.

To slow the reaction, the methyl ether variant (Figure 6.6.B) was synthesized and subjected to the same conditions (Figure 6.7). The formation of toluene was significantly slower than for the acetate (a) and could be monitored more accurately by 1H-NMR. After 8 minutes the toluene peaks (7.25-7.15 ppm) begin to appear as a small down field peak around 10.5 ppm that likely corresponds to the free acid and a singlet at 4.6 ppm that closely corresponds to the isobutylene alkene.

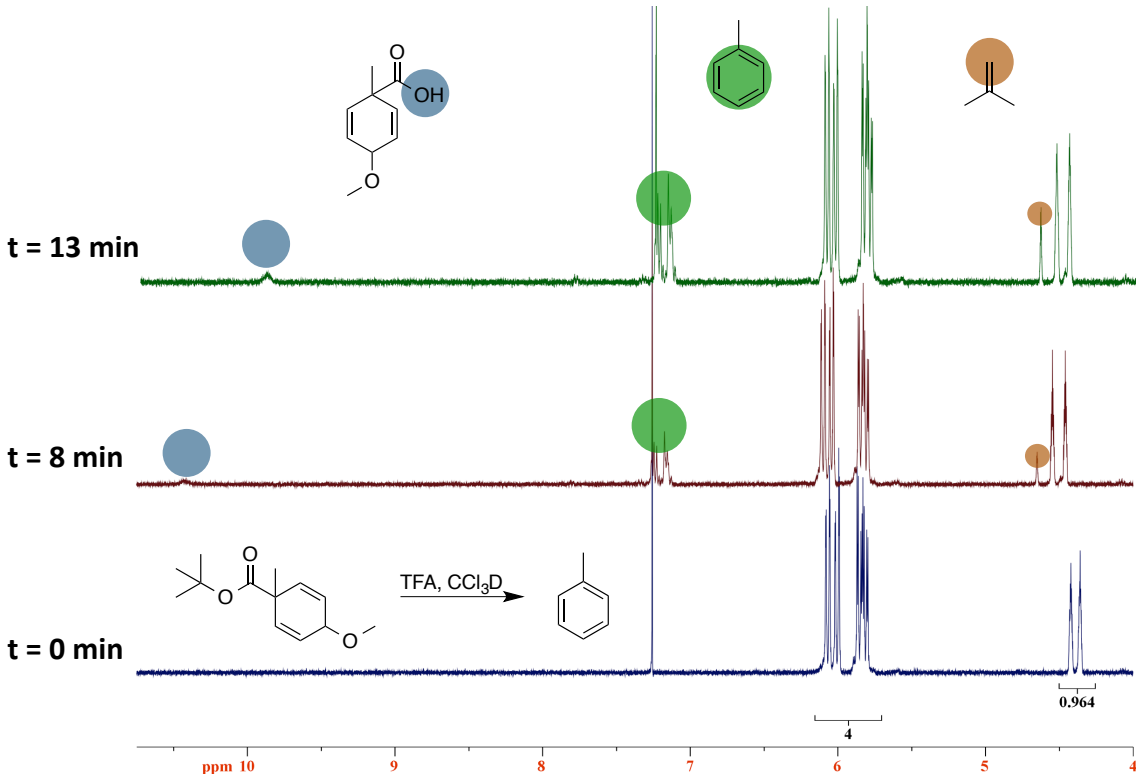

Figure 6.7: ^{1}H-NMR spectrum monitoring the generation of toluene. (See full spectrum Appendix B, Figure B.2)

These results suggest that the monomer readily decarboxylates upon hydrolysis of the ester; although the hydrolysis of the methyl ether still cannot be ruled out as a primary pathway.

Together with the acetate experiment and the previous attempts to hydrolyze the ester anionicly, the evidence suggests the monomer will aromatize upon formation of an ion at the carboxylic acid and is unstable upon cleavage of either diallyic bond. While the exact mechanism is uncertain, it is now known that the 1,4-cyclohexyldiene backbone is

sensitive to both acid and base conditions and readily forms toluene. On the basis of these promising qualitative results, the synthesis of the polymer was undertaken.

6.4 POLYMERIZATION

The choice of monomer ester underwent considerable thought and screening. Depending on the method of polymerization chosen, anionic vs. transesterification, different leaving group properties are beneficial. In the case of Lewis acid catalyzed transesterification, the ability to remove the resulting alcohol from the reaction mixture promotes the desired forward reaction. The removal of the alcohol shifts the equilibrium of the reaction toward the product, as there is less competition for the reverse transesterification, as described by la Chatelier's principle. Therefore a leaving group that may be boiled off or trapped by molecular sieves becomes an ideal candidate.

In the case of anionic polymerization, it is best if the hydrolyzed ester has a slightly lower pKa than that of the polymer's propagating chain end. This presents a bit of a conundrum, as the ability to drive off the resulting alcohol is also important to promote the forward reaction. Most good leaving groups have a lower pKa than the nucleophile, resulting in the leaving group 'stealing' the anion of the polymerization resulting in an unreactive alkali salt. Therefore the leaving group must have a lower pKa but not so much lower that it shuts down the living chain end. Figure 6.8 illustrates the competition between alcohol of the hydrolyzed ester and the chain end.

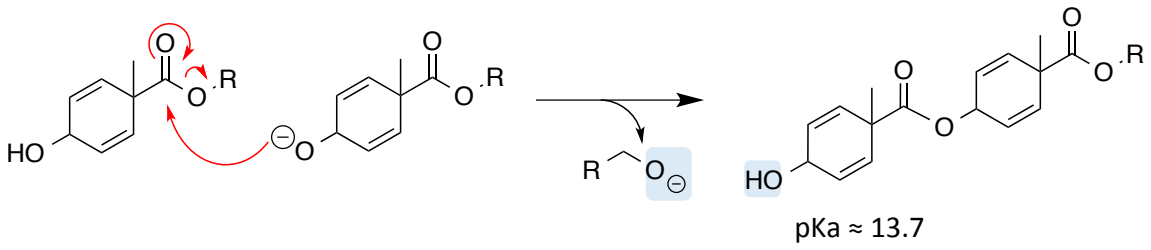

Figure 6.8: Illustration of anionic polymerization of the aromatizing unzip polymer.

Table 6.2 shows a table of the three main types of alcohols considered for leaving groups and compares and contrasts their positive and negative aspects in the proposed synthetic scheme.

	Good Leaving Group?	Difference in pKa	Removable from Flask?
HO CF_3	Good	Medium	Easy
HO CH_3	Ok	Small	Easy
OH	Good	Large	Hard/Impossible

Table 6.2: Table comparing and contrasting the characteristics of various alcohol leaving groups.

Fluorinated alcohols such as trifluoroethanol (TFE) are excellent leaving groups and have pKa's lower than that of alkyl alcohols and can be tuned by varying the number of attached fluorine atoms to the alkyl backbone. For example, TFE has a pKa of 12.5

whereas hexafluoro-2-propanol (HFIP) has a pKa of 9.3. The literature indicates that HFIP does not form an azeotrope with toluene but does form an 8:2 alcohol to benzene azeotrope.(*167*) Table 6.3 shows the efficiency of 4Å and 5Å molecular sieves to remove TFE and HFP from a 4:1 solution of toluene to alcohol. After 24hrs approximately 50% of the TFE is removed from solution, showing that molecular sieves may be used to remove TFE from the reaction.

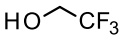

TFE-OH	initial	4hr	24hr
MS 4A	18.5%	14.8%	14.9%
MS 5A	19.1%	13.8%	**10.6%**

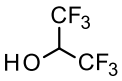

HFIP-OH	initial	4hr	24hr
MS 4A	19.2%	16.4%	16.4%
MS 5A	19.0%	16.4%	16.7%

Table 6.3: Tables comparing TFE and HFP absorption by molecular sieves.

Methanol and ethanol have higher pKa's than the diallylic alcohol at 16 and 15.5 respectively. This allows for efficient anion transfer but results in very slow nucleophilic displacement by the monomer. Because methanol and ethanol are efficiently removed from the reaction by the use of molecular sieves (4Å and 5Å respectively), they are excellent leaving groups for use in Lewis acid catalyzed transesterification reactions.

Phenols are well known for being excellent leaving groups in anionic and Lewis acid catalyzed transesterification reactions. The pKa of phenols is easily tuned through substituents strategically placed on the aromatic ring to give a range from pKa 9.95 of basic phenol all the way down to 5.7 of pentafluorophenol. Since phenols are regularly

used in transesterification and transcarbamylation reactions because they afford high yields with mild conditions, these were the first target group screened.

Unfortunately, based on these experiments, phenols do not appear to be suitable for transesterification polymerization (Table 6.4). While the pKa of phenol is much lower than the polymer chain end, we postulated that the failure to find any degree of polymerization is due to the inability to remove phenol from the reaction mixture because of its large size and high boiling point.

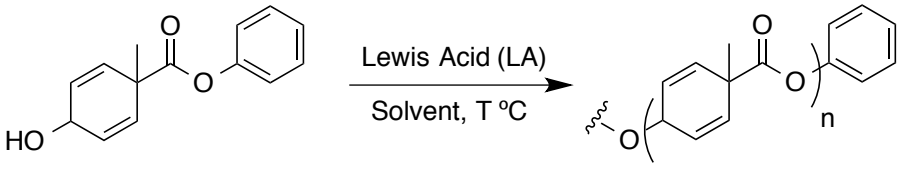

Entry	LA	Solvent	T ºC	n = ?
1	DBTL	Tol	110	0
2	DBTL	DMSO	120	0
3	$TiCl_4$	Tol	110	0
4	$Ti(OPh)_4$	Tol	110	0
5	$Ti(OPh)_4$	DMSO	120	0

DBTL = dibutyltin diluarate

Table 6.4: Reaction table screening Lewis acid catalyst with phenyl ester monomer.

The methylester monomer was subjected to a similar screen of Lewis Acids along with the addition of 4Å molecular sieves to remove methanol from the reaction mixture. The results of these reactions are shown in Table 6.5 Using dibutyltin diluarate (DBTL) as the catalyst (Entry 2) an oligomer with 9 repeat units was formed. The other Lewis acids tested either showed no reactivity, or in the case of scandium triflate (5) and Otera's

catalyst (6) spontaneously reacted giving 2-methyl-benzoic acid methyl ester upon addition to the reaction flask.

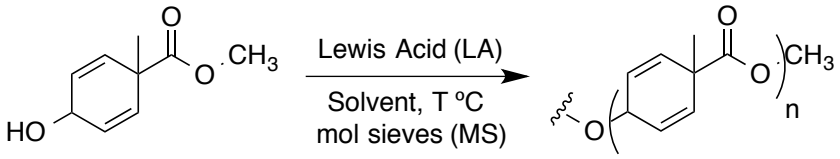

Entry	LA	Solvent	MS	T °C	n = ?
1	DBTL	Tol	n/a	110	0
2	DBTL	Tol	4Å	110	9
3	$TiCl_4$	Tol	4Å	110	0
4	$Ti(OiPr)_4$	Tol	4Å	110	0
5	$Sc(OTf)_3$	Tol	4Å	110	0
6	Otera's	Tol	4Å	110	0

Otera's = 1-Hydroxy-3-(isothiocyanato)-1,1,3,3-tetrabutyldistannoxane dimer
DBTL = dibutyltin diluarate

Table 6.5: Reaction table screening Lewis acid catalyst with methyl ester monomer.

After the initial success with DBTL and the methylester monomer, the screening then focused on anionic initiators and fluorinated esters. Both TFE and HFIP monomers were synthesized for screening. It should be noted that when the TFE monomer was tested with DBTL it gave similar results as the methylester monomer discussed above.

The results of the anionic initiation screen are shown in Table 6.6. The best result, Entry 3, used TFE-monomer, *n*BuLi, toluene and 4Å molecular sieves to give a short polymer having 11 repeat units (MW ≈ 1,600). The final optimization reactions were run testing various solvents and temperatures; a sample of the conditions is listed as Entries 6-11 of Table 6.6.

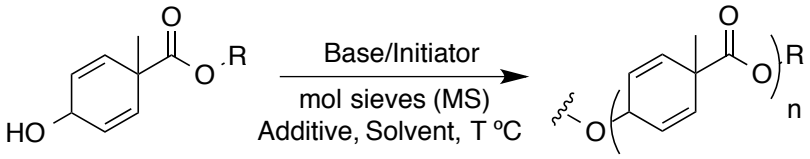

Entry	R =	Base	Solvent	Additive	MS	T ºC	n = ?
1	CH_3	P_2-tBu	Tol	n/a	4Å	110	5
2	CH_2CF_3	P_2-tBu	Tol	n/a	4Å	110	9
3	CH_2CF_3	n-BuLi	Tol	12-C-4	4Å	110	11
4	$CH(CF_3)_2$	n-BuLi	Tol	12-C-4	n/a	110	6
5	$CH(CF_3)_2$	P_2-tBu	Tol	n/a	n/a	110	6
6	CH_2CF_3	n-BuLi	MTBE	12-C-4	4Å	55	~ 5
7	CH_2CF_3	n-BuLi	DMA	12-C-4	4Å	140	0
8	CH_2CF_3	n-BuLi	Dioxane	12-C-4	4Å	100	~ 4
9	CH_2CF_3	n-BuLi	DMSO	12-C-4	4Å	100	0
10	CH_2CF_3	n-BuLi	THF	12-C-4	4Å	66	0
11	CH_2CF_3	n-BuLi	2-Me-THF	12-C-4	4Å	80	~ 4

DMA = dimethylacetamide; 12-C-4 = 12-crown-4 ether; P_2-tBu = Phosphazene Base: (1-tert-Butyl-2,2,4,4,4-pentakis(dimethylamino)-2λ^5,4λ^5-catenadi(phosphazene)

Table 6.6: Reaction table screening anionic initiators with various monomers.

During the solvent screening, it was found that temperatures above 110 ºC caused the polymer that forms to decompose (Entry 7 & anisole--not listed). Temperatures below 70 ºC gave very clean oligomers, but none of them grew beyond 5 repeat units. Entry 3 shows the largest repeat unit result from our screening, which was conducted by Kensuke Matsuzawa. This resulted after optimizing the ratio of equivalents of nBuLi to monomer. Figure 6.9 shows the GPC traces of polymers made with 0.07 to 0.0075 equivalents of nBuLi. (Up to 0.2 equivalents were also tested) After several months of screening solvents, initiators, equivalents of initiators, monomers, and temperatures the best

polymerization conditions found are shown in Entry 3 of Table 6.6 using 0.01 equivalents of initiator.

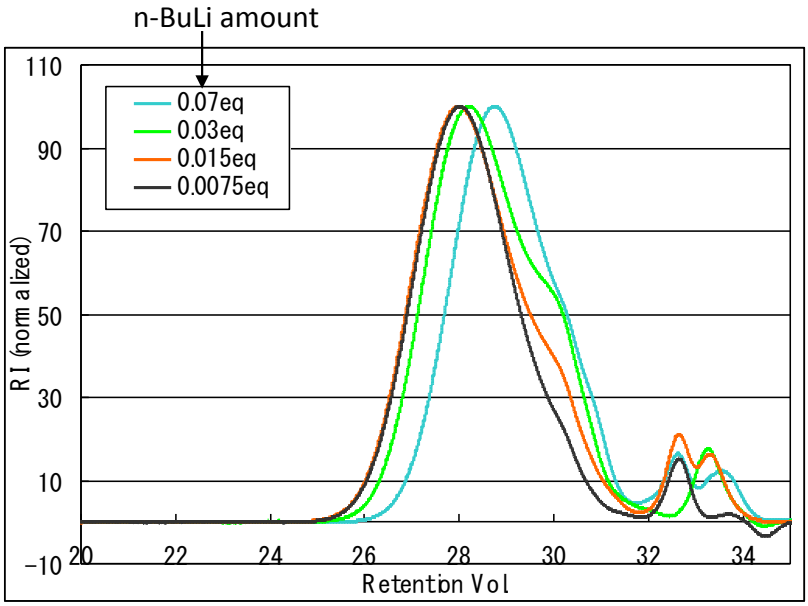

Figure 6.9: GPC trace showing optimal equivalents of nBuLi to monomer. (Data from Kensuke Matsuzawa)

6.5 SOLUTION EXPOSURE STUDIES

An *o*-nitrobenzyl capped polyester (mw: ~1,350) was made via the optimized conditions described in the previous section using a monomer initiator that had the o-nitrobenzyl ester pre-installed. The capped polymer was subjected to broadband UV light in deuterated acetonitrile and monitored by ^{1}H-NMR. After nearly three hours the benzyl peaks of the end cap (5.45 ppm) were completely gone in the NMR spectrum showing fairly efficient end cap cleavage (Figure 6.10). Figure 6.11 shows the full ^{1}H-NMR

spectrum of the exposure study and reveals the formation of toluene closely corresponds to the depletion of the end-cap.

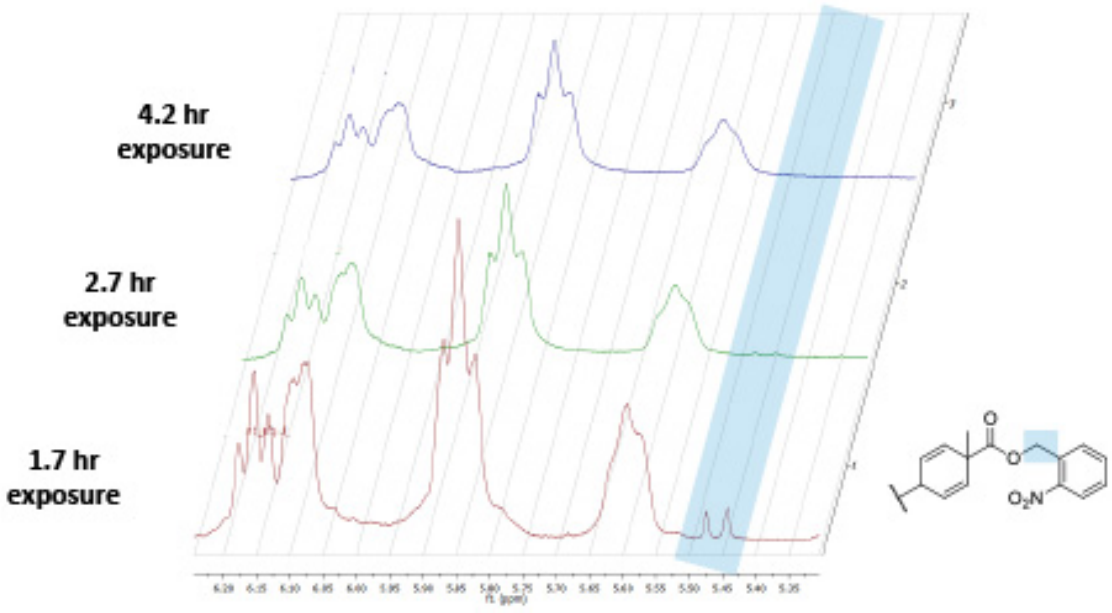

Figure 6.10: ^{1}H-NMR spectrum of o-nitrobenzyl capped polymer exposed to broadband UV light in deuterated acetonitrile monitoring the cleavage of the endcap.

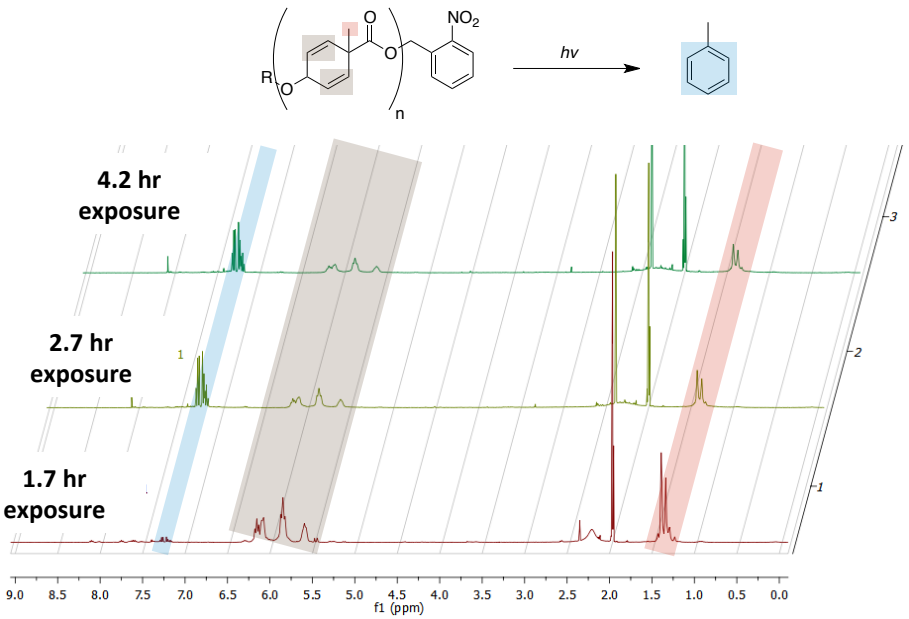

Figure 6.11: ^{1}H-NMR spectrum of o-nitrobenzyl capped polymer exposed to broadband UV light in deuterated acetonitrile monitoring the generation of toluene.

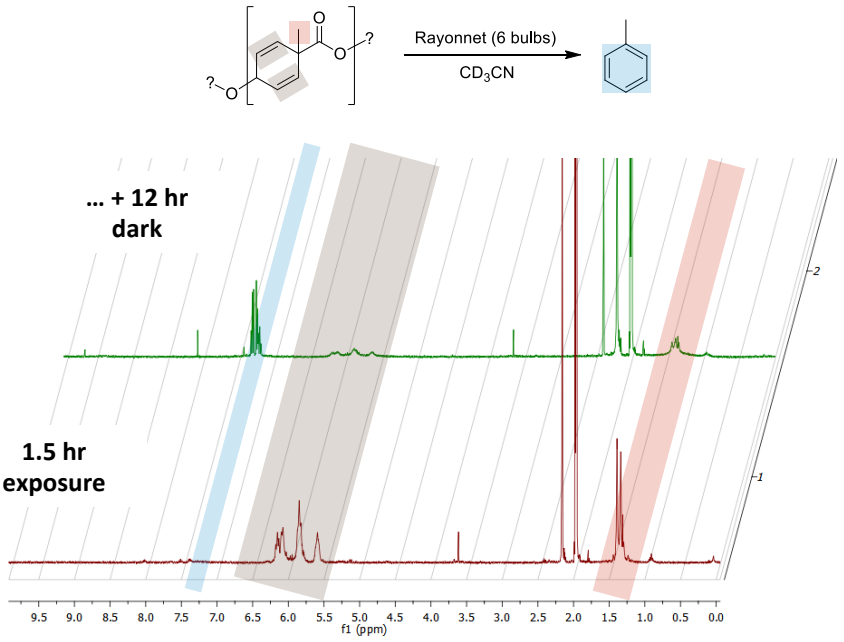

Figure 6.12: ^{1}H-NMR spectrum of the plain polyester polymer exposed to broadband UV light in deuterated acetonitrile monitoring the generation of toluene.

These results suggest that the cleavage of the end-cap results in the depolymerization and aromatization of the polymer. It was surprising to find that the control exposure study on the non-end capped polyester shows nearly identical depolymerization! Figure 6.12 shows that the end cap is not necessary for the polymer to aromatize into toluene. This is an incredibly exciting result, showing that the polymer backbone is inherently sensitive to UV exposure, which makes it an ideal unzipping polymer for EUV exposure.

6.6 THIN FILM EXPOSURE STUDY

After the promising results of the solution-based exposure study, the aromatizing polyester was tested in thin films. Silicon wafers were prepared with 72 nm films of Brewer ARC29A before 50 nm films of aromatizing polyester were deposited from a 5wt% solution in PMGEA. The contrast curve experiment was run in the same manner as explained in chapter 3.5, with a Cymer 248 nm KF excimer light source used for in-lab exposures. The results of the contrast curve are shown in Figure 6.13. The blue trace shows that even at very large doses >2,000 mJ/cm^2 the polymer only thins about 30 %. One concern is that the aromatizing polymer forms toluene, which is highly absorbent at 248 nm. Even still, this result shows that the polyester is not sensitive enough in thin film form to act as a single component resist at 248 nm.

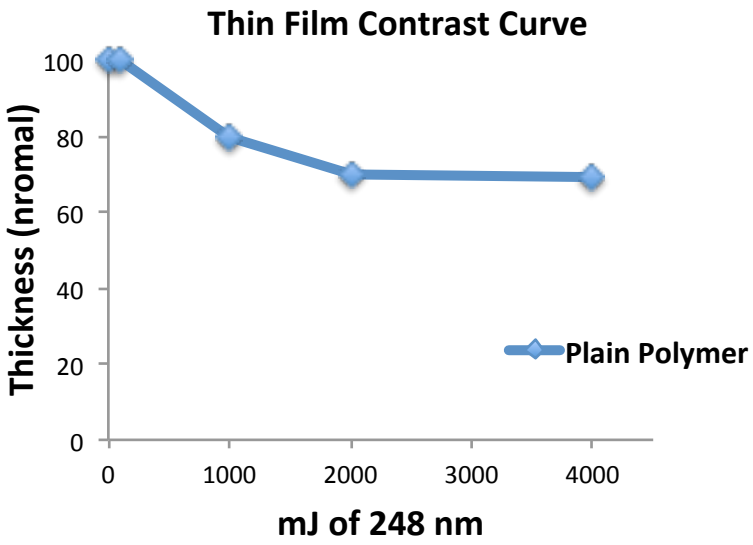

Figure 6.13: Percent film remaining vs. exposure to 248 nm light.

6.7 DISSOLUTION INHIBITION

The next stage of thin film studies examined the use of the aromatizing polyester as a polymeric dissolution inhibitor (PDI) in novolac. Novolac/Polyester formulations were made in PGMEA, cyclohexenone, and diglyme and the dissolution inhibition properties were studied as shown in Figure 6.14.

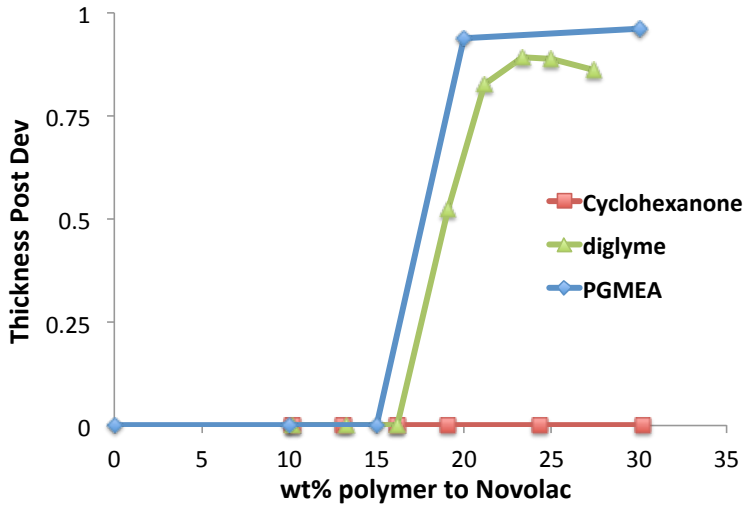

Figure 6.14: Percent film remaining vs aromatizing polyester wt % to novolac in various casting solvents.

For both PGMEA and digylme, 15 wt% polyester showed no inhibition of novolac in standard TMAH, 25 wt% inhibited with a 60 sec development. It is interesting to note that no dissolution inhibition is seen when using cyclohexenone as a casting solvent even at 30 wt% polyester to novolac. The effects of casting solvent on novolac dissolution is a known phenomenon and is believed to be related to the large amount of residual solvent that novolac retains after the post application bake.(*168*) The retention of the residual solvent is one reason why novolac is a common resist polymer to test phase compatibility with PDIs, as compatibility is often tunable via the casting solvent.

6.8 EUV EXPOSURE STUDY

EUV exposure experiments were preformed at Lawrence Berkeley National Laboratory's Advanced Light Source (ALS). Contrast curves were preformed on both polyester/novolac blends and plain polyester films cast at ~50 nm onto blank silicon wafers. Figure 6.15.A shows the contrast curve of 25 wt% polyester/novolac cast with PGME. The dose to clear is approximately 10 mJ/cm^2. The low dose response of our PDI resist was exciting, as it is an excellent proof-of-concept result. It is interesting to note that the aromatizing polyester/novolac blends crosslink at high dose (> 100 mJ) resulting in a negative tone behavior (Figure 6.15.B). This sort of cross-linking behavior has been reported with other mixed polyphenol systems such as poly(hydroxystyrene-co-*t*butylacrylate).(*169*)

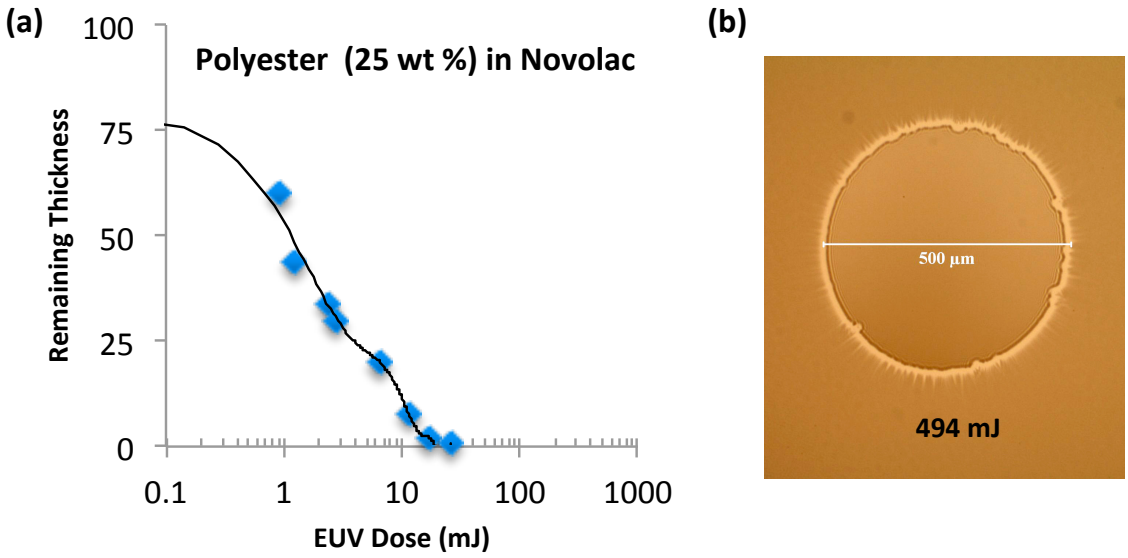

Figure 6.15: (a) EUV contrast curve of 25 wt% aromatizing polyester to novolac cast with PGMEA. (b) Image of cross-linked resist at high dose.

The dose-to-clear was also evaluated for the single component aromatizing polyester and found to be approximately 30 mJ/cm^2 for a 50 nm thick film. Unfortunately a proper contrast curve could not be measured as the sample partially destroyed upon shipment from California to Texas.

6.9 FUTURE WORK

Future EUV exposure studies are in the works in collaboration with Intel Portland. Extensive contrast curve studies exploring PDI loading and development screens are necessary to fully characterize and optimize the two-component resist. These studies are expected to take place within a few months of this publication. New resist materials are also in the works to study phase compatibility and dissolution inhibition. A polymer blend that does not crosslink is ideal for high sensitivity. The two fluorinated Promerous resists illustrated in Figure 6.16 will be screened. The fluorinated alcohols of these resists have similar pKa's to novolac and are efficiently inhibited by macromolecular DNQ derivatives.(*170*, *171*) These polynorobornene fluoroacetone (PNBFA) polymers were originally developed for 154 nm light sources. We suspect that the low MW of our PDI along with the similar pKa of the PNBFA will provide favorable conditions for phase compatibility.

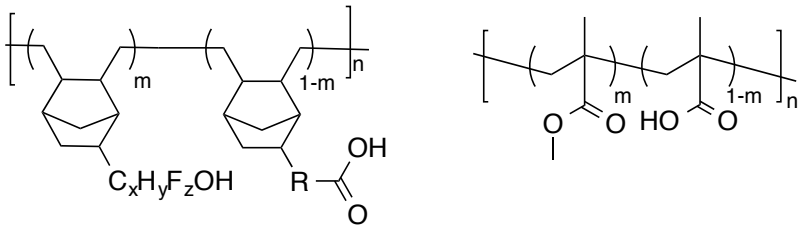

Figure 6.16: Illustrations of two resist polymers that will be screened for phase compatibility and dissolution inhibition.

The length of the aromatizing polyester also needs to be improved to increase the amplification of these resist systems. Ideally the size would be double what they are now (mw: ~3,000). Optimization studies are ongoing, and a new collaborative effort with the Phillips group to further screen Lewis acid and carbene-mediated transesterification is underway. A new synthetic strategy is being concurrently pursued in light of the fact that the polymer is inherently sensitive to EUV. The target monomers and resulting polymeric structure are shown in Figure 6.17.

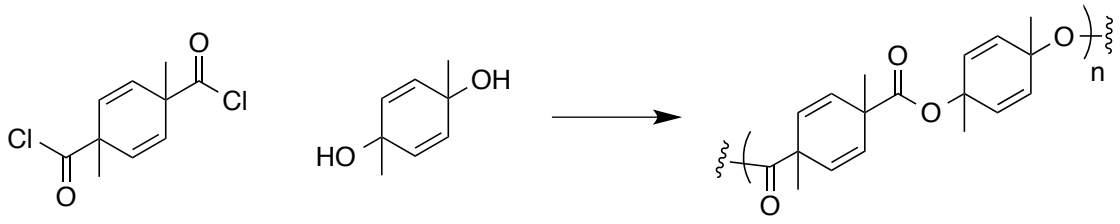

Figure 6.17: Illustration of modified aromatizing unzip poymer.

Chapter 7: Conclusion

The continuing delay of a powerful and stable EUV source has brought the microlithography industry to an impasse. Either a new ultra sensitive chemically amplified resist (CAR) must be created or a brand new method of lithography must be developed. New approaches to lithography such as nanoimprint and directed self-assembly (DSA) have made great gains in the past decade,(*27*, *172*) but the industry is hesitant to break away from the tried and true photolithography. Therefore the industry has adopted step-intensive double patterning processes such as litho-freeze, litho-etch (LFLE) to create structures below the resolution limit of current immersion 193 tools.(*173*) The flash memory market has optimized and utilized self-aligned double patterning (SADP)(*174*). With a modern fabrication, it takes a single microprocessor 30-60 days to go from bare silicon to the final product. The bottleneck of the entire process is the photolithographic steps, which account for up to 30% of the total cost of manufacturing.(*6*) Therefore doubling or tripling the number of lithographic steps drastically increases the cost of manufacturing. A new approach to increasing resolution of current 193 tools without extra processing steps or a new form of amplified EUV resist is greatly needed to drive down costs and keep pace with Moore's Law.

7.1 PITCHDIVISION LITHOGRAPHY

Pitchdivision is a resolution doubling process developed in the Willson labs,(*31*) which extends the capability of ArF lithography. The incorporation of both a photoacid generator (PAG) and photobase generator (PBG) into a standard 193 polymer matrix allows for a single exposure to double the line density of a grating mask. This doubling of the density allows for the Raleigh factor (k_1) to be below the hard physical limit of 0.25. The first successful demonstration of pitchdivision was shown by Dr. Xinyu Gu and Dr. Robert Bristol, with the printing of 110 nm lines and spaces from a 220 nm mask. This demonstration produced an effective k_1 of ~ 0.125!

Pitchdivision unfortunately suffers from severe line edge roughness (LER), which results from a convolution of a number of factors such as the quality of the aerial image at the high and low dose regions, standing wave phenomenon at high dose, and low chemical contrast. To ameliorate these factors, interference lithography tools were used to create true sinusoidal aerial images, film thickness was shrunk to minimize standing waves(*111*), and a new type of two-stage PBG was created to increase the slopes of the net acid production. By utilizing a sinusoidal aerial image along with a sharper net acid profile, the LER should be improved. This is because the acid concentration profile is determined by the aerial image in conjunction with the resist chemistry.

Before this project, there was limited published work on kinetically linked two-stage photoreactions,(*80*) despite significant interest in photoreactions where rate constants, k_1 and k_2 are approximately equal.(*20*, *21*, *81-84*) The combination of high interest and lack of antecedence meant that a multi-pronged approach was necessary.

Three separate classes of two-stage PBGs were synthesized: (i) an aromatizing PBG,(*87*, *88*) (ii) protected benzophenone and benzoin PBGs and (iii) symmetrical carbamates. In the end, the symmetrical carbamate PBGs proved to have similar k_1 and k_2 values (3 : 4) and showed a significant improvement in LER over the single stage variant.

7.1.1 Conclusions

The successful development of a number of two-stage PBGs was accomplished. In many cases, the unpredictable nature of photoreactions and side product formation proved to be a difficult challenge in the quantification of amine generation. Other times, such as the photoaromatization PBG, the kinetics of the first stage and second stage are too different to result in any real improvements in chemical contrast. Ultimately the best two-stage PBG in this study, was the first one imagined but, by far, the most elusive to synthesize. Through collaborative effort, CHA-BisNO2 was synthesized, and its model compound A-BisNO2 is the first reported kinetically matched two-stage photoreaction developed. This CHA-BisNO2 showed a marked improvement in imaging fidelity compared to the one-stage variant, CHA-NO2. In alignment with the original hypothesis, this improvement results from improved chemical contrast obtained through higher order kinetics. The initial delay of the two-stage PBG reaction allows for the resist to maintain more of its native chemical contrast in the low dose region. This also allows for increased PBG loadings that lead to sharper contrast in the high dose region. The optimized formulations used to print the images shown in Figures 4.73-4.75 have a difference in PBG loading of 233 %, resulting in a 60 % improvement in negative-tone LWR. Further

refinement of pitchdivision chemistry has even greater potential to improve the LER. Extensive modeling and screening of various PAGs to L-PBGs and the use of a higher boiling point amines would allow for a more uniform net acid production with decreased diffusion and evaporation of the base; although the effort for the reward may not be worth it in the end. In the fast paced world of semiconductor development, windows of opportunity are easily missed. Currently, industry trends are already focusing its sight on the sub 22 nm node and beyond, even significant improvements in pitchdivision lithography are not likely to allow it to print images at these resolutions.(*111*) In the end, a significant improvement in LWR and LER was realized through novel two-stage PBGs, which are the first kinetically matched cascade photoreactions.

7.2 UNZIPPING EUV RESISTS

EUV lithography demands very high resist sensitivity, much higher sensitivity than that of CAR formulations that are in use for 193 nm today. This higher sensitivity is required because a 193 nm resist that typically requires an imaging dose of ca. 20 mJ/cm^2 would require nearly 400 mJ/cm^2 of EUV radiation in order to capture the same number of incident photons per unit area, since EUV is so inherently photon limited. Using CARs for generating small features with weak EUV sources is challenging. The more you increase the sensitivity of the resist (> [PAG_0]), the more significant the bias.(*122*, *123*) The larger the bias, the larger the line-edge roughness. Adding quenchers to the resist formulation,(*125*) or tethering the catalyst to polymer chains(*126*) limits the blur and the bias, at the cost of speed.

This three way trade-off has been called many things, but the most memorable description is “The Triangle of Death”.(*127*) In this description, the area of the triangle that links resolution (bias), line-edge roughness, and speed is constant for a given CAR system. One can change the length of any of the legs of the triangle, but then the other two will change because these variables are not independent, thus area will always remain constant.

To escape the Triangle of Death, a new approach using dissolution inhibiting polymers that depolymerize upon exposure to EUV was explored. The breaking of the polymer bonds allows for large amplification without the need of catalysis. The basic proof of concept was previously demonstrated with polyphthalaldehyde (PPHA), PAG, and Novolac blends(*7*) and non-catalytically with pure PMMA resists.(*131*) The aim of the project is to marry these two examples together. To find a dissolution inhibiting system similar to the PPHA/Novolac blend with a polymer that is inherently sensitive to EUV such as PMMA.

7.2.1 Conclusions

A new aliphatic polyester was developed which self-immolates upon exposure to EUV to form toluene and carbon dioxide. This aromatizing polyester has shown promising early results. It effectively acts as a dissolution inhibitor for Novolac resins with an approximate dose to clear (E_0) of 11 mJ.

Future EUV exposure studies are in the works in collaboration with Intel. Extensive contrast curve studies exploring PDI loading and development screens are

necessary to fully characterize and optimize the two-component resist. These studies are expected to take place within a few months of this publication. New resist materials are also in the works to study phase compatibility and dissolution inhibition. A polymer blend that does not crosslink is ideal for high sensitivity. The two fluorinated Promerous resists illustrated in Figure 6.16 will be screened. The fluorinated alcohols of these resists have similar pKa's to novolac and are efficiently inhibited by macromolecular DNQ derivatives.(*170*, *171*) These polynorobornene fluoroacetone (PNBFA) polymers were originally developed for 154 nm light sources. We suspect that the low MW of our PDI along with the similar pKa of the PNBFA will provide favorable conditions for phase compatibility.

The length of the aromatizing polyester also needs to be improved to increase the amplification of these resist systems. Ideally the size would be double what they are now (mw: ~3,000). Optimization studies are ongoing, and a new collaborative effort with the Phillips group to further screen Lewis acid and carbene-mediated transesterification is underway. A new synthetic strategy is being concurrently pursued in light of the fact that the polymer is inherently sensitive to EUV. The target monomers and resulting polymeric structure are shown previously in Figure 6.17.

Appendix A: Synthesis and Characterization of Photobase Generators

The starting materials were purchased from Sigma-Aldrich Co. and used without further purification unless otherwise noted.

The intermediate compounds and the final products of the synthesis schemes were characterized with a variety of instruments. ^{1}H-NMR spectra were obtained on a Varian MR (400 MHz) or a Varian Unity spectrometer (300 MHz). All chemical shifts are reported in ppm and referenced to residual pronated solvents, such as $CDCl_3$ at 7.26 ppm and DMSO-d_6 at 2.54 ppm. ^{13}C-NMR spectra were recorded on a Varian MR (100 MHz) or a Varian Unity spectrometer (75 MHz) routinely with broadband decoupling, and all chemical shifts are referenced to residual solvents, such as $CDCl_3$ at 77.00 ppm and DMSO-d6 at 39.5 ppm. UV spectroscopy (UV-Vis) was performed on a HP UV-Vis spectrometer. IR spectroscopy (IR) was conducted on a Nicolet Magna-IR 500 with an extended compartment for reflective FTIR measurements. Melting temperatures of the intermediate species were collected on a Meltemp II apparatus in open capillary tubes.

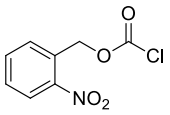

2-nitrobenzyl chloroformate:(*175*) To a cooled (0 °C) solution of triphosgene (23.505 g, 79.2 mmol) in dry toluene (125 mL) was added dropwise 2-nitrobenzyl alcohol (495 mL of a 1.6 M in THF, 79.2 mmol) over 40 minutes. The reaction was then stirred at RT for 4.5 hours and monitored by TLC. After completion of the reaction, the solvents were removed by reduced pressure to yield the product as a light green oil which was used without further purification. TLC R_f 0.86

(DCM); ^{1}H-NMR ($CDCl_3$, 400 MHz) δ 8.20 (d, J = 8.2 Hz, 1H), 7.66 (m, J = 32.3, 14.9, 7.4 Hz, 3H), 5.76 (s, 2H).

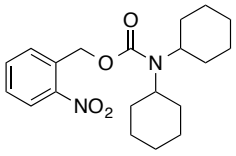

N,N-dicyclohexyl O-(2-nitrobenzyl)carbamate **(DCHA-NO2):**(*30*) O-nitrobenzyl alcohol (5.00 g, 32.6 mmol) was dissolved into 100 mL of distilled dioxane. The solution was cooled to 0 °C in an ice bath. To this solution was slowly added a solution of phosgene (20 % in toluene, 35.0 mL, 65.2 mmol). The reaction mixture was then allowed to heat up to 50 °C and stirred overnight. The mixture was evaporated, and the phosgene was quenched in a trap by a mixture of methanol and ammonia water. After evaporation, dicyclohexylamine (23.6 g, 26.0 mL, 130 mmol) was added dropwise, and the solution was stirred overnight. The mixture was added to a solution of sodium carbonate (100 mL, 10 wt.%) and extracted with ether (100 mL x2). The extract was successively washed with water twice and brine. After drying over anhydrous MgSO4, the solvent was evaporated. The residue was purified using column chromatography on silica gel with 1:15 ethyl acetate/hexane as the eluent. A yellow solid was obtained after evaporation (9.26 g, 25.4 mmol, 78.0 %); mp: 61 ~ 62 °C; ^{1}H-NMR (400 MHz; $CDCl_3$): δ 7.96 (dd, *J* = 8.2, 1.2 Hz, 1H), 7.58-7.54 (m, 1H), 7.48 (dd, *J* = 7.8, 1.1 Hz, 1H), 7.40-7.34 (m, 1H), 5.43 (s, 2H), 3.42-3.35 (m, 2H), 1.71-1.64 (m, 7H), 1.61-1.48 (m, 6H), 1.27-1.14 (m, 5H), 1.07-0.96 (m, 2H); ^{13}C-NMR (101 MHz; cdcl3): δ 154.7, 147.5, 133.5, 128.7, 128.2, 124.7, 63.1, 42.7, 31.3, 30.6, 26.1, 25.2, 22.6; IR (KBr, cm^{-1}): 1699, 1525, 1337; HR-MS (EI): calcd for $C_{20}H_{28}N_2O_4$ [M+H]+: 360.20491. Found: 360.2047.

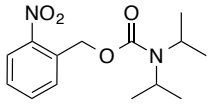

N,N-diisopropyl O-(2-nitrobenzyl)carbamate **(DIPA-NO2):** O-nitrobenzyl alcohol (5.00 g, 32.6 mmol) was dissolved into 100 mL of distilled dioxane. The solution was cooled to 0 ºC in an ice bath. To this solution was slowly added a solution of phosgene (20 % in toluene, 35.0 mL, 65.2 mmol). The reaction mixture was then allowed to heat up to 50 ºC and stirred overnight. The mixture was evaporated, and the phosgene was quenched in a trap by a mixture of methanol and ammonia water. After evaporation, diisopropylamine (13.1 g, 18.2 mL, 130 mmol) was added dropwise, and the solution was stirred overnight. The mixture was added to a solution of sodium carbonate (100 mL, 10 wt.%) and extracted with ether (100 mL x2). The extract was successively washed with water twice and brine. After drying over anhydrous MgSO4, the solvent was evaporated by reduced pressure. The residue was purified using column chromatography on silica gel with 1:15 ethyl acetate/hexane as the eluent. A yellow viscous liquid was obtained after evaporation (6.30 g, 22.5 mmol, 69.2 %). ^{1}H-NMR (400 MHz; $CDCl_3$): δ 7.98 (dd, *J* = 8.2, 1.2 Hz, 1H), 7.58 (td, *J* = 7.5, 1.1 Hz, 1H), 7.51-7.50 (m, 1H), 7.41-7.37 (m, 1H), 5.46 (s, 2H), 3.88 (t, *J* = 0.4 Hz, 2H), 1.18 (sextet, *J* = 7.7 Hz, 12H); ^{13}C-NMR (101 MHz; cdcl3): δ 154.5, 147.5, 133.6, 128.9, 128.3, 124.8, 63.1, 46.0, 20.9. IR (neat, cm^{-1}): 1675, 1525, 1275 cm^{-1}; HR-MS (EI): calcd for $C_{14}H_{21}N_2O_4$ [M+H]+: 281.1501. Found: 281.1502.

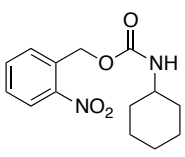

2-nitrobenzyl N-cyclohexylcarbamate **(CHA-NO2):**(*48*) To a solution of 2-nitrobenzyl alcohol (7.47 g, 48.78 mmol) in dry toluene (200 mL) was

added neat cyclohexyl isocyanate (6.85 mL, 53.66 mmol). After stirring under reflux for 48 hours (TLC), the solvent was removed by reduced pressure and replaced with Et_2O. The solution was washed twice with water, rinsed with brine, and dried over Na_2SO_4. Removal of Et_2O by reduced pressure afforded white-yellow solid as product (13.46 g, 48.4 mmol, 99.0 %). m.p. 104 °C - 106 °C; TLC R_f 0.51 (30% EtOAc/Hexanes); ^{1}H NMR (400 MHz, $CDCl_3$) δ 8.08 (dd, *J* = 8.2, 1.1 Hz, 1H), 7.69 – 7.54 (m, 2H), 7.46 (t, *J* = 7.6 Hz, 1H), 5.49 (s, 2H), 4.73 (s, 1H), 3.49 (s, 1H), 2.02 – 1.03 (m, 10H); ^{13}C NMR (101 MHz, $CDCl_3$) δ 154.88, 147.45, 133.63, 133.34, 128.85, 128.46, 124.91, 62.99, 50.03, 33.35, 25.42, 24.76; IR (neat): 3312, 2937, 2855, 1693, 1520, 1335, 1232, 1054, cm^{-1}; HRMS (ESI): Exact mass calcd for $C_{14}H_{18}N_2NaO_4$ $[M+Na]^+$: 301.11588. Found: 301.11634.

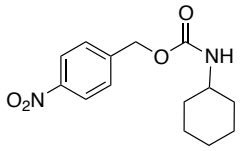

4-nitrobenzyl cyclohexylcarbamate:(*176*) To a solution of 4-nitrobenzyl alcohol (7.5 g, 49.0 mmol) in dry toluene (210 mL) was added neat cyclohexyl isocyanate (6.9 mL, 54.0 mmol). After stirring under reflux for 48 hours, the solvent was removed by reduced pressure and replaced with Et_2O. The solution was washed twice with water, rinsed with brine, and dried over Na_2SO_4. Removal of Et_2O by reduced pressure afforded white-yellow solid as product (12.9 g, 46.5 mmol, 95.0 %). TLC R_f 0.42 (20 % EtOAc/Hex); ^{1}H-NMR (400 MHz; $CDCl_3$): δ 8.21 (d, J = 8.6 Hz, 2H), 7.51 (d, J = 8.6 Hz, 2H), 5.25-5.18 (m, 2H), 4.77-4.71 (m, 1H), 3.54-3.46 (m, 1H), 1.97-1.93 (m, 2H), 1.72 (dq, J = 13.2, 4.0 Hz, 2H), 1.65-1.58 (m, 1H), 1.41-1.30 (m, 2H), 1.23-1.11 (m, 3H). ^{13}C-NMR (101 MHz; cdcl3): δ

155.0, 147.5, 144.2, 128.0, 123.7, 64.9, 50.1, 33.3, 25.4, 24.7. HRMS (ESI): Exact mass calcd for $C_{14}H_{18}N_2NaO_4$ $[M+Na]^+$: 301.11643. Found: 301.11588.

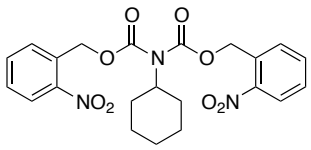

Bis(2-nitrobenzylcarboxy)cyclohexylamine **(CHA-BisNO2):** To a cooled (0 °C) solution of 2-nitrobenzyl cyclohexylcarbamate (11.02 g, 39.6 mmol) in dry toluene (475 mL) was added dropwise $KN(TMS)_2$ (83.2 mL of 0.5 M tol sol, 41.6 mmol) over 23 minutes. After stirring for 10 minutes, 2-nitrobenzyl chloroformate (198 mL of 4.0 M tol sol, 79.2 mmol) was added dropwise over 33 minutes. The reaction was then allowed to warmed to RT and stirred for 14 hours (TLC), concentrated by reduced pressure, and ran through a short plug of silica (DCM). Further purification by flash column chromatography (50% DCM/toluene) and recrystallization ($MeOH/H_2O$ then EtOAc/Hexanes) yielded white solid as product (3.08 g, 6.73 mmol, 17.0 %). m.p. 103 °C - 105 °C; TLC R_f 0.69 (DCM); ^1H NMR (400 MHz, $CDCl_3$) δ 8.11 (d, J = 8.1 Hz, 2H), 7.63 (dt, J = 14.8, 7.3 Hz, 4H), 7.49 (t, J = 7.6 Hz, 2H), 5.66 (s, 4H), 4.14 (tt, J = 11.6, 3.4 Hz, 1H), 2.01 – 1.58 (m, 7H), 1.21 (dq, J = 80.2, 13.2 Hz, 3H); ^{13}C NMR (101 MHz, $CDCl_3$) δ 153.49, 147.30, 133.89, 131.70, 129.09, 128.91, 125.09, 65.37, 58.74, 30.17, 26.20, 25.13; IR (neat): 2933, 2857, 1731, 1707, 1524, 1341, 1215, 1093, 727 cm^{-1}; HRMS (ESI): Exact mass calcd for $C_{22}H_{23}N_3NaO_8$ $[M+Na]^+$: 480.13774. Found: 480.13819.

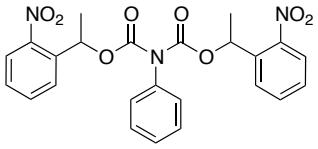

Bis(1-(2-nitrophenyl)ethylcarboxy)aniline **(A-BisMeNO2):** To a cooled (0 °C) solution of (2-nitrophenyl)ethyl phenylcarbamate (4.0 g, 14.0 mmol, 1 eq) in dry toluene (100 mL) was added dropwise $LiN(TMS)_2$ (2.6 g in 50 mL toluene, 15.4 mmol, 1.1 eq) over 6 minutes. After stirring for 10 minutes, 1-(2-nitrophenyl)ethyl chloroformate (6.4 g in 50 mL toluene, 28.0 mmol, 2 eq) was added dropwise over 26 minutes. The reaction was then allowed to warmed to RT and stirred for 16 hours (TLC), concentrated in vacuo, and ran through a short plug of silica (DCM). Further purification by flash column chromatography (100% DCM -> 20% EtOAc) and recrystallization (EtOAc/Hexanes) yielded white solid as product (2.5 g, 37 %). m.p. 115-123 °C; TLC R_f 0.6 (DCM); ^{1}H-NMR (400 MHz; $CDCl_3$): δ 7.96 (dt, J = 8.2, 1.6 Hz, 2H), 7.58-7.51 (m, 2H), 7.48-7.38 (m, 5H), 7.32-7.27 (m, 2H), 7.20-7.16 (m, 2H), 6.43 (quintet, J = 6.2 Hz, 2H), 1.61-1.56 (m, 6H); ^{13}C-NMR (101 MHz; CDCl3): δ 156.3, 147.7, 138.7, 133.9, 128.5, 127.3, 124.6, 68.9, 22.3; IR (neat): 1794, 1749, 1519, 1258, 1057, cm^{-1} HRMS (ESI): Exact mass calcd for $C_{24}H_{21}N_3O_8$ $[M+Na]^+$: 502.12263. Found: 502.12235.

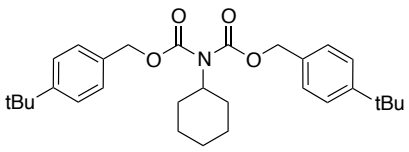

Bis(4-tert-butylbenzylcarboxy)cyclohexylamine: To a cooled (0 °C) solution of 4-tert-butylbenzyl cyclohexylcarbamate (1.0 g, 3.5 mmol, 1 eq) in dry toluene (20 mL) was added dropwise $KN(TMS)_2$ (7.3 mL of a 0.5 M in toluene, 3.6 mmol) over 20 minutes. After stirring for 10 minutes, 4-tertbutylbenzyl chloroformate (2.3g of 1 M tol sol, 10.4 mmol) was added dropwise over 30 minutes. The reaction was

warmed to RT, stirred for 16 hours (TLC), and concentrated by reduced pressure. Purification by flash column chromatography (100% hexanes) provided the product as a clear oil (1.5 g, 3.2 mmol, 90.0 %). TLC R_f 0.62 (5% EtOAc/Hex); ^{1}H-NMR (400 MHz; $CDCl_3$): δ 7.42-7.40 (dt, J = 2.1, 8.6 Hz, 4H), 7.33-7.30 (dt, *J* = 2.1, 8.6 Hz, 4H), 5.22 (s, 4H), 4.16 (tt, *J* = 12.1, 3.6 Hz, 1H), 1.96 (td, *J* = 12.4, 3.7 Hz, 2H), 1.84-1.77 (m, 4H), 1.66-1.60 (m, 1H), 1.37-1.35 (m, 19H), 1.29 (m, 1H), 1.16-1.05 (m, 1H).; ^{13}C-NMR (101 MHz; cdcl3): δ 154.2, 151.3, 132.4, 128.1, 68.4, 58.1, 34.6, 31.5, 30.2, 26.3, 25.3; IR (neat): 1296, 1743, 1702, 1322, 1213, 1085 cm^{-1}; HRMS (ESI): Exact mass calcd for $C_{22}H_{23}N_3NaO_8$ $[M+Na]^+$: 480.13774. Found: 480.13819.

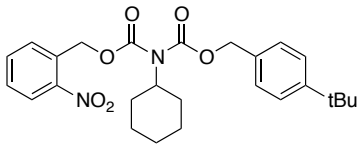

N-4-tert-butylbenzylcarboxy, N-2-nitrobenzylcarboxy cyclohexylamine: To a cooled (0 °C) solution of 4-tertbutyl cyclohexylcarbamate (140 mg, 0.50 mmol) in dry toluene (8 mL) was added dropwise $KN(TMS)_2$ (1.0 mL of 0.5 M tol sol, 0.52 mmol) over 23 minutes. After stirring for 10 minutes, 2-nitrobenzyl chloroformate (213 mg, 0.99 mmol) in 5 mL tol was added dropwise over 10 minutes. The reaction was then allowed to warmed to RT and stirred for 14 hours (TLC), concentrated by reduced pressure, and ran through a short plug of silica (DCM). Further purification by flash column chromatography (50% DCM/toluene) and recrystallization ($MeOH/H_2O$ then EtOAc/Hexanes) yielded white solid as product (166 mg, 0.35 mmol, 71.0 %).^{1}H-NMR (400 MHz; $CDCl_3$): δ 8.11 (dd, *J* = 7.9, 1.6 Hz, 1H), 7.64-7.62 (m, 1H), 7.49-7.44 (m,

2H), 7.37-7.26 (m, 5H), 5.63 (s, 2H), 5.23 (s, 2H), 4.14 (ddd, *J* = 9.0, 7.2, 6.7 Hz, 1H), 1.95-1.78 (m, 8H), 1.32-1.29 (m, 12H), 1.15-1.08 (m, 2H); 13-C NMR (101 MHz; CDCl3): δ 154.4, 153.9, 151.7, 147.1, 134.2, 132.3, 129.1, 128.8, 128.5, 125.9, 125.3, 68.9, 65.2, 58.6, 34.9, 31.5, 30.1, 26.9, 25.5; IR (neat): 2937, 1741, 1706, 1528, 1318, 1216 cm^{-1}; HRMS (ESI): Exact mass calcd for $C_{26}H_{33}N_2O_6$ [M+H]+: 469.2339. Found: 469.2346.

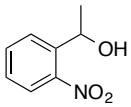

2-nitrophenyl ethanol:(*177*) To a cooled (0 °C) solution of 1-(2-nitrophenyl)ethanone (100 g, 605 mmol) in methanol (500 mL) was slowly added sodium borohydride (68.7 g, 1.82 mmol) in small portions over 35 minutes. The reaction was then allowed to warm to RT and stirred for 3 hours (TLC). Afterwards, the reaction was cooled to 0 °C and carefully quenched with water followed by 1 M HCl. The reaction mixture was concentrated by reduced pressure and resuspended in 1 L of Et_2O. The solution was washed with 3 M HCl, saturated $NaHCO_3$, rinsed with brine, and dried over Na_2SO_4. Removal of Et_2O by reduced pressure followed by bump distillation afforded pale yellow oil as product (90.3 g, 546 mmol, 90.3%). TLC R_f 0.41 (DCM); ^1H NMR (400 MHz, $CDCl_3$) δ 7.90 (dd, J = 8.2, 1.3 Hz, 1H), 7.84 (dd, J = 7.9, 1.4 Hz, 1H), 7.65 (td, J = 7.9, 1.3 Hz, 1H), 7.46 – 7.39 (m, 1H), 5.42 (q, J = 6.3 Hz, 1H), 2.43 (s, 1H), 1.57 (d, J = 6.4 Hz, 3H); ^{13}C NMR (101 MHz, $CDCl_3$) δ 147.80, 140.87, 133.62, 128.11, 127.55, 124.30, 65.55, 24.17; IR (neat): 3359, 2979, 2933, 2871, 1519, 1344, 1071, 855, 787, 745 cm^{-1}; HRMS (CI): Exact mass calcd for $C_8H_9NO_3$ $[M]^-$: 167.0582. Found: 167.0583.

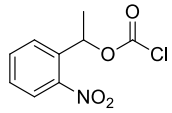

1-(2-nitrophenyl)ethyl chloroformate:(*178*) To a cooled (0 °C) solution of 2-nitrophenyl ethanol (0.858 g, 5.13 mmol) in dry THF (25 mL) was rapidly added 15% (w/w) phosgene in toluene (10.26 mL, 15.39 mmol) in one portion. The reaction was then allowed to warm to RT and stirred for 36 hours (TLC). After completion of the reaction, the solvents were removed by reduced pressure to give the product as a light green oil which was used without further purification. TLC R_f 0.68 (30% EtOAc/Hexanes); ^{1}H NMR (400 MHz, $CDCl_3$) δ 8.04 (d, J = 8.0 Hz, 1H), 7.77 – 7.66 (m, 2H), 7.52 (t, J = 6.8 Hz, 1H), 6.46 (q, J = 6.2 Hz, 1H), 1.77 (d, J = 6.4 Hz, 3H).

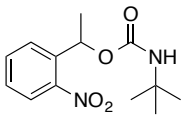

1-(2-nitrophenyl)ethyl tert-butylcarbamate **(TBA-MeNO2):** To a solution of 2-nitrophenyl ethanol (1.50 g, 8.97 mmol) in dry toluene (42 mL) was added t-butyl isocyanate (1.12 mL, 9.87) and titanium(IV) tetra-t-butoxide (2.7 mL of a 0.56 M in toluene, 1.5 mmol). After stirring at RT for 32 hours, the solution was concentrated by reduced pressure and purified by flash column chromatography (20% EtOAc/Hexanes) to yield pale yellow solid as product (1.28g, 54%). m.p. 83 °C - 86 °C; TLC R_f 0.59 (30% EtOAc/Hexanes); ^{1}H NMR (400 MHz, $CDCl_3$) δ 7.94 (d, J = 8.1 Hz, 1H), 7.62 (d, J = 3.1 Hz, 2H), 7.41 (ddd, J = 8.4, 5.6, 3.2 Hz, 1H), 6.23 (dd, J = 12.1, 5.8 Hz, 1H), 4.74 (s, 1H), 1.59 (d, J = 6.1 Hz, 3H), 1.28 (s, 9H); ^{13}C NMR (101 MHz, $CDCl_3$) δ 153.49, 147.37, 139.12, 133.46, 127.99, 126.96, 124.47, 67.88, 50.46, 28.86, 22.37. IR (neat): 3398, 3345, 2974, 2935, 2873, 1703, 1522, 1085, 1068, 744 cm^{-1};

HRMS (ESI): Exact mass calcd for $C_{13}H_{18}N_2NaO_4$ $[M+Na]^+$: 289.11588. Found: 289.11588.

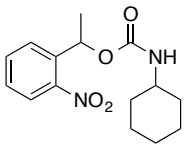

1-(2-nitrophenyl)ethyl cyclohexylcarbamate **(CHA-MeNO2):**(*48*) To a solution of 2-nitrophenyl ethanol (5.00 g, 29.9 mmol) in dry toluene (140 mL) was added cyclohexyl isocyanate (4.20 mL, 32.9 mmol). The reaction mixture was stirred at 115 °C under reflux for 48 hours. Afterwards, toluene was removed by reduced pressure and the residue was resuspended in 250 mL of Et_2O. The solution was washed successively with water (x2), brine, and dried over Na_2SO_4. Removal of Et_2O by reduced pressure followed by flash column chromatography (EtOAc/Hexanes) afforded a pale yellow oil as product (6.28 g, 71.9%). TLC R_f 0.51 (30% EtOAc/Hexanes); ^{1}H-NMR (400 MHz, $CDCl_3$) δ 7.91 (d, J = 8.1 Hz, 2H), 7.70 – 7.57 (m, 4H), 7.45 – 7.36 (m, 2H), 6.23 (q, J = 6.3 Hz, 2H), 4.86 (d, J = 7.5 Hz, 2H), 3.58 – 3.22 (m, 2H), 2.05 – 0.98 (m, 27H); ^{13}C-NMR (101 MHz, $CDCl_3$) δ 154.50, 147.52, 138.92, 133.51, 128.05, 127.09, 124.25, 68.19, 49.85, 33.26, 25.38, 24.77, 22.24; IR (neat): 3400, 3316, 2931, 2854, 1694, 1522, 1344, 1227, 1063, 747 cm^{-1}; HRMS (ESI): Exact mass calcd for $C_{15}H_{21}N_2NaO_4$ $[M+Na]^+$: 315.13153. Found: 315.13150.

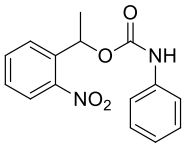

1-(2-nitrophenyl)ethyl phenylcarbamate **(A-MeNO2):** To a cooled (0 °C) solution of 1-(2-nitrophenyl)ethyl chloroformate (2.02 g, 8.97 mmol) in dry THF (20 mL) and dry toluene (20 mL) was added aniline (1.64 mL, 17.9 mmol) dropwise over 2 minutes. After stirring for 10 minutes at 0 °C, triethylamine (3.00 mL,

21.5 mmol) was added dropwise over 2 minutes. The reaction was warmed to RT and stirred for 22h (TLC). The reaction was concentrated by reduced pressure and the residue was resuspended in 125 mL of Et_2O. The solution was washed successively with NH_4Cl (x2), water, brine, and dried over Na_2SO_4. The organic layer was concentrated by reduced pressure and purified by flash column chromatography (DCM) to yield a pale yellow solid as product (2.24 g, 7.82 mmol, 87.2 %). m.p. 78 °C - 80 °C; TLC R_f 0.68 (DCM), 0.50 (30% EtOAc/Hexanes); ^{1}H-NMR (400 MHz, $CDCl_3$) δ 7.95 (d, J = 8.2 Hz, 1H), 7.75 – 7.56 (m, 2H), 7.42 (t, J = 6.9 Hz, 1H), 7.33 (d, J = 8.1 Hz, 2H), 7.31 – 7.24 (m, 2H), 7.05 (t, J = 7.3 Hz, 1H), 6.72 (s, 1H), 6.37 (q, J = 6.5 Hz, 1H), 1.69 (d, J = 6.5 Hz, 3H); ^{13}C-NMR (101 MHz, $CDCl_3$) δ 152.20, 147.55, 138.30, 137.48, 133.63, 129.05, 128.35, 127.02, 124.53, 123.63, 118.57, 69.12, 22.21; IR (neat): 3357, 3319, 3064, 2982, 2936, 2872, 1713, 1523, 1221, 746 cm^{-1}; HRMS (ESI): Exact mass calcd for $C_{15}H_{15}N_2NaO_4$ $[M+Na]^+$: 309.08458. Found: 309.08458.

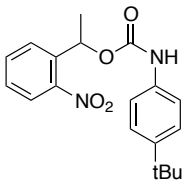

1-(2-nitrophenyl)ethyl 4-tert-butylphenylcarbamate: To a cooled (0 °C) solution of 1-(2-nitrophenyl)ethyl chloroformate (0.90 g, 3.9 mmol) in dry THF (20 mL) was added 4-tert-butylaniline (0.85 mL, 7.8 mmol) dropwise over 2 minutes. After stirring for 10 minutes at 0 °C, triethylamine (1.1 mL, 7.8 mmol) was added dropwise over 2 minutes. The reaction was warmed to RT and stirred for 22 hours (TLC). The reaction was concentrated by reduced pressure and the residue was resuspended in 50 mL of Et_2O. The solution was washed successively with NH_4Cl (x2), water, brine, and dried over Na_2SO_4. The organic layer was concentrated by reduced

pressure and purified by flash column chromatography (10% EtOAc/Hex) and recrystallization from EtOH to yield the product as an orange crystalline solid (0.31 g, 0.9 mmol, 23.1 %). TLC R_f 0.47 (30% EtOAc/Hexanes); ^{1}H-NMR (400 MHz; $CDCl_3$): δ 7.96 (dd, *J* = 8.2, 1.3 Hz, 1H), 7.66-7.61 (m, 2H), 7.44-7.40 (m, 1H), 7.31-7.24 (m, 4H), 6.65 (dd, *J* = 0.7, 0.4 Hz, 1H), 6.36 (d, *J* = 6.5 Hz, 1H), 1.68 (d, *J* = 6.5 Hz, 3H), 1.28 (s, 9H); ^{13}C-NMR (101 MHz; cdcl3): δ 147.5, 146.6, 138.4, 134.8, 133.7, 128.3, 127.0, 125.8, 124.6, 34.3, 31.2, 22.2; IR (neat): 3318, 2960, 1711, 1521, 1342, 1216, 1061 cm^{-1}; HRMS (ESI): Exact mass calcd for $C_{19}H_{22}N_2NaO_4$ $[M+Na]^+$: 365.14773. Found: 365.14704.

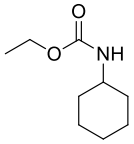

Ethyl cyclohexylcarbamate:(*179*) To a cooled (-78 °C) solution of cyclohexylamine (13.8 mL, 120 mmol) and triethylamine (33.5 mL, 240 mmol) in dry THF (105 mL) was added dropwise ethyl chloroformate (9.52 mL, 100 mmol). The reaction was allowed to warm to RT and stirred for 20 hours (GC-FID). The crude reaction mixture was filtered, the residue was washed with Et_2O. The filtrate was concentrated by reduced pressure and resuspended with 250 mL Et_2O and 100 mL EtOAc. The solution was washed successively with sat. NH_4Cl (x2), water, brine and dried over Na_2SO_4. Removal of the solvent by reduced pressure afforded a white solid as product (10.42 g, 75.2 mmol, 62.7%). ^{1}H NMR (400 MHz, $CDCl_3$) δ 4.55 (s, 1H), 4.11 (td, J = 13.9, 6.9 Hz, 2H), 3.47 (s, 1H), 2.04 – 1.50 (m, 6H), 1.44 – 1.00 (m, 7H).

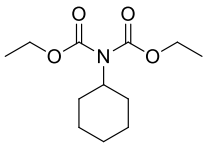

Bis(ethylcarboxy)cyclohexylamine:(*180*) To a cooled (-78 °C) solution of ethyl cyclohexylcarbamate (10.4 g, 60.7 mmol) in dry THF (210 mL) was added dropwise *n*butyllithium (24.5 mL of a 2.5 M in hexanes, 61.3 mmol) over 7 minutes. The reaction was stirred for 3 minutes at -78 °C and ethyl chloroformate (6.60 mL, 69.3 mmol) was added over 2 minutes. The reaction was allowed to warm to RT and stirred for 1 hour. The solution was distilled under reduced pressure to afford a clear oil (13.3 g, 54.7 mmol, 90.1%). ^{1}H NMR (400 MHz, $CDCl_3$) δ 4.20 (q, J = 7.1 Hz, 4H), 4.01 (ddt, J = 15.7, 11.9, 3.7 Hz, 1H), 1.92 – 1.52 (m, 7H), 1.35 – 1.18 (m, 8H), 1.15 – 0.99 (m, 1H). ^{13}C NMR (101 MHz, $CDCl_3$) δ 154.32, 62.64, 57.62, 30.26, 26.22, 25.29, 14.10; IR (neat): 1745, 1704, 1319, 1215, 1091 cm^{-1}.

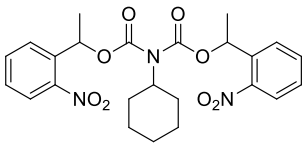

Bis(1-(2-nitrophenyl)ethylcarboxy)cyclohexylamine **(CHA-BisMeNO2):** To a solution of 2-nitrophenyl ethanol (3.34 g, 20.0 mmol) and finely crushed 5 Å molecular sieves (15 g) in dry toluene (15 mL) was added titanium tetrachloride (1.00 mL of 1M tol sol, 1.00 mmol). The reaction was stirred at RT for 15 minutes and bis(ethylcarboxy)cyclohexylamine (486 mg, 2.00 mmol) was added. After stirring at RT for 24 hours, the crude reaction mixture was filtered and the residue washed with toluene. The filtrate was concentrated by reduced pressure and purified by flash column chromatography (DCM then EtOAc/Hexanes) to afford a white powder as product (0.284 g, 5.84 mmol, 29.2 %). TLC R_f 0.43 (20% EtOAc/Hexanes); ^{1}H NMR (400 MHz, $CDCl_3$) δ 8.01 – 7.92 (m, 2H), 7.72 – 7.57 (m, 4H), 7.50 – 7.38 (m, 2H), 6.37 (dq, J = 10.5, 6.5 Hz, 2H), 4.05 – 3.93 (m, 1H), 1.93 – 1.49 (m, 13H), 1.30 –

0.96 (m, 3H); IR (neat): 2933, 1731, 1707, 1524, 1341, 1215, 727 cm^{-1}; HRMS (ESI): Exact mass calcd for $C_{24}H_{27}N_3NaO_8$ $[M+Na]^+$: 508.16904. Found: 508.16889.

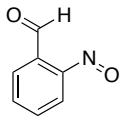

2-nitrosobenzaldehyde:(*49*) To a cooled (-30 ºC) solution of 2-nitrobenzyl alcohol (0.60 g, 3.9 mmol) and 2,6-di-tert-butyl-4-methylpyridine (0.88 g, 4.3 mmol) in dry DCM (15 mL) was added dropwise triflateanhydride (0.66 mL in 20 mL DCM, 3.9 mmol) over 30 minutes. The reaction was warmed to 0 ºC and stirred for 20 minutes before quenching with aq. $NaHCO_3$ (20 mL). The organic layer was washed with H_2O (20 mL) and brine (20 mL), dried ($MgSO_4$), filtered, and concentrated by reduced pressure. The crude oil was purified by flash chromatography (27% EtOAc/Hex) to yield a light green solid (0.50 g, 95%) R_f 0.48 (20% EtOAc/Hex); ^{1}H-NMR (400 MHz; $CDCl_3$): δ 12.08 (s, 1H), 8.23-8.21 (dd, J = 8, 0.9, 1H), 7.91 (t, J = 7.5 Hz, 1H), 7.70-7.66 (td, J = 7.4, 1.2, 1H), 6.43 (dd, J = 8.1, 0.6 Hz, 1H).^{13}C-NMR (101 MHz; $CDCl_3$): δ 193.61, 162.24, 136.77, 134.28, 132.84, 127.86, 106.60.

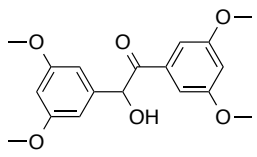

Tetramethoxybenzoin **(MBen)**: The compound was synthesized following the procedure outlined by Cameron and co-workers.(*58*) ^{1}H-NMR (400 MHz; $CDCl_3$): δ 7.05 (d, *J* = 2.2 Hz, 2H), 6.60 (t, *J* = 2.3 Hz, 1H), 6.46 (d, *J* = 2.3 Hz, 2H), 6.35 (t, *J* = 2.2 Hz, 1H), 5.79 (d, *J* = 6.2 Hz, 1H), 4.48 (dd, *J* = 6.2, 0.2 Hz, 1H), 3.75 (d, *J* = 12.7 Hz, 12H); ^{13}C-NMR (101 MHz; cdcl3): δ 198.4, 161.2, 160.7, 141.1, 135.1, 106.8, 106.3, 105.7, 100.5, 76.3, 55.53, 55.35.

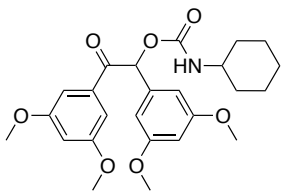

Tetramethoxybenzoin cyclohexylcarbamate **(CHA-MBen):** The compound was synthesized following the procedure outlined by Cameron and co-workers.(*58*) ^{1}H-NMR (400 MHz; $CDCl_3$): δ 7.09 (d, *J* = 2.3 Hz, 2H), 6.67 (s, 1H), 6.59 (t, *J* = 2.0 Hz, 3H), 6.40 (t, *J* = 2.3 Hz, 1H), 4.93-4.91 (m, 1H), 3.76 (d, *J* = 9.7 Hz, 12H), 3.50-3.46 (m, 1H), 1.99-1.89 (m, 2H), 1.99-1.89 (m, 2H), 1.68 (d, *J* = 0.6 Hz, 2H), 1.60-1.54 (m, 2H), 1.31-1.30 (m, 2H), 1.17-1.15 (m, 3H); ^{13}C-NMR (101 MHz; cdcl3): δ 198.4s, 161.1, 136.5, 136.0, 106.6, 106.0, 101.2, 55.50, 55.35, 49.7, 33.1, 25.4, 24.8.

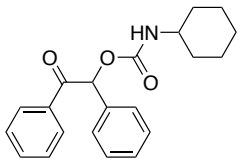

Benzoin cyclohexylcarbamate **(CHA-Ben):** The compound was synthesized following the procedure outlined by Cameron and co-workers.(*58*) A flame-dried flask equipped with a reflux condenser and a magnetic stirbar was charged with a solution of benzoin (8.00 g, 37.2 mmol, 1 eq), cyclohexyl isocyanate (5.30 mL, 41.5 mmol, 1.1 eq) and dry toluene (300 mL) and refluxed for 72 h. The reaction solution was diluted with Et_2O and washed with H_2O. The desired compound was recrystallized from Hex and EtOAc to give white crystals (7.9 g, 23.8 mmol 64.0 %). m.p. 110-150 ºC; ^{1}H-NMR (400 MHz; cdcl3): δ 7.97-7.94 (m, 2H), 7.52-7.45 (m, 3H), 7.41-7.31 (m, 5H), 6.85 (s, 1H), 4.95 (d, J = 7.8, 1H), 3.52-3.43 (m, 1H), 1.97-1.87 (m, 2H), 1.71-1.54 (m, 3H), 1.37-1.08 (m, 5H); ^{13}C-NMR (101 MHz; cdcl3): δ 195.1, 154.7, 134.8, 134.1, 133.3, 129.17, 129.02, 128.8, 128.5, 50.1, 33.2, 25.4, 24.6; HRMS (CI): Exact mass calcd for $C_{21}H_{23}NNaO_3$ [M+Na]+: 360.15756. Found: 360.15725.

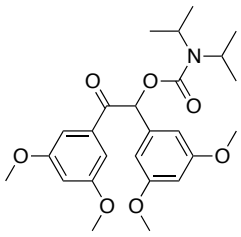

Tetramethoxybenzoin diisopropylcarbamate **(DIPA-MBen):** MBen (4.19 g, 12.6 mmol) was dissolved into 35 mL of toluene. The solution was cooled to 0 °C in an ice bath. To this solution was slowly added a solution of diisopropyl chlorocarbonate (6.19 g, 37.8 mmol, in 15 mL toluene). The reaction mixture was refluxed and stirred overnight before diluting with Et_2O and washing successively with sat. NH_4Cl (x2), water, brine, and drying with Na_2SO_4. The organic layer was concentrated by reduced pressure and the residue was purified by crystallization from EtOAc/Hex to afford the product as a white crystalline solid. (4.13 g, 8.99 mmol, 71.3 %); ^{1}H-NMR (400 MHz; $CDCl_3$): δ 7.11 (d, *J* = 2.3 Hz, 2H), 6.72 (s, 1H), 6.63 (d, *J* = 2.1 Hz, 2H), 6.58 (t, *J* = 2.3 Hz, 1H), 6.40 (t, *J* = 2.3 Hz, 1H), 3.76 (d, *J* = 7.5 Hz, 12H), 1.22-1.18 (m, 12H); ^{13}C-NMR (101 MHz; cdcl3): δ 194.6, 161.0, 160.6, 154.2, 136.9, 136.4, 106.6, 105.6, 99.7, 77.6, 77.2, 55.3; IR (neat): 1690, 1594, 1294, 1205, 1156 cm^{-1}; HRMS (CI): Exact mass calcd for $C_{25}H_{33}NO_7$ [M]+: 459.2257. Found: 459.2254.

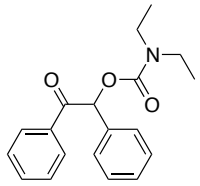

Benzoin diethylcarbamate **(DE-Ben):** Benzoin (4.00 g, 18.8 mmol) was dissolved into 20 mL of toluene. The solution was cooled to 0 °C before adding pyridine (3.00 mL, 37.7 mmol). To this solution was slowly added diethyl carbamoylchloride (11.9 mL, 94.23 mmol). The reaction mixture was refluxed and stirred overnight before diluting with Et_2O and washing successively with sat. NH_4Cl (x2), water, brine, and drying with Na_2SO_4. The organic layer was

concentrated by reduced pressure and the residue was purified by crystallization from ethanol to afford the product as a white crystalline solid. (2.40 g, 7.71 mmol, 41.0 %). m.p. 115-117 ºC; ^{1}H-NMR (400 MHz; cdcl3): δ 7.98-7.95 (m, 2H), 7.52-7.46 (m, 3H), 7.42-7.29 (m, 5H), 6.85 (s, 1H), 3.43-3.25 (m, 4H), 1.27-1.09 (m, 6H). 13-C NMR (75 MHz; cdcl3): δ 195.27, 155.05, 135.01, 134.32, 133.22, 128.91, 128.78, 128.55, 128.37, 77.59, 42.06, 41.64, 13.98, 13.43; IR (neat): 2975, 1689, 1426, 1166 cm^{-1}; HRMS (CI): Exact mass calcd for $C_{19}H_{21}NNaO_3$ [M+Na]+: 334.14191. Found: 334.14154.

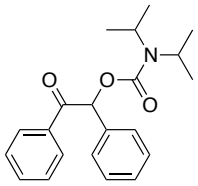

Benzoin diisopropylcarbamate **(DIPA-Ben):** Benzoin (5.00 g, 23.6 mmol) was dissolved into 25 mL of toluene. The solution was cooled to 0 °C before adding triethylamine (3.45 mL, 24.74 mmol). To this solution was slowly added diisopropyl chlorocarbonate (7.71 g, 42.1 mmol). The reaction mixture was refluxed and stirred overnight before diluting with Et_2O and washing successively with sat. NH_4Cl (x2), water, brine, and drying with Na_2SO_4. The organic layer was concentrated by reduced pressure and the residue was purified by crystallization from ethanol to afford the product as a white crystalline solid. (5.80 g, 17.2 mmol, 73.0 %). m.p. 115-116 ºC; ^{1}H-NMR (400 MHz; cd3cn): δ 8.02-7.99 (m, 2H), 7.63-7.58 (m, 1H), 7.56-7.46 (m, 4H), 7.42-7.34 (m, 3H), 6.88 (s, 1H), 4.00-3.96 (m, 2H), 1.33-1.16 (m, 12H); ^{13}C-NMR (101 MHz; cdcl3): δ 195.2, 154.7, 135.0, 134.3, 133.1, 128.87, 128.84, 128.75, 128.56, 128.53, 77.5; IR (neat): 2960, 1685, 1438, 1297 cm^{-1}; HRMS (ESI): Exact mass calcd for $C_{21}H_{26}NO_3$ [M+H]+: 340.1913. Found: 340.1909.

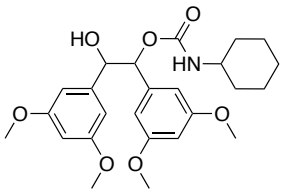

1,2-bis(3,5-dimethoxyphenyl)-2-hydroxyethyl cyclohexylcarbamate: To a cooled (0 °C) solution of CHA-MBen (600 mg, 1.31 mmol) in methanol (5 mL) and THF (5 mL) was slowly added sodium borohydride (99.0 mg, 2.62 mmol) in small portions over 35 minutes. The reaction was then allowed to warm to RT and stirred for 3 hours (TLC). Afterwards, the reaction was cooled to 0 °C and carefully quenched with water followed by 1 M HCl. The reaction mixture was concentrated by reduced pressure and resuspended in 25 mL of Et_2O. The solution was washed successively with sat $NaHCO_3$, water, brine, and dried over Na_2SO_4. Removal of Et_2O by reduced pressure followed by bump distillation afforded pale yellow oil as product (596 mg, 1.30 mmol, 99.0%). ^{1}H-NMR (400 MHz; $CDCl_3$): δ 6.28-6.18 (m, 6H), 5.69 (d, *J* = 4.6 Hz, 1H), 4.85 (d, *J* = 8.0 Hz, 2H), 3.58 (dd, *J* = 11.6, 5.4 Hz, 12H), 3.31-3.29 (m, 2H), 1.78-1.72 (m, 2H), 1.57-1.56 (m, 2H), 1.50-1.46 (m, 1H), 1.22-1.18 (m, 2H), 1.04-0.95 (m, 3H); ^{13}C-NMR (101 MHz; cdcl3): δ 160.3, 154.9, 142.0, 138.9, 105.5, 105.0, 100.1, 79.2, 76.4, 55.2, 50.0, 33.1, 25.4, 24.7; IR (neat): 3370, 2937, 1702, 1597, 1203, 1153, 1061 cm^{-1}; HRMS (ESI): Exact mass calcd for $C_{25}H_{35}NaNO_7$ [M+Na]+: 482.2155 Found: 482.2151.

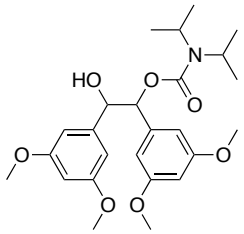

1,2-bis(3,5-dimethoxyphenyl) -2-hydroxyethyl diisopropylcarbamate: To a cooled (0 °C) solution of DIPA-MBen (4.08 g, 8.84 mmol) in methanol (15 mL) and THF (20 mL) was

slowly added sodium borohydride (1.00 g, 26.5 mmol) in small portions over 5 minutes. The reaction was then allowed to warm to RT and stirred for 3 hours (TLC). Afterwards, the reaction was cooled to 0 °C and carefully quenched with water followed by 1 M HCl. The reaction mixture was concentrated by reduced pressure and resuspended in 25 mL of Et_2O. The solution was washed successively with sat $NaHCO_3$, water, brine, and dried over Na_2SO_4. Removal of Et_2O by reduced pressure followed by bump distillation afforded milky white oil as product (2.80 g, 6.07 mmol, 68.7 %). R_f 0.37 (40% EtOAc/Hex); ^{1}H-NMR (400 MHz; CDCl3): δ 6.38-6.27 (m, 6H), 5.82 (dd, J = 71.3, 5.9, 1H), 4.93-4.80 (m, 1H), 3.99-3.93 (m, 2H), 3.75-3.65 (m, 12H), 3.38-3.30 (m, 1H), 1.30-1.10 (m, 12H); ^{13}C-NMR (101 MHz; cdcl3): δ 160.4, 155.3, 154.9, 142.1, 139.7, 105.4, 105.0, 100.3, 81.1, 80.2, 77.9, 77.6, 55.2, 46.2, 21.0; IR (neat): 3440, 2966, 1600, 1463, 1431, 1153 cm^{-1}; HRMS (ESI): Exact mass calcd for $C_{25}H_{35}NaNO_7$ [M+Na]+: 484.2311. Found: 484.2307.

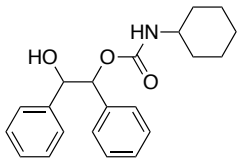

2-hydroxy-1,2-diphenylethyl cyclohexylcarbamate: To a cooled (0 °C) solution of CHA-Ben (600 mg, 1.78 mmol) in methanol (5 mL) and THF (10 mL) was slowly added sodium borohydride (135 mg, 3.57 mmol) in small portions over 5 minutes. The reaction was then allowed to warm to RT and stirred for 3 hours (TLC). Afterwards, the reaction was cooled to 0 °C and carefully quenched with water followed by 1 M HCl. The reaction mixture was concentrated by reduced pressure and resuspended in 25 mL of Et_2O. The solution was

washed successively with sat $NaHCO_3$, water, brine, and dried over Na_2SO_4. Removal of Et_2O by reduced pressure followed by distillation afforded pale white solid as product (593 mg, 1.75 mmol, 98.0 %). m.p. 124-130 ºC; ^{1}H-NMR (400 MHz; cdcl3): δ 7.28-7.23 (m, 5H), 7.23-7.07 (m, 5H), 5.89 (d, J = 4.8, 1H), 5.03 (s, 1H), 4.70-4.67 (m, 1H), 3.46-3.35 (m, 1H), 2.78-2.68 (m, 1H), 1.96-1.78 (m, 2H), 1.76-1.54 (m, 3H), 1.37-1.24 (m, 2H), 1.20-1.01 (m, 3H); ^{13}C-NMR (101 MHz; cdcl3): δ 154.91, 139.40, 136.43, 128.11, 128.04, 128.02, 127.91, 127.77, 127.53, 127.24, 127.11, 126.94, 79.42, 49.98, 22.25, 25.42, 24.74; IR (neat): 3333, 2930, 1696, 1511, 1229, 1058 cm^{-1}; HRMS (CI): Exact mass calcd for $C_{21}H_{25}NNaO_3$ [M+Na]+: 362.17321. Found: 362.17293.

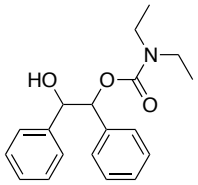

2-hydroxy-1,2-diphenylethyl diethylcarbamate: To a cooled (0 °C) solution of DE-Ben (1.46 g, 4.70 mmol) in methanol (30 mL) was slowly added sodium borohydride (267 mg, 7.05 mmol) in small portions over 5 minutes. The reaction was then allowed to warm to RT and stirred for 1 hour (TLC). Afterwards, the reaction was cooled to 0 °C and carefully quenched with water followed by 1 M HCl. The reaction mixture was concentrated by reduced pressure and resuspended in 25 mL of Et_2O. The solution was washed successively with sat $NaHCO_3$, water, brine, and dried over Na_2SO_4. Removal of Et_2O by reduced pressure afforded a white solid as product (1.46 g, 4.65 mmol, 99.0 %). m.p. 96-98 ºC; ^{1}H-NMR (400 MHz; $CDCl_3$): δ 7.30-7.03 (m, 10H), 5.87 (dd, *J* = 54.6, 6.2 Hz, 1H), 4.92 (dd, *J* = 27.9, 6.2 Hz, 1H), 3.43-3.20 (m, 5H), 1.15-1.03 (m, 6H). ^{13}C-NMR (75 MHz; cdcl3): δ 155.67, 155.40, 139.68, 139.54, 128.11, 128.01, 127.96, 127.90, 127.78, 127.72, 127.69,

127.30, 127.23, 127.17, 81.16, 80.12, 77.75, 77.44, 42.00, 41.45, 14.23, 13.38; IR (neat): 3422, 2978, 1677, 1430, 1275, 1172, 701 cm^{-1}; HRMS (ESI): Exact mass calcd for $C_{19}H_{24}NO_3$ [M+H]+: 314.1756. Found: 314.1760.

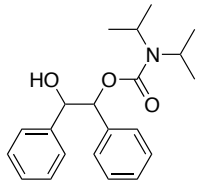

2-hydroxy-1,2-diphenylethyl diisopropylcarbamate: To a cooled (0 °C) solution of DIPA-Ben (2.70 g, 7.95 mmol) in methanol (20 mL) was slowly added sodium borohydride (602 mg, 15.9 mmol) in small portions over 5 minutes. The reaction was then allowed to warm to RT and stirred for 1 hour (TLC). Afterwards, the reaction was cooled to 0 °C and carefully quenched with water followed by 1 M HCl. The reaction mixture was concentrated by reduced pressure and resuspended in 45 mL of Et_2O. The solution was washed successively with sat $NaHCO_3$, water, brine, and dried over Na_2SO_4. Removal of Et_2O by reduced pressure afforded a white solid as product (2.63 g, 7.71 mmol, 97.0 %). m.p. 96-98 ºC; ^{1}H-NMR (400 MHz; CDCl3): δ 7.30-7.09 (m, 10H), 5.96 (dd, J = 63.1, 6.1, 1H), 4.99-4.92 (m, 1H), 3.98-3.86 (m, 2H), 3.76 (dd, J = 8.7, 4.5, 1H), 1.22-1.15 (m, 12H); ^{13}C-NMR (101 MHz; cdcl3): δ 154.3, 139.9, 136.9, 128.04, 127.92, 127.74, 127.70, 127.5, 127.23, 127.11, 81.4, 80.3, 78.1, 77.7, 46.5, 21.1; IR (neat): 3409, 2967, 1674, 1437, 1298, 1050 cm^{-1}; HRMS (CI): Exact mass calcd for $C_{21}H_{27}NNaO_3$ [M+Na]+: 364.18886. Found 364.18831.

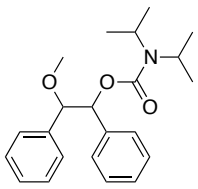

2-methoxy-1,2-diphenylethyl diisopropylcarbamate: To a cooled (0 °C) solution of Red-DIPA-Ben (1.05 g, 3.07 mmol) in DMF (20 mL) was slowly added KHMDS (7.36 mL of 0.5 M tol sol, 3.68 mmol) dropwise over 10 minutes. The reaction was stirred for 30 minutes before MeI (286 μL, 4.60 mmol) was added dropwise over 1 minute. The reaction was warmed to RT and stirred over night (TLC). The reaction was quenched with sat. NH_4 and diluted with Et_2O (20 mL). The solution was washed successively with sat $NaHCO_3$, water, brine, and dried over Na_2SO_4. The organic layer was concentrated by reduced pressure and purified by flash chromatography (20 % EtOAc/Hex) to afforded a clear oil as product (1.00 g, 2.82 mmol, 92.0 %). R_f 0.62 (20 % EtOAc/Hex); ^{1}H-NMR (400 MHz; cdcl3): δ 7.27-7.15 (m, 8H), 7.07-7.01 (m, 2H), 5.91 (dd, J = 15.2, 6.5, 1H), 4.48 (dd, *J* = 15.9, 6.5, 1H), 3.96-3.76 (m, 1H), 3.23 (d, *J* = 21.8, 3H), 1.40-1.06 (m, 12H); ^{13}C-NMR (101 MHz; cdcl3): δ 155.22, 154.18, 138.09, 138.00, 137.84, 137.57, 127.95, 127.89, 127.78, 127.74, 127.69, 127.65, 127.55, 127.48, 86.42, 86.10, 78.81, 78.35, 57.23, 57.05, 45.6, 20.90; IR (neat): 3028, 2970, 2935, 2824, 1693, 1495, 1432, 1367, 1289, 1211, 1156, 1111 cm^{-1}; Exact mass calcd for $C_{22}H_{29}NO_3$ [M+]: 378.20451. Found: 378.20402.

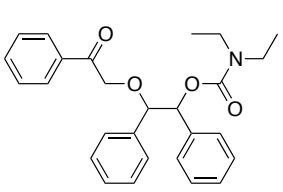

2-(2-oxo-2-phenylethoxy)-1,2-diphenylethyl diethylcarbamate **(DE-Ben2):** To a cooled (0 °C) solution of 2,6 di-*tert*-butyl-4-methylpyridine (480 mg, 2.34 mmol) and phenacyltriflate ether (440 mg, 1.64 mmol) in dichloroethane (25 mL) was slowly added Red-DE-Ben (336 mg, 1.17 mmol) in dichloroethane (15 mL) dropwise over 10 minutes. The reaction was

refluxed and stirred over night (TLC). The reaction was quenched with sat. NH_4 and diluted with Et_2O (20 mL). The solution was washed successively with sat $NaHCO_3$, water, brine, and dried over Na_2SO_4. The organic layer was concentrated by reduced pressure and purified by flash chromatography (10 % EtOAc/Hex) to afforded a yellow oil as product (148 mg, 0.344 mmol, 29.4 %). R_f 0.51 (20% EtOAc/Hex); ^{1}H-NMR (400 MHz; cdcl3): δ 7.88-7.86 (m, 2H), 7.56-7.50 (m, 1H), 7.43-7.38 (m, 2H), 7.24-7.13 (m, 6H), 7.10-7.05 (m, 4H), 6.01 (d, J = 7.0, 1H), 4.83 (d, J = 7.0, 1H), 4.57 (dd, J= 18, 88, 2H), 3.41-3.20 (m, 4H), 1.22-0.97 (m, 6H); ^{13}C-NMR (101 MHz; cdcl3): δ 196.0, 154.9, 137.5, 136.7, 135.1, 133.3, 128.5, 128.2, 128.0, 127.70, 127.64, 127.58, 84.8, 78.6, 71.8, 41.8, 41.2, 14.2, 13.4; IR (neat): 1685, 1441, 1297, cm^{-1}; HRMS (ESI): Exact mass calcd for $C_{27}H_{30}NO_4$ [M+H]: 432.2175. Found: 432.2176.

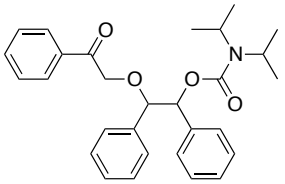

2-(2-oxo-2-phenylethoxy)-1,2-diphenylethyl diisopropylcarbamate **(DIPA-Ben2):** To a cooled (0 °C) solution of 2,6 di-*tert*-butyl-4-methylpyridine (3.21 g, 15.6 mmol) and phenacyltriflate ether (2.94 mg, 10.9 mmol) in dichloroethane (100 mL) was slowly added Red-DIPA-Ben (2.67 g, 7.82 mmol) in dichloroethane (80 mL) dropwise over 5 minutes. The reaction was refluxed and stirred over night (TLC). The reaction was quenched with sat. NH_4 and diluted with Et_2O (50 mL). The solution was washed successively with sat $NaHCO_3$, water, brine, and dried over Na_2SO_4. The organic layer was concentrated by reduced pressure and purified by flash chromatography (10 % EtOAc/tol) to afforded a yellow oil as product (1.10 g, 2.39 mmol, 30.5 %). R_f 0.2

(DCM); ^{1}H-NMR (400 MHz; $CDCl_3$): δ 7.76 (dt, *J* = 8.1, 1.4 Hz, 2H), 7.51-7.47 (m, 1H), 7.36-7.32 (m, 2H), 7.30-7.20 (m, 10H), 5.99 (d, *J* = 5.9 Hz, 1H), 4.86 (t, *J* = 5.4 Hz, 1H), 4.50 (dd, *J* = 15.8, 67.0 Hz, 2H), 3.82 (dt, *J* = 13.5, 6.7 Hz, 2H), 1.05 (s, 12H); ^{13}C-NMR (101 MHz; cdcl3): δ 195.8, 153.9, 137.7, 137.2, 135.0, 133.2, 128.4, 128.18, 128.17, 128.14, 128.08, 127.7, 84.8, 78.2, 72.0, 45.8, 20.8; IR (neat): 2966, 1685, 1434, 1289, 1130, 1044, 699 cm^{-1}; HRMS (CI): Exact mass calcd for $C_{29}H_{33}NNaO_4$ [M+Na]: 482.23073. Found: 482.22992.

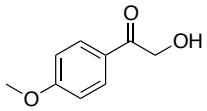

4'-methoxy-2-hydroxyacetophenone: The following compound was synthesized following the procedure outlined by Wong and co-workers.(*64*) Performed on a 21.8 mmol scale. Isolated 3.08 g (18.5 mmol, 84.9 %). m.p. 105-107 ºC. ^{1}H-NMR (400 MHz; cdcl3): δ 7.92-7.89 (m, 2H), 6.99-6.96 (m, 2H), 4.82 (d, J = 4.6, 2H), 3.89 (s, 3H), 3.57 (t, J = 4.6, 1H). ^{13}C-NMR (75 MHz; cdcl3): δ 196.67, 164.36, 130.00, 126.32, 114.16, 64.98, 55.57.

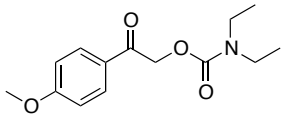

2-(4-methoxyphenyl)-2-oxoethyl diethylcarbamate **(DE-APC):** 4'-methoxy-2-hydroxyacetophenone (1.00 g, 6.00 mmol) was dissolved into 10 mL of toluene. The solution was cooled to 0 °C before adding pyridine (1.00 mL, 12.4 mmol). To this solution was slowly added diethyl chlorocarbonate (3.80 mL, 30.1 mmol). The reaction mixture was refluxed and stirred overnight before diluting with Et_2O and washing successively with sat. NH_4Cl (x2), water, brine, and drying with Na_2SO_4. The organic layer was concentrated by reduced pressure, and the residue was

purified by flash chromatography (10-40 % EtOAc/Hex) to afford the product as a soft yellow solid. (766 mg, 2.89 mmol, 48.1 %). m.p. 58-59 ºC; ^{1}H-NMR (400 MHz; cdcl3): δ 7.85 (d, J = 8.6, 2H), 6.88 (d, J = 8.6, 2H), 5.25 (s, 2H), 3.79 (s, 3H), 3.32-3.30 (m, 4H), 1.14 (d, J = 24.7, 6H); ^{13}C-NMR (101 MHz; cdcl3): δ 192.1, 163.8, 155.2, 129.9, 127.4, 113.8, 66.2, 55.4, 41.7, 13.6; IR (neat): 2974, 2935, 1689, 1600, 1575, 1513, 1477, 1459, 1431, 1379, 1263, 1238, 1164, 1112, 1026 cm^{-1}; HRMS (CI): Exact mass calcd for $C_{14}H_{19}NaNO_4$ [M+Na]: 288.12118. Found: 288.12111.

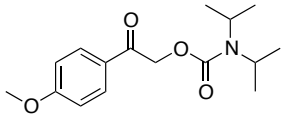

2-(4-methoxyphenyl)-2-oxoethyl diisopropylcarbamate **(DIPA-APC):** 4'-methoxy-2-hydroxyacetophenone (4.50 g, 27.1 mmol) was dissolved into 30 mL of toluene. The solution was cooled to 0 °C before adding triethylamine (4.00 mL, 28.4 mmol). To this solution was slowly added diisopropyl chlorocarbonate (6.65 g, 40.6 mmol). The reaction mixture was refluxed and stirred overnight before diluting with Et_2O and washing successively with sat. NH_4Cl (x2), water, brine, and drying with Na_2SO_4. The organic layer was concentrated by reduced pressure, and the residue was purified by flash chromatography (10-40 % EtOAc/Hex) to afford the product as a light yellow oil (6.22 g, 21.2 mmol, 78.2 %). R_f 0.35 (20 % EtOAc/Hex); ^{1}H-NMR (400 MHz; cdcl3): δ 7.92-7.90 (m, 2H), 6.95-6.93 (m, 2H), 5.31 (s, 2H), 3.87 (s, 3H), 1.28-1.24 (m, 12H). ^{13}C-NMR (101 MHz; cdcl3): δ 192.2, 171.1, 163.8, 154.8, 130.0, 127.6, 113.9, 66.0, 60.4, 55.5; IR (neat): 2968, 2934, 1689, 1601, 1439, 1238 cm^{-1}; HRMS (CI): Exact mass calcd for $C_{16}H_{23}NNaO_4$ [M+Na]: 316.15248. Found: 316.15195.

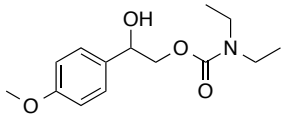

2-hydroxy-2-(4-methoxyphenyl)ethyl diethylcarbamate: To a cooled (0 °C) solution of DE-APC (1.00 g, 3.77 mmol) in methanol (20 mL) was slowly added sodium borohydride (~300 mg, 7.54 mmol) in small portions over 5 minutes. The reaction was then allowed to warm to RT and stirred for 1 hour (TLC). Afterwards, the reaction was cooled to 0 °C and carefully quenched with water followed by 1 M HCl. The reaction mixture was concentrated by reduced pressure and resuspended in 35 mL of Et_2O. The solution was washed successively with sat $NaHCO_3$, water, brine, and dried over Na_2SO_4. Removal of Et_2O by reduced pressure and purification by flash chromatography (45 % EtOAc/Hex) afforded a clear oil as product (788 mg, 2.95 mmol, 78.2 %). ^{1}H-NMR (400 MHz; $CDCl_3$): δ 7.26-7.22 (m, 2H), 6.83-6.79 (m, 2H), 4.82 (t, *J* = 5.7 Hz, 1H), 4.15-4.13 (m, 2H), 3.73 (s, 3H), 3.21-3.18 (m, 4H), 1.03 (t, *J* = 7.9 Hz, 6H); ^{13}C-NMR (101 MHz; cdcl3): δ 159.1, 156.4, 132.8, 127.4, 113.7, 72.4, 70.3, 55.2, 41.9, 41.3, 13.9, 13.3; IR (neat): 3417, 2972, 1675, 1276, 1244, 1173 cm^{-1}; HRMS (EI): Exact mass calcd for $C_{14}H_{22}NO_4$ [M+H]+: 268.1549. Found: 268.1545.

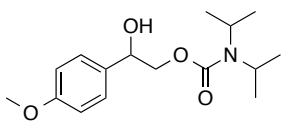

2-hydroxy-2-(4-methoxyphenyl)ethyl diisopropylcarbamate: To a cooled (0 °C) solution of DIPA-APC (3.00 g, 10.2 mmol) in methanol (20 mL) was slowly added sodium borohydride (~600 mg, 15.9 mmol) in small portions over 2 minutes. The reaction was then allowed to warm to RT and stirred for 1 hour (TLC). Afterwards, the reaction was cooled to 0 °C and carefully quenched with

water followed by 1 M HCl. The reaction mixture was concentrated by reduced pressure and resuspended in 50 mL of Et_2O. The solution was washed successively with sat $NaHCO_3$, water, brine, and dried over Na_2SO_4. Removal of Et_2O by reduced pressure and purification by flash chromatography (45 % EtOAc/Hex) afforded a clear oil as product (2.00 g, 6.77 mmol, 66.4 %). ^{1}H-NMR (400 MHz; $CDCl_3$): δ 7.32-7.29 (m, 2H), 6.89-6.86 (m, 2H), 4.91 (q, *J* = 4.3 Hz, 1H), 4.23 (d, *J* = 5.6 Hz, 2H), 4.05-3.78 (m, 5H), 3.61 (d, *J* = 3.3 Hz, 1H), 1.26-1.18 (m, 12H); ^{13}C-NMR (101 MHz; CDCl3): δ 159.3, 156.2, 133.1, 127.6, 114.0, 73.2, 70.3, 55.4, 46.4, 21.3; IR (neat): 3422, 2972, 1667, 1511, 1440, 1301, 1247, 1035 cm^{-1}; HRMS (ESI): Exact mass calcd for $C_{16}H_{26}NO_4$ [M+H]+: 296.1862. Found: 296.1863.

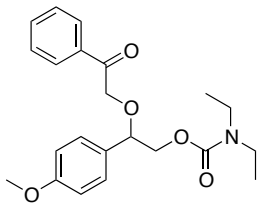

2-(4-methoxyphenyl)-2-(2-oxo-2-phenylethoxy)ethyl diethylcarbamate **(DE-APC2):** To a cooled (0 °C) solution of 2,6 di-*tert*-butyl-4-methylpyridine (307 mg, 1.50 mmol) and phenacyltriflate ether (281 mg, 1.05 mmol) in dichloroethane (10 mL) was slowly added Red-DE-APC (200 mg, 0.76 mmol) in dichloroethane (10 mL) dropwise over 10 minutes. The reaction was refluxed and stirred over night (TLC). The reaction was quenched with sat. NH_4 and diluted with Et_2O (20 mL). The solution was washed successively with sat $NaHCO_3$, water, brine, and dried over Na_2SO_4. The organic layer was concentrated by reduced pressure and purified by flash chromatography (10 % EtOAc/tol) to afforded a yellow oil as product (98.0 mg, 0.23 mmol, 30.0 %). R_f 0.62 (20 % EtOAc/Hex); ^{1}H-NMR (400 MHz; cdcl3): δ 7.89-7.86 (m, 2H), 7.57-7.53 (m, 1H), 7.45-7.40 (m, 2H),

7.33-7.29 (m, 2H), 6.91-6.87 (m, 2H), 4.75-4.56 (m, 3H), 4.33-4.25 (m, 2H), 3.81 (s, 2H), 3.32-3.17 (m, 4H), 1.14-1.00 (m, 6H); ^{13}C-NMR (101 MHz; cdcl3): δ 195.8, 159.7, 155.7, 135.0, 133.4, 129.6, 128.58, 128.49, 127.9, 114.0, 80.3, 73.8, 71.4, 68.1, 55.3, 41.5, 26.2, 13.6 IR (neat): 2934, 1693, 1610, 1599, 1513, 1479, 1449, 1427, 1379, 1273, 1246, 1170, 1135, 1069, 1072, 1025 cm^{-1}; HRMS (ESI): Exact mass calcd for $C_{22}H_{27}NNaO_5$ [M+Na]+: 408.1787. Found: 408.17829.

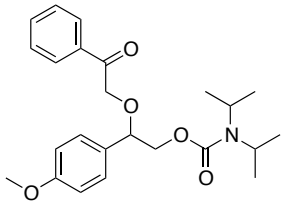

2-(4-methoxyphenyl)-2-(2-oxo-2-phenylethoxy)ethyl diisopropylcarbamate **(DIPA-APC2):** To a cooled (0 °C) solution of 2,6 di-*tert*-butyl-4-methylpyridine (2.85 g, 13.88 mmol) and phenacyltriflate ether (2.60 g, 9.72 mmol) in dichloroethane (100 mL) was slowly added Red-DE-APC (2.05 g, 6.94 mmol) in dichloroethane (30 mL) dropwise over 15 minutes. The reaction was refluxed and stirred over night (TLC). The reaction was washed successively with sat $NaHCO_3$, water, brine, and dried over Na_2SO_4. The organic layer was concentrated by reduced pressure and purified by flash chromatography (25 % EtOAc/Hex) to afforded yellow oil as product (300 mg, 0.725 mmol, 10.4 %). ^{1}H-NMR (400 MHz; cdcl3): δ 7.89-7.85 (m, 2H), 7.56-7.26 (m, 6H), 6.93-6.85 (m, 2H), 4.77-4.57 (m, 3H), 4.37-4.26 (m, 2H), 3.99-3.71 (m, 5H), 1.30-1.06 (m, 12H). ^{13}C-NMR (101 MHz; cdcl3): δ 196.7, 159.7, 155.2, 135.0, 133.3, 129.7, 128.61, 128.53, 127.9, 113.4, 80.4, 71.6, 67.6, 55.6; IR (neat): 2968, 1685, 1512, 1291,

1248, 1134 cm^{-1}; HRMS (ESI): Exact mass calcd for $C_{24}H_{31}NNaO_5$ [M+Na]+: 436.2100. Found: 436.20937.

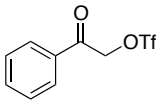

2-oxo-2-phenylethyl trifluoromethanesulfonate: ^{1}H-NMR (400 MHz; CDCl3): δ 7.92-7.89 (m, 2H), 7.72-7.68 (m, 1H), 7.58-7.53 (m, 2H), 5.68 (s, 2H).

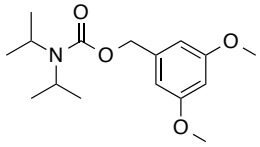

N,N-diisopropyl O-(3,5-dimethoxybenzyl)carbamate **(DIPA-DM):**(*30*) To a round bottom flask was added 3,5-dimethoxybenzyl alcohol (1.01 g, 6.00 mmol), 4-Dimethylaminopyridine (0.073 g, 0.6 mmol), triethyl amine (0.607 g, 0.836 mL, 6.00 mmol), and 30 mL of dioxane. The mixture was cooled to 0 ºC in an ice bath. Diisopropylcarbamoyl chloride (0.982 g, 6.00 mmol), dissolved in 10 mL of distilled dioxane, was added slowly to the cold mixture. After 15 min, the combined solution was warmed to room temperature and stirred for overnight. TLC analysis of the solution was used to monitor the reaction extent. After 24 hours, the solvent was evaporated in vacuo, leaving yellow slurry. The mixture was extracted with 30 mL of ether, washed with water and brine, and dried with $MgSO_4$. The solution was concentrated in vacuo, and the crude product was purified by column chromatography on silica gel with 1:15 ethyl acetate/hexane in the beginning and 1:9 after the first fraction was obtained. A clear viscous liquid was obtained after evaporation. Yield: 50%; ^{1}H-NMR (300 MHz, CDCl3, δ): 6.49 (d, 2H), 6.37 (t, 1H), 5.05 (s, 2H), 4.03 (m, 2H), 3.76 (s, 6H), 1.20 (d, 12H); HR-MS (ESI): calcd for $C_{16}H_{25}NO_4$ [M+H]+: 295.1784. Found: 295.1785.

Appendix B: Synthesis and Characterization of Monomers and Polymers

The starting materials were purchased from Sigma-Aldrich Co. and used without further purification unless otherwise noted. The characterization tools were the same as those described in Appendix A, with all molecular weights were measured on an Agilent 1100 series isopump with an autosampler and a Viscotek Model 302 tetra-detector platform referenced to a polystyrene standard.

B.1 Monomer Synthesis

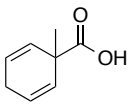

1-methylcyclohexa-2,5-diene-1-carboxylic acid: The following compound was synthesized following the procedure outlined by Engelhardt and co-workers.(*181*) Performed on a 100 mmol scale. Isolated 12.4 g (89.7 mmol, 89.7 %). TLC R_f 0.33 (20 % EtOAc/Hex); ^{1}H-NMR (400 MHz; $CDCl_3$): δ 12.28 (s, 1H), 5.81 (m, 4H), 2.65 (m, 2H), 1.36 (s, 3H).^{13}C-NMR (101 MHz; $CDCl_3$): δ 182.10, 128.01, 124.91, 43.65, 27.20, 25.83.

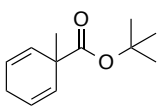

Tert-butyl 1-methylcyclohexa-2,5-diene-1-carboxylate: The following compound was synthesized following the procedure outlined by Binmore and co-workers.(*182*) Performed on a 7.2 mmol scale. Isolated 0.78 g (5.6 mmol, 50 %). TLC R_f 0.75 (20% EtOAc/Hex); ^{1}H-NMR (400 MHz; $CDCl_3$): δ 5.77 (s, 4H), 2.63 (m,

2H), 1.44 (s, 9H), 1.29 (s, 3H). ^{13}C-NMR (101 MHz; $CDCl_3$): δ 174.46, 129.12, 123.98, 80.45, 44.38, 27.91, 27.44, 25.94.

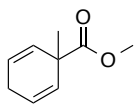

Methyl 1-methylcyclohexa-2,5-diene-1-carboxylate: To a solution of 1-methylcyclohexa-2,5-diene-1-carboxylic acid (1.00g, 7.24 mmol) in benzene (3 mL) and methanol (3 mL) was added H_2SO_4 (300 µL). The reaction mixture was refluxed for 1 hr and monitored by TLC. Upon completion, the reaction solution was diluted with Et_2O (30 mL) and washed with H_2O (55 mL). The organic portion was dried over Na_2SO_4, filtered, and concentrated by reduced pressure to yield a clear oil as product (1.00 g, 6.57 mmol, 91.0 %). TLC R_r 0.67 (20 % EtOAc/Hex); ^{1}H-NMR (400 MHz; $CDCl_3$): δ 5.79-5.70 (m, 4H), 3.67-3.63 (m, 3H), 2.62-2.59 (m, 2H), 1.28 (s, 3H); ^{13}C-NMR (101 MHz; $CDCl_3$): δ 175.65, 128.64, 124.42, 52.22, 43.80, 27.37, 25.84; IR (neat): 3030, 2970, 2950, 2860, 2810, 1730, 1430 cm^{-1}; HRMS (CI): Exact mass calcd for $C_9H_{12}O_2$ [M]+: 152.08373 Found: 153.0917.

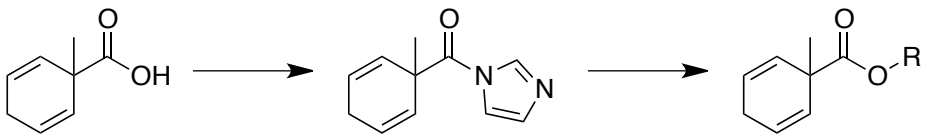

Representative Procedure for Ester Formation Sequence:

In a 250 mL round-bottom flask equipped with a stirbar, 1-methylcyclohexa-2,5-diene-1-carboxylic acid (321 mmol, 1 equiv) was dissolved in DCM (0.5 M, 700 mL).

While stirring at RT, carbonyldiimidazole (1.05 equiv, 337.4 mmol, 54.7 g) was added portion wise over 10 minutes. The formation of 1*H*-imidazole was monitored by TLC (R_f = 0.41, 1:1 EtOAc/Hex). The reaction was filtered through celite and evaporated under reduced pressure at 22 °C until the volume was approximately 100 mL. The remaining solution of 1*H*-imidazolyl 1-methylcyclohexa-2,5-diene-1-carboxylate

in DCM is transferred to a 500 mL round-bottom flask equipped with magnetic stirbar and rubber septum. To the flask is added 80 mL of alcohol followed by K_2CO_3 (3.21 mmol, 450 mg, 0.01 eqiuv). After stirring 16 h, the reaction was evaporated under reduced pressure at 22 ºC. The crude reaction material was diluted with EtOAc, washed with saturated ammonium chloride and brine, dried over magnesium sulfate and evaporated under reduced pressure. The crude ester was then purified by distillation to give a clear oil material.

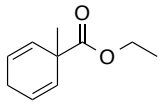

Ethyl 1-methylcyclohexa-2,5-diene-1-carboxylate: Performed on a 80 mmol scale. Isolated 12.1 g (72.8 mmol, 91.0 %) after two steps. TLC Rf 0.77 (40% EtOAc/Hex); ^{1}H-NMR (400 MHz; $CDCl_3$): δ 5.74-5.68 (m, 4H), 4.05 (dt, *J* = 9.1, 6.4 Hz, 2H), 2.56 (dq, *J* = 3.8, 1.3 Hz, 2H), 1.24 (s, 3H), 1.16 (td, *J* = 7.1, 2.7 Hz, 3H). ^{13}C-NMR (101 MHz; CDCl3): δ 175.2, 129.5, 124.5, 60.9, 43.9, 27.6, 26.0, 14.3; IR (neat): 3497, 2978, 1725, 1251, 1110, 1022 cm^{-1}; HRMS (CI): Exact mass calcd for $C_{10}H_{14}O_2$ [M]+: 166.09938. Found: 166.0988.

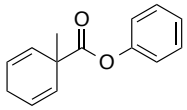

Phenyl 1-methylcyclohexa-2,5-diene-1-carboxylate: Performed on a 7.2 mmol scale. Isolated 0.78 g (5.6 mmol, 50.0 %). TLC R_f = 0.49 in (20% EtOAc : Hex). ^{1}H-NMR (400 MHz; $CDCl_3$): δ 7.37-7.33 (m, 2H), 7.23-7.19 (m, 1H), 7.07-7.05 (m, 2H), 5.91-5.90 (m, 4H), 2.72-2.71 (m, 2H), 1.49 (d, *J* = 2.2 Hz, 3H); ^{13}C-NMR (101 MHz; $CDCl_3$): δ 151.1, 129.3, 128.1, 125.8, 124.9, 121.4, 44.2, 34.6, 27.0, 26.1; IR (neat): 1490, 1590, 1750, 2810, 2860, 2920, 2970, 3020 cm^{-1}; HRMS (ESI): Exact mass calcd for $C_{14}H_{14}NaO_2$ $[M+Na]^+$: 237.08915. Found 237.08792.

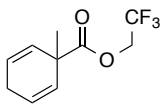

2,2,2-trifluoroethyl 1-methylcyclohexa-2,5-diene-1-carboxylate: Performed on a 188 mmol scale. Isolated 12.1 g (54.9 mmol, 29.2 %). ^{1}H-NMR (400 MHz; $CDCl_3$): δ 5.88-5.84 (m, 2H), 5.76 (dt, *J* = 10.5, 2.0 Hz, 2H), 4.46 (q, *J* = 8.4 Hz, 2H), 2.66 (tq, *J* = 3.3, 2.1 Hz, 2H), 1.38-1.37 (m, 3H); ^{13}C-NMR (101 MHz; $CDCl_3$): δ 173.5, 127.3, 125.3, 60.5, 43.8, 27.1, 25.8; IR (neat): 1747, 1282, 1162, 1101, 700 cm^{-1}; HRMS (CI): Exact mass calcd for $C_{10}H_{12}F_3O_2$ $[M+H]^+$: 221.0789. Found: 221.0792.

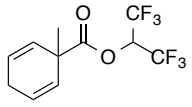

1,1,1,3,3,3-hexafluoropropan-2-yl 1-methylcyclohexa-2,5-diene-1-carboxylate: Performed on a 21.7 mmol scale. Isolated 4.12 g (14.3 mmol, 66.0 %). ^{1}H-NMR (400 MHz; $CDCl_3$): δ 5.86-5.81 (m, 2H), 5.69-5.62 (m, 3H), 2.62-2.59 (m, 2H), 1.34 (d, *J* = 2.2 Hz, 3H); ^{13}C-NMR (101 MHz; $CDCl_3$): δ 171.7, 126.6, 126.1, 66.6, 43.9, 26.7, 25.8; IR (neat): 1767, 1202, 1098, 700, 687 cm^{-1}; HRMS (CI): Exact mass calcd for $C_{11}H_{10}F_6O_2$ $[M-H]^-$: 287.0507. Found: 287.0511.

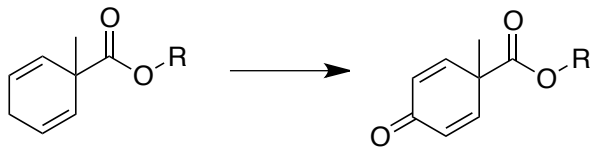

Representative Procedure for R-1-methylcyclohexa-2,5-diene-1-ester Oxidation:

In a 500 mL round-bottom flask equipped with a mechanical overhead stirrer, R 1-methylcyclohexa-2,5-diene-1-carboxylate (62.6 mmol, 10.4 g, 1 equiv), pyridinium dichromate (187.7 mmol, 70.61g, 3 equiv), tBu-OOH (187.7 mmol, 3 equiv) and celite (11.0 g) are dissolved into benzene (190 mL). The reaction is stirred for 16h and monitored by TLC (product $R_f \approx 0.5$: 40% EtOAc/Hex). The reaction is filtered and washed with EtOAc (150 mL). The organic solution was washed successively with NH_4Cl (x2), water, brine, and dried over Na_2SO_4. The organic layer was concentrated by reduced pressure and purified by distillation to yield the product as pale yellow oil.

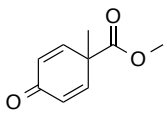

Methyl 1-methyl-4-oxocyclohexa-2,5-diene-1-carboxylate: Performed on a 90.2 mmol scale. Isolated 11.7 g (70.4 mmol, 78.1 %) TLC $R_f = 0.27$ (100 % DCM); bp: 140 ºC at 2.4 torr. ^{1}H-NMR (400 MHz; $CDCl_3$): δ 7.00-6.97 (m, 2H), 6.25-6.22 (m, 2H), 3.68 (s, 3H), 1.50 (s, 3H). ^{13}C-NMR (101 MHz; $CDCl_3$): δ 184.8, 171.0, 148.9, 128.9, 53.1, 48.0, 24.8; IR (neat): 3020, 2960, 2920, 1730, 1660, 1430 cm^{-1}; HRMS (CI): Exact mass calcd for C_9H_{10},aO_3 [M+Na]+: 189.05276. Found 189.05184.

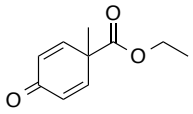

Ethyl 1-methyl-4-oxocyclohexa-2,5-diene-1-carboxylate: Performed on a 62.6 mmol scale. Isolated 7.23 g (40.1 mmol, 64 %) TLC R_f = 0.48 (40% EtOAc : Hex);); bp: 85 ºC at 1.2 torr; ^{1}H-NMR (400 MHz; $CDCl_3$): δ 6.91-6.87 (m, 2H), 6.11-6.07 (m, 2H), 4.00 (qd, *J* = 7.1, 1.3 Hz, 2H), 1.37 (d, *J* = 1.2 Hz, 3H), 1.08 (td, *J* = 7.1, 1.3 Hz, 3H). ^{13}C-NMR (101 MHz; CDCl3): δ 185.0, 170.5, 148.9, 128.9, 62.2, 48.2, 25.0, 14.2; IR (neat): 1728, 1706, 1664, 1225, 862 cm^{-1}; HRMS (CI): Exact mass calcd for $C_{10}H_{12}O_3$ [M]+: 180.07864. Found 180.0788.

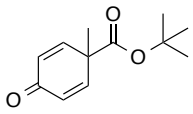

Tert-butyl 1-methyl-4-oxocyclohexa-2,5-diene-1-carboxylate: Performed on a 5.0 mmol scale. Isolated 0.5 g (2.3 mmol, 47 %). TLC R_f = 0.45 in (20% EtOAc : Hex); bp: 110 ºC at 0.9 torr; ^{1}H-NMR (400 MHz; $CDCl_3$): δ 6.97 (d, *J* = 12 Hz, 2H), 6.21 (d, *J* = 12 Hz, 2H), 1.46 (s, 3H), 1.39 (s, 9H). ^{13}C-NMR (101 MHz; $CDCl_3$): δ 185.18, 169.57, 149.62, 128.68, 82.97, 49.04, 27.80, 24.79; IR (neat): 2983, 1669, 1631, 1362, 1183, 1070, 860 cm^{-1}; HRMS (ESI): Exact mass calcd for $C_{12}H_{16}NaO_3$ [M+Na]$^+$: 231.09971. Found: 231.09902.

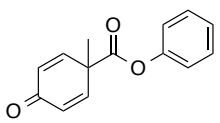

Phenyl 1-methyl-4-oxocyclohexa-2,5-diene-1-carboxylate: Performed on a 65.3 mmol scale. Isolated 11.9 g (52.1 mmol, 79.8 %). TLC R_f = 0.27 in (20% EtOAc : Hex); m.p. 69-71 ºC; ^{1}H-NMR (400 MHz; $CDCl_3$): δ 7.39 (t, *J* = 7.8 Hz, 2H), 7.25 (t, *J* = 7.9 Hz, 1H), 7.18 (d, *J* = 10.1 Hz, 2H), 7.07 (d, *J* = 7.7 Hz, 2H), 6.39 (d, *J* = 10.1 Hz, 2H), 1.71 (s, 3H). ^{13}C-NMR (101 MHz; $CDCl_3$): δ 184.74, 169.37, 150.35, 148.20, 129.57, 126.43, 121.04, 48.23, 24.94; IR (neat): 1752,

1666, 1190, 1175, 1093, 862 cm^{-1}; HRMS (ESI): Exact mass calcd for $C_{14}H_{12}NaO_3$ $[M+Na]^+$: 251.06841. Found: 251.06767.

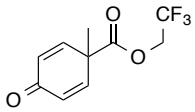

2,2,2-trifluoroethyl 1-methyl-4-oxocyclohexa-2,5-diene-1-carboxylate: Performed on a 54.9 mmol scale. Isolated 10.3 g (44.0 mmol, 80.1 %). TLC R_f 0.36 (30% EtOAc/Hex); ^{1}H-NMR (400 MHz; $CDCl_3$): δ 7.05-6.32 (m, 4H), 4.53 (q, *J* = 8.2 Hz, 2H), 1.64-1.61 (m, 3H). ^{13}C-NMR (101 MHz; $CDCl_3$): δ 184.4, 168.8, 147.2, 129.3, 61.4, 48.0, 24.9; IR (neat): 1754, 1669, 1284, 1168, 1112 cm^{-1}; HRMS (ESI): Exact mass calcd for $C_{10}H_9F_3NaO_3$ $[M+Na]^+$: 257.0401. Found: 257.0395.

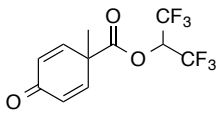

1,1,1,3,3,3-hexafluoropropan-2-yl 1-methyl-4-oxocyclohexa-2,5-diene-1-carboxylate: Performed on a 14.3 mmol scale. Isolated 1.66 g (5.49 mmol, 38.4 %). ^{1}H-NMR (400 MHz; $CDCl_3$): δ 7.02-6.98 (m, 2H), 6.39-6.35 (m, 2H), 5.74 (dt, *J* = 11.9, 5.9 Hz, 1H), 1.64 (s, 3H); ^{13}C-NMR (101 MHz; $CDCl_3$): δ 184.1, 167.9, 146.1, 130.1, 67.3, 47.5, 24.6; IR (neat): 1774, 1672, 1234, 1200, 1102 cm^{-1}; HRMS (ESI): Exact mass calcd for $C_{11}H_8F_6NaO_3$ $[M+Na]^+$: 325.0275. Found 325.0272.

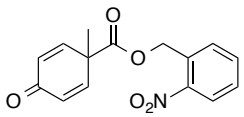

2-nitrobenzyl 1-methyl-4-oxocyclohexa-2,5-diene-1-carboxylate: In a 50 mL round-bottom flask phenyl 1-methyl-4-oxocyclohexa-2,5-diene-1-carboxylate (12.1 mmol, 3.00g), 2-nitrobenzyl alcohol (15.8 mmol, 2.41 g), and dibutyltin diluarate (2.36 mmol, 1.56 mL) were dissolved in toluene (26 mL.). The reaction was heated to 100 ºC and stirred for 18 h. The organic solution was diluted with

Et_2O (30 ml) and washed successively with NH_4Cl (x2), water, brine, and dried over Na_2SO_4. The organic layer was concentrated by reduced pressure and purified by flash chromatography (SiO_2, 30% EtOAc/Hex) to yield 3.225 g (11.23 mmol, 84.5 %) as a yellow oil. TLC R_f = 0.15 in (30% EtOAc : Hex); ^{1}H-NMR (400 MHz; $CDCl_3$): δ 8.11 (dd, *J* = 8.2, 1.3 Hz, 1H), 7.66 (td, *J* = 7.6, 1.3 Hz, 1H), 7.56-7.51 (m, 1H), 7.47 (ddt, *J* = 7.7, 1.1, 0.3 Hz, 1H), 7.07-7.03 (m, 2H), 6.37-6.33 (m, 2H), 5.55 (s, 2H), 1.61 (d, *J* = 2.1 Hz, 3H). ^{13}C-NMR (101 MHz; $CDCl_3$): δ 184.7, 170.0, 148.3, 133.8, 130.8, 129.36, 129.16, 125.2, 64.6, 48.3, 24.7; IR (neat): 1736, 1667, 1526, 1343, 1223, 1175, 853 cm^{-1}; HRMS (ESI): Exact mass calcd for $C_{15}H_{13}NNaO_5$ $[M+Na]^+$: 310.06914. Found: 310.06710.

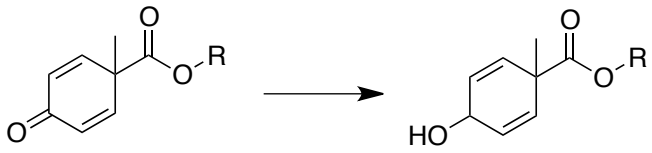

Representative Procedure for R-1-methyl-4-oxocyclohexa-2,5-diene-1-carboxylate Reduction:

To a cooled (0 °C) solution of R 1-methyl-4-oxocyclohexa-2,5-diene-1-carboxylate (20.2 mmol) and cerium chloride heptahydrate (8.27 g, 22.2 mmol) in methanol (100 mL) was slowly added sodium borohydride (1.53 g, 40.4 mmol) in small portions over 15 minutes. The reaction was then allowed to warm to RT and stirred for 20 minutes (TLC). The reaction was cooled to 0 °C again and carefully quenched with water (400 mL) followed by NH_4Cl (50 mL). The reaction mixture was concentrated by

reduced pressure and resuspended in 200 mL of Et_2O. The solution was washed successively with water, brine, and dried over Na_2SO_4. Removal of Et_2O by reduced pressure followed by bump distillation afforded a clear oil as product.

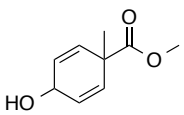

Methyl 4-hydroxy-1-methylcyclohexa-2,5-diene-1-carboxylate: Performed on a 18.0 mmol scale. Isolated 2.28 g (13.5 mmol, 75.1 %). TLC R_f 0.18 (30% EtOAc/Hex) ^{1}H-NMR (400 MHz; $CDCl_3$): δ 6.00-5.95 (m, 4H), 4.55-4.44 (m, 1H), 3.70-3.68 (m, 3H), 1.58 (t, *J* = 2.1 Hz, 1H), 1.37 (d, *J* = 25.3 Hz, 3H). ^{13}C-NMR (101 MHz; $CDCl_3$): δ 174.0, 131.5, 127.6, 61.6, 52.5, 44.9, 26.2; IR (neat): 3440, 1730, 1664, 1237, 1115, 859 cm^{-1}; HRMS (CI): Exact mass calcd for $C_9H_{12}O_3$ $[M]^-$: 168.0786. Found: 168.0784.

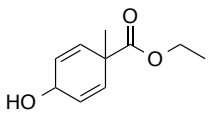

Ethyl 4-hydroxy-1-methylcyclohexa-2,5-diene-1-carboxylate: Performed on a 39.0 mmol scale. Isolated 5.69 g (31.2 mmol, 80.1 %). B.P. 72 ºC @ 1 torr . ^{1}H-NMR (400 MHz; $CDCl_3$): δ 5.90-5.84 (m, 4H), 4.41 (d, *J* = 32.4 Hz, 1H), 4.06 (qdd, *J* = 7.1, 4.5, 0.8 Hz, 2H), 2.70-2.63 (m, 1H), 1.32-1.24 (m, 3H), 1.20-1.14 (m, 3H). ^{13}C-NMR (101 MHz; CDCl3): δ 174.3, 131.31, 131.11, 128.3, 128.0, 61.37, 44.8, 26.5, 26.2, 14.2; IR (Neat): 3441, 2982, 1730, 1238, 1113, 1023, 862 cm^{-1}; HRMS (CI): Exact mass calcd for $C_{10}H_{14}O_3$ $[M]^-$: 182.0943. Found: 182.0939.

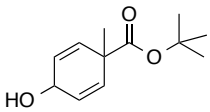

Tert-butyl 4-hydroxy-1-methylcyclohexa-2,5-diene-1-carboxylate: Performed on a 55.3 mmol scale. Isolated 8.69 g (41.3 mmol, 74.7 %). TLC R_f 0.20 (20% EtOAc/Hex); ^{1}H-NMR (400 MHz; $CDCl_3$): δ 5.92-5.87 (m, 4H), 4.44 (dd, *J* = 36.3, 8.1 Hz, 1H), 2.11 (d, *J* = 8.9 Hz, 1H), 1.40 (dd, *J* = 5.5, 1.0 Hz, 9H), 1.29 (dd, *J* = 24.8, 0.9 Hz, 3H). ^{13}C-NMR (101 MHz; $CDCl_3$): δ 173.0, 131.8, 131.4, 127.7, 127.4, 81.3, 81.1, 61.9, 61.7, 45.42, 45.27, 27.9, 26.2, 26.0; IR (neat): 3307, 2978, 1716, 1254, 1167, 1118 cm^{-1}; HRMS (ESI): Exact mass calcd for $C_{12}H_{18}NaO_3$ $[M+ Na]^+$: 233.11536. Found: 233.11461.

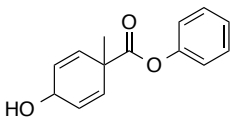

Phenyl 4-hydroxy-1-methylcyclohexa-2,5-diene-1-carboxylate: Performed on a 8.76 mmol scale. Isolated 1.85 g (8.03 mmol, 91.7 %). TLC R_f 0.31 (30% EtOAc/Hex); ^{1}H-NMR (400 MHz; $CDCl_3$): δ 7.40-7.36 (m, 2H), 7.26-7.23 (m, 1H), 7.06-7.04 (m, 2H), 6.15-6.06 (m, 4H), 1.63 (d, *J* = 10.1 Hz, 1H), 1.49 (d, *J* = 2.6 Hz, 3H); ^{13}C-NMR (101 MHz; $CDCl_3$): δ 172.5, 150.7, 130.4, 129.5, 128.6, 125.9, 121.2, 61.8, 44.9, 25.9; IR (neat): 3333, 1744, 1186, 1087, 1020, 739, 688 cm^{-1}; HRMS (ESI): Exact mass calcd for $C_{14}H_{14}NaO_3$: $[M+Na]^+$: 253.0841. Found: 253.0831.

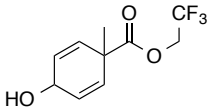

2,2,2-trifluoroethyl 4-hydroxy-1-methylcyclohexa-2,5-diene-1-carboxylate: Performed on a 76.6 mmol scale. Isolated 11.4 g (49.1 mmol, 64.1 %). TLC R_f 0.36 (30% EtOAc/Hex); ^{1}H-NMR (400 MHz; $CDCl_3$): δ 6.03-5.88 (m, 4H), 4.52-4.40 (m, 3H), 1.43-1.36 (m, 3H). ^{13}C-NMR (101 MHz; $CDCl_3$): δ 172.2, 130.1, 129.7, 128.7,

61.7, 61.4, 60.7, 44.5, 26.1, 25.6; IR (neat): 3353, 17468, 1284, 1164, 1104, 974 cm^{-1}; HRMS (ESI): Exact mass calcd for $C_{10}H_{11}F_3NaO_3$ $[M+Na]^+$: 259.0558. Found: 259.0552

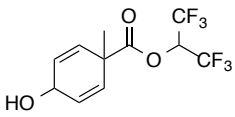

1,1,1,3,3,3-hexafluoropropan-2-yl 4-hydroxy-1-methylcyclohexa-2,5-diene-1-carboxylate: Performed on a 23.1 mmol scale. Isolated 3.09 g (10.2 mmol, 44.0 %). TLC R_f 0.35 (30% EtOAc/Hex); ^{1}H-NMR (400 MHz; $CDCl_3$): δ 6.10-6.03 (m, 2H), 5.99-5.88 (m, 2H), 5.75-5.67 (m, 1H), 4.52 (ddt, *J* = 34.4, 3.2, 1.6 Hz, 1H), 1.59 (d, *J* = 4.8 Hz, 1H), 1.49-1.41 (m, 3H). ^{13}C-NMR (101 MHz; $CDCl_3$): δ 170.5, 129.61, 129.45, 129.2, 128.7, 67.1, 61.7, 61.4, 44.5, 25.9, 25.3; IR (neat): 3213, 1765, 1217, 1203, 1099 cm-1; HRMS (ESI): Exact mass calcd for $C_{11}H_{10}F_6NaO_3$ $[M+Na]^+$: 327.0432. Found: 327.0429.

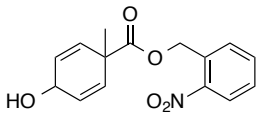

2-nitrobenzyl 4-hydroxy-1-methylcyclohexa-2,5-diene-1-carboxylate: Performed on a 10.8mmol scale. Isolated 2.52 g (8.88 mmol, 82.3 %). TLC R_f 0.21 (30% EtOAc/Hex); ^{1}H-NMR (400 MHz; $CDCl_3$): δ 8.08 (td, *J* = 9.0, 1.2 Hz, 1H), 7.67-7.63 (m, 1H), 7.54-7.48 (m, 2H), 6.05-5.93 (m, 4H), 5.49 (d, *J* = 3.7 Hz, 2H), 4.57-4.46 (m, 1H), 1.81-1.64 (m, 1H), 1.41 (d, *J* = 29.4 Hz, 3H). ^{13}C-NMR (101 MHz; $CDCl_3$): δ 172.7, 170.7, 133.7, 133.0, 132.5, 128.90, 128.79, 125.0, 124.16, 124.01, 64.0, 44.8, 26.6, 25.5, 21.7; IR (neat): 3372, 1729, 1526, 1341, 1228, 1108, 726 cm^{-1}; HRMS (CI): Exact mass calcd for $C_{15}H_{15}NO_5$ $[M]^+$: 289.0950. Found: 289.0952.

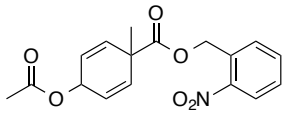

2-nitrobenzyl 4-acetoxy-1-methylcyclohexa-2,5-diene-1-carboxylate: To a chilled solution (0 ºC) of 2-nitrobenzyl 4-hydroxy-1-methylcyclohexa-2,5-diene-1-carboxylate (1.10 g, 3.81 mmol) in acetic anhydride (10 mL) was added dimethylaminopyridine (63 mg, 0.52 mmol) and triethylamine (1.40 mL, 10.4 mmol). The reaction was stirred for 3 hours before diluting with Et_2O (100 mL) and washing successively with sat. NH_4Cl (x2), water, brine, and drying with Na_2SO_4. The organic layer was concentrated by reduced pressure and the residue was purified by flash chromatography (SiO_2, 30 % EtOAc/Hex) to yield the product as a clear oil (1.15 g, 3.47 mmol, 91.1 %). TLC R_f 0.44 (30% EtOAc/Hex); ^{1}H-NMR (400 MHz; $CDCl_3$): δ 8.10 (ddd, *J* = 8.3, 5.3, 1.3 Hz, 1H), 7.67-7.63 (m, 1H), 7.58-7.48 (m, 2H), 6.17-6.06 (m, 2H), 5.94-5.89 (m, 2H), 5.68 (dtd, *J* = 9.0, 3.3, 1.6 Hz, 1H), 5.52 (d, *J* = 10.2 Hz, 2H), 2.08 (dd, *J* = 7.2, 5.4 Hz, 3H), 1.47-1.41 (m, 3H). ^{13}C-NMR (101 MHz; $CDCl_3$): δ 172.7, 170.7, 133.7, 133.0, 132.5, 128.90, 128.79, 125.0, 124.16, 124.01, 64.0, 44.8, 26.6, 25.5, 21.7; IR (neat): 1730, 1527, 1344, 1230, 1106 cm^{-1}; HRMS (ESI): Exact mass calcd for $C_{17}H_{17}NNaO_6$ $[M+Na]^+$: 354.09536. Found: 354.09523.

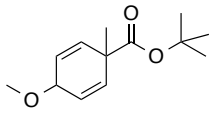

Tert-butyl 4-methoxy-1-methylcyclohexa-2,5-diene-1-carboxylate: To a chilled solution (0 ºC) of *t*-butyl 4-hydroxy-1-methylcyclohexa-2,5-diene-1-carboxylate (200 mg, 0.951 mmol) in DMF (10 mL) was slowly added NaH (60 wt% in oil, 40.1 mg, 1.05 mmol). After 15 minutes, MeI (89.0 μL, 1.43 mmol) was added dropwise to the reaction mixture and stirred for 30 minutes before diluting with

Et_2O and washing successively with sat. NH_4Cl (x2), water, brine, and drying with Na_2SO_4. The organic layer was concentrated by reduced pressure and the residue was purified by flash chromatography (SiO_2, 20 % EtOAc/Hex) to yield the product as a clear oil (124 mg, 0.553 mmol, 58.1 %). TLC R_f 0.64 (100% DCM); ^{1}H-NMR (400 MHz; $CDCl_3$): δ 6.08-6.00 (m, 2H), 5.85 (dd, *J* = 15.9, 3.2 Hz, 2H), 3.25 (d, *J* = 27.1 Hz, 3H), 1.43-1.42 (m, 9H), 1.32 (d, *J* = 24.6 Hz, 3H). ^{13}C-NMR (101 MHz; CDCl3): δ 172.9, 134.0, 133.2, 125.0, 81.1, 69.4, 68.6, 53.6, 52.3, 45.4, 28.0, 26.7, 25.9; IR (neat): 2983, 1724, 1248, 1164, 1115 cm^{-1}; HRMS (ESI): Exact mass calcd for $C_{13}H_{20}NaO_3$ $[M+Na]^+$: 247.1310 Found: 247.1304

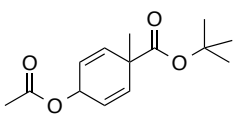

Tert-butyl 4-acetoxy-1-methylcyclohexa-2,5-diene-1-carboxylate: To a chilled solution (0 ºC) of *t*-butyl 4-hydroxy-1-methylcyclohexa-2,5-diene-1-carboxylate (300 mg, 1.43 mmol) in acetic anhydride (10 mL) was added dimethylaminopyridine (17 mg, 0.143 mmol) and triethylamine (398 μL, 2.85 mmol). The reaction was stirred for 30 minutes before diluting with Et_2O and washing successively with sat. NH_4Cl (x2), water, brine, and drying with Na_2SO_4. The organic layer was concentrated by reduced pressure and the residue was purified by flash chromatography (SiO_2, 20 % EtOAc/Hex) to yield the product as a clear oil (315 mg, 1.24 mmol, 87.0 %) TLC R_f 0.72 (100% DCM); ^{1}H-NMR (400 MHz; $CDCl_3$): δ 6.12 (dd, *J* = 10.2, 1.5 Hz, 1H), 6.04 (dd, *J* = 10.2, 1.5 Hz, 1H), 5.82 (ddd, *J* = 10.2, 3.2, 1.6 Hz, 2H), 5.65-5.61 (m, 1H), 2.06 (d, *J* = 3.8 Hz, 3H), 1.42 (s, 9H), 1.33 (d, *J* = 26.1 Hz, 3H). ^{13}C-NMR (101 MHz; CDCl3): δ 172.5, 170.7, 133.93, 133.78, 123.4, 81.3, 64.5,

45.3, 28.0, 27.0, 25.8, 21.3; IR (neat): 1724, 1368, 1231, 1114 cm^{-1}; HRMS (ESI): Exact mass calcd for $C_{14}H_{20}NaO_4$ $[M+Na]^+$: 275.1259. Found: 275.1252.

B.2 POLYMER SYNTHESIS

Representative Lewis Acid Mediated Polymerization Procedure

A 10 mL RBF equipped with a 4Å MS packed dean-stark trap, reflux condenser, and a stir bar was charged with monomer (1 equiv.), dibutyltin diluarate (0.3 equiv) and toluene (3 mL). The reaction was heated to 120 ºC and stirred for 24 h followed by addition of H_2O at 0 ºC (5 mL). The reaction mixture is diluted with Et_2O and washed successively with NH_4Cl, water and brine, dried over Na_2SO_4 and concentrated by reduced pressure. The crude polymer mixture is purified by flash chromatography (SiO_2, 30% EtOAc/Hex). The Mw is determined by ^{1}H-NMR and by GPC with polystyrene standards.

Representative Anionic Polymerization Procedure

A 10 mL RBF equipped with a 4Å MS packed dean-stark trap, reflux condenser, and a stir bar was charged with monomer (1 equiv.), 12-crown-4 (0.3 equiv) and toluene (3 mL). After cooling reaction flask to -78 °C in an isopropyl alcohol/dry ice bath, n-butyllithium (0.1 equiv) was added dropwise. The reaction was heated to 120 ºC and stirred for 24 h followed by addition of H_2O at 0 ºC (5 mL). The reaction mixture is diluted with Et_2O and washed successively with NH_4Cl, water and brine, dried over Na_2SO_4 and concentrated by reduced pressure. The crude polymer mixture is purified by

flash chromatography (SiO_2, 30% EtOAc/Hex). The Mw is determined by ^{1}H-NMR and by GPC with polystyrene standards.

o-Nitrobenzyl alcohol initiated polymerization

A 10 mL RBF equipped with a 4Å MS packed dean-stark trap, reflux condenser, and a stir bar was charged with 2-nitrobenzyl 4-hydroxy-1-methylcyclohexa-2,5-diene-1-carboxylate (0.05 equiv.), 12-crown-4 (0.3 equiv) and toluene (2 mL). After cooling reaction flask to -78 °C in an isopropyl alcohol/dry ice bath, n-butyllithium (0.1 equiv) was added dropwise. After stirring for 15 minutes a solution of monomer (1 equiv) in toluene (2 mL) was added dropwise over 5 minutes. The reaction was heated to 120 ºC and stirred for 24 h followed by addition of H_2O at 0 ºC (5 mL). The reaction mixture is diluted with Et_2O and washed successively with NH_4Cl, water and brine, dried over Na_2SO_4 and concentrated by reduced pressure. The crude polymer mixture is purified by flash chromatography (SiO_2, 30% EtOAc/Hex). The Mw is determined by ^{1}H-NMR and by GPC with polystyrene standards.

B.2.1 POLYMERIZATION SETUP

Figure B.1: Picture of the polymerization set up. A RBF equipped with a 4Å molecular sieve filled Dean-Stark trap and reflux condenser.

B.3 ^{1}H-NMR

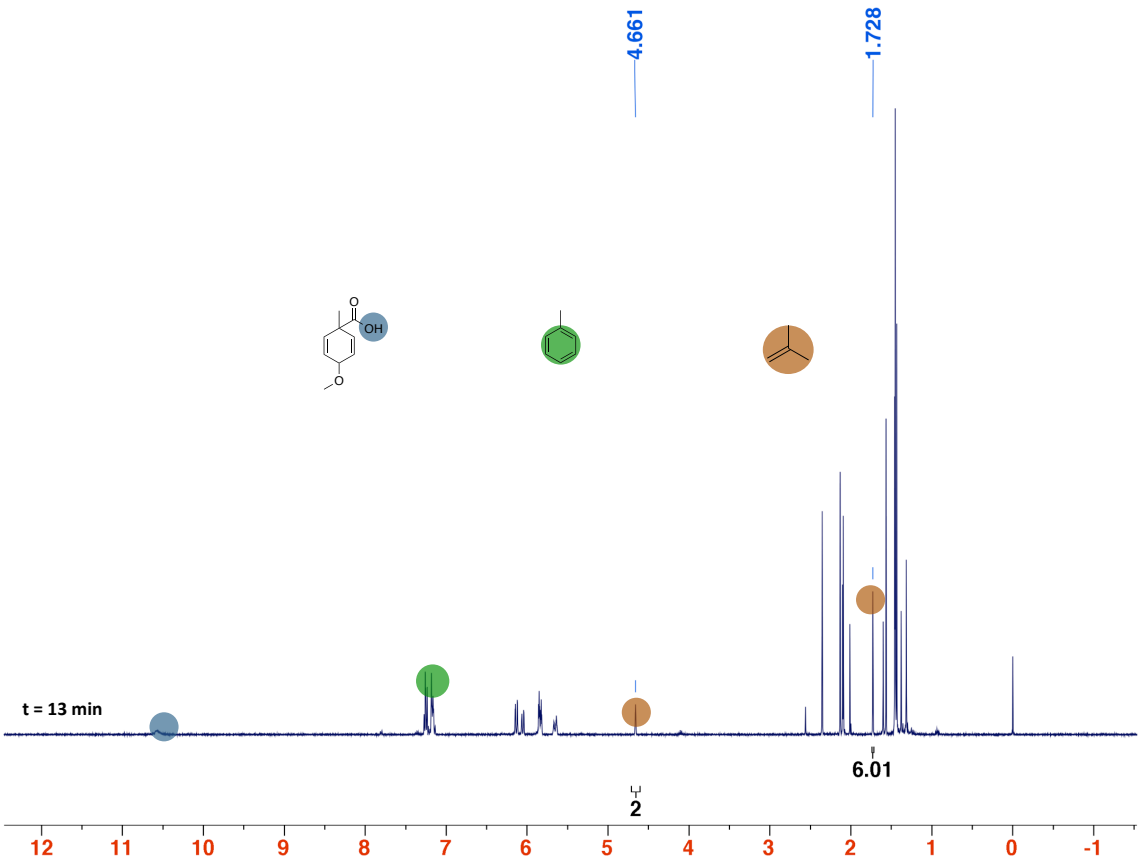

Figure B.2: Full spectrum of Figure 6.7

Appendix C: Direct C-C Coupling of Methanol and Allenes Employing a Homogeneous Iridium Catalyst(*183*)

Methanol is an abundant (35 million metric tons per year), renewable chemical feedstock, yet its use as a one-carbon building block in fine chemical synthesis is highly underdeveloped. Here, using a homogenous iridium catalyst developed in our laboratory, we report a direct, byproduct-free C-C coupling of methanol and allenes to furnish higher alcohols that incorporate all-carbon quaternary centers. A catalytic mechanism involving turnover-limiting methanol oxidation, a consequence of the high energetic demand of methanol dehydrogenation, is corroborated through a series of competition kinetics experiments. This process represents the first catalytic C-C coupling of methanol to provide discrete products of hydrohydroxymethylation.

C.1 MAIN

The development of byproduct-free catalytic C-C bond formations that employ abundant, renewable feedstocks represents an important step in defining sustainable paradigms for bulk and fine chemical manufacture.(*184-187*) With an annual global production estimated at 35 million metric tons per year (close to 12 billion gallons), methanol is vastly abundant.(*188*) However, use of methanol as a C1-feedstock in catalytic C-C coupling is restricted to dehydrative oligomerizations, such as the methanol-to-gasoline (MTG)(*189*) and methanol-to-olefins (MTO)(*190*) processes,(*189-194*) and methanol carbonylation (the Monsanto and Cativa processes),(*195-198*) the

latter being the second largest volume application of homogenous catalysis. Homogeneous catalytic C-C couplings of methanol beyond carbonylative processes remain highly uncommon.(*189-199*)

Alkene hydroformylation is the largest volume application of homogenous metal catalysis and may be viewed as the prototypical "C-C bond forming hydrogenation."(*200*) In the course of developing hydrogen-mediated C-C couplings beyond hydroformylation, our laboratory uncovered a broad class of catalytic transformations in which alcohols and π-unsaturated reactants are directly converted to products of formal carbinol C-H functionalization or "*hydrohydroxyalkylation.*"(*201-203*) In such transformations, removal of hydrogen from an alcohol reactant, an oxidation, generates an aldehyde and a metal hydride, which triggers reductive generation of a transient organometallic nucleophile via hydrometallation of a p-unsaturated reactant. The resulting electrophile-nucleophile pair combines to form products of carbonyl addition."(*204-217*) In this way, carbonyl addition is achieved from the alcohol oxidation level in the absence of stoichiometric byproducts. Further, by merging alcohol oxidation and C-C bond construction events, one circumvents discrete alcohol oxidation and use of pre-metallated nucleophiles, which typically are required for carbonyl additions of non-stabilized carbanions, while providing access to more tractable synthetic building blocks in the form of alcohols.

While catalytic C-C couplings of various p-unsaturated reactants have been achieved using higher alcohols, (*204-217*) direct C-C couplings of methanol have proven elusive, likely due to the relatively high energetic demand of methanol dehydrogenation

(DH = +84 kJ/mol) compared to the dehydrogenation of higher alcohols, such as ethanol (DH = +68 kJ/mol).(*218-220*) Here, using a homogenous iridium catalyst developed in our laboratory, we report the first catalytic C-C couplings of methanol to furnish discrete products of hydrohydroxymethylation, as demonstrated by the regioselective conversion of 1,1-disubstituted allenes **1a**-**1l** to homoallylic neopentyl alcohols **2a**-**2l**. Notably, these transformations promote the direct conversion of methanol to higher alcohols in the absence of stoichiometric byproducts.

C.2 RESULTS

In an initial series of experiments, ruthenium(*204*, *206-209*, *221*) and iridium(*210-217*) complexes that had proven effective in catalytic C-C couplings of π-unsaturated reactants to higher alcohols were assayed in corresponding couplings of methanol. Consistent with prior observations,(*222*) the ruthenium complexes established thusfar(*202*, *222*) are inefficient in attempted catalytic C-C couplings of methanol. In contrast, the *ortho*-cyclometallated π-allyl iridium *C,O*-benzoate complex(*212*) derived from $[Ir(cod)Cl]_2$, allyl acetate, 3-nitrobenzoic acid and BIPHEP [2,2'-bis(diphenylphosphino)biphenyl] catalyzes the C-C coupling of methanol to 1,1-disubstituted allene **1a** to provide the homoallylic neopentyl alcohol **2a** in 29% isolated yield (Table C.1, entry 1). By adjusting the loading of methanol and tuning the electronic features of the *C,O*-benzoate moiety, the yield of **2a** was increased to 44% yield (Table C.1, entry 6). After screening various chelating triarylphosphine ligands, it was found that the catalyst modified by DPPF [1,1'-bis(diphenylphosphino)ferrocene], designated

DPPF-I, was superior, ultimately providing **2a** in 67% isolated yield (Table C.1, entry 12). The structural assignment of **DPPF-I** has been corroborated by single crystal X-ray diffraction analysis (Figure C.1).

Optimal conditions employing precatalyst **DPPF-I** were applied to diverse 1,1-disubstituted allenes **1a**-**1l**. The corresponding homoallylic neopentyl alcohols **2a**-**2l** were isolated in yields ranging from 59-70% (Table C.2). As allenes **1a**-**1l** are employed as limiting reagents, the relatively modest yields were due to competitive protonolysis of the transient allyliridium complex to furnish products of allene transfer hydrogenation, which could be isolated from the reaction mixture. *Remarkably, although dehydrogenation of the primary alcohol products **2a**-**2l** is anticipated to be less endothermic than dehydrogenation of methanol,*(*218-220*) *further oxidation of the alcohol products **2a**-**2l** to the corresponding aldehydes is not observed*. At the stage of the homoallylic iridium alkoxide, a hexa-coordinate 18-electron complex, the olefin moiety of the product occupies the last remaining coordination site required for β-hydride elimination, disabling the kinetic pathway for product oxidation (Figure C.1).

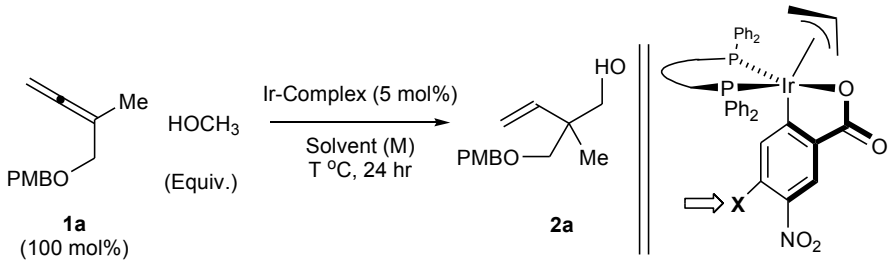

1a
(100 mol%)

2a

Ir-Complex

Entry	Ligand, X	MeOH (Equiv.)	Solvent (M)	T °C	Yield 2a
1	BIPHEP, H	10	PhMe (1 M)	80	29%
2	BIPHEP, H	15	PhMe (1 M)	80	39%
3	BIPHEP, H	20	PhMe (1 M)	80	36%
4	BIPHEP, OMe	15	PhMe (1 M)	80	37%
5	BIPHEP, CN	15	PhMe (1 M)	80	39%
6	BIPHEP, Cl	15	PhMe (1 M)	80	44%
7	DPPF, Cl	15	PhMe (1 M)	80	63%
⇨ **8**	**DPPF, Cl**	**15**	**PhMe (2 M)**	**80**	**67%**
9	DPPF, Cl	15	THF (2 M)	80	55%
10	DPPF, Cl	Neat	MeOH (1 M)	80	34%
11	DPPF, Cl	15	PhMe (2 M)	100	61%
12	DPPF, Cl	15	PhMe (2 M)	70	42%

[a]Yields are of material isolated by silica gel chromatography and represent the average of two runs. See Supporting Information for further details.

Table C.1. Selected optimization data in the iridium catalyzed C-C coupling of methanol to allene **1a**.[a]

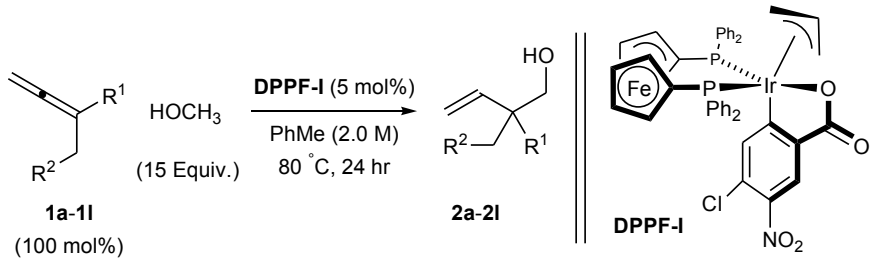

1a-**1l**
(100 mol%)

2a-**2l**

DPPF-I

1a, R^1 = Me, R^2 = OPMB	**1b**, R^1 = *n*-Pr, R^2 = OPMB	**1c**, R^1 = *i*-Pr, R^2 = OPMB
1d, R^1 = *c*-Pr, R^2 = OPMB	**1e**, R^1 = *c*-Pent, R^2 = OPMB	**1f**, R^1 = Bn, R^2 = OPMB
1g, R^1 = Me, R^2 = NPhth	**1h**, R^1 = *n*-Pr, R^2 = NPhth	**1i**, R^1 = *i*-Pr, R^2 = NPhth
1j, R^1 = *c*-Pr, R^2 = NPhth	**1k**, R^1 = *c*-Pent, R^2 = NPhth	**1l**, R^1 = Bn, R^2 = NPhth

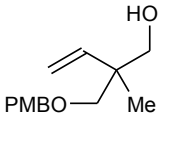

67% Yield, **2a**

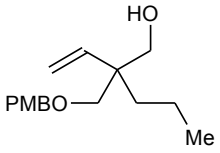

64% Yield, **2b**

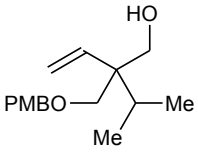

65% Yield, **2c**

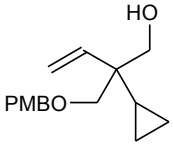

60% Yield, **2d**

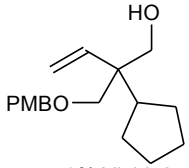

59% Yield, **2e**

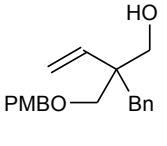

68% Yield, **2f**

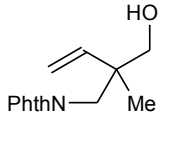

70% Yield, **2g**[b]

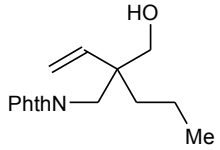

65% Yield, **2h**[b]

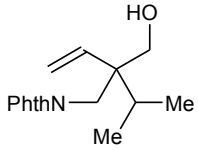

65% Yield, **2i**[b]

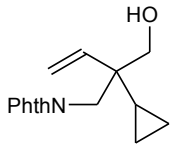

67% Yield, **2j**[b]

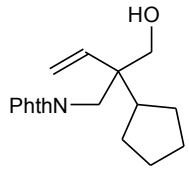

66% Yield, **2k**[c]

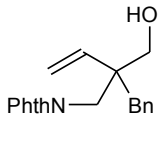

65% Yield, **2l**

[a]Yields are of material isolated by silica gel chromatography and represent the average of two runs. See Supporting Information for further details. [b]Reaction was conducted at 95 °C for 48 hr. [c]Reaction was conducted at 95 °C for 72 hr.

Table C.2. Iridium catalyzed C-C coupling of methanol to allenes **1a-1l**.[a]

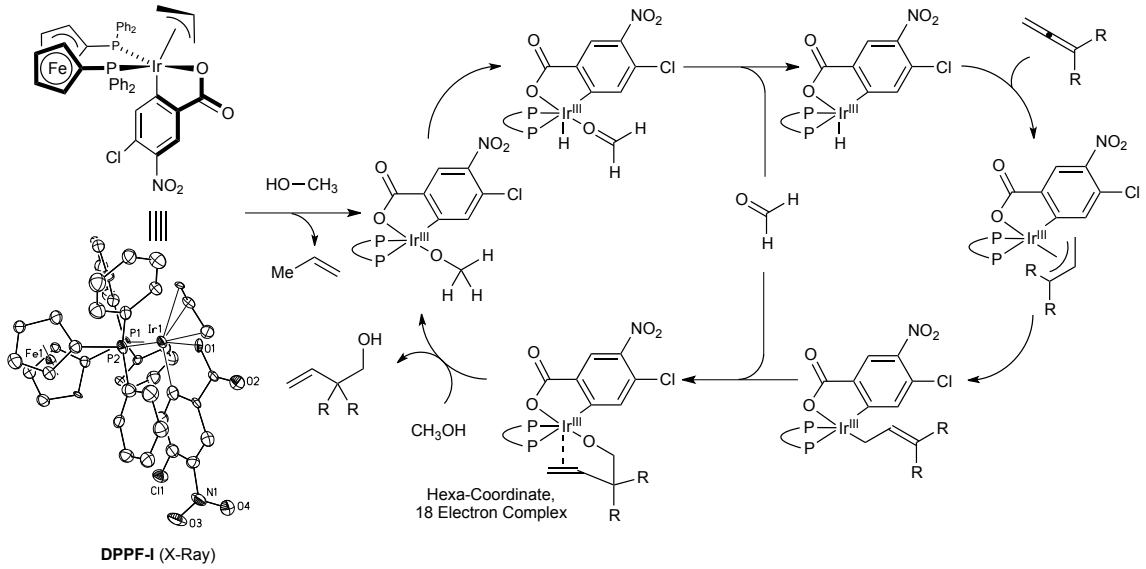

Figure C.1. General catalytic mechanism for the iridium catalyzed C-C coupling of methanol and the structure of **DPPF-I** as determined by single crystal X-ray diffraction analysis. Following protonolysis of the precatalyst p-allyl to enter the catalytic cycle, b-hydride elimination of the resulting iridium methoxide produces a transient iridium hydride species and releases formaldehyde. Hydrometallation of the allene and addition of the resulting Ir s-allyl to formaldehyde furnishes the observed alcohol. Further oxidation of the coupling product is prohibited by coordination of the homoallylic olefin to the iridium center.

Further insight into the catalytic mechanism is availed through deuterium labeling experiments (Figure C.2). Exposure of 1,1-disubstituted allene **1g** to standard conditions for iridium-catalyzed hydrohydroxymethylation employing d_4-methanol produced *deuterio*-**2g** (Figure C.2, a). As determined by ^{1}H and ^{2}H NMR analyses, complete deuterium incorporation (>99% ^{2}H) is observed at the carbinol methylene. However, deuterium incorporation at the interior vinylic position is incomplete (82% ^{2}H) and deuterium incorporation at the vinylic terminus (9% ^{2}H) also is observed. These data suggest reversible allene hydrometallation to form a transient vinyl iridium species. In contrast, only trace quantities of deuterium (<1% ^{2}H) were detected at the carbinol methylene when the experiment was carried out using CH_3OD (Figure C.2, b). In an effort to uncover the turn-over limiting step of the catalytic cycle, a series of competition kinetic experiments were performed (Figure C.2, c and d). The product obtained upon exposure of allene **1g** to equimolar quantities of methanol and d_4-methanol incorporates a lower proportion of deuterium at the carbinol methylene (33% ^{2}H), consistent with a normal primary kinetic isotope effect (k_H/k_D = 2.0). However, corresponding competition kinetic experiments involving benzyl alcohol and d_2-benzyl alcohol reveal no significant kinetic effect (k_H/k_D = 1.1) (Figure C.2, c and d).(*223-228*) These data suggest dehydrogenation/oxidation is turnover-limiting in the catalytic C-C coupling of methanol and 1,1-disubstituted allenes.

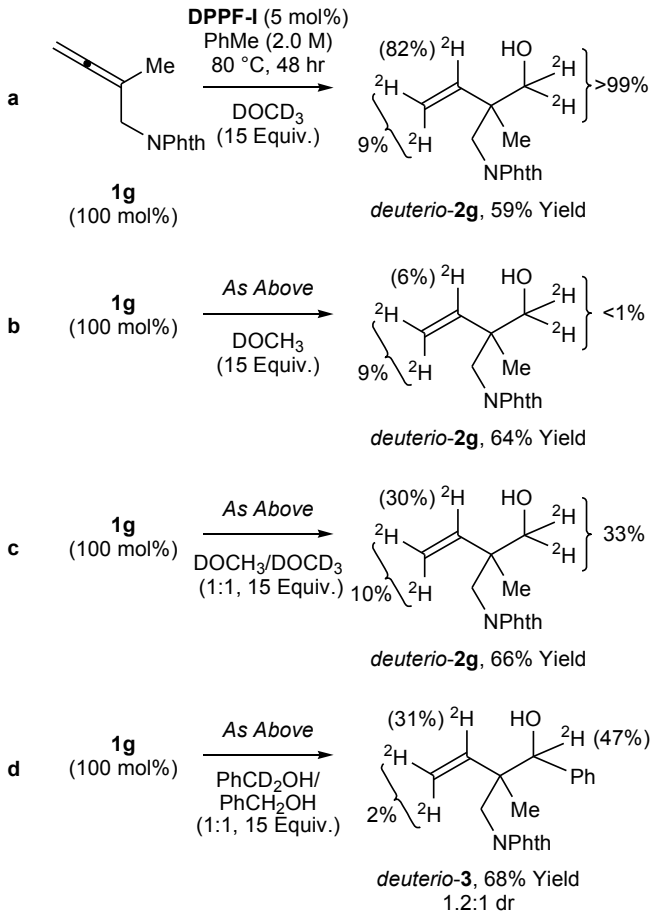

Figure C.2: Deuterium labeling and competition kinetics experiments. Experiments **a** and **b** corroborate reversible allene hydrometallation. Experiments c and d corroborate turnover-limiting methanol dehydrogenation.

C.3 DISCUSSION

Turnover-limiting dehydrogenation/oxidation in the catalytic C-C coupling of methanol and 1,1-disubstituted allenes, as corroborated by competition kinetics (Figure 2, c and d), are consistent with several empirical observations. For example, the temperature required for methanol C-C coupling (80-95 °C) is significantly higher than temperatures

employed in related hydrohydroxyalkylations of allylic or benzylic primary alcohols (30-40 °C).(*217*) The collective data suggest that while dehydrogenation/oxidation is the turnover-limiting event in C-C couplings of methanol, carbonyl addition is likely the turnover-limiting event in reactions of higher alcohols. This assertion is made despite the absence of a detectable secondary inverse isotope effect in the competition kinetic experiments involving benzyl alcohol and d_2-benzyl alcohol (Figure C2, d), as such isotope effects are often too small to easily detect. This divergence in turnover-limiting events stems not only from the relative energetic demands of methanol versus higher alcohol oxidation, but also the relative electrophilicities of the resulting aldehydes: monomeric formaldehyde is far more reactive toward carbonyl addition in comparison to substituted aldehydes.

The ability of iridium versus ruthenium-based catalysts to promote catalytic C-C couplings of methanol is consistent with the observed change in turnover-limiting events. The high energetic demand of methanol dehydrogenation can be attenuated through stabilization of the resulting metal hydride. Third row transition metals such as iridium generally form stronger metal-hydrogen bonds than second row transition metals.(*229*) Formation of a strong Ir-H bond compensates for the loss of a strong methanol C-H bond, which may, in accordance with Hammond's postulate, make the activation barrier of the methanol dehydrogenation event less endothermic.

In summary, we report the first catalytic C-C coupling of methanol to provide discrete products of hydrohydroxymethylation, as illustrated in hydrohydroxymethylations of 1,1-disubstituted allenes **1a-1l** to form homoallylic

neopentyl alcohols **2a**-**2l**. Isotopic labeling studies, including competition kinetics experiments, corroborate reversible allene hydrometallation and turnover-limiting methanol dehydrogenation/oxidation. Future studies will focus on the development of second-generation catalysts for enantio- and diastereoselective alcohol-unsaturate C-C couplings, including enantioselective variants of the present transformation.

C.4 EXPERIMENTAL

All reactions were run under an atmosphere of argon. Tetrahydrofuran (THF) and toluene were obtained from Pure-Solv MD-5 Solvent Purification System (Innovative Technology). Anhydrous solvents were transferred by oven-dried syringe. Sealed tubes (13×100 mm^2) were purchased from Fisher Scientific and were dried in an oven overnight and cooled under a stream of argon prior to use. Cesium carbonate was purchased from Alfa Aesar and was used directly without further purification. Allyl acetate was purchased from Sigma-Aldrich and purified by distillation prior to use. Methanol was distilled from magnesium and stored over 3Å molecular sieves under an argon atmosphere. Analytical thin-layer chromatography (TLC) was carried out using 0.25 mm commercial silica gel plates (Dynamic Adsorbents F_{254}). Visualization was accomplished with UV light followed by dipping in a *p*-anisaldehyde solution and heating. Purification of reaction products was carried out by flash column chromatography using Silicycle silica gel (40-63 ìm).

C.5 SPECTROSCOPY & SPECTROMERTY

Infrared spectra were recorded on a Thermo Nicolet 380 spectrometer. High-resolution mass spectra (HRMS) were obtained on a Karatos MS9 and are reported as m/z (relative intensity). Accurate masses are reported for the molecular ion (M+H, M or M-H) or a suitable fragment ion. ^{1}H-NMR spectra were recorded on Varian Gemini (300 MHz) or Varian Gemini (400 MHz) spectrometers at ambient temperature unless otherwise noted and are reported in ppm using solvent as the internal standard ($CDCl_3$ at 7.26 ppm, C_6D_6 at 7.15 ppm, $(CD_3)_2CO$ at 2.05 or CD_3OD at 3.31). Data are reported as: multiplicity (s = singlet, d = doublet, t = triplet, q = quartet, m = multiplet), integration and coupling constant(s) in Hz. ^{13}C-NMR spectra were recorded on a Varian Gemini (75 MHz) or Varian Gemini (100 MHz) spectrometer. Chemical shifts are reported in ppm from tetramethylsilane, with the residual solvent resonance employed as the internal standard ($CDCl_3$ at 77.0 ppm).

C.6 GENERAL METHODS

DPPF-I (14.8 mg, 0.0150 mmol, 5 mol%) and allene **1g** (0.642 g, 0.300 mmol, 100 mol%) were added to an oven-dried sealed pressure tube equipped with a magnetic stir bar. The tube was capped with a rubber septum and was purged with argon for 5 minutes. Toluene (0.15 mL, 2.0 M) and methanol (0.120 mL, 4.50 mmol, 1500 mol%) were added via syringe. The rubber septum was removed and the pressure tube was immediately sealed with a plastic screwcap. The reaction mixture was allowed to stir at

95 °C for 48 h. The tube was cooled to room temperature and solvents were removed *in vacuo*. The reaction mixture was subjected to column chromatography (SiO_2; 12% EtOAc/hexanes) to provide neopentyl alcohol **2g** as a white powder (0.052 g, 70%).

C.6.1 Preparation of *DPPF*-I:

A pressure tube equipped with a magnetic stirbar was charged with $[Ir(cod)Cl]_2$ (416.6 mg, 0.62 mmol, 100 mol%), 1,1'-bis(diphenylphosphino)-ferrocene (DPPF, 687.6 mg, 1.24 mmol, 200 mol%), Cs_2CO_3 (808.3 mg, 2.48 mmol, 400 mol%) and 4-Cl-3-NO_2BzOH (500 mg, 2.48 mmol, 400 mol%). The tube was purged with argon and an outlet for 5 minutes, followed by the addition of allyl acetate (340μL, 3.1 mmol, 500 mol%) in THF (12.4 mL, 0.05 M). The mixture was stirred for 30 min at room temperature under argon. The reaction mixture was then stirred for 90 min at 80 °C. Upon cooling to ambient temperature, the reaction mixture was diluted with CH_2Cl_2 (10 mL), filtered through a celite plug, washed with CH_2Cl_2 (50 mL) and concentrated *in vacuo* at ambient temperature. The compound was purified by flash chromatography (SiO_2, 20% Et_2O/CH_2Cl_2) and concentrated *in vacuo* at ambient temperature. A magnetic stirbar is added and the light brown gum was dissolved in 3 mL THF, stirred and precipitated upon rapid addition of 30 mL HPLC grade hexanes. Gravity filtration, followed by removal of trace solvents *in vacuo* gives a bright yellow powder (1.11 g, 1.13 mmol, 91 % yield).

A small amount of the powder was recrystallized by slow diffusion of Et_2O into

CH_2Cl_2 at ambient temperature to give small orange crystals. Single crystal X-ray diffraction data has been deposited in the CSD.

C.6.2 Preparation of Allenes 1a-1f

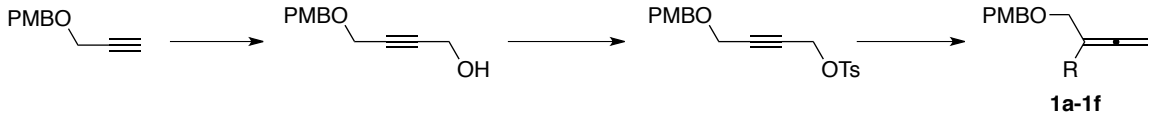

1a-1f

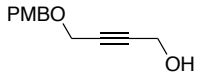

4-(4-Methoxybenzyloxy)buy-2-yn-1-ol was synthesized according to the procedure of Sabitha and coworkers.[1] To a stirred -78 ºC solution of paramethoxylbenzylpropargylether (3.4 g, 20 mmol) and 2-propylmagensium bromide (2.0 M, 22 mmol) in anhydrous THF (10 mL) was added paraformaldehyde (2.0g, 22 mmol) portionwise and allowed to slowly warm to room temperature while stirring for 16 h. The reaction was quenched with aqueous NH_4Cl (20 mL) and extracted with EtOAc (20 mL x 3). The combined organic layer was washed with brine, dried over $NaSO_4$, concentrated and purified by column chromatography (1% MeOH/CH_2Cl_2) to yield a colorless oil (3.9 g, 19 mmol, 95 %). The spectroscopic properties matched those reported in the literature.(*230*)

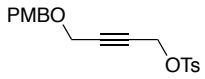

4-(4-Methoxybenzyloxy)but-2-ynyltosylate was synthesized according to the general procedure of Posner and coworkers.[2] To a solution of 4-(4-methoxybenzyloxy)buy-2-yn-1-ol (1.8g, 8.6 mmol) in Et_2O (43 mL) was added freshly ground KOH (2.4 g, 43mmol). The mixture was cooled to -30 °C, and tosyl chloride (1.8g, 9.5 mmol) was added in one portion. After stirring at -30 °C for 3 h, the

mixture was added to water (10 mL), and the aqueous layer was extracted with EtOAc (3 × 15 mL). The combined organic layers were rinsed with brine, dried over $MgSO_4$, concentrated *in vacuo*, and purified by flash column chromatography (25% EtOAc/hexanes) to give the product as a colorless oil (2.8 g, 8.2 mmol, 95 %). The spectroscopic properties matched those reported in the literature.(*231*)

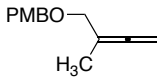

1-Methoxy-4-((2-methylbuta-2,3-dienyloxy)methyl)benzene, 1a. To a cooled (0 ºC) suspension of CuCN (5.15 g, 57.9 mmol) and LiCl (4.98 g, 115.8 mmol) in dry THF (95 mL) was added MeMgBr (19.3 mL of a 3.0 M in Et_2O, 57.9 mmol). After stirring for 30 minutes, the solution was further chilled to −78 ºC and 4-(4-methoxybenzyloxy)but-2-ynyltosylate (6.68 g, 19.3 mmol) was added dropwise over 60 minutes. After an hour of stirring at −78 ºC, the reaction was quenched with saturated NH_4Cl. After extraction with Et_2O (60 mL x 3), the combined organic layers were washed with brine (50 mL x 1), dried over Na_2SO_4, and concentrated. Purification by flash column chromatography (SiO_2, 13% EtOAc/Hexanes) gave allene **1a** (2.84 g, 13.9 mmol, 72%) as colorless oil. TLC R_f 0.68 (20% EtOAc/Hexanes); ^{1}H-NMR ($CDCl_3$, 400 MHz) 7.28-7.26 (m, 2H), 6.89-6.86 (m, 2H), 4.71-4.69 (m, 2H), 4.43 (s, 2H), 3.97 (t, J = 2.2 Hz, 2H), 3.80 (t, J = 3.5 Hz, 3H), 1.74 (t, J = 3.1 Hz, 3H); ^{13}C-NMR (300 MHz) 206.9, 159.0, 130.1, 129.3, 113.6, 95.6, 74.3, 71.4, 70.9, 55.1, 15.5; IR (neat): 2948, 2905, 2835, 1959, 1612, 1512, 1441, 1209, 1011, 846 cm^{-1}; HRMS (CI): Exact mass calcd for $C_{13}H_{15}O_2$ $[M]^+$: 203.1070. Found: 203.1072.

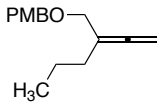

1-Methoxy-4-((2-vinylidenepentyloxy)methyl)benzene, 1b. To a cooled (0 ºC) suspension of CuCN (1.929 g, 21.68 mmol) and LiCl (1.864 g, 43.35 mmol) in dry THF (36 mL) was added PrMgCl (10.8 mL of a 2.0 M in THF, 21.7 mmol). After stirring for 30 minutes, the solution was further chilled to −78 ºC and 4-(4-methoxybenzyloxy)but-2-ynyltosylate (2.50 g, 7.22 mmol) was added dropwise over 60 minutes. After an hour of stirring at −78 ºC, the reaction was quenched with saturated NH_4Cl. After extraction with Et_2O (60 mL x 3), the combined organic layers were washed with brine (50 mL x 1), dried over Na_2SO_4, and concentrated. Purification by flash column chromatography (SiO_2, 15% EtOAc/Hexanes) gave allene **1b** (1.11 g, 4.77 mmol, 66 %) as colorless oil. TLC R_f 0.72 (20% EtOAc/Hexanes); ^{1}H-NMR ($CDCl_3$, 400 MHz) 7.29-7.26 (m, 2H), 6.91-6.86 (m, 2H), 4.78-4.74 (m, 2H), 4.43 (s, 2H), 4.00 (t, J = 2.0 Hz, 2H), 3.81 (s, 3H), 2.03 (tt, J = 7.3 Hz, J = 3.6 Hz, 2H), 1.56-1.45 (m, 2H), 0.94 (t, J = 7.3 Hz, 3H); ^{13}C-NMR (400 MHz) 206.8, 159.1, 130.4, 129.4, 113.7, 100.4, 75.5, 71.1, 70.7, 55.2, 31.1, 20.6, 13.9; IR (neat): 3313, 2956, 2931, 2869, 1956, 1612, 1585, 1512, 1463, 1356, 1301, 1245, 1172, 1067, 1035, 942, 844, 819, 757, 709 cm^{-1}; HRMS (CI): Exact mass calcd for $C_{15}H_{20}O_2$ $[M]^+$: 232.1463. Found: 232.1464.

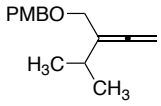

1-((2-Isopropylbuta-2,3-dienyloxy)methyl)-4-methoxybenzene, 1c: To a cooled (0 ºC) suspension of CuCN (1.929 g 21.68 mmol) and LiCl (1.864 g, 43.35 mmol) in dry THF (36.0 mL) was added *i*- PrMgBr (10.8 mL of a 2.0 M in THF, 21.7 mmol). After stirring for 30 minutes, the solution was further chilled to −78 ºC and 4-(4-methoxybenzyloxy)but-2-ynyltosylate (2.50 g, 7.22 mmol) was added dropwise over

60 minutes. After an hour of stirring at −78 ºC, the reaction was quenched with saturated NH_4Cl. After extraction with Et_2O (50 mL x 3), the combined organic layers were washed with brine (50 mL x 1), dried over Na_2SO_4, and concentrated. Purification by flash column chromatography (SiO_2, 15 % EtOAc/Hexanes) gave allene **1c** (1.04 g, 4.48 mmol, 62 %) as colorless oil. TLC R_f 0.72 (20% EtOAc/Hexanes); ^{1}H-NMR ($CDCl_3$, 300 MHz) δ 7.26 (d, *J* = 8.3 Hz, 2H), 6.87 (d, *J* = 8.3 Hz, 2H), 4.80-4.78 (m, 2H), 4.42 (s, 2H), 4.04 (s, 2H), 3.80 (s, 3H), 2.31 (septet of t, J = 6.8 Hz, J = 3.4 Hz, 1H), 1.06 (d, *J* = 6.8 Hz, 6H); ^{13}C-NMR (75 MHz) 206.0, 159.1, 130.4, 129.4, 106.7, 71.2, 69.6, 55.2, 27.4, 21.5; IR (neat): 2960, 2932, 2868, 2836, 1954, 1718, 1612, 1513, 1246, 1062, 1034, 845, 819 cm^{-1}; HRMS (CI): Exact mass calcd for $C_{15}H_{20}O_2$ $[M]^+$: 232.1463. Found: 232.1465.

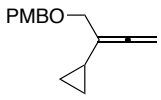

1-((2-Cyclopropylbuta-2,3-dienyloxy)methyl)-4-methoxybenzene, 1d: To a cooled (0 ºC) suspension of CuCN (1.543 g 17.34 mmol) and LiCl (1.491 g, 34.68 mmol) in dry THF (6.0 mL) was added *c*- PrMgBr (34.7 mL of a 0.5 M in THF, 17.34 mmol). After stirring for 30 minutes, the solution was further chilled to −78 ºC and 4-(4-methoxybenzyloxy)but-2-ynyltosylate (2.00 g, 5.78 mmol) was added dropwise over 60 minutes. After an hour of stirring at −78 ºC, the reaction was quenched with saturated NH_4Cl. After extraction with Et_2O (50 mL x 3), the combined organic layers were washed with brine (50 mL x 1), dried over Na_2SO_4, and concentrated. Purification by flash column chromatography (SiO_2, 15 % EtOAc/Hexanes) gave allene **1d** (932 mg, 4.05 mmol, 70 %) as colorless oil. TLC R_f 0.67 (20% EtOAc/Hexanes); ^{1}H-NMR

($CDCl_3$, 400 MHz) δ 7.28 (d, *J* = 8.7 Hz, 2H), 6.88 (d, *J* = 8.7 Hz, 2H), 4.80 (dt, *J* = 2.5 Hz, 2.1 Hz, 2H), 4.46 (s, 2H), 4.07 (t, *J* = 2.1 Hz, 2H), 3.80 (s, 3H), 1.26 (ttt, *J* = 7.4, 3.3, 2.5 Hz, 1H), 0.72-0.68 (m, 2H), 0.47-0.43 (m, 2H); ^{13}C-NMR (75 MHz) 205.6, 159.1, 130.4, 129.5, 113.7, 103.9, 77.1, 71.1, 70.7, 55.2, 9.6, 6.4; IR (neat): 3000, 2933, 2835, 1953, 1716, 1512, 1245, 1073, 1034, 847, 817 cm^{-1}; HRMS (CI): Exact mass calcd for $C_{15}H_{17}O_2$ $[M-H]^-$: 229.1231. Found: 229.1229.

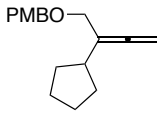

1-((2-Cyclopentylbuta-2,3-dienyloxy)methyl)-4-methoxybenzene, 1e: To a cooled (0 ºC) suspension of CuCN (2.315 g 26.01 mmol) and LiCl (2.237 g, 52.02 mmol) in dry THF (105.9 mL) was added *c*-C_5H_9MgBr (13.0 mL of a 2.0 M in Et_2O, 26.0 mmol). After stirring for 30 minutes, the solution was further chilled to −78 ºC and 4-(4-methoxybenzyloxy)but-2-ynyltosylate (7.21g, 21.19 mmol) was added dropwise over 60 minutes. After an hour of stirring at −78 ºC, the reaction was quenched with saturated NH_4Cl. After extraction with Et_2O (50 mL x 3), the combined organic layers were washed with brine (50 mL x 1), dried over Na_2SO_4, and concentrated. Purification by flash column chromatography (SiO_2, 15 % EtOAc/Hexanes) gave allene **1e** (1.33 g, 5.14 mmol, 60 %) as colorless oil. TLC R_f 0.72 (20% EtOAc/Hexanes); ^{1}H-NMR ($CDCl_3$, 400 MHz) δ 7.30 (d, *J* = 8.7 Hz, 2H), 6.90 (d, *J* = 8.7 Hz, 2H), 4.81 (td, J = 3.0 Hz, 2.1 Hz, 2H), 4.46 (s, 2H), 4.07 (t, *J* = 2.1 Hz, 2H), 3.79 (s, 3H), 2.50 (ttt, *J* = 8.1 Hz, 7.4 Hz, 3.0 Hz, 1H), 1.91-1.84 (m, 2H), 1.73-1.44 (m, 6H); ^{13}C-NMR (100 MHz) 205.6, 159.0, 130.2, 129.2, 113.5, 104.6, 76.2, 71.0, 70.3, 54.9, 38.8, 31.4, 24.7; IR (neat): 2950, 2864, 1952, 1612, 1512, 1245, 1172, 1066, 1035, 843, 819 cm^{-1}; HRMS (CI): Exact mass

calcd for $C_{17}H_{22}O_2$ [M-H]$^-$: 258.1620. Found: 258.1598.

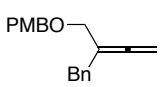

1-((2-Benzylbuta-2,3-dienyloxy)methyl)-4-methoxybenzene, 1f: To a cooled (0 ºC) suspension of CuCN (2.670 g, 30.00 mmol) and LiCl (2.580 g, 60.00 mmol) in dry THF (48.0 mL) was added freshly prepared BnMgBr (18.8 mL of a 1.6 M in Et_2O, 30 mmol) via a cannula. After stirring for 30 minutes, the solution was further chilled to −78 ºC and 4-(4-methoxybenzyloxy)but-2-ynyltosylate (3.460 g, 10.00 mmol) was added dropwise over 60 minutes. After an hour of stirring at −78 ºC, the reaction was quenched with saturated NH_4Cl. After extraction with Et_2O (50 mL x 3), the combined organic layers were washed with brine (50 mL x 1), dried over Na_2SO_4, and concentrated. Purification by flash column chromatography (SiO_2, 2% EtOAc/Hexanes) gave allene **1f** (1.07 g, 3.82 mmol, 38 %) as colorless oil. TLC R_f 0.63 (20 % EtOAc/Hexanes); ^{1}H-NMR ($CDCl_3$, 300 MHz) δ 7.30-7.18 (m, 7H), 6.88-6.85 (m, 2H), 4.75-4.73 (m, 2H), 4.41 (s, 2H), 3.94 (s, 2H), 3.80 (s, 3H), 3.39 (s, 2H); ^{13}C-NMR (400 MHz) 207.4, 159.2, 139.1, 130.2, 129.5, 129.0, 128.2, 126.2, 113.7, 100.1, 75.5, 71.2, 69.6, 55.2, 36.1; IR (neat): 3027, 2907, 2835, 1957, 1611, 1512, 1245, 1172, 1069, 1033, 846, 818, 698 cm^{-1}; HRMS (CI): Exact mass calcd for $C_{19}H_{20}O_2$ [M-H]$^-$: 279.1385. Found: 279.1385.

C.6.3 Preparation of Allenes 1g-1l

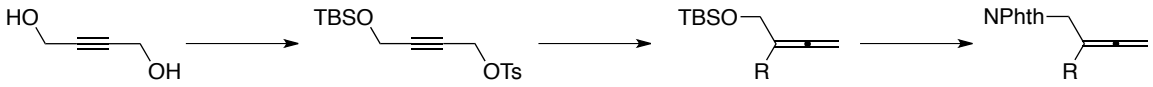

4-(tert-Butyldimethylsilyloxy)but-2-ynyltosylate was prepared according to the procedure of Garcia and coworkers.(*232*)

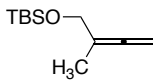

tert-Butyldimethyl(2-vinylidenepropyloxy)silane: To a cooled (0 oC) suspension of CuCN (2.325 g, 26.43 mmol) and LiCl (2.272 g, 52.86 mmol) in dry THF (33.6 mL) was added freshly prepared MeMgI (25 mL of a 1.1 M in Et_2O, 26.40 mmol) via a cannula. After stirring for 30 minutes, the solution was further chilled to −78 ºC and 4-(*tert*-butyldimethylsilyloxy)but-2-ynyltosylate (3.00 g, 8.81 mmol) was added dropwise over 60 minutes. After an hour of stirring at −78 ºC, the reaction was quenched with saturated NH_4Cl. After extraction with Et_2O (50 mL x 3), the combined organic layers were washed with brine (50 mL x 1), dried over Na_2SO_4, and concentrated. Purification by flash column chromatography (SiO_2, 2% EtOAc/Hexanes) gave the titled compound (1.40 g, 7.06 mmol, 80 %) as colorless oil. Spectral data was consistent with that recorded in the literature.(*233*)

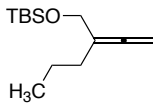

tert-Butyldimethyl(2-vinylidenepentyloxy)silane: To a cooled (0 ºC) suspension of CuCN (5.69 g, 63.4 mmol) and LiCl (5.39 g, 127 mmol) in dry THF (83 mL) was added *n*-PrMgCl (31.7 mL of a 2.0 M in Et_2O, 63.4 mmol). After stirring for 30 minutes, the solution was further chilled to −78 ºC and 4-(*tert*-butyldimethylsilyloxy)but-2-ynyltosylate (7.50 g, 21.15 mmol) was added dropwise over

60 minutes. After an hour of stirring at −78 ºC, the reaction was quenched with saturated NH_4Cl. After extraction with Et_2O (60 mL x 3), the combined organic layers were washed with brine (50 mL x 1), dried over Na_2SO_4, and concentrated. Purification by flash column chromatography (SiO_2, 2 % EtOAc/Hexanes) gave the titled compound 3.28 g, 14.4 mmol, 68 %) as a colorless oil. TLC R_f 0.31 (100 % Hexanes); ^{1}H-NMR ($CDCl_3$, 300 MHz) δ 4.74 (tt, *J* = 3.3, 2.5 Hz, 2H), 4.15 (t, *J* = 2.5 Hz, 2H), 2.00 (tt, *J* = 7.6, 3.3 Hz, 2H), 1.49 (qt, *J* = 7.6, 7.3 Hz, 2H), 0.95 (t, *J* = 7.3 Hz, 3H), 0.93 (s, 9H), 0.09 (s, 6H); ^{13}C-NMR (100 MHz) 205.6, 103.4, 76.0, 64.3, 30.6, 25.9, 20.7, 18.4, 13.9, - 5.3; IR (neat): 2956, 2929, 2857, 1959, 1463, 1253, 1070, 800, 774 cm^{-1}; HRMS (CI): Exact mass calcd for $C_{13}H_{26}OSi$ $[M+H]^+$: 227.2831. Found: 227.1831.

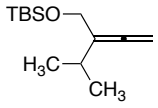

tert-Butyl(2-isopropylbuta-2,3-dienyloxy)dimethylsilane: To a cooled (0 ºC) suspension of CuCN (5.660 g, 63.56 mmol) and LiCl (5.470 g, 127.1 mmol) in dry THF (105.9 mL) was added *i*-PrMgCl (31.8 mL of a 2.0 M in THF, 63.6 mmol). After stirring for 30 minutes, the solution was further chilled to −78 ºC and 4-(*tert*-butyldimethylsilyloxy)but-2-ynyltosylate (7.210 g, 21.19 mmol) was added dropwise over 60 minutes. After an hour of stirring at −78 oC, the reaction was quenched with saturated NH_4Cl. After extraction with Et_2O (60 mL x 3), the combined organic layers were washed with brine (50 mL x 1), dried over Na_2SO_4, and concentrated. Purification by flash column chromatography (SiO_2, 2 % EtOAc/Hexanes) gave the titled compound (3.36 g, 14.8 mmol, 70 %) as colorless oil. TLC R_f 0.34 (100 % Hexanes); ^{1}H-NMR ($CDCl_3$, 400 MHz) δ 4.76 (td, *J* = 2.6, 2.6 Hz, 2H), 4.18 (t, *J* = 2.6 Hz, 2H), 2.28

(septet of t, J = 6.8, 2.6 Hz, 1H), 1.04 (d, J = 6.8 Hz, 6H), 0.90 (s, 9H), 0.07 (s, 6H); ^{13}C-NMR (100 MHz) 204.8, 109.9, 77.1, 63.1, 26.9, 25.9, 21.6, 18.4, - 5.3; IR (neat): 2958, 2929, 2857, 1956, 1463, 1252, 1062, 800, 774 cm^{-1}; HRMS (CI): Exact mass calcd for $C_{13}H_{26}OSi$ $[M+H]^+$: 227.2831. Found: 227.1831.

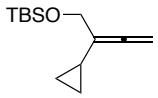

tert-Butyl(2-cyclopropylbuta-2,3-dienyloxy)dimethylsilane: To a cooled (0 ºC) suspension of CuCN (4.700 g, 52.86 mmol) and LiCl (4.550 g, 105.7 mmol) in dry THF (11.8 mL) was added *c*-PrMgBr (105.7 mL of a 0.5 M in THF, 52.86 mmol). After stirring for 30 minutes, the solution was further chilled to −78 ºC and 4-(*tert*-butyldimethylsilyloxy)but-2-ynyltosylate (6.000 g, 17.62 mmol) was added dropwise over 60 minutes. After an hour of stirring at −78 ºC, the reaction was quenched with saturated NH_4Cl. After extraction with Et_2O (60 mL x 3), the combined organic layers were washed with brine (50 mL x 1), dried over Na_2SO_4, and concentrated. Purification by flash column chromatography (SiO_2, 2% EtOAc/Hexanes) gave the titled compound (2.96 g, 13.2 mmol, 74 %) as colorless oil. TLC R_f 0.31 (100 % Hexanes); ^{1}H-NMR ($CDCl_3$, 400 MHz) δ 4.76 (td, J = 2.6, 2.6 Hz, 2H), 4.21 (t, J = 2.6 Hz, 2H), 1.22 (ttt, J = 7.9, 5.3, 2.6 Hz, 1H), 0.91 (s, 9H), 0.69-0.64 (m, 2H), 0.44-0.40 (m, 2H), 0.08 (s, 6H); ^{13}C-NMR (100 MHz) 204.6, 107.0, 77.6, 64.2, 25.9, 18.4, 9.2, 6.2, -5.2; IR (neat): 2954, 2928, 2856, 1956, 1471, 1462, 1253, 1075, 833, 773 cm^{-1}; HRMS (CI): Exact mass calcd for $C_{13}H_{25}OSi$ $[M+H]^+$: 225.1675. Found: 225.1673.

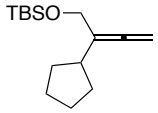

tert-Butyl(2-cyclopentylbuta-2,3-dienyloxy)dimethylsilane: To a cooled (0

ºC) suspension of CuCN (4.794 g, 52.86 mmol) and LiCl (4.546 g, 105.7 mmol) in dry THF (91.1 mL) was added *c*-C_5H_9MgBr (26.4 mL of a 2.0 M in Et_2O, 52.9 mmol). After stirring for 30 minutes, the solution was further chilled to −78 ºC and 4-(*tert*-butyldimethylsilyloxy)but-2-ynyltosylate (5.685 g, 16.69 mmol) was added dropwise over 60 minutes. After an hour of stirring at −78 ºC, the reaction was quenched with saturated NH_4Cl. After extraction with Et_2O (60 mL x 3), the combined organic layers were washed with brine (50 mL x 1), dried over Na_2SO_4, and concentrated. Purification by flash column chromatography (SiO_2, 2% EtOAc/Hexanes) gave the titled compound (3.19 g, 12.6 mmol, 76 %) as colorless oil. TLC R_f 0.40 (100 % Hexanes); ^{1}H-NMR ($CDCl_3$, 400 MHz) δ 4.75 (td, *J* = 3.0, 2.4 Hz, 2H), 4.17 (t, *J* = 2.4 Hz, 2H), 2.41 (ttt, *J* = 8.2, 7.5, 3.0 Hz, 1H), 1.85-1.77 (m, 2H), 1.67-1.39 (m, 6H), 0.90 (s, 9H), 0.07 (s, 6H); ^{13}C-NMR (100 MHz) 204.5, 108.1, 77.0, 64.0, 38.4, 31.6, 25.9, 24.9, 18.4, -5.3; IR (neat): 2953, 2928, 2857, 1955, 1471, 1462, 1252, 1067, 834, 773 cm^{-1}; HRMS (CI): Exact mass calcd for $C_{15}H_{29}OSi$ $[M+H]^+$: 253.1988. Found: 253.1989.

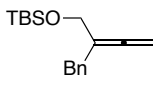

tert-Butyl(2-benzylbuta-2,3-dienyloxy)dimethylsilane: To a cooled (0 ºC) suspension of CuCN (2.325 g, 26.43 mmol) and LiCl (2.272 g, 52.86 mmol) in dry THF (33.6 mL) was added freshly prepared BnMgBr (25 mL of a 1.1 M solution in Et_2O, 26.40 mmol) via a cannula. After stirring for 30 minutes, the solution was further chilled to −78 ºC and 4-(tert-butyldimethylsilyloxy)but-2-ynyltosylate (3.00 g, 8.81 mmol) was added dropwise over 60 minutes. After an hour of stirring at −78 ºC, the reaction was quenched with saturated NH_4Cl. After extraction with Et_2O (50 mL x 3),

the combined organic layers were washed with brine (50 mL x 1), dried over Na_2SO_4, and concentrated. Purification by flash column chromatography (SiO_2, 2 % EtOAc/Hexanes) gave the titled compound (1.70 g, 6.17 mmol, 70 %) as colorless oil. TLC R_f 0.21 (100 % Hexanes); ^{1}H-NMR ($CDCl_3$, 400 MHz) δ 7.32-7.20 (m, 5H), 4.75-4.73 (m, 2H), 4.10 (t, *J* = 2.0 Hz, 2H), 3.39 (s, 2H), 0.93 (s, 9H), 0.06 (s, 6H); ^{13}C-NMR (100 MHz) 204.5, 108.1, 77.0, 64.0, 38.4, 31.6, 25.9, 24.9, 18.4, 5.3; IR (neat): 2953, 2928, 2856, 1960, 1494, 1253, 1069, 834, 774, 729, 697, 668 cm^{-1}; HRMS (CI): Exact mass calcd for $C_{17}H_{27}OSi$ $[M+H]^+$: 275.1831. Found: 275.1825.

C.6.4 Representative Procedure for TBS Deprotection/Mitsunobu Sequence to give Allenes 1g-1l:

In a 250 mL round-bottom flask equipped with a magnetic stirbar, the TBS-protected allenol (1 equiv, 13.2 mmol) was dissolved in Et_2O (0.5 M, 27 mL) and then cooled to 0 °C while stirring. Tetrabutylammonium fluoride (1.0 M in THF, 2 equiv, 26.5 mmol, 26.5 mL) was added dropwise over 5 min and the solution was stirred for 70 min and allowed to warm to room temperature. The reaction was quenched with a saturated solution of ammonium chloride and extracted three times with Et_2O. The combined organic extracts were dried over magnesium sulfate and evaporated under reduced pressure at 22°C until the volume was approximately 30 mL. The remaining solution of allenol in THF is transferred to a 500 mL round-bottom flask equipped with magnetic stirbar and rubber septum. To the flask is added THF (0.1 M, 132 mL), followed by triphenylphosphine (7.62 g, 29.0 mmol). The reaction is cooled to 0 °C and diisopropylethylamine (5.06 mL, 29.0 mmol) and phthalimide (3.88 g, 26.4 mmol) are

added. Diisopropyl azodicarboxylate (5.72 mL, 29.04 mmol, 2.2 equiv) is then added dropwise over 60 min. The flask is allowed to warm to ambient temperature and is stirred for an additional 30 minutes (monitored by TLC; EtOAc/Hexanes 20%). The reaction is quenched with saturated ammonium chloride, taken up in EtOAc, washed with brine, dried over magnesium sulfate and evaporated under reduced pressure. The crude allene is then purified by flash chromatography (SiO_2; 10% EtOAc/Hexanes) and recrystallized from hexanes to give a white crystalline material.

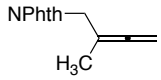

2-(2-Methylbuta-2,3-dienyl)isoindoline-1,3-dione, **1g***:* Performed on1 a 7.3 mmol scale. Isolated 1.39 g (6.5 mmol, 89%) after two steps. TLC R_f 0.42 (20% EtOAc/Hexanes); H NMR ($CDCl_3$, 300 MHz) δ 7.89-7.83 (m, 2H), 7.75-7.69 (m, 2H), 4.66 (qt, *J* = 3.5 Hz, 3.1 Hz, 2H), 4.21 (t, *J* = 3.5 Hz, 2H), 1.75 (t, *J* = 3.1 Hz, 3H); ^{13}C-NMR (75 MHz) 205.3, 167.9, 133.9, 132.0, 123.3, 95.2, 40.1, 16.2; IR (neat): 3051, 2978, 1966, 1767, 1701, 1613, 1380, 1359, 1334, 1087, 1037, 944, 756, 720, 707 cm-1; HRMS (CI): Exact mass calcd for $C_{13}H_{12}NO_2$ $[M+1]^+$: 214.0864. Found: 214.0868. M.p. 80.5 °C.

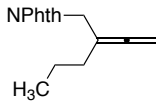

2-(2-Vinylidenepentyl)isoindoline-1,3-dione, **1h***:* Performed on a 13.2 mmol scale. Isolated 2.10 g (8.7 mmol, 66%) after two steps. TLC R_f 0.48 (20% EtOAc/Hexanes); ^{1}H-NMR ($CDCl_3$, 300 MHz) δ 7.88-7.83 (m, 2H), 7.75-7.70 (m, 2H), 4.71-4.69 (m, 2H), 4.22 (t, *J* = 3.3 Hz, 2H), 2.04-1.94 (m, 2H), 1.52 (tq, *J* = 7.6 Hz, 7.4 Hz, 2H), 0.95 (t, *J* = 7.4 Hz, 3H); ^{13}C-NMR (75 MHz) 204.8, 167.8, 133.8, 132.0,

123.2, 100.0, 78.6, 39.2, 31.7, 20.5, 13.7; IR (neat): 2957, 2922, 2871, 2359, 1960, 1764, 1708, 1613, 1465, 1425, 1390, 1318, 1190, 1120, 1081, 945, 865, 726, 707 cm-1; HRMS (CI): Exact mass calcd for $C_{15}H_{15}NO_2$ $[M]^+$: 241.1103. Found: 241.1100. M.p. 55.0 °C.

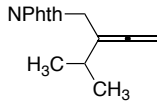

2-(2-iso-Propylbuta-2,3-dienyl)isoindoline-1,3-dione, **1i***:* Performed on a 11.2 mmol scale. Isolated 0.81 g (3.4 mmol, 30%) after two steps. TLC R_f 0.48 (20% EtOAc/Hexanes); ^{1}H-NMR ($CDCl_3$, 400 MHz) δ 7.87-7.83 (m, 2H), 7.73-7.69 (m, 2H), 4.71 (td, *J* = 3.6, 2.7 Hz, 2H), 4.26 (t, *J* = 3.6 Hz, 2H), 2.22 (septet of t, *J* = 6.8 Hz, 2.7 Hz, 1H), 1.11 (d, *J* = 6.8 Hz, 6H); ^{13}C-NMR (100 MHz) 203.6, 167.8, 133.8, 132.1, 123.2, 106.6, 79.8, 38.0, 28.5, 21.4; IR (neat): 3053, 2963, 2868, 1960, 1769, 1708, 1394, 1121, 1107, 946, 746, 711 cm-1; HRMS (CI): Exact mass calcd for $C_{15}H_{15}NO_2$ $[M]^+$: 241.1103. Found: 241.1100. M.p. 79.4 °C.

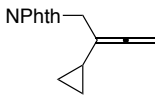

2-(2-Cyclopropylbuta-2,3-dienyl)isoindoline-1,3-dione, **1j***:* Performed on a 11.2 mmol scale. Isolated 2.32 g (9.7 mmol, 87%) after two steps. TLC R_f 0.44 (20% EtOAc/Hexanes); ^{1}H-NMR ($CDCl_3$, 400 MHz) δ 7.85 (dd, *J* = 5.4, 3.0 Hz, 2H), 7.72 (dd, *J* = 5.5, 3.0 Hz, 2H), 4.74 (td, *J* = 3.3, 2.6 Hz, 2H), 4.35 (t, *J* = 3.3 Hz, 2H), 1.18 (ttt, *J* = 7.9, 5.2, 2.6 Hz, 1H), 0.69-0.65 (m, 2H), 0.44-0.41 (m, 2H); ^{13}C-NMR (100 MHz) 204.0, 167.9, 133.8, 132.1, 123.2, 103.3, 79.6, 39.4, 10.0, 6.2; IR (neat): 2991, 2953, 2924, 1961, 1768, 1708, 1117, 866 cm^{-1}; HRMS (CI): Exact mass calcd for $C_{15}H_{13}NO_2$ $[M]^+$: 239.0946. Found: 239.0947. M.p. 83.7 °C.

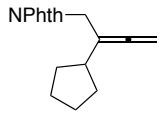

2-(2-Cyclopentylbuta-2,3-dienyl)isoindoline-1,3-dione, **1k**: Performed on a 11.9 mmol scale. Isolated 2.32 g (8.7 mmol, 73%) after two steps. TLC R_f 0.48 (20% EtOAc/Hexanes); ^{1}H-NMR ($CDCl_3$, 400 MHz) δ 7.86-7.81 (m, 2H), 7.72-7.67 (m, 2H), 4.67 (td, *J* = 3.6, 3.0 Hz, 2H), 4.24 (t, *J* = 3.6 Hz, 2H), 2.37 (ttt, *J* = 8.2, 7.0, 3.0 Hz, 1H), 1.90-1.81 (m, 2H), 1.70-1.45 (m, 6H); ^{13}C-NMR (100 MHz) 203.4, 167.9, 133.8, 132.1, 123.2, 104.5, 79.5, 39.6, 38.9, 31.5, 25.0; IR (neat): 2956, 2925, 2858, 2359, 2323, 1964, 1768, 1466, 1425, 1390, 1321, 1103, 942, 862, 738, 711 cm^{-1}; HRMS (CI): Exact mass calcd for $C_{17}H_{17}NO_2$ $[M]^+$: 267.1259. Found: 267.1260. M.p. 88.7 °C.

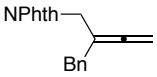

2-(2-Benzylbuta-2,3-dienyl)isoindoline-1,3-dione, **1l***:* Performed on a 5.4 mmol scale. Isolated 1.10 g (3.8 mmol, 70%) after two steps. TLC R_f 0.40 (20% EtOAc/Hexanes); ^{1}H-NMR ($CDCl_3$, 400 MHz) δ 7.82-7.76 (m, 2H), 7.70-7.64 (m, 2H), 7.27-7.22 (m, 4H), 7.16-7.11 (m, 1H), 4.75-4.71 (m, 2H), 4.21 (t, *J* = 3.1 Hz, 2H), 3.39 (t, *J* = 1.9 Hz, 2H); ^{13}C-NMR (100 MHz) 206.2, 167.8, 138.2, 133.8, 132.0, 128.7, 128.3, 126.3, 123.1, 99.1, 78.2, 38.9, 37.1; IR (neat): 3027, 2918, 1961, 1772, 1709, 1425, 1389, 1107, 947, 856, 721, 710, 698 cm^{-1}; HRMS (CI): Exact mass calcd for $C_{19}H_{15}NO_2$ $[M]^+$: 289.1103. Found: 289.1104. M.p. 45.8 °C.

C.11 Procedure for Allene Hydrohydroxymethylation and Spectral Data (Table C.2)

DPPF-**I** (14.8 mg, 0.015 mmol, 5 mol%) and allene (0.30 mmol, 100 mol%) were added to an oven-dried sealed tube equipped with a magnetic stirring bar. The tube was capped

with a rubber septum and was purged with argon and an outlet for 5 minutes. Toluene (2.0 M, 0.15 mL) and methanol (0.12 mL, 1500 mol%) were then added via syringe. The rubber septum was removed and the tube was immediately sealed with a plastic screwcap. The reaction mixture was allowed to stir at 80 °C or 95 °C for the time specified in Table 2 in the main manuscript. The tube was cooled to room temperature and solvents were removed *in vacuo*. Purification was carried out by column chromatography (SiO_2; EtOAc/Hexanes).

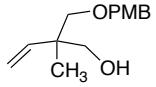

2-((4-Methoxybenzyloxy)methyl)-2-methylbut-3-en-1-ol, **2a***:* Isolated 0.047 g (average of two runs, 67%) as a clear colorless oil after column chromatography (12% EtOAc/Hexanes). TLC R_f 0.23 (20% EtOAc/Hexanes); ^{1}H-NMR ($CDCl_3$, 300 MHz) δ 7.25-7.22 (m, 2H), 6.89-6.84 (m, 2H), 5.83 (dd, *J* = 17.6, 11.1 Hz, 1H), 5.14-5.06 (m, 2H), 4.44 (s, 2H), 3.78 (s, 3H), 3.52 (t, *J* = 5.8 Hz, 2H), 3.43 (d, *J* = 8.8 Hz, 1H), 3.34 (d, *J* = 8.8 Hz, 1H), 2.57 (t, *J* = 5.8 Hz, 1H), 1.02 (s, 3H); ^{13}C-NMR (75 MHz) 159.1, 141.4, 130.0, 129.1, 114.2, 113.7, 76.4, 73.1, 69.2, 55.1, 42.6, 18.9; IR (neat): 3430, 2933, 2860, 1697, 1512, 1246, 1091, 1031, 819 cm^{-1}; HRMS (CI): Exact mass calcd for $C_{14}H_{20}O_3$ $[M]^+$: 236.1412. Found: 236.1414.

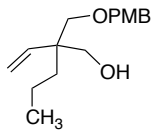

2-((4-Methoxybenzyloxy)methyl)-2-vinylpentan-1-ol, **2b***:* Isolated 0.051 g (average of two runs, 64%) as a clear colorless oil after column chromatography (12% EtOAc/Hexanes). TLC R_f 0.31 (20% EtOAc/Hexanes); ^{1}H-NMR ($CDCl_3$, 400 MHz) δ 7.30-7.22 (m, 2H), 6.90-6.86 (m, 2H),

5.64 (dd, *J* = 17.9, 11.2 Hz, 1H), 5.16 (dd, *J* = 11.2, 1.1 Hz, 1H), 5.01 (dd, *J* = 17.9, 1.1 Hz, 1H), 4.47 (d, *J* = 11.7 Hz, 1H), 4.44 (d, *J* = 11.7 Hz, 1H), 3.81 (s, 3H), 3.60 (d, *J* = 5.7 Hz, 2H), 3.52 (d, *J* = 8.9 Hz, 1H), 3.43 (d, *J* = 8.9 Hz, 1H), 2.56 (t, *J* = 6.0 Hz, 1H), 1.43-1.38 (m, 2H), 1.30-1.14 (m, 2H), 0.88 (t, *J* = 7.2 Hz, 3H); ^{13}C-NMR (100 MHz) 159.2, 140.5, 130.0, 129.2, 114.9, 113.8, 75.0, 73.3, 68.3, 55.2, 45.4, 35.3, 16.6, 14.8; IR (neat): 3475, 2956, 2931, 2870, 1586, 1513, 1246, 1089, 1035, 915, 820 cm^{-1}; HRMS (CI): Exact mass calcd for $C_{16}H_{24}O_3$ $[M]^+$: 264.1725. Found: 264.1725.

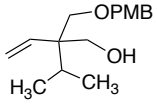

2-((4-Methoxybenzyloxy)methyl)-2-isopropylbut-3-en-1-ol, **2c***:* Isolated 0.052 g (average of two runs, 65%) as a clear colorless oil after column chromatography (12% EtOAc/Hexanes). TLC R_f 0.31 (20% EtOAc/Hexanes); ^{1}H-NMR ($CDCl_3$, 400 MHz) δ 7.26-7.23 (m, 2H), 6.89-6.87 (m, 2H), 5.62 (dd, *J* = 18.0, 11.3 Hz 1H), 5.19 (dd, *J* = 11.3, 1.0 Hz, 1H), 4.97 (dd, *J* = 18.0, 1.0 Hz, 1H), 4.49 (d, *J* = 11.7 Hz, 1H), 4.44 (d, *J* = 11.7 Hz, 1H), 3.81 (s, 3H), 3.76-3.66 (m, 2H), 3.61 (d, *J* = 9.0 Hz, 1H), 3.56 (d, *J* = 9.0 Hz, 1H), 2.79 (s, 1H), 2.08 (septet, *J* = 6.9 Hz, 1H), 0.87 (d, *J* = 6.9 Hz, 3H), 0.82 (d, *J* = 6.9 Hz, 3H); ^{13}C-NMR (100 MHz) 159.3, 137.5, 129.9, 129.2, 115.6, 113.8, 74.4, 73.3, 67.6, 55.3, 47.2, 28.3, 17.2, 17.1; IR (neat): 3456, 2960, 2874, 1612, 1512, 1245, 1079, 1033, 914, 819 cm^{-1}; HRMS (CI): Exact mass calcd for $C_{16}H_{24}O_3$ $[M]^+$: 264.1725. Found: 264.1727.

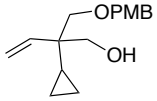

2-((4-Methoxybenzyloxy)methyl)-2-cyclopropylbut-3-en-1-ol, **2d.:** Isolated 0.047 g (average of two runs, 60%) as a clear colorless oil after column chromatography (12% EtOAc/Hexanes). TLC R_f 0.21 (20% EtOAc/Hexanes); ^{1}H-NMR ($CDCl_3$, 400 MHz) δ 7.26-7.24 (m, 2H), 6.90-6.87 (m, 2H), 5.41 (ddd, *J* = 17.8, 11.2, 0.8 Hz, 1H), 5.19 (dt, *J* = 11.2, 1.1 Hz, 1H), 5.07 (ddd, *J* = 17.8, 1.3, 1.0 Hz, 1H), 4.48 (s, 2H), 3.81 (d, *J* = 0.9 Hz, 3H), 3.75-3.67 (m, 2H), 3.59 (d, *J* = 9.0 Hz, 1H), 3.52 (dd, *J* = 9.0, 0.8 Hz, 1H), 2.61 (t, *J* = 6.1 Hz, 1H), 0.86-0.79 (m, 1H), 0.35-0.19 (m, 4H); ^{13}C-NMR (100 MHz) 159.2, 136.6, 130.0, 129.2, 116.7, 113.8, 75.5, 73.3, 68.6, 55.2, 44.5, 13.6, -0.85. -0.92; IR (neat): 3439, 3079, 3004, 2860, 2360, 1611, 1512, 1245, 1086, 1032, 918, 820 cm^{-1}; HRMS (CI): Exact mass calcd for $C_{16}H_{22}O_3$ $[M]^+$: 262.1569. Found: 262.1571.

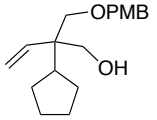

2-((4-Methoxybenzyloxy)methyl)-2-cyclopentylbut-3-en-1-ol, **2e**: Isolated 0.051 g (average of two runs, 59%) as a clear colorless oil after column chromatography (12% EtOAc/Hexanes). TLC R_f 0.31 (20% EtOAc/Hexanes); ^{1}H-NMR ($CDCl_3$, 400 MHz) δ 7.26-7.23 (m, 2H), 6.90-6.87 (m, 2H), 5.68 (dd, *J* = 18.0, 11.3 Hz, 1H), 5.22 (dd, *J* = 11.3, 1.2 Hz, 1H), 5.03 (dd, *J* = 18.0, 1.2 Hz, 1H), 4.48 (d, *J* = 11.7 Hz, 1H), 4.43 (d, *J* = 11.7 Hz, 1H), 3.80 (s, 3H), 3.71 (dd, *J* = 11.0, 5.1 Hz, 1H), 3.66 (dd, *J* = 11.0, 7.0 Hz, 1H), 3.62 (d, *J* = 9.0 Hz, 1H), 3.51 (d, *J* = 9.0 Hz, 1H), 2.81 (dd, *J* = 7.0, 5.1 Hz, 1H), 2.18-2.09 (m, 1H), 1.66-1.59 (m, 1H), 1.51-1.47 (m, 5H), 1.29-1.18 (m, 2H); ^{13}C-NMR (100 MHz) 159.2, 137.6, 129.9, 129.2, 116.2, 113.8, 75.3, 73.3, 68.3, 55.2, 46.9, 41.3, 26.5, 26.4, 25.3, 25.2; IR (neat): 3456, 2949, 2865, 1611, 1512, 1301, 1245,

1172, 1082, 1033, 915, 819 cm^{-1}; HRMS (CI): Exact mass calcd for $C_{18}H_{26}O_3$ $[M]^+$: 290.1882. Found: 290.1880.

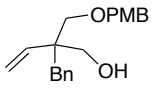

2-Benzyl-2-((4-methoxybenzyloxy)methyl)but-3-en-1-ol, **2f***:* Isolated 0.064 g (average of two runs, 68%) as a clear colorless oil after column chromatography (12% EtOAc/Hexanes). TLC R_f 0.23 (20% EtOAc/Hexanes); ^{1}H-NMR ($CDCl_3$, 400 MHz) δ 7.30-7.16 (m, 7H), 6.93-6.90 (m, 2H), 5.66 (dd, *J* = 18.0, 11.8 Hz, 1H), 5.16 (d, *J* = 11.8 Hz, 1H), 4.92 (d, *J* = 18.0 Hz, 1H), 4.48 (d, *J* = 11.7 Hz, 1H), 4.46 (d, *J* = 11.7 Hz, 1H), 3.82 (s, 3H), 3.66-3.58 (m, 2H), 3.48 (d, *J* = 8.9 Hz, 1H), 3.39 (d, *J* = 8.9 Hz, 1H), 2.86 (d, *J* = 13.2 Hz, 1H), 2.79 (d, *J* = 13.2 Hz, 1H), 2.58 (dd, *J* = 6.7, 5.1 Hz, 1H); ^{13}C-NMR (100 MHz) 159.3, 139.9, 137.3, 130.7, 129.9, 129.3, 127.7, 126.1, 115.4, 113.8, 73.8, 73.2, 67.5, 55.2, 46.2, 38.9; IR (neat): 3458, 3027, 2858, 1611, 1512, 1245, 1172, 1084, 1031, 819, 702 cm^{-1}; HRMS (CI): Exact mass calcd for $C_{20}H_{24}O_3$ $[M]^+$: 312.1725. Found: 312.1726.

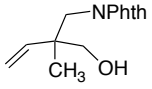

2-(2-(Hydroxymethyl)-2-methylbut-3-enyl)isoindoline-1,3-dione, **2g***:* Isolated 0.052 g (average of two runs, 70%) as a white powder after column chromatography (12% EtOAc/Hexanes). TLC R_f 0.17 (20% EtOAc/Hexanes); ^{1}H-NMR ($CDCl_3$, 400 MHz) δ 7.87 (dd, *J* = 5.5, 3.0 Hz, 2H), 7.76 (dd, *J* = 5.5, 3.0 Hz, 2H), 5.94 (dd, *J* = 17.7, 11.1 Hz, 1H), 5.14 (dd, *J* = 11.1, 1.0 Hz, 1H), 5.11 (dd, *J* = 17.7, 1.0 Hz, 1H), 3.73 (d, *J* = 14.0 Hz, 1H), 3.68 (d, *J* = 14.0 Hz, 1H), 3.55 (dd, *J* = 7.9, 7.3 Hz, 1H), 3.39 (dd, *J* = 12.1, 7.9 Hz, 1H), 3.31 (dd, *J* = 12.1, 7.3 Hz, 1H), 1.06 (s, 3H);

^{13}C-NMR (100 MHz) 169.5, 141.5, 134.3, 131.7, 123.5, 114.4, 66.5, 43.8, 42.7, 20.0; IR (neat): 3458, 3100, 2985, 2950, 2923, 1962, 1766, 1698, 1612, 1465, 1388, 1322, 1085, 927, 870, 707 cm^{-1}; HRMS (CI): Exact mass calcd for $C_{14}H_{15}O_3$ $[M]^+$: 245.1052. Found: 245.1054. M.p. 57.5 °C.

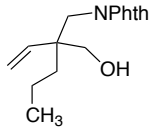

2-(2-(Hydroxymethyl)-2-vinylpentyl)isoindoline-1,3-dione, **2h***:* Isolated 0.053 g (average of two runs, 65%) as a clear colorless oil after column chromatography (12% EtOAc/Hexanes). TLC R_f 0.23 (20% EtOAc/Hexanes); ^{1}H-NMR ($CDCl_3$, 400 MHz) δ 7.89-7.84 (m, 2H), 7.78-7.73 (m, 2H), 5.81 (dd, *J* = 18.0, 11.3 Hz, 1H), 5.12 (d, *J* = 11.3 Hz, 1H), 4.91 (d, *J* = 18.0 Hz, 1H), 3.74 (d, *J* = 14.1 Hz, 1H), 3.71 (d, *J* = 14.1 Hz, 1H), 3.64 (t, *J* = 7.0 Hz, 1H), 3.46 (d, *J* = 7.0 Hz, 2H), 1.52-1.47 (m, 1H), 1.43-1.26 (m, 3H), 0.92 (t, *J* = 6.9 Hz, 3H); ^{13}C-NMR (100 MHz) 169.6, 140.9, 134.3, 131.7, 123.5, 114.9, 63.0, 46.7, 42.1, 36.2, 16.7, 14.7; IR (neat): 3500, 2957, 2933, 2871, 1771, 1699, 1391, 908, 724, 713 cm^{-1}; HRMS (CI): Exact mass calcd for $C_{16}H_{19}NO_3$ $[M+H]^+$: 274.1443. Found: 274.1444.

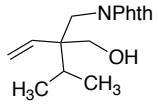

2-(2-(Hydroxymethyl)-2-isopropylbut-3-enyl)isoindoline-1,3-dione, **2i***:* Isolated 0.053 g (average of two runs, 65%) as a white powder after column chromatography (12% EtOAc/Hexanes). TLC R_f 0.27 (20% EtOAc/Hexanes); ^{1}H-NMR ($CDCl_3$, 400 MHz) δ 7.85 (dd, *J* = 5.5, 3.0 Hz, 2H), 7.74 (dd, *J* = 5.5, 3.0 Hz, 2H), 5.86 (dd, *J* = 18.1, 11.5 Hz, 1H), 5.12 (d, *J* = 11.5 Hz, 1H), 4.81 (d, *J* = 18.1 Hz, 1H), 3.93 (d, *J* = 14.1 Hz, 1H), 3.78 (d, *J* = 14.1 Hz, 1H), 3.68-3.61 (m, 2H), 3.48-3.40

(m, 1H), 1.99 (septet, J = 6.9 Hz, 1H), 1.05 (d, J = 6.9 Hz, 3H), 0.92 (d, J = 6.9 Hz, 3H); ^{13}C-NMR (100 MHz) 169.7, 138.1, 134.2, 131.7, 123.4, 115.9, 61.6, 48.5, 41.3, 30.2, 17.6, 17.4; IR (neat): 3500, 2962, 1771, 1698, 1467, 1387, 1346, 1085, 984, 917, 900, 743, 712 cm^{-1}; HRMS (CI): Exact mass calcd for $C_{16}H_{20}NO_3$ $[M+1]^+$: 274.1443. Found: 274.1448. M.p. 85.1 °C.

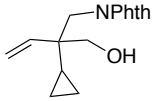

2-(2-Cyclopropyl-2-(hydroxymethyl)but-3-enyl)isoindoline-1,3-dione, **2j**: Isolated 0.055 g (average of two runs, 67%) as a white powder after column chromatography (12% EtOAc/Hexanes). TLC R_f 0.18 (20% EtOAc/Hexanes); ^{1}H-NMR ($CDCl_3$, 400 MHz) δ 7.86 (dd, J = 5.4, 3.1 Hz, 2H), 7.75 (dd, J = 5.4, 3.1 Hz, 2H), 5.54 (dd, J = 18.0, 11.4 Hz, 1H), 5.13 (d, J = 11.4 Hz, 1H), 4.98 (d, J = 18.0 Hz, 1H), 3.90 (d, J = 14.1 Hz, 1H), 3.86 (d, J = 14.1 Hz, 1H), 3.70 (dd, J = 8.3, 7.0 Hz, 1H), 3.53 (dd, J = 12.1, 7.0 Hz, 1H), 3.48 (dd, J = 12.1, 8.3 Hz, 1H), 0.98-0.91 (m, 1H), 0.48-0.32 (m, 3H), 0.27-0.20 (m, 1H); ^{13}C-NMR (100 MHz) 169.6, 136.9, 134.2, 131.7, 123.5, 116.9, 64.6, 45.7, 42.2, 14.6, -0.09, -0.13; IR (neat): 3471, 3073, 3003, 2939, 1768, 1697, 1393, 1334, 1062, 907, 745, 712 cm^{-1}; HRMS (CI): Exact mass calcd for $C_{16}H_{18}NO_3$ $[M+1]^+$: 272.1287. Found: 272.1289. M.p. 104.1 °C.

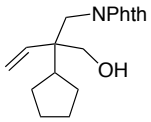

2-(2-Cyclopentyl-2-(hydroxymethyl)but-3-enyl)isoindoline-1,3-dione, **2k.** Isolated 0.059 g (average of two runs, 66%) as a white powder after column chromatography (12% EtOAc/Hexanes). TLC R_f 0.27 (20% EtOAc/Hexanes); ^{1}H-NMR ($CDCl_3$, 400 MHz) δ 7.87-7.83 (m, 2H), 7.77-7.72 (m, 2H), 5.92 (dd, J = 18.1,

11.5 Hz, 1H), 5.14 (d, *J* = 11.5 Hz, 1H), 4.84 (d, *J* = 18.1 Hz, 1H), 3.88 (d, *J* = 14.1 Hz, 1H), 3.77 (d, *J* = 14.1 Hz, 1H), 3.72 (dd, *J* = 8.3, 7.0 Hz, 1H), 3.50 (d, *J* = 8.3 Hz, 1H), 3.49 (d, *J* = 7.0 Hz, 1H), 2.17 (tt, *J* = 9.9, 7.9 Hz, 1H), 1.85-1.80 (m, 1H), 1.74-1.47 (m, 6H), 1.31-1.21 (m, 1H); ^{13}C-NMR (100 MHz) 169.7, 138.0, 134.2, 131.7, 123.5, 116.2, 63.0, 48.3, 42.2, 41.8, 26.8, 26.6, 25.6, 25.0; IR (neat): 3468, 2953, 2870, 1771, 1700, 1393, 987, 917, 744, 711 cm^{-1}; HRMS (CI): Exact mass calcd for $C_{18}H_{21}NO_3$ $[M+H]^+$: 300.1600. Found: 300.1601. M.p. 105.0 °C.

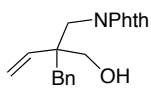

2-(2-Benzyl-2-(hydroxymethyl)but-3-enyl)isoindoline-1,3-dione, **2l.** Isolated 0.063 g (average of two runs, 65%) as a white powder after column chromatography (12% EtOAc/Hexanes). TLC R_f 0.17 (20% EtOAc/Hexanes); ^{1}H-NMR ($CDCl_3$, 400 MHz) δ 7.87-7.83 (m, 2H), 7.76-7.71 (m, 2H), 7.28-7.18 (m, 5H), 5.89 (dd, *J* = 18.1, 11.4 Hz, 1H), 5.00 (d, *J* = 11.4 Hz, 1H), 4.60 (d, *J* = 18.1 Hz, 1H), 3.85 (d, *J* = 14.1 Hz, 1H), 3.76 (d, *J* = 14.1 Hz, 1H), 3.67 (dd, *J* = 8.9, 6.3 Hz, 1H), 3.41 (dd, *J* = 11.5, 6.3 Hz, 1H), 3.37 (dd, *J* = 11.5, 8.9 Hz, 1H), 2.96 (d, *J* = 13.1 Hz, 1H), 2.73 (d, *J* = 13.1 Hz, 1H); ^{13}C-NMR (100 MHz) 169.5, 140.0, 136.6, 134.3, 131.6, 130.8, 128.7, 126.3, 123.5, 115.5, 61.4, 47.7, 42.7, 40.7; IR (neat): 3501, 3062, 3029, 2974, 2936, 2866, 1770, 1701, 1392, 1349, 993, 913, 713, 702 cm^{-1}; HRMS (CI): Exact mass calcd for $C_{20}H_{19}NO_3$ $[M]^+$: 321.1365. Found: 321.1362. M.p. 100.1 °C.

C.6.5 Deuterium Labeling and Competition Experiments

Allene **1g** was subjected to four separate experiments with d_0-, d_1- and d_4-methanol under otherwise identical conditions as those used for the preparation of alcohol **2g**. Deuterium incorporation was determined in the isolated product ***deuterio*-2g** by integration of the corresponding signals in the ^{1}H-NMR (400 MHz, $CDCl_3$) and ^{2}H-NMR (77 MHz, $CHCl_3$) spectra.

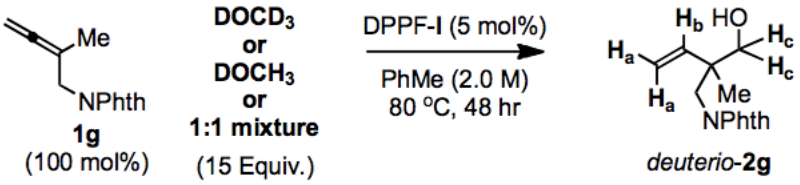

Entry	Methanol Source	Deuterium Incorporation (%)		
		H_a	H_b	H_c
1	CD_3OD	9	82	>99
2	CH_3OD	9	6	<1
3	CD_3OD/CH_3OD (1:1)	10	30	33
4	CD_3OD/CH_3OH (1:1)	6	30	37

Complete deuterium incorporation from CD_3OD at H_c (entry 1) is consistent with a mechanistic scenario of methanol oxidation followed by reductive formaldehyde coupling. Incomplete deuterium incorporation in positions H_a and H_b is indicative of reversible allene hydrometallation/β-hydride elimination prior to C-C bond formation.

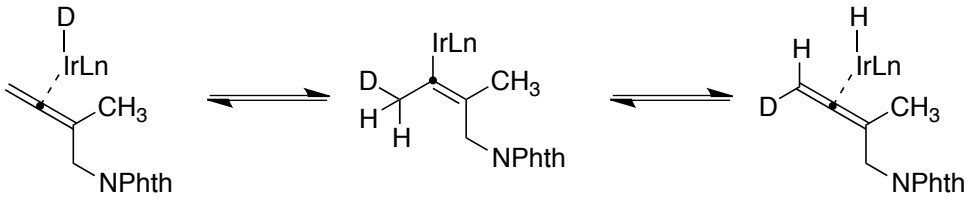

To probe for kinetic isotope effects present in the catalytic cycle, competition experiments were carried out between methanol isotopologues. Exposure of allene **1g** to otherwise typical reaction conditions employing a 1:1 (v/v, prepared by pre-mixing 500 μL of each component) mixture of either CH_3OD (entry 3) or CH_3OH (entry 4) with CD_3OD resulted in deuterium incorporation at H_c of only 33 % and 37 %, respectively. The observed k_H/k_D for the catalytic cycle is 2.0. One possible interpretation of this result is a small normal primary kinetic isotope effect (KIE) due to a kinetically significant step in which a C-H bond is broken. (*223-228*, *234*)The small observed k_H/k_D value may also be rationalized as the product of one or more other catalytic steps of comparable rate for which an inverse kinetic isotope effect is present. In either case, this result suggests that oxidation of methanol to formaldehyde is rate-determining. In contrast, if C-C bond-formation were rate-limiting, an inverse secondary KIE would be expected since the deuterium-bearing carbon would change hybridization from sp^2 to sp^3.

In contrast, iridium-catalyzed hydrohydroxyalkylation of allenes with allylic or benzylic primary alcohols occur at temperatures as low as 30 °C and crossover studies have shown that oxidation is rapid for these substrates.(*217*) In order to evaluate whether benzylic alcohols possess a different turnover-limiting step than methanol, competition experiments were carried out between $PhCD_2OH$ and $PhCH_2OH$. Exposure of allene **1g** (64 mg, 0.30 mmol) to otherwise typical reaction conditions employing a 1:1 mixture of $PhCD_2OH$ and $PhCH_2OH$ resulted in deuterium incorporation of 47 % at the carbinol position. The observed k_H/k_D for the catalytic cycle is therefore ≈1.1. This result

demonstrates that unlike methanol, when benzyl alcohol is employed as substrate, oxidation to the aldehyde is not the turnover-limiting step in the catalytic cycle.

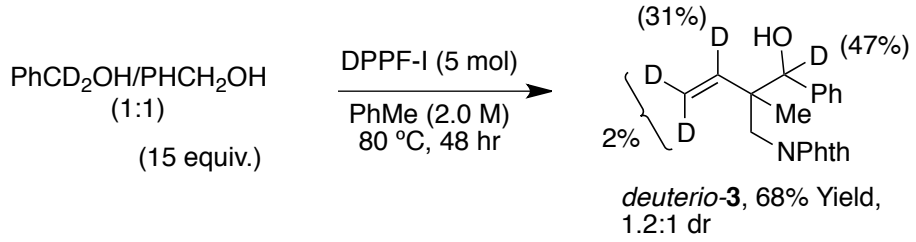

deuterio-**3**, 68% Yield, 1.2:1 dr

***deuterio*-2-(2-(Hydroxy(phenyl)methyl)-2-methylbut-3-enyl)isoindoline-1,3-dione (*deuterio*-3).** *DPPF*-**I** (14.8 mg, 0.015 mmol, 5 mol%) and allene **1g** (64 mg, 0.30 mmol, 100 mol%) were added to an oven-dried sealed tube equipped with a magnetic stirring bar. The tube was capped with a rubber septum and was purged with argon and an outlet for 5 minutes. Toluene (2.0 M, 0.15 mL) and a 1:1 (v/v, 466 µL, 1500 mol%, prepared by pre-mixing each component) mixture of $PhCD_2OH$ and $PhCH_2OH$ were then added via syringe. The rubber septum was removed and the tube was immediately sealed with a plastic screwcap. The reaction mixture was allowed to stir at 80 °C for 48h. The tube was cooled to room temperature and toluene was removed *in vacuo*. Purification was carried out by column chromatography (SiO_2; 15% EtOAc/Hexanes) to yield a mixture of the titled compound and benzyl alcohol. The mixture was heated to 40 °C *in vacuo* for 72h to remove excess benzyl alcohol and then resubmitted to column chromatography (SiO_2; 15 % EtOAc/Hexanes) to yield 65.9 mg of the titled compound (68 %, 1.2:1 dr). The spectral data were consistent with the corresponding *protio* compound.(*209*)

Glossary

A-BisMeNO2	Bis(1-(2-nitrophenyl)ethylcarboxy)cyclohexylamine
A-MeNO2	1-(2-nitrophenyl)ethylcarboxy cyclohexylamine
ACN	Acetonitrile
AD-DM2	Bis(3,5-dimethoxybenzylcarboxy)adamantylamine
AFM	Atomic force microscopy
BDE	Bond dissociation energy
Bis-NO2	Bis-2-nitrobenzylcarbamate
CAR	Chemically amplified resists
CD	Critical dimension
CHA-Ben	N-cyclohexyl benzoincarbamate
CHA-BisMeNO2	Bis(1-(2-nitrophenyl)ethylcarboxy)cyclohexylamine
CHA-BisNO2	Bis(2-nitrobenzylcarboxy)cyclohexylamine
CHA-COUM2	(*E*)-*N*-cyclohexyl-3-(2-hydroxyphenyl)acrylamide
CHA-MeNO2	*1-(2-nitrophenyl)ethylcarboxy cyclohexylamine*
DBTL	Dibutyltin diluarate
DBU	1,8-Diazabicycloundec-7-ene
DCHA-NO2	2-nitrobenzyl dicyclohexylcarbamate
DCM	Dichloromethane
DE-ACP1	2-(4-methoxyphenyl)-2-oxoethyl diethylcarbamate

DE-ACP2	2-(4-methoxyphenyl)-2-(2-oxo-2-phenylethoxy)ethyl diethylcarbamate
Ddz	3,5-dimethoxybenzylcarbamate
DIPA	Diisopropylamine
DIPA-Ben	Diisopropylbenzoin carbamate
DIPA-DM	3,5-dimethoxybenzyl diisopropylcarbamate
DIPA-NO2	2-nitrobenzyl diisoproplyamine
DMSO	Dimethylsulfoxide
DNQ	Diazonapthoquinone
DPL	Double patterning lithography
DUV	Deep ultraviolet
E_0	Positive threshold
E_n	Negative threshold
EDCI	1-Ethyl-3-(3-dimethylaminopropyl)carbodiimide
EUV	Extreme ultraviolet
GC	Gas chromatography
GPC	Gel permeation chromatography
HFIP	Hexafluoroisopropanol
HP	Half pitch
HRMS	High resolution mass spectroscopy
IC	Ion chromatography
IPA	Isopropyl alcohol

IR	Infrared
ITRS	International technology roadmap for semiconductors
KHMDS	Potassium hexamethyldisilizane
LER	Line edge roughness
LiHMDS	Lithium hexamethyldisilizane
LWR	Line width roughness
Mn	Number average molecular weight
MS	Molecular sieve
Mw	Weight average molecular weight
MW	Molecular weight
NBA	2-Nitro benzyl alcohol
NCAR	Non-chemically amplified resists
NMR	Nuclear magnetic resonance
OX-2	Benzophenone oxime ester base generator
PA-OX1	1-(6-(((cyclohexylideneamino)oxy)carbonyl)-3,4-dimethylcyclohexa-2,4-dien-1-yl)propan-2-one
PA-OX2	5-(((cyclohexylideneamino)oxy)carbonyl)-5-(2-oxo-2-phenylethyl)cyclohex-2-en-1-one
PAB	Post apply bake
PAG	Photoacid generator
P-Ben	Phenacylether-protected benzophenone
PBG	Photobase generator

PDC	Pyridinium dichromate
PDI	Polymeric dissolution inhibitor
PEB	Post exposure bake
PGMEA	Propylene glycol monomethyl ether acetate
PHA	Phthalaldehyde
PMMA	Poly(methyl methacrylate)
P-OX2	Protected benzophenone oxime ester base generator
PPG	Photo-labile protecting group
PPM	Parts per million
PPHA	Polyphthalaldehyde
PS	Polystyrene
RI	Refractive index
SEM	Scanning electron microscope
t-BOC	tert-Butyl carbonate
T_c	Ceiling temperature
TEA	Triethyl amine
TFE	Trifluoroethanol
THF	Tetrahydrofuran
TMAH	Tetramethyl ammonium hydroxide
TMS	Trimethyl silyl
TFA	Trifluoroacetic acid
UV	Ultraviolet

Bibliography

1. The Porticus Center*www.porticus.org* (available at http://www.porticus.org/).

2. J. Fowler, Oracle Press Release*oracle.com* (2010).

3. G. E. Moore, Progress in digital integrated electronics. *Electron Devices Meeting, 1975 International* **21**, 11–13 (1975).

4. J. R. Adams, thesis, University of Texas at Austin (2009).

5. Intel Marks 60th Anniversary of the Transistor*intel.com* (2007).

6. C. Mack, *Fundamental Principles of Optical Lithography* (Wiley, 2011).

7. J. Strahan, thesis, University of Texas at Austin (2010).

8. L. F. Thompson, C. G. Willson, M. J. Bowden, Eds., *Introduction to Microlithography (ACS Professional Reference Book)* (American Chemical Society, ed. 2, 1994).

9. J. Pacansky, J. R. Lyerla, Photochemical Decomposition Mechanisms for AZ-Type Photoresists. *IBM J. Res. & Dev.* **23**, 42–55 (1979).

10. G. H. Smith, Sensitized aromatic iodonium or aromatic sulfonium salt photoinitiator systems. United States Patent US 4,250,053. (1981)

11. ITRS 2001*www.itrs.net* (2002) (available at http://www.itrs.net/Links/2001ITRS/Home.htm).

12. T. Ito, S. Okazaki, Pushing the limits of lithography. *Nature* **406**, 1027–1031 (2000).

13. D. Basting, G. Marowsky, Eds., *Excimer Laser Technology*

(Springer-Verlag, Berlin/Heidelberg, 2005).

14. Intel drops 157-nm tools from lithography roadmap, *eetimes.com* (available at http://eetimes.com/electronics-news/4092441/Intel-drops-157-nm-tools-from-lithography-roadmap).

15. M. Rothschild, A roadmap for optical lithography. *Optics and Photonics News* **21**, 26–31 (2010).

16. J. Yan, A. El-Dakrouri, M. Laroussi, M. C. Gupta, 121.6 nm radiation source for advanced lithography. *Journal of Vacuum Science & Technology B: Microelectronics and Nanometer Structures* **20**, 2574 (2002).

17. K. Akihiro Takanashi *et al.*, Pattern forming apparatus, United States Patent US 4,480,910. (1984)

18. B. J. Lin, The k3 coefficient in nonparaxial λ/NA scaling equations for resolution, depth of focus, and immersion lithography. *J. Micro/Nanolith. MEMS MOEMS* **1**, 7 (2002).

19. S. Owa, H. Nagasaka, A. Chen, B. Lin, A. Yen, Eds. Immersion lithography: its history, current status and future prospects. *Proc SPIE, Lithography Asia*, 714015 (2008).

20. A. J. Berro *et al.*, C. L. Henderson, Ed. Optical threshold layer and intermediate state two-photon PAG approaches to double exposure lithography. *Proc SPIE, Advances in Resist Materials and Processing Technology XXVI*, 72731B (2009).

21. R. Bristol *et al.*, C. L. Henderson, Ed. Double-exposure materials for pitch division with 193nm lithography: requirements, results. *Proc SPIE, Advances in Resist Materials and Processing Technology XXVI* **7273**, 727307 (2009).

22. N. A. O'Connor *et al.*, Toward the Design of a Sequential Two Photon Photoacid Generator for Double Exposure Photolithography. *Chemistry of Materials* **20**, 7374–7376 (2008).

23. P. Zimmerman, Double patterning lithography: double the trouble or double the fun?*SPIE Newsroom* (2009), doi:10.1117/2.1200906.1691.

24. T. Kakizawa *et al.*, Freezing Material Development for Double Patterning Process. *J. Photopol. Sci. Technol.* **22**, 641–646 (2009).

25. M. Hori *et al.*, in (International Society for Optics and Photonics, 2008), vol. 6923, p. 69230H.

26. C. Bencher *et al.*, D. J. C. Herr, Ed. Self-assembly patterning for sub-15nm half-pitch: a transition from lab to fab. *Proc. SPIE, Alternative Lithographic Technologies III* **7970**, 79700F (2011).

27. C. M. Bates *et al.*, Polarity-Switching Top Coats Enable Orientation of Sub-10-nm Block Copolymer Domains. *Science* **338**, 775–779 (2012).

28. All Double-Patterining Variations Lead to Rome *spectrum.ieee.org* (available at http://spectrum.ieee.org/images/nov08/images/doub03.pdf).

29. C.-S. Koay *et al.*, Evaluation of double-patterning techniques for advanced logic nodes. *Proc SPIE, Optical Microlithography XXIII* **7640**, 764009 (2010).

30. X. Gu, thesis, University of Texas at Austin (2011).

31. X. Gu *et al.*, A New Materials-based Pitch Division Technique. *J. Photopol. Sci. Technol.* **22**, 773–781 (2009).

32. A. Katnani, N. Patel, P. Rabidoux, Preparing a film forming photoresist composition used in manufacture of integrated circuit chips. United States Patent US 6,114,082 A. (2000)

33. T. H. Fedynyshyn, Multi-tone resist compositions, United States Patent US 8,110,339 B2. (2012)

34. H. Zhang, Y. Du, M. D. F. Wong, R. O. Topaloglu, W. Conley,

Ed. Characterization and decomposition of self-aligned quadruple patterning friendly layout. *Proc SPIE, Optical Microlithography XXV* **8326**, 83260F1 (2012).

35. K. Nakayama *et al.*, M. E. Mason, J. L. Sturtevant, Eds. Self-aligned double and quadruple patterning layout principle. *Proc SPIE, Design for Manufacturability through Design-Process Integration VI* **8327**, 83270V1 (2012).

36. J. C. Sheehan, R. M. Wilson, A. W. Oxford, Photolysis of methoxy-substituted benzoin esters. Photosensitive protecting group for carboxylic acids. *J Am Chem Soc* **93**, 7222–7228 (1971).

37. M. Pirrung, J. Bradley, Dimethoxybenzoin carbonates: photochemically-removable alcohol protecting groups suitable for phosphoramidite-based DNA synthesis. *The Journal of Organic Chemistry* **60**, 1116–1117 (1995).

38. A. P. Pelliccioli, J. Wirz, Photoremovable protecting groups: reaction mechanisms and applications. *Photochem. Photobiol. Sci.* **1**, 441–458 (2002).

39. A. Høgset, L. Prasmickaite, T. E. Tjelle, K. Berg, Photochemical transfection: a new technology for light-induced, site-directed gene delivery. *Hum. Gene Ther.* **11**, 869–880 (2000).

40. C. Kutal, Photoinitiated Cross-Linking and Image Formation in Thin Polymer Films Containing a Transition Metal Compound. *Journal of the Electrochemical Society* **134**, 2280 (1987).

41. D. R. McKean *et al.*, Base-catalyzed photosensitive polyimide. *Proc SPIE, Advances in Resist Technology and Processing X* **1925**, 192507 (1993).

42. K. Suyama, M. Shirai, Photobase generators: Recent progress and application trend in polymer systems. *Progress in Polymer Science* **34**, 194–209 (2009).

43. C. R. Szmanda *et al.*, W. Conley, Ed. Simple method for measuring acid generation quantum efficiency at 193 nm. *Proc SPIE, Advances in Resist Technology and Processing XVI* **3678**, 367857 (1999).

44. M.-K. Leung, J. M. J. Frechet, J. F. Cameron, C. G. Willson, Design and Synthesis of Photoactive Polymer Systems Based on Amine-Catalyzed Intramolecular Imidization of Polymer Side Chains. *Macromolecules* **28**, 4693–4700 (1995).

45. J. M. J. Frechet *et al.*, Photogenerated Base in Resist and Imaging Materials: Design of Functional Polymers Susceptible to Base Catalyzed Decarboxylation. *Chemistry of Materials* **9**, 2887–2893 (1997).

46. M. Endo, Y. Tani, M. Sasago, N. Nomura, o-Nitrobenzyl Ester Based Deep UV Resist for KrF Excimer Laser Lithography. *Polymer Journal* **21**, 603–607 (1989).

47. T. Nishikubo, E. Takehara, A. Kameyama, Photogeneration of polyfunctional amines and novel thermal curing reactions of epoxy resin and polyurethane oligomer using these amines. *J. Polym. Sci. A Polym. Chem.* **31**, 3013–3020 (1993).

48. J. F. Cameron, J. M. J. Frechet, Photogeneration of organic bases from o-nitrobenzyl-derived carbamates. *J Am Chem Soc* **113**, 4303–4313 (1991).

49. M. J. Kurth, M. M. Olmstead, M. J. Haddadin, Claimed 2,1-benzisoxazoles are indazalones. *J Org Chem* **70**, 1060–1062 (2005).

50. C. L. Yoo, J. C. Fettinger, M. J. Kurth, Stannous Chloride in Alcohol: A One-Pot Conversion of 2-Nitro- N-arylbenzamides to 2,3-Dihydro-1 H-quinazoline-4-ones. *J Org Chem* **70**, 6941–6943 (2005).

51. C. Birr, W. Lochinger, G. Stahnke, P. Lang, [The , -dimethyl-3,5-dimethoxybenzyloxycarbonyl (Ddz) residue, an N-protecting

group labile toward weak acids and irradiation]. *Justus Liebigs Ann. Chem.* **763**, 162–172 (1972).

52. J. F. Cameron, J. M. J. Frechet, Base catalysis in imaging materials. 1. Design and synthesis of novel light-sensitive urethanes as photoprecursors of amines. *J Org Chem* **55**, 5919–5922 (1990).

53. R. Givens, P. Athey, L. Kueper III, B. Matuszewski, J. Xue, Photochemistry of. alpha.-keto phosphate esters: photorelease of a caged cAMP. *J Am Chem Soc* **114**, 8708–8710 (1992).

54. J. M. Peach, A. J. Pratt, J. S. Snaith, Photolabile benzoin and furoin esters of a biologically active peptide. *Tetrahedron* **51**, 10013–10024 (1995).

55. J. Cameron, C. Willson, J. Fréchet, Photogeneration of amines from α-keto carbamates: design and preparation of photoactive compounds. *Journal of the Chemical Society, Perkin Transactions 1* **1997**, 2429–2442 (1997).

56. C. S. Rajesh, R. S. Givens, J. Wirz, Kinetics and Mechanism of Phosphate Photorelease from Benzoin Diethyl Phosphate: Evidence for Adiabatic Fission to an α-Keto Cation in the Triplet State. *J Am Chem Soc* **122**, 611–618 (2000).

57. R. Givens *et al.*, Photochemistry of phosphate esters: alpha-keto phosphates as a photoprotecting group for caged phosphate. *J Am Chem Soc* **115**, 6001–6012 (1993).

58. J. Cameron, C. Willson, J. Fréchet, Photogeneration of amines from α-keto carbamates: Photochemical studies. *J Am Chem Soc* **118**, 12925–12937 (1996).

59. M. Remeš *et al.*, Gas-phase fragmentation of deprotonated p-hydroxyphenacyl derivatives. *J Org Chem* **76**, 2180–2186 (2011).

60. W. W. Epstein, M. Garrossian, p-Methoxyphenacyl esters as photodeblockable protecting groups for phosphates. *J. Chem.*

Soc., Chem. Commun., 532–533 (1987).

61. J. E. Baldwin, A. W. McConnaughie, M. G. Moloney, A. J. Pratt, S. Bo Shin, New photolabile phosphate protecting group. *Tetrahedron* **46**, 6879–6884 (1990).

62. R. Givens, L. Kueper III, Photochemistry of phosphate esters. *Chem Rev* **93**, 55–66 (1993).

63. R. S. Givens *et al.*, The Photo-Favorskii Reaction of p-Hydroxyphenacyl Compounds Is Initiated by Water-Assisted, Adiabatic Extrusion of a Triplet Biradical. *J Am Chem Soc* **130**, 3307–3309 (2008).

64. F. F. Wong *et al.*, An efficient and convenient transformation of α-haloketones to α-hydroxyketones using cesium formate. *Journal of Organometallic Chemistry* **694**, 3452–3455 (2009).

65. B. Holtzman, thesis, University of Texas at Austin (1999).

66. B. Heath, thesis, University of Texas at Austin (2006).

67. S. Postnikov, thesis, University of Texas at Austin, Austin (1999).

68. J. F. Cameron, J. M. J. Frechet, Solid state quantum yield determination of a novel base photogenerator. *Journal of Photochemistry and Photobiology A: Chemistry* **59**, 105–113 (1991).

69. R. S. Givens *et al.*, p-Hydroxyphenacyl photoremovable protecting groups - Robust photochemistry despite substituent diversity. *Canadian Journal of Chemistry* **89**, 364–384 (2011).

70. X. Gu *et al.*, R. Allen, Ed. Photobase generator assisted pitch division. *Proc SPIE, Advances in Resist Materials and Processing Technology XXVII* **7639**, 763906 (2010).

71. International Technology Roadmap for Semiconductors, *itrs.net* (available at http://www.itrs.net/reports.html).

72. Y. Wei, R. L. Brainard, *Advanced Processes for 193-nm Immersion Lithography* (SPIE Press, 2009).

73. J. H. Kim, Y.-H. Kim, S. M. Chon, Influence of acid diffusion length on line edge roughness in KrF photoresists. *J. Photopol. Sci. Technol.* **17**, 379–384 (2004).

74. M. Yoshizawa, S. Moriya, Study of the acid-diffusion effect on line edge roughness using the edge roughness evaluation method. *Journal of Vacuum Science & Technology B* **20**, 1342–1347 (2002).

75. S. Kang *et al.*, Characterization of the Photoacid Diffusion Length and Reaction Kinetics in EUV Photoresists with IR Spectroscopy. *Macromolecules* **43**, 4275–4286 (2010).

76. D. N. Tuan, H. Yamamoto, S. Tagawa, Study on Resist Performance of Polymer-Bound and Polymer-Blended Photo-Acid Generators. *Jpn. J. Appl. Phys.* **51**, 086503 (2012).

77. T. Kozawa, J. J. Santillan, T. Itani, P. P. Naulleau, O. R. Wood II, Eds. Modeling and simulation of acid diffusion in chemically amplified resists with polymer-bound acid generator. *Proc SPIE, Extreme Ultraviolet (EUV) Lithography III* **8322**, 832206 (2012).

78. Y. Cho *et al.*, R. D. Allen, M. H. Somervell, Eds. Polymer-bound photobase generators and photoacid generators for pitch division lithography. *Proc. SPIE, Advances in Resist Materials and Processing Technology XXVIII* **7972**, 797221 (2011).

79. *Advances in Resist Materials and Processing Technology XXVIII*.

80. M. C. Pirrung, W. H. Pieper, K. P. Kaliappan, M. R. Dhananjeyan, Combinatorial discovery of two-photon photoremovable protecting groups. *P Natl Acad Sci Usa* **100**, 12548–12553 (2003).

81. A. Berro, thesis, University of Texas at Austin (2009).

82. D. Shykind, R. Bristol, J. Roberts, J. Blackwell, Y. Borodovsky, R. D. Allen, Ed. Reaction kinetics of non-reciprocal photo-base generator (NRPBG) patterning. *Proc SPIE, Advances in Resist Materials and Processing Technology XXVII* **7639**, 76391Y (2010).

83. A. Poonawala, Y. Borodovsky, P. Milanfar, D. G. Flagello, Ed. ILT for double exposure lithography with conventional and novel materials. *Proc. SPIE, Optical Microlithography XX* **6520**, 65202Q (2007).

84. S. Lee *et al.*, in H. J. Levinson, M. Dusa, Eds. (International Society for Optics and Photonics, 2008), vol. 6924, pp. 69242A–69242A–12.

85. P. J. Wagner, A. E. Kemppainen, H. N. Schott, Effects of ring substituents on the type II photoreactions of phenyl ketones. How interactions between nearby excited triplets affect chemical reactivity. *J Am Chem Soc* **95**, 5604–5614 (1973).

86. J. Lalevee *et al.*, Investigation of the photochemical properties of an important class of photobase generators: the O-acyloximes. *Journal of Photochemistry and Photobiology A: Chemistry* **151**, 27–37 (2002).

87. N. J. Turro *et al.*, Study of a two-stage photobase generator for photolithography in microelectronics. *J Org Chem* **78**, 1735–1741 (2013).

88. Y. Hagiwara *et al.*, Design and synthesis of a photoaromatization-based two-stage photobase generator for pitch division lithography. *J Org Chem* **78**, 1730–1734 (2013).

89. R. Binkley, H. Jarrell, Type II Reactions From The Photolysis Of The Phenacyl Ether of 1,2:3,4-Di-O-Isoproplidene-a-D-Galactopyranose. *Journal of Carbohydrates, Nucleosides, Nucleotides* **7**, 347–364 (1980).

90. A. Turner, S. Pizzo, G. Rozakis, N. Porter, Photochemical

activation of acylated. alpha.-thrombin. *J Am Chem Soc* **109**, 1274–1275 (1987).

91. P. J. Wagner, G. S. Hammond, Mechanism of Type II Photoelimination. *J Am Chem Soc* **87**, 4009–4011 (1965).

92. P. J. Wagner, Solvent effects on type II photoelimination of phenyl ketones. *J Am Chem Soc* **89**, 5898–5901 (1967).

93. K.-I. Ito, Y. Shigeru, Y.-U. Kawata, K. Ito, M. Tsunooka, Photo-initiated and thermal curing of epoxides by the use of photo-base generators bearing acyloxyimino groups. *Canadian Journal of Chemistry* **73**, 1924–1932 (1995).

94. Y. Akagi, H. Fukui, M. Fukuoka, K. Yamamoto, Photoresponsive gas-generating material, micropump and microfluid device, United States Patent US 20,110,014,096 A1. (2009)

95. K. G. Edwards, J. R. Stoker, Biosynthesis of coumarin: the isomerization stage. *Phytochemistry* **6**, 655–661 (1967).

96. B. WANG, A. ZHENG, A photo-sensitive protecting group for amines based on coumarin chemistry. *Chemical & pharmaceutical bulletin* **45**, 715–718 (1997).

97. R. Hershfield, G. L. Schmir, Lactonization of ring-substituted coumarinic acids. Structural effects on the partitioning of tetrahedral intermediates in esterification. *J Am Chem Soc* **95**, 7359–7369 (1973).

98. M. Z. Jin, L. Yang, L. M. Wu, Y. C. Liu, Z. L. Liu, Novel photoinduced aromatization of Hantzsch 1, 4-dihydropyridines. *Chem Commun*, 2451–2452 (1998).

99. H. K. Kim, C. K. Ober, Acid-catalyzed photoaromatization of poly(cyclohexadiene-1,2-diol) derivatives into polyphenylene. *Polymer Bulletin* **28**, 33–40 (1992).

100. V. F. Traven, I. V. Ivanov, New reaction of photoaromatization of

aryl-and hetarylpyrazolines. *Russian Chemical Bulletin* **57**, 1063–1069 (2008).

101. P. J. Wagner, Type II photoelimination and photocyclization of ketones. *Acc Chem Res* **4**, 168–177 (1971).

102. H. Tran, E. Jackson, J. Eldo, R. Kanjolia, S. B. Rananavare, Photochemical reactivity of bis-carbamate photobase generators. *Nanotechnology (IEEE-NANO)*, 1683–1688 (2011).

103. J. W. Chamberlin, Use of the 3,5-Dimethoxybenzyloxycarbonyl Group as a Photosensitive N-Protecting Group. *J Org Chem* **31**, 1658–1660 (1966).

104. E. V. Anslyn, D. A. Dougherty, *Modern Physical Organic Chemistry* (University Science Books, 2006).

105. A. F. Abdel-Magid, K. G. Carson, B. D. Harris, C. A. Maryanoff, R. D. Shah, Reductive Amination of Aldehydes and Ketones with Sodium Triacetoxyborohydride. Studies on Direct and Indirect Reductive Amination Procedures. *J Org Chem* **61**, 3849–3862 (1996).

106. S. G. Smith, M. P. Hanson, Control of the site of alkylation of ambident anions. *J Org Chem* **36**, 1931–1933 (1971).

107. A. L. Kurz, I. P. Beletskaya, A. Macías, O. A. REUTOV, Ratio of C- and O-Isomers in Ethylation of Alkali Enolates of Ethyl Acetoacetate in Hexamethyl-Phosphoramide and Dimethyl Sulfoxide. *Tetrahedron Letters*, 3679–3682 (1968).

108. N. Kornblum, R. Seltzer, P. Haberfield, Solvation as a Factor in the Alkylation of Ambident Anions: The Importance of the Dielectric Factor. *J Am Chem Soc* **85**, 1148–1154 (1963).

109. M. 1. O. 1. Smith, *March's advanced organic chemistry : reactions, mechanisms, and structure.* (Hoboken, New Jersey : Wiley, 2013).

110. A. L. Kurts, I. P. Beletskaya, A. Masias, S. S. Yufit, O. A. REUTOV, Reactivity of ambident anions. *Russ Chem Bull* **17**, 1387–1390 (1968).

111. X. Gu *et al.*, R. D. Allen, M. H. Somervell, Eds. Photobase generator enabled pitch division: a progress report. *Proc. SPIE, Advances in Resist Materials and Processing Technology XXVIII* **7972**, 79720F (2011).

112. C. Willson, H. Ito, J. Fréchet, T. Tessier, F. Houlihan, Approaches to the Design of Radiation-Sensitive Polymeric Imaging Systems with Improved Sensitivity and Resolution. *Journal of the Electrochemical Society* **133**, 181 (1986).

113. C. G. Willson, H. Ito, J. M. J. Frechet, F. Houlihan, *Chemical Amplification in the Design of Polymers for Resist Applications*. *International Union of Pure and Applied Chemistry* **28** (1982).

114. S. A. MacDonald, J. M. J. Frechet, H. Ito, C. Grant Willson, Resist materials. *Microelectronic Engineering* **3**, 277–278 (1985).

115. S. A. MacDonald, C. G. Willson, J. M. Frechet, Chemical amplification in high-resolution imaging systems. *Acc Chem Res* **27**, 151–158 (1994).

116. D. C. Brandt *et al.*, O. R. Wood, E. M. Panning, Eds. LPP EUV source readiness for NXE 3300B. *Proc. SPIE, Extreme Ultraviolet (EUV) Lithography V* **9048**, 90480C–90480C–8 (2014).

117. D. C. Brandt *et al.*, B. M. La Fontaine, P. P. Naulleau, Eds. LPP source system development for HVM. *Extreme Ultraviolet (EUV) Lithography III* **7969**, 79691H (2011).

118. D. C. Brandt, I. V. Fomenkov, A. I. Ershov, W. N. Partlo, B. La Fontaine, P. Naulleau, Eds. LPP source system development for HVM. *Proc SPIE, Extreme Ultraviolet (EUV) Lithography*, 76361I (2010).

119. D. C. Brandt, I. V. Fomenkov, LPP source system development for HVM. *Proc. SPIE, Alternative Lithographic Technologies*, 727103 (2009).

120. H. Mizoguchi *et al.*, LPP-EUV light source development for high volume manufacturing lithography. *International Society for Optics and Photonics*, 86790A–86790A–11 (2013).

121. M. Stewart, thesis, University of Texas at Austin, Austin (2003).

122. E. K. Lin, Direct Measurement of the Reaction Front in Chemically Amplified Photoresists. *Science* **297**, 372–375 (2002).

123. J. E. Meiring, T. B. Michaelson, A. T. Jamieson, G. M. Schmid, C. G. Willson, J. L. Sturtevant, Ed. Using mesoscale simulation to explore photoresist line edge roughness. *Proc. SPIE, Advances in Resist Technology and Processing XXII* **5753**, 350 (2005).

124. M. D. Stewart, M. H. Somervell, H. V. Tran, S. V. Postnikov, C. G. Willson, F. M. Houlihan, Ed. Study of acid transport using IR spectroscopy and SEM. *Proc SPIE, Advances in Resist Technology and Processing XVII* **3999**, 665 (2000).

125. T. B. Michaelson *et al.*, J. L. Sturtevant, Ed. Understanding the role of base quenchers in photoresists. *Proc. SPIE, Advances in Resist Technology and Processing XXI* **5376**, 1282–1293 (2004).

126. A. R. Pawloski *et al.*, Line edge roughness and intrinsic bias for two methacrylate polymer resist systems. *Journal of Microlithography Microfabrication and Microsystems* **5**, 023001–023001–11 (2006).

127. R. Gronheid, F. V. Roey, D. V. Steenwinckel, Using KLUP for understanding Trends in EUV resist performance. *J Photopol Sci Technol* **21**, 429–434 (2008).

128. R. Gronheid, Frequency multiplication of lamellar phase block copolymers with grapho-epitaxy directed self-assembly sensitivity to prepattern. *J. Micro/Nanolith. MEMS MOEMS* **11**,

031303 (2012).

129. A. De Silva, N. M. Felix, C. K. Ober, Molecular Glass Resists as High-Resolution Patterning Materials. *Adv. Mater.* **20**, 3355–3361 (2008).

130. G. M. Gallatin *et al.*, F. M. Schellenberg, Ed. Resolution, LER, and sensitivity limitations of photoresists. *Proc. SPIE, Emerging Lithographic Technologies XII* **6921**, 69211E (2008).

131. H. Solak, Paul Scheerer Institute. *Proceedings of Mico and Nano Engineering* (2005).

132. G. Odian, *Principles of Polymerization* (John Wiley & Sons, ed. 4, 2007).

133. M. P. Stevens, *Polymer Chemistry* (Oxford University Press, 1999).

134. H. R. Allcock, F. W. Lampe, J. E. Mark, *Contemporary Polymer Chemistry* (Prentice Hall, 2003).

135. H. Ito, A Sensitive, Etch Resistant, Positive Tone E-Beam Resist System. *Journal of the Electrochemical Society* **135**, 1504 (1988).

136. M. J. Bowden, A Sensitive Novolac-Based Positive Electron Resist. *Journal of the Electrochemical Society* **128**, 1304 (1981).

137. E. Reichmanis, A. E. Novembre, R. G. Tarascon, A. Shugard, New Silicon-Containing Electron-Beam Resist Systems. *Polymers for High Technology: ACS Symposium* **346**, 110–121 (1987).

138. H. Shiraishi, A. Isobe, F. Murai, S. Nonogaki, Novolac Based Positive Electron-Beam Resist Containing a Polymeric Dissolution Inhibitor - Preparation and Exposure Characteristics. *Polymers in Electronics: ACS Symposium* **242**, 167–176 (1984).

139. A. Isobe, D. Makino, M. Shirai, Electron beam or X-ray reactive image-formable resinous composition, United States Patent US 4,513,077 A. (1985)

140. M. M. Coleman, P. C. Painter, J. F. Graf, *Specific interactions and the miscibility of polymer blends* (Technomic Publishing Company, 1995).

141. P. Munk, T. M. Aminabhavi, *Introduction to macromolecular science* (John Wiley & Sons, New York, 1992), pp. xv–522.

142. M. G. Olah, J. S. Robbins, M. S. Baker, S. T. Phillips, End-Capped Poly(benzyl ethers): Acid and Base Stable Polymers That Depolymerize Rapidly from Head-to-Tail in Response to Specific Applied Signals. *Macromolecules* **46**, 5924–5928 (2013).

143. S. Li, M. L. Szalai, R. M. Kevwitch, D. V. McGrath, Dendrimer Disassembly by Benzyl Ether Depolymerization. *J Am Chem Soc* **125**, 10516–10517 (2003).

144. M. L. Szalai, R. M. Kevwitch, D. V. McGrath, Geometric disassembly of dendrimers: dendritic amplification. *J Am Chem Soc* **125**, 15688–15689 (2003).

145. J. S. Robbins, K. M. Schmid, S. T. Phillips, Effects of Electronics, Aromaticity, and Solvent Polarity on the Rate of Azaquinone-Methide-Mediated Depolymerization of Aromatic Carbamate Oligomers. *J Org Chem* **78**, 3159–3169 (2013).

146. A. P. Esser-Kahn, N. R. Sottos, S. R. White, J. S. Moore, Programmable microcapsules from self-immolative polymers. *J Am Chem Soc* **132**, 10266–10268 (2010).

147. M. A. Dewit, A. Beaton, E. R. Gillies, A reduction sensitive cascade biodegradable linear polymer. *J. Polym. Sci. A Polym. Chem.* **48**, 3977–3985 (2010).

148. M. A. Dewit, E. R. Gillies, A cascade biodegradable polymer based on alternating cyclization and elimination reactions. *J Am Chem Soc* **131**, 18327–18334 (2009).

149. M. A. Dewit, A. Nazemi, S. Karamdoust, A. Beaton, E. R. Gillies, in *pubs.acs.org*, ACS Symposium Series. (American

Chemical Society, Washington, DC, 2011), vol. 1066, pp. 9–21.

150. E. K. Chen, R. A. McBride, E. R. Gillies, Self-Immolative Polymers Containing Rapidly Cyclizing Spacers: Toward Rapid Depolymerization Rates. *Macromolecules* **45**, 7364–7374 (2012).

151. W. Seo, S. T. Phillips, Patterned plastics that change physical structure in response to applied chemical signals. *J Am Chem Soc* **132**, 9234–9235 (2010).

152. J. M. J. Fréchet *et al.*, in *Functional Polymers*, (Springer US, Boston, MA, 1989), pp. 193–200.

153. Y. Nagasaki, N. Yamazaki, M. Kato, Polymers degradable under environmental conditions through end-modification of poly (α-methylstyrene) derivatives. *Die Angewandte Makromolekulare Chemie* **247**, 163–178 (1997).

154. H. Ito, M. Ueda, Syntheses of Acetophenone Enol Ester Polymers and Their Conversion to Poly(Phenylacetylenes). *Macromolecules* **23**, 2885–2894 (1990).

155. T. Ishizone, K. Ohnuma, Y. Okazawa, A. Hirao, S. Nakahama, Anionic Polymerization of Monomers Containing Functional Groups. 12. Anionic Equilibrium Polymerization of 4-Cyano-α-methylstyrene. *Macromolecules* **31**, 2797–2803 (1998).

156. G. I. Peterson, M. B. Larsen, A. J. Boydston, Controlled Depolymerization: Stimuli-Responsive Self-Immolative Polymers - Macromolecules (ACS Publications). *Macromolecules* **45**, 7317–7328 (2012).

157. A. G. Schultz, F. P. Lavieri, M. Macielag, M. Plummer, 2, 5-Cyclohexadien-1-one to bicyclo [3.1. 0] hexenone photorearrangement. Development of the reaction for use in organic synthesis. *J Am Chem Soc* **109**, 3991–4000 (1987).

158. P. Mueller, J. Rocek, Oxidation of hydroaromatic systems. IV. Chromic acid oxidation of cycloheptatriene. *J Am Chem Soc* **96**,

2836–2840 (1974).

159. A. L. J. Beckwith, D. H. Roberts, Formation of some bi- and tricyclic systems by radical ring closure. *J Am Chem Soc* **108**, 5893–5901 (1986).

160. W. G. Salmond, M. A. Barta, J. L. Havens, Allylic oxidation with 3, 5-dimethylpyrazole. Chromium trioxide complex steroidal. DELTA. 5-7-ketones. *The Journal of Organic Chemistry* **43**, 2057–2059 (1978).

161. J. L. Luche, Lanthanides in organic chemistry. 1. Selective 1, 2 reductions of conjugated ketones. *J Am Chem Soc* **100**, 2226–2227 (1978).

162. T. J. Burkey, M. Majewski, D. Griller, Heats of formation of radicals and molecules by a photoacoustic technique. *J Am Chem Soc* **108**, 2218–2221 (1986).

163. K. B. Clark *et al.*, Studies of the formation and stability of pentadienyl and 3-substituted pentadienyl radicals. *J Org Chem* **56**, 5535–5539 (1991).

164. A. B. Trenwith, Dissociation of 1,3-hexadiene and the resonance energy of the pentadienyl radical. *J. Chem. Soc., Faraday Trans. 1* **76**, 266 (1980).

165. D. F. McMillen, D. M. Golden, Hydrocarbon bond dissociation energies. *Annual Review of Physical Chemistry* **33**, 493–532 (1982).

166. S. J. Blanksby, G. B. Ellison, Bond dissociation energies of organic molecules. *Acc Chem Res* **36**, 255–263 (2003).

167. D. G. Button, Azeotropic Distillation of Hydrocarbons with Hexafluoroisopropyl Alcohol, United States Patent US 3,284,348. (1966)

168. D. R. McKean, S. A. MacDonald, R. D. Johnson, N. J. Clecak, C.

G. Willson, Characterization of a Novolak-based three-component deep-UV resist. *Chemistry of Materials* **2**, 619–624 (1990).

169. T. H. Fedynyshyn, R. B. Goodman, A. Cabral, C. Tarrio, T. B. Lucatorto, R. D. Allen, Ed. Polymer photochemistry at the EUV wavelength. *Proc SPIE, Advances in Resist Materials and Processing Technology XXVII* **7639**, 76390A (2010).

170. B. K. Mueller, E. Elce, A. M. Grillo, P. A. Kohl, Positive-tone, aqueous-developable, polynorbornene dielectric: Lithographic, and dissolution properties. *Journal of Applied Polymer Science* **127**, 4653–4661 (2012).

171. T. Hoskins *et al.*, Bis(trifluoromethyl)carbinol-Substituted Polynorbornenes: Dissolution Behavior. *Macromolecules* **37**, 4512–4518 (2004).

172. Molecular Imprints, Inc. (MII) Delivers Industry's First 450mm Advanced Lithography System to a Leading Semiconductor Manufacturer in Support of the Global 450mm Initiative *prnewswire.com* (2013) (available at http://www.prnewswire.com/news-releases/molecular-imprints-inc-mii-delivers-industrys-first-450mm-advanced-lithography-system-to-a-leading-semiconductor-manufacturer-in-support-of-the-global-450mm-initiative-187375501.html).

173. White Paper: Introduction to Intel's 32 nm Process Technology *download.intel.com* (2009) (available at http://download.intel.com/pressroom/kits/32nm/westmere/Intel_32nm_Overview.pdf).

174. C. Ngai, Manufacturing Ready Self-Aligned Double Patterning for 3xnm Flash Production, *sematech.org* (2008) (available at http://www.sematech.org/meetings/archives/litho/8352/pres/D1_DP_P05_Ngai.pdf).

175. R. G. Dyer, K. D. Turnbull, Hydrolytic Stabilization of Protected p-Hydroxybenzyl Halides Designed as Latent Quinone Methide

Precursors. *J Org Chem* **64**, 7988–7995 (1999).

176. H. L. S. Maia, M.-J. Medeiros, M.-I. Montenegro, D. Pletcher, The cathodic cleavage of the 4-nitrobenzyloxycarbonyl group from amine derivatives in aprotic conditions. *J. Chem. Soc., Perkin Trans. 2*, 409 (1988).

177. M. Su, J. Wang, X. Tang, Photocaging Strategy for Functionalisation of Oligonucleotides and Its Applications for Oligonucleotide Labelling and Cyclisation. *Chem. Eur. J.* **18**, 9628–9637 (2012).

178. M. de L. dos Santos Cristiano, J. Davies, S. Dowd, R. Johnstone, M. J. Pratt, Photoactive materials applicable to imaging systems United States Patent US 6,384,264. (2002)

179. A. D. Wright, R. D. Bowen, K. R. Jennings, Chemical ionization mass spectra of urethanes. *J. Chem. Soc., Perkin Trans. 2*, 1521–1528 (1989).

180. K. Gerlach *et al.*, Carboxylic acid amides as factor xa inhibitors, European Patent Application WO 2,008,135,526 A1. (2008)

181. U. Engelhardt, A. Sarkar, T. Linker, Efficient Enantioselective Total Synthesis of (−)-Epipodophyllotoxin. *Angew Chem Int Edit* **42**, 2487–2489 (2003).

182. G. Binmore, J. C. Walton, L. Cardellini, Radical-chain decomposition of cyclohexa-1,4-diene-3-carboxylates and 2,5-dihydrofuran-2-carboxylates. *J. Chem. Soc., Chem. Commun.*, 27 (1995).

183. J. Moran, A. Preetz, R. A. Mesch, M. J. Krische, Iridium-catalysed direct C-C coupling of methanol and allenes. *Nat Chem* **3**, 287–290 (2011).

184. P. Anastas, N. Eghbali, Green chemistry: principles and practice. *Chem. Soc. Rev.* **39**, 301–312 (2010).

185. R. A. Sheldon, The E factor: fifteen years on. *Green Chemistry* **9**, 1273–1283 (2007).

186. J. H. Clark, Green chemistry for the second generation biorefinery—sustainable chemical manufacturing based on biomass. *Journal of Chemical Technology and Biotechnology* **82**, 603–609 (2007).

187. J.-P. Lange, Sustainable chemical manufacturing: a matter of resources, wastes, hazards, and costs. *ChemSusChem* **2**, 587–592 (2009).

188. The Methanol Institute*The Methanol Institute* (available at http://www.methanol.org/).

189. C. CHANG, The conversion of methanol and other O-compounds to hydrocarbons over zeolite catalysts. *Journal of Catalysis* **47**, 249–259 (1977).

190. M. Stöcker, Methanol-to-hydrocarbons: catalytic materials and their behavior. *Microporous and Mesoporous Materials* **29**, 3–48 (1999).

191. G. A. Olah, G. K. S. Prakash, R. E. Williams, K. Wade, Á. Molnár, *Hypercarbon Chemistry* (John Wiley & Sons, 2011).

192. J. F. Haw, W. Song, D. M. Marcus, J. B. Nicholas, The mechanism of methanol to hydrocarbon catalysis. *Acc Chem Res* **36**, 317–326 (2003).

193. J. E. Bercaw *et al.*, Conversion of methanol to 2,2,3-trimethylbutane (triptane) over indium(III) iodide. *Inorg Chem* **46**, 11371–11380 (2007).

194. J. H. Ahn, B. Temel, E. Iglesia, Selective homologation routes to 2,2,3-trimethylbutane on solid acids. *Angew Chem Int Ed Engl* **48**, 3814–3816 (2009).

195. P. Kalck, P. Serp, in *Iridium Complexes in Organic Synthesis*, L.

Oro, C. Claver, Eds. (John Wiley & Sons, New York, 2008), pp. 195–210.

196. A. Haynes, in *Catalytic Carbonylation Reactions*, Topics in Organometallic Chemistry. (Springer Berlin Heidelberg, 2006), vol. 18, pp. 179–205.

197. J. H. Jones, The Cativa Process for the Manufacture of Acetic Acid. *Platinum Metals Review* **44**, 94 (2000).

198. P. M. Maitlis, A. Haynes, G. J. Sunley, M. J. Howard, Methanol carbonylation revisited: thirty years on. *J. Chem. Soc., Dalton Trans.*, 2187 (1996).

199. E.-A. Jo, J.-H. Lee, C.-H. Jun, Rhodium(I)-catalyzed one-pot synthesis of dialkyl ketones from methanol and alkenes through directed sp3 C-H bond activation of N-methylamine. *Chem Commun*, 5779–5781 (2008).

200. K. Weissermel, H.-J. Arpe, *Industrial Organic Chemistry* (Weinheim : Wiley-VCH, ed. 4, 2003).

201. R. L. Patman, J. F. Bower, I. S. Kim, M. J. Krische, Formation of C-C Bonds via Catalytic Hydrogenation and Transfer Hydrogenation: Vinylation, Allylation, and Enolate Addition of Carbonyl Compounds and Imines. *Aldrichimica Acta* **41**, 95–104 (2008).

202. J. F. Bower, I. S. Kim, R. L. Patman, M. J. Krische, Catalytic Carbonyl Addition through Transfer Hydrogenation: A Departure from Preformed Organometallic Reagents. *Angew Chem Int Edit* **48**, 34–46 (2009).

203. S. B. Han, I. S. Kim, M. J. Krische, Enantioselective iridium-catalyzed carbonyl allylation from the alcohol oxidation level via transfer hydrogenation: minimizing pre-activation for synthetic efficiency. *Chem Commun*, 7278–7287 (2009).

204. F. Shibahara, J. F. Bower, M. J. Krische, Diene Hydroacylation

from the Alcohol or Aldehyde Oxidation Level via Ruthenium-Catalyzed C-C Bond-Forming Transfer Hydrogenation: Synthesis of beta,gamma-Unsaturated Ketones. *J Am Chem Soc* **130**, 14120–14122 (2008).

205. F. Shibahara, J. F. Bower, M. J. Krische, Ruthenium-Catalyzed C− C Bond Forming Transfer Hydrogenation: Carbonyl Allylation from the Alcohol or Aldehyde Oxidation Level Employing Acyclic 1, 3-Dienes as Surrogates to Preformed Allyl Metal Reagents. *J Am Chem Soc* **130**, 6338–6339 (2008).

206. H. Han, M. J. Krische, Direct ruthenium-catalyzed C-C coupling of ethanol: diene hydro-hydroxyethylation to form all-carbon quaternary centers. *Org Lett* **12**, 2844–2846 (2010).

207. R. L. Patman, M. R. Chaulagain, V. M. Williams, M. J. Krische, Direct vinylation of alcohols or aldehydes employing alkynes as vinyl donors: a ruthenium catalyzed C-C bond-forming transfer hydrogenation. *J Am Chem Soc* **131**, 2066–2067 (2009).

208. V. M. Williams, J. C. Leung, R. L. Patman, M. J. Krische, Hydroacylation of 2-butyne from the alcohol or aldehyde oxidation level via ruthenium catalyzed C-C bond forming transfer hydrogenation. *Tetrahedron* **65**, 5024–5029 (2009).

209. J. R. Zbieg, E. L. McInturff, M. J. Krische, Allenamide hydro-hydroxyalkylation: 1,2-amino alcohols via ruthenium-catalyzed carbonyl anti-aminoallylation. *Org Lett* **12**, 2514–2516 (2010).

210. J. F. Bower, R. L. Patman, M. J. Krische, Iridium-catalyzed C-C coupling via transfer hydrogenation: Carbonyl addition from the alcohol or aldehyde oxidation level employing 1,3-cyclohexadiene. *Org Lett* **10**, 1033–1035 (2008).

211. J. R. Zbieg, T. Fukuzumi, M. J. Krische, Iridium-Catalyzed Hydrohydroxyalkylation of Butadiene: Carbonyl Crotylation. *Adv Synth Catal* **352**, 2416–2420 (2010).

212. I. S. Kim, M.-Y. Ngai, M. J. Krische, Enantioselective iridium-

catalyzed carbonyl allylation from the alcohol or aldehyde oxidation level using allyl acetate as an allyl metal surrogate. *J Am Chem Soc* **130**, 6340–6341 (2008).

213. I. S. Kim, M.-Y. Ngai, M. J. Krische, Enantioselective Iridium-Catalyzed Carbonyl Allylation from the Alcohol or Aldehyde Oxidation Level via Transfer Hydrogenative Coupling of Allyl Acetate: Departure from Chirally Modified Allyl Metal Reagents in Carbonyl Addition. *J Am Chem Soc* **130**, 14891–14899 (2008).

214. I. S. Kim, S. B. Han, M. J. Krische, anti-Diastereo- and Enantioselective Carbonyl Crotylation from the Alcohol or Aldehyde Oxidation Level Employing a Cyclometallated Iridium Catalyst: alpha-Methyl Allyl Acetate as a Surrogate to Preformed Crotylmetal Reagents. *J Am Chem Soc* **131**, 2514–2520 (2009).

215. Y. Lu, I. S. Kim, A. Hassan, D. J. Del Valle, M. J. Krische, 1,n-Glycols as Dialdehyde Equivalents in Iridium-Catalyzed Enantioselective Carbonyl Allylation and Iterative Two-Directional Assembly of 1,3-Polyols. *Angew Chem Int Edit* **48**, 5018–5021 (2009).

216. Y. J. Zhang, J. H. Yang, S. H. Kim, M. J. Krische, anti-Diastereo- and enantioselective carbonyl (hydroxymethyl) allylation from the alcohol or aldehyde oxidation level: allyl carbonates as allylmetal surrogates. *J Am Chem Soc* **132**, 4562–4563 (2010).

217. S. B. Han, I. S. Kim, H. Han, M. J. Krische, Enantioselective Carbonyl Reverse Prenylation from the Alcohol or Aldehyde Oxidation Level Employing 1, 1-Dimethylallene as the Prenyl Donor. *J Am Chem Soc* **132**, 12517–12517 (2010).

218. M. Qian, M. A. Liauw, G. Emig, Formaldehyde synthesis from methanol over silver catalysts. *Applied Catalysis A: General* **238**, 211–222 (2003).

219. W.-H. Lin, H.-F. Chang, A study of ethanol dehydrogenation reaction in a palladium membrane reactor. *Catalysis Today* **97**, 181–188 (2004).

220. K. TANI, A. ISEKI, T. YAMAGATA, Efficient transfer hydrogenation of alkynes and alkenes with methanol catalysed by hydrido(methoxo)iridium(III) complexes. *Chem Commun* **0**, 1821–1822 (1999).

221. F. Shibahara, M. J. Krische, Formation of C–C Bonds via Ruthenium-catalyzed Transfer Hydrogenation: Carbonyl Addition from the Alcohol or Aldehyde Oxidation Level. *Chemistry Letters* **37**, 1102–1107 (2008).

222. T. Smejkal, H. Han, B. Breit, M. J. Krische, All-carbon quaternary centers via ruthenium-catalyzed hydroxymethylation of 2-substituted butadienes mediated by formaldehyde: beyond hydroformylation. *J Am Chem Soc* **131**, 10366–10367 (2009).

223. D. Beaupere, L. Nadjo, R. Uzan, P. Bauer, New aspects of the transfer hydrogenation of α, β-unsaturated ketones by alcohols in the presence of hydridotetrakis (triphenylphosphine)rhodium(I): Part II. 1H NMR study and isotope effects. *Journal of Molecular Catalysis* **20**, 185–193 (1983).

224. D. Beaupere, P. Bauer, L. Nadjo, R. Uzan, Transfer hydrogenation between alcohols and α,β unsaturated ketones with RhH(PPh3)4 as catalyst. Evidence for regiospecificity and an unusual rate-limiting step. *Journal of Organometallic Chemistry* **238**, C12–C14 (1982).

225. C. P. Casey, J. B. Johnson, Kinetic isotope effect evidence for a concerted hydrogen transfer mechanism in transfer hydrogenations catalyzed by [p-(Me2CH) C6H4Me] Ru-(NHCHPhCHPhNSO2C6H4-p-CH3). *The Journal of Organic Chemistry* **68**, 1998–2001 (2003).

226. J. B. Johnson, J.-E. Bäckvall, Mechanism of ruthenium-catalyzed hydrogen transfer reactions. Concerted transfer of OH and CH hydrogens from an alcohol to a (Cyclopentadienone)ruthenium complex. *The Journal of Organic Chemistry* **68**, 7681–7684 (2003).

227. C. A. Sandoval, T. Ohkuma, K. Muñiz, R. Noyori, Mechanism of asymmetric hydrogenation of ketones catalyzed by BINAP/1,2-diamine-rutheniumII complexes. *J Am Chem Soc* **125**, 13490–13503 (2003).

228. N. Pannetier *et al.*, Kinetics and mechanism of ruthenacycle-catalyzed asymmetric hydrogen transfer. *Organometallics* **27**, 5852–5859 (2008).

229. P. O. Stoutland, R. G. Bergman, S. P. Nolan, C. D. Hoff, The thermodynamic driving force for C-H activation at iridium. *Polyhedron* **7**, 1429–1440 (1988).

230. G. Sabitha, C. S. Reddy, J. S. Yadav, Total syntheses of the highly potent anti-cancer polyacetylenes,(S)-18-hydroxyminquartynoic acid,(S)-minquartynoic acid and (E)-15, 16-dihydrominquartynoic acid. *Tetrahedron Letters* **47**, 4513–4516 (2006).

231. G. Posner *et al.*, Malaria-infected mice are cured by oral administration of new artemisinin derivatives. *Journal of medicinal chemistry* **51**, 1035–1042 (2008).

232. P. Garcia *et al.*, Synthesis of Tricyclic Fused 3‐Aminopyridines through Intramolecular CoI‐Catalyzed [2+ 2+ 2] Cycloaddition between Ynamides, Nitriles, and Alkynes. *Chem. Eur. J.* **15**, 2129–2139 (2009).

233. I. S. Kim, M. J. Krische, Iridium-catalyzed hydrocarboxylation of 1,1-dimethylallene: Byproduct-free reverse prenylation of carboxylic acids. *Org Lett* **10**, 513–515 (2008).

234. F. H. Westheimer, The Magnitude of the Primary Kinetic Isotope Effect for Compounds of Hydrogen and Deuterium. *Chem Rev* **61**, 265–273 (1961).